



**HAL**  
open science

# Design of label-free immunosensors : from surface functionalization to analyte detection

Yacine Mazouzi

► **To cite this version:**

Yacine Mazouzi. Design of label-free immunosensors : from surface functionalization to analyte detection. Analytical chemistry. Sorbonne Université, 2021. English. NNT : 2021SORUS344 . tel-04348084

**HAL Id: tel-04348084**

**<https://theses.hal.science/tel-04348084v1>**

Submitted on 16 Dec 2023

**HAL** is a multi-disciplinary open access archive for the deposit and dissemination of scientific research documents, whether they are published or not. The documents may come from teaching and research institutions in France or abroad, or from public or private research centers.

L'archive ouverte pluridisciplinaire **HAL**, est destinée au dépôt et à la diffusion de documents scientifiques de niveau recherche, publiés ou non, émanant des établissements d'enseignement et de recherche français ou étrangers, des laboratoires publics ou privés.

# Sorbonne Université

Ecole doctorale 397 – Physique et Chimie des Matériaux

*Laboratoire de Réactivité de Surface (LRS) – UMR 7197*

## **Design of label-free immunosensors: from surface functionalization to analyte detection**

Par Yacine Mazouzi

Thèse de doctorat de Physique et Chimie des Matériaux

Dirigée par Souhir Boujday

Présentée et soutenue publiquement le 15 Décembre 2021

Devant un jury composé de :

<b>Mme Dominique Costa</b>	Directrice de Recherche	Rapportrice
<b>Mme Thérèse Leblois</b>	Professeure	Rapportrice
<b>Mr Vincent Humblot</b>	Chargé de Recherche	Examineur
<b>Mr Olivier Pluchery</b>	Professeur	Examineur
<b>Mme Michèle Salmain</b>	Directrice de Recherche	Examinatrice
<b>Mme Anne Vallée</b>	Maître de Conférences	Examinatrice
<b>Mme Souhir Boujday</b>	Professeure	Directrice de thèse



“Hold yourself responsible for a higher standard than anybody else expects of you. Never excuse yourself. Never pity yourself. Be a hard master to yourself and be lenient to everybody else.”

---

**Henry Ward Beeche**





# Outline

General Introduction .....	1
<b>Chapter 1. Strategies for label-free immunosensors engineering on gold and silica surfaces .</b>	<b>5</b>
1.1 Introduction .....	7
1.2 Overview on immunosensors .....	8
1.2.1 Antibody and its fragments.....	8
1.2.2 Brief history on antibody and its applications in biology and medicine.....	9
1.2.3 Immunosensors and detection strategies.....	11
1.2.4 Challenges with antibody immobilization in immunosensor engineering.....	12
1.3 General functionalization strategies for antibody immobilization .....	13
1.3.1 Physisorption .....	14
1.3.2 Chemisorption <i>via</i> antibody modification .....	16
1.3.3 Antibody immobilization on modified surfaces .....	17
1.3.3.1 Covalent-based strategies .....	17
1.3.3.1.1 Self-assembled monolayers (SAMs).....	17
1.3.3.1.2 Polymers.....	19
1.3.3.1.3 Crosslinking strategies .....	20
1.3.3.2 Affinity-based strategies.....	24
1.3.3.2.1 Avidin-biotin strategy .....	24
1.3.3.2.2 Fc-binding Protein A/G.....	25
1.3.4 Conclusion of the section: comparison of immobilization strategies .....	27
1.4 Specificity in functionalization to immunosensor design.....	31
1.4.1 Mixed SAMs.....	31
1.4.2 Strategies to prevent non-specific adsorption in immunosensor .....	32
1.4.2.1 Polyethylene glycol (PEG) to prevent non-specific interactions .....	32
1.4.2.2 Blocking functional groups to prevent non-specific adsorption.....	33
1.4.2.3 Adsorption of BSA to prevent non-specific interaction .....	33
1.5 Conclusion .....	34
<b>Chapter 2. An experimental study of chain length and terminal group effects on the organization of thiolate Self-Assembled Monolayers (SAMs) onto gold surfaces.....</b>	<b>47</b>
2.1 Introduction.....	49
2.2 Experimental procedure.....	50
2.3 Results and discussion .....	51
2.3.1 Effect of chain length.....	51
2.3.2 Effect of terminal group and pH of functionalization.....	55
2.4 Conclusion .....	63
2.5 Supporting Information .....	67

<b>Chapter 3. Surface charge of acid terminated thiolate SAMs on gold</b> .....	86
3.1 Introduction.....	88
3.2 Experimental procedure.....	89
3.3 Results and discussion.....	90
3.3.1 Surface characterization.....	90
3.3.2 Electrokinetic measurements.....	92
3.4 Conclusion.....	95
3.5 Supplementary Information.....	98
<b>Chapter 4. Design and analytical performances of a diclofenac biosensor for water resources monitoring</b> .....	100
4.1 Introduction.....	100
4.2 Experimental procedure.....	101
4.2.1 Anti-diclofenac antibody binding test and regeneration.....	101
4.2.2 Combined QCM-D and LSPR measurements.....	102
4.2.3 Competitive assay for diclofenac detection in buffer.....	102
4.2.4 Quantification of diclofenac in surface water samples.....	102
4.3 Results and discussion.....	103
4.3.1 Surface functionalization.....	103
4.3.2 Biosensor design and regeneration.....	105
4.3.3 Combined QCM-D & LSPR measurements.....	107
4.3.4 DCF Biosensing in buffers.....	108
4.3.5 DCF quantification in surface water samples.....	111
4.4 Conclusion.....	114
4.5 Supporting Information.....	118
<b>Chapter 5. A rapid and efficient method for label-free immunosensing of extracellular vesicle subtypes</b> .....	138
5.1 Introduction.....	140
5.2 Results and discussion.....	142
5.2.1 EVs physisorption on antibody-free substrates.....	143
5.2.2 Immunosensing of 7Q/7Q EVs with QCM-D.....	145
5.2.3 Immunosensing of EVs subtypes with combined QCM-D and NPS methods.....	147
5.3 Conclusion.....	150
5.4 Supplementary Information.....	154
General conclusion and perspectives.....	172
Appendixes.....	
Publications and communications.....	A
PhD-related activities.....	C
Thesis' synopsis ( <i>french</i> ).....	D





## General Introduction

Biosensors are analytical devices able to specifically detect and quantify targets of interest in complex media. Rapid and sensitive detection of molecules of interest is crucial in nowadays' society, as illustrated with the recent development of SARS-Cov2-related biosensors. Regardless of the envisioned application, biosensor composition remains unchanged and comprises the species of interest, *i.e.* the analyte, a bioreceptor able to detect it specifically and sensitively through molecular recognition, and a transducer that will translate the recognition phenomenon into a measurable signal.

Since a universal approach for biosensor engineering does not exist, sensing layer elaboration is crucial to achieve highly specific and sensitive detection platforms. Therefore, mastering the immobilization of the bioreceptor as well as its density and accessibility are imperative.

Thus, it is often necessary to confer a functionality to the surface to allow the grafting of the bioreceptor while avoiding non-specific adsorptions onto the sensor surface.

Immunosensors, *i.e.* biosensors using antibodies as bioreceptors, are one of the most popular classes of biosensors as antibodies offer great affinity toward an analyte with high specificity and selectivity. Yet, antibody adsorption on surfaces raises many challenges to tackle, such as mastering antibody grafting, surface coverage, antibody orientation, and conserved recognition ability. Antibody immobilization to planar surfaces can be addressed using various strategies. Adsorption can simply rely on the physisorption of the antibody on the surface or adopt more elaborated routes *via* antibody chemisorption. The latter is often preferred since it offers higher antibody grafting with conserved detection ability and allows enhanced biorecognition ability and sensor performances. Chemisorption strategies involved antibody chemisorption *via* modification of its functional groups or surface modifications with covalent or affinity-based approaches.

Self-assembled monolayers (SAMs) are one of the most investigated strategies since they offer tremendous versatility related to the nature of the anchoring organic molecules or substrates composing the SAMs. Ranging from alkanethiols on metallic surfaces (*e.g.* gold) to organosilicon on hydroxylated surfaces (*e.g.* SiO<sub>2</sub>/Si) and carboxylic acids and alkyl phosphates on oxide substrates, SAMs can be employed to tether functional groups and provide robust anchorage points for antibody immobilization.

Therefore, this thesis manuscript is composed of five chapters addressing objectives ranging from fundamental aspects to more applied research works.

Fundamental understanding of the organic-inorganic interface during the adsorption of functional molecules at the solid-liquid interface is first tackled and is followed by applicative research projects related to the development of immunosensors using piezoelectric and optical transduction methods for the detection of various analytes.

The first chapter is a literature review tackling surface functionalization strategies to design label-free immunosensors on planar gold and silica surfaces. We review general aspects related to immunosensors as well as a historical perspective on antibodies and key milestones appertained to their applications. Label-free detection configurations are presented with the challenges to overcome when designing immunosensors, *i.e.* antibody density, conserved activity, and orientation, to develop sensitive and reliable biosensing platforms.

Hence, we present various immobilization strategies on planar gold and silica substrates as physisorption and chemisorption. The latter comprised various approaches based on covalent immobilization onto self-assembled monolayers (SAMs) or polymers, as well as affinity-based procedures with avidin-biotin and Fc-binding proteins. In addition, comparative perspective of various immobilization scenarios is also presented. The last section of this review is dedicated to specific features in surface functionalization for immunosensor applications such as mixed SAMs to increase IgG density and sensing ability as well as blocking strategies to avoid non-specific adsorption to provide selective platform detection.

The second chapter of this thesis deals with the effect of chain length and terminal group on the organization of thiolate SAMs on gold surfaces. Both order and coordination mode of sulfur atoms to gold surfaces of alkyl (CH<sub>3</sub>) and carboxylic (COOH) terminated SAMs of increasing chain length were investigated. In addition, we also study the influence of the pH of functionalization of ethanolic solution in the formation of COOH SAMs.

Investigations relied on complementary surface characterization techniques, *i.e.* Water Contact Angle (WCA), Polarization Modulation InfraRed Reflection Absorption Spectroscopy (PM-IRRAS) and X-Ray Photoelectron Spectroscopy (XPS).

The third chapter is a short presentation of the effect of chain length on surface charge of COOH-terminated thiolate SAMs on gold surfaces. Electrokinetic measurements allowed us to

determine the surface isoelectric point (IEP) of functionalized substrates which is suggested to differ from the  $pK_a$  of free molecules in the bulk phase and to evolve with chain length.

The fourth chapter is dedicated to the development of a label-free piezoelectric immunosensor for the quantification of diclofenac (DCF) in river water samples and the related content was published in the journal ACS Sensors in August 2021 (Impact Factor: 7.7).

Indeed, DCF is a non-steroidal anti-inflammatory drug (NSAID) and one of the most consumed pain killers worldwide. Because of inefficient wastewater treatment, DCF is considered as an emerging water pollutant and is often monitored using chromatographic methods. Although these methods are selective and sensitive, they are not easily amenable to on-site detection. In this context, various biosensing setups have been implemented with the only possible assay format being of the competitive type. In this work, the sensing layer was carefully constructed at the surface of silica-coated quartz crystal microbalance with dissipation (QCM-D) sensors with a slight modification regarding DCF immobilization thanks to an optimized activation process. The binding of a monoclonal highly affine anti-DCF antibody was mainly studied using QCM-D measurement. The competitive QCM-D immunosensing device was built and tested in buffer media to determine the analytical performances of the biosensor and employed to quantify DCF in river water samples collected in the Seine and Marne rivers in France.

The last chapter of this manuscript is dedicated to the design of a label-free immunosensor to detect extracellular vesicles (EV) in buffer media using piezoelectric and optical transduction methods, namely with QCM-D and NanoPlasmonic Sensing (NPS). Extracellular vesicles (EVs) are nano-sized secreted particles surrounded by a double-layer lipid membrane and have emerged as key modulators of a wide range of biological processes in normal and disease conditions. As such, EVs are considered as promising circulating biomarkers with strong diagnostic potential to distinguish disease-associated states from normal conditions. In addition, we probed changes in the physico-chemical properties, *i.e.* viscoelastic properties, of small EVs that may occur between normal and disease conditions. Thus, this label-free approach was employed to characterize CD63- and CD81-positive small EVs isolated from mouse striatal cells that are homozygous for normal or mutated Huntingtin (Htt), a protein involved in Huntington's disease.

Ultimately, this thesis manuscript ends with conclusions and perspectives appertained to the work presented herein, ranging from surface functionalization to immunosensors engineering.





---

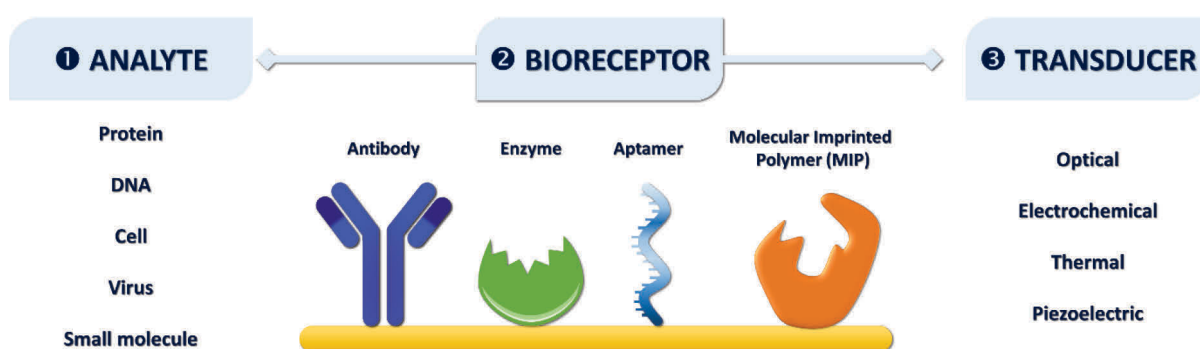
**Chapter 1. Strategies for label-free immunosensors  
engineering on gold and silica surfaces**

---



## 1.1 Introduction

Rapid and sensitive detection of molecules of interest is crucial in nowadays' society, as eloquently exemplified by the recent development of SARS-Cov2-related biosensors<sup>1-3</sup> and wearable biosensing platforms.<sup>4,5</sup> Biosensors, first introduced by Clark and Lyons in the 1960s<sup>6,7</sup>, are analytical devices designed to specifically detect and quantify an analyte in complex media<sup>8-10</sup> and have been implemented for a large number of applications ranging from healthcare<sup>11-13</sup> to food quality control<sup>14-16</sup> and environmental monitoring.<sup>17-19</sup> Regardless of the envisioned application, a biosensor involves the following components (**Figure 1. 1**): the species of interest, *i.e.* the analyte, a bioreceptor able to detect it specifically and sensitively through molecular recognition, *e.g.* antibodies<sup>20,21</sup>, aptamers<sup>22-24</sup>, enzymes<sup>25-28</sup> or molecular imprinted polymers (MIP)<sup>29,30</sup>, and a transducer that will translate the recognition phenomenon into a measurable signal.<sup>31,9,32</sup>



**Figure 1. 1.** Schematic representation of biosensor setup. ❶ Analytes may vary from small molecules<sup>33,34</sup>, to DNA<sup>35</sup> or even more complex targets like proteins<sup>36</sup> and viruses.<sup>37,38</sup> ❷ Bioreceptor nature is often dependent on the target and the envisioned application with for instance the use of antibody<sup>20,21</sup>, enzyme<sup>25,26</sup>, cell<sup>39</sup>, aptamer<sup>22-24</sup> or Molecular Imprinted Polymer (MIP).<sup>29,30</sup> ❸ Transduction techniques are as well related to the application and assay condition, with most widespread techniques being optical<sup>40,41</sup>, electrochemical<sup>42,43</sup> and piezoelectric<sup>44,1</sup> ones.

Immunosensors, *i.e.* biosensors using antibody as bioreceptor, are one of the most popular classes of biosensors as antibodies offer great affinity toward an analyte with high specificity and selectivity.<sup>10,20</sup> These features are also harnessed in the design of immunoassays<sup>45</sup> such as in enzyme-linked immunosorbent assay (ELISA)<sup>46,47</sup> and lateral flow immunoassay (LFIA) tests.<sup>48,49</sup> Nevertheless, these techniques often require expensive reagents and various steps, *e.g.* fixation, detection and revelation stages.

Furthermore, immunosensors gather the previous advantages of immunoassays while offering possible rapid and on-site detection. Yet, antibody adsorption on surfaces raises many challenges to tackle such as mastering antibody grafting, surface coverage, antibody orientation and conserved recognition ability. This review aims at giving an overview of the methods for antibody grafting onto planar surfaces in order to develop sensitive immunosensors, with focus on planar gold and metal oxide surfaces. Since biosensing platforms are not restricted to planar surfaces, we refer to the following relevant references for adsorption of antibodies on spherical and anisotropic nanoparticles for biosensor engineering.<sup>50–53</sup>

In what follows, we review general aspects related to immunosensors with notably the presentation of antibody (IgG) and its fragments structures as well as a historical perspective on antibody and key milestones appertained to its applications. Subsequently, immunosensor and the label free detection configurations are presented with regards to the challenges to overcome when designing immunosensor. Indeed, antibody density, conserved activity and orientation have to be mastered in order to develop sensitive and reliable biosensing platforms. Hence, the following section presents various immobilization strategies on planar gold and silica substrates as physisorption or chemisorption. The latter comprised various approaches based on covalent immobilization onto self-assembled monolayers (SAMs) or polymers, as well as affinity-based procedures with avidin-biotin and Fc-binding proteins. In addition, comparative perspective of various immobilization scenarios is also presented. The last section of this review is dedicated to specific features in surface functionalization for immunosensor applications such as mixed SAMs to increase IgG density and sensing ability as well as blocking strategies to avoid non-specific adsorption in order to provide selective detection.

## 1.2 Overview on immunosensors

### 1.2.1 Antibody and its fragments

Antibodies or immunoglobulins (Ig) are glycoproteins produced by the immune system in response to exogenous species called antigens.<sup>54</sup> They offer high affinity toward a specific antigen, similarly to the lock-and-key complex formation introduced by Fisher in 1894<sup>55,56</sup>, and are classified into five main types: namely IgA, IgD, IgE, IgM and IgG which is the most abundant type in human serum accounting for ~70%. IgG are Y-shaped proteins with dimensions of  $14 \times 12 \times 4$  nm and are composed of four polypeptide chains with two heavy chains (~ 50 kDa) and two light chains (~ 25 kDa) linked to one another through non-covalent

and disulfide bridges, notably in the hinge region (**Figure 1. 2**).<sup>57</sup> The IgG tail is known as the fragment crystallizable domain (Fc) and the double-ended parts of the antibody as the antigen-binding fragments (Fab). The Fab domain displays a hypervariable region forming the antigen-binding site, *i.e.* paratope, responsible for the target specific binding *via* non-covalent interactions, *e.g.* hydrogen bonding, electrostatic forces, hydrophobic interactions and Van der Waals forces. In contrast, the antibody-binding sites present on an antigen are called epitopes. Generally, a protein antigen comprises more than one epitope. Furthermore, research works were also devoted to the engineering of antibody fragments in order to reduce the size of the biorecognition element using various strategies, with notably the development of monovalent fragment antigen binding (Fab) and single chain fragment variable (scFv).<sup>58–60</sup>

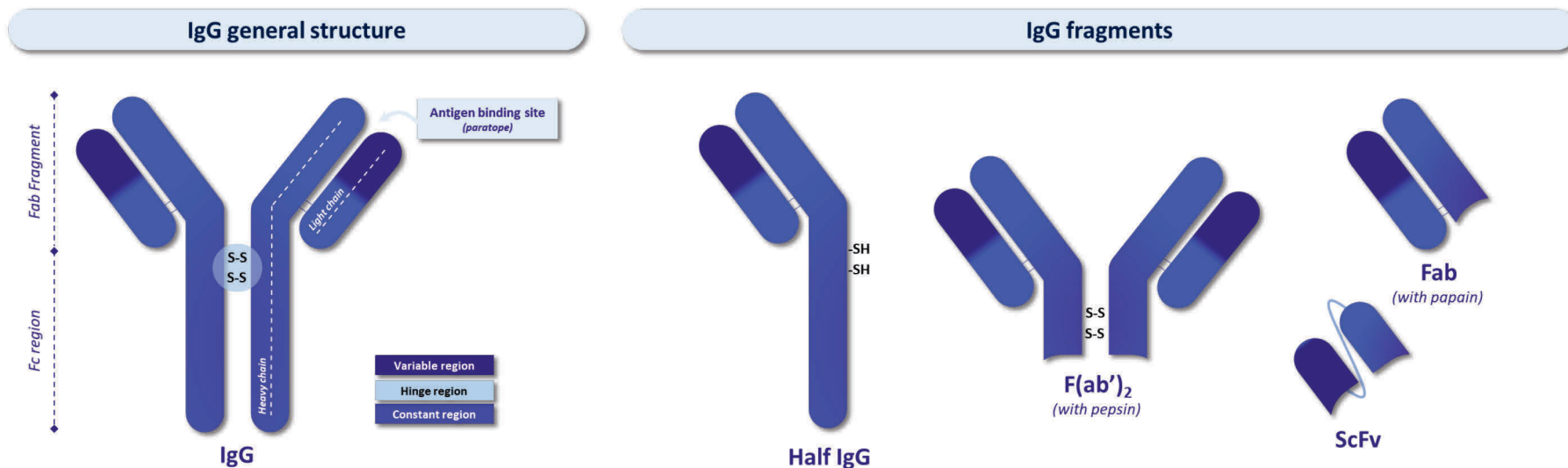
### 1.2.2 Brief history on antibody and its applications in biology and medicine

Key milestones related to antibodies and their applications in therapy<sup>61,62</sup>, *e.g.* antibody-drug conjugates<sup>63,64</sup>, and immunosensors<sup>20,21</sup> since the 1900s are presented in **Figure 1. 2**.

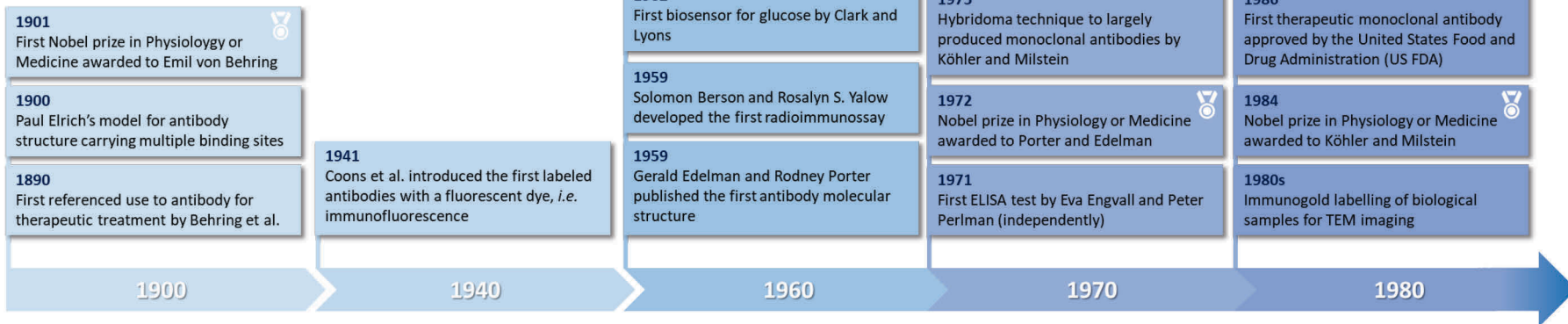
The first reference to antibody use in medicine dates from the 1900s with notably work from Behring *et al.* on animals' immunization from diphtheria and tetanus<sup>65</sup> which awarded him later the first Nobel prize in Physiology or Medicine in 1901.<sup>66</sup>

Forty years later, Albert H. Coons developed a pioneering method consisting in labeling antibodies with a fluorescent dye to identify antigens present in biological tissues, this work was the birth of immunofluorescence.<sup>67</sup> Few decades later, the general structure of antibody was introduced by Gerald Edelman and Rodney Porter (1959)<sup>68</sup> for which they received the Nobel prize in Physiology or Medicine in 1972.<sup>69</sup>

After digestion of rabbit antibodies with papain, Porter showed that one antibody fragment was found to crystallize, which was later called F<sub>c</sub> fragment for Fragment crystallizable. Thus, it is worth mentioning that within 50 years<sup>70</sup>, thanks to progress in characterization techniques, it was possible to finely decipher antibody structures, *e.g.* works from Harris *et al.* on the structure of mouse IgG (PDB ID: 1IGT, 1IGY)<sup>71,72</sup> and the first resolved structure of a human IgG (PDB ID: 1HZH) in 2001.<sup>73</sup> In the 1960s, a tremendous breakthrough was achieved with the development of immunoassays<sup>45</sup> thanks to the contribution from Solomon Berson and Rosalyn Yalow with the first radioimmunoassay to measure endogenous plasma insulin<sup>74</sup>, which led Rosalyn Yalow to conjointly receive the Nobel prize in Physiology or Medicine<sup>75</sup>, as well as the development of enzyme-linked immunosorbent assays (ELISA) in the 1970s.<sup>76–78</sup>



### Key milestones for antibody and its applications



**Figure 1. 2.** Top panel: General structure of IgG-type antibody and its fragments obtained through reduction for half-IgG or enzymatic cleavages for F(ab')<sub>2</sub> and Fab fragments. Bottom panel: Key milestones for antibody related discoveries and its applications.

Furthermore, another major breakthrough in the immunology field was the development of the hybridoma technique by Köhler and Milstein in 1975 which allowed the large-scale production of monoclonal antibodies<sup>79</sup>, *i.e.* antibodies with monovalent affinity toward a single epitope. This discovery revolutionized antibody applications since it offered higher affine IgG and production of immunoreagents with constant properties, in contrast to polyclonal antibodies, and led them to receive the Nobel Prize in 1984.<sup>80</sup>

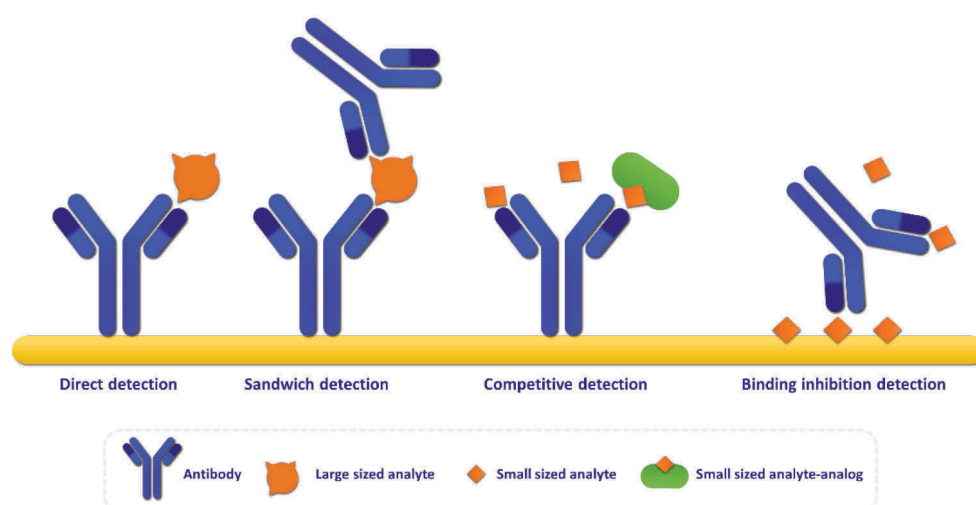
Therefore, new improvements were possible in the following decades such as immunogold labeling of biological samples for Transmission Electron Microscopy (TEM) imaging<sup>81–84</sup>, immunosensors<sup>85–87</sup> and commercialized therapeutic antibodies as a result of the approval by the United States Food and Drug Administration (FDA).<sup>88</sup>

### 1.2.3 Immunosensors and detection strategies

Immunosensor exploits the same features as immunoassays that is high selectivity and affinity toward a target antigen while being user friendly, amenable to on-site detection and often requiring less expensive reagents. Its engineering relies either on the immobilization of an antibody, *i.e.* the biorecognition element, or an analog of the analyte depending on the detection format. Indeed, the antibody molecule and its fragments carry chemical functions such as amine, carboxylic acid and thiol groups allowing grafting onto surfaces.<sup>89</sup>

This immobilization relies either on antibody chemical modification or surface functionalization and will be discussed later in this review. Besides, immunosensor format often depends on the envisioned application, targeted analyte and transducing technique.

Thus, several configurations exist as presented in **Figure 1. 3**.



**Figure 1. 3.** Schematic representation of immunosensor detection formats with from left to right: direct, sandwich, competitive and binding inhibition detection assays.



One of the most investigated strategies relies on the direct immobilization of antibody on the surface of the transducer which will allow to detect an antigen present in the sample thus creating an exploitable signal measured by the transducer. Consequently, in the sandwich format, a second antibody directed toward another epitope can be used to generate an additional detectable signal and enhance the assay sensitivity.<sup>90</sup> Yet, the latter may not be applicable for the detection of small sized analytes since they often carry only one epitope.<sup>91</sup>

Alternatively, small sized analytes can be detected by competitive or binding inhibition assays. In the competitive assay, the antibody is immobilized on the transducer's surface and will be able to interact competitively with the analyte and its analog, *i.e.* an analyte conjugated to a larger molecule. On the other hand, in the binding inhibition assay, antibody is first incubated with the sample containing the analyte. Subsequently, the mixture is flown over the sensor surface covered with an analog of the analyte to which the antibody can competitively bind. In both assays, the binding response is inversely related to the analyte concentration.

### 1.2.4 Challenges with antibody immobilization in immunosensor engineering

An ideal label-free immunosensor should answer specifications related to biosensor performances such as sensitivity, specificity and offer reliable quantitative detection. Furthermore, antibody immobilization raises many challenges to tackle. Besides the conservation of the biological activity of the antibody over ranges of temperature, pH and ionic strengths, mastering its grafting in terms of surface coverage and orientation is crucial.

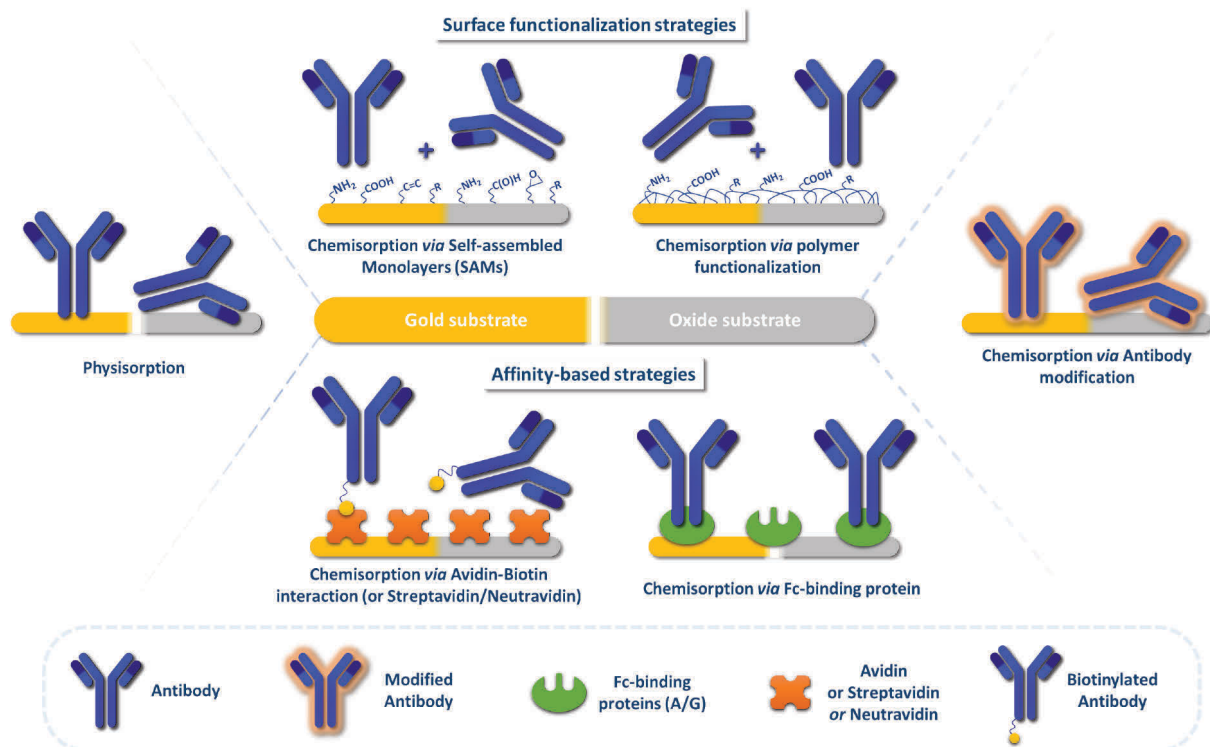
Indeed, surface coverage should be addressed to reach the optimal density of antibody onto the surface to achieve higher recognition capacity as well as to prevent non-specific adsorption from other biomolecules. Conjointly, antibody adsorption might also lead to random orientation on the surface, therefore antibody orientation is a key factor to be addressed in immunosensor engineering. A controlled antibody orientation will maximize paratopes' accessibility to the analyte and lead to enhanced analytical performances. Therefore, this review aims to give an overview of methods for antibody grafting onto planar surfaces in order to develop sensitive immunosensors, with focus on gold and metal oxide (*e.g.* silica) surfaces which are the most investigated surfaces in this field. These surfaces are considered as model substrates and have been historically used for their known surface properties, commercial availability and can be probed with number of surface analytical techniques. Furthermore, these surfaces are well suited to various transduction techniques such as Surface Plasmon Resonance (SPR) and Quartz Crystal Microbalance (QCM).

### 1.3 General functionalization strategies for antibody immobilization

Antibody immobilization to planar surfaces can be addressed using various strategies (Figure 1. 4). Adsorption can simply rely on the physisorption of the antibody on the surface or adopt more elaborated routes *via* antibody chemisorption.<sup>92,93</sup>

The latter is often preferred since it offers higher antibody grafting with conserved detection ability and allows enhanced biorecognition ability and sensor performances.

Chemisorption strategies involved antibody chemisorption *via* modification of its functional groups or surface modifications with covalent or affinity-based approaches.

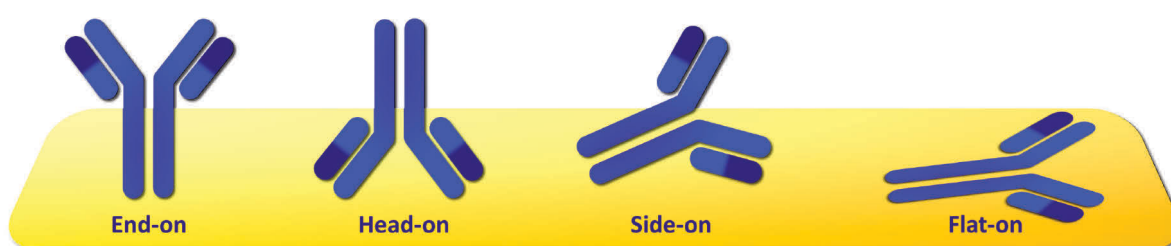


**Figure 1. 4.** Strategies for antibody immobilization onto planar surfaces: *via* physisorption or chemisorption *via* antibody modification, surface functionalization using Self-Assembled monolayers (SAMs) or polymers and affinity-based immobilization *via* Avidin-Biotin and Fc-binding protein strategies.

### 1.3.1 Physisorption

Direct antibody physisorption onto non-coated or functionalized surfaces is the most straightforward strategy since it does not require modifications of either the antibody or the substrate surface. Antibody residues will loosely interact with the surface through hydrogen bonding, electrostatic, hydrophobic and Van der Waals interactions.

Nevertheless, this strategy does not allow to control antibody orientation and might lead to random adsorption configurations and reduced sensing ability, *i.e.* end-on, head-on, side-on and flat-on orientations (**Figure 1. 5**).<sup>94</sup>

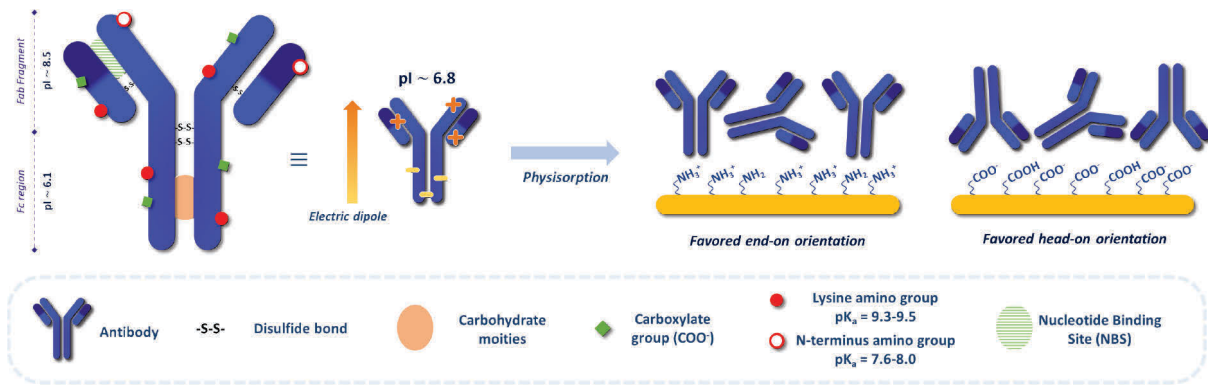


**Figure 1. 5.** Possible orientations of antibody during random adsorption with end-on, head-on, side-on and flat-on orientations.

Chen *et al.* investigated antibodies adsorption onto functionalized gold surfaces bearing various chemical groups, *i.e.* amine ( $\text{NH}_2$ ) and carboxylic acid ( $\text{COOH}$ ) groups.

The highest antigen/antibody ratio was obtained for the  $\text{NH}_2$  surface chemistry, indicating that the pH of immobilization and related surface charge affect the antibody binding ability as well as its orientation as probed by Surface Plasmon Resonance (SPR) and Atomic Force Microscopy (AFM).<sup>95</sup> Indeed, antibody adsorption was performed in a low ionic strength buffer at pH close to the isoelectric point (pI) of antibody (pH 6.8), comprised between the ones of its  $\text{F}(\text{ab}')_2$  and Fc fragments (**Figure 1. 6**).

Therefore, antibody can interact less randomly with either positively or negatively charged surfaces. Subsequently, time-of-flight secondary ion mass spectrometry (ToF-SIMS) and AFM were employed to investigate antibody orientation onto functionalized gold and silicon surfaces.<sup>96,97</sup> Wang *et al.* suggested that antibody possessing a dipolar moment preferentially adopt a “head-on” orientation onto  $\text{COOH}$ -terminated surface and an “end-on” configuration onto  $\text{NH}_2$ -terminated one, which are respectively negatively and positively charged at neutral pH (**Figure 1. 6**).<sup>96</sup>



**Figure 1. 6.** Main functional groups present on immunoglobulin G (IgG). Isoelectric point (pI) for IgG and its Fab and Fc domains. At neutral pH, IgG presents an electric dipole and its physisorption can be electrostatically oriented on amine (NH<sub>2</sub>) and carboxylic acid (COOH) terminated surfaces, respectively positively and negatively charged. Adapted from <sup>95-97</sup>

Moreover, antibodies are also known to adsorb non-specifically on hydrophobic surfaces as shown by Wiseman *et al.* on alkane-terminated gold substrate.<sup>98</sup> In this work, anti-streptavidin IgG adsorption was monitored *in-situ* using quartz crystal microbalance with dissipation (QCM-D) and its orientation was probed using streptavidin and protein G, referred as orientation probes, which bind respectively the Fab and Fc domains.

Thus, preadsorbing streptavidin and protein G prior to IgG immobilization led respectively to head-on and side-on orientations. Moreover, the authors showed that IgG adsorption on bare hydrophobic substrate led to sub-monolayer formation at low IgG coverage with limited binding of streptavidin and protein G. At higher concentration, orientation probes bound to adsorbed IgG and saturated at values of 0.45 streptavidin/IgG and 0.95 Protein G/IgG. These results suggested a favored flat-on orientation at low coverage which linearly evolved with IgG concentration leading to end-on or side-on orientations.

Therefore, the physisorption approach leads to random antibody immobilization but can be somehow controlled *via* electrostatic and/or hydrophobic interactions.

Yet, this strategy relies on weak individual interactions which can lead to antibody desorption and is limited by working conditions, *e.g.* pH, ionic forces, therefore chemisorption *via* antibody or surface modification is often preferred.

### 1.3.2 Chemisorption *via* antibody modification

Antibody chemisorption offers higher stability since it involves covalent bonding and can be addressed through (i) modification of antibody functional groups and/or (ii) surface functionalization. The former has mainly been studied in the literature on planar gold surfaces and gold nanoparticles.<sup>52</sup> Indeed, antibodies carry various functional groups related to its amino acid composition that can be used for surface immobilization.

Among the large variety of reactive groups, *e.g.* hydroxyl from serine and threonine, phenol from tyrosine or imidazole from histidine, more investigations have been dedicated to antibody chemisorption using amine groups from N-terminus and lysines, carboxylic acid from C-terminus, glutamic acid and aspartic acid residues and also to thiol group from cysteine residues.<sup>89,93</sup>

For direct immobilization on gold surfaces, chemisorption exploits the strong affinity between sulfur and gold to form a strong covalent bond.

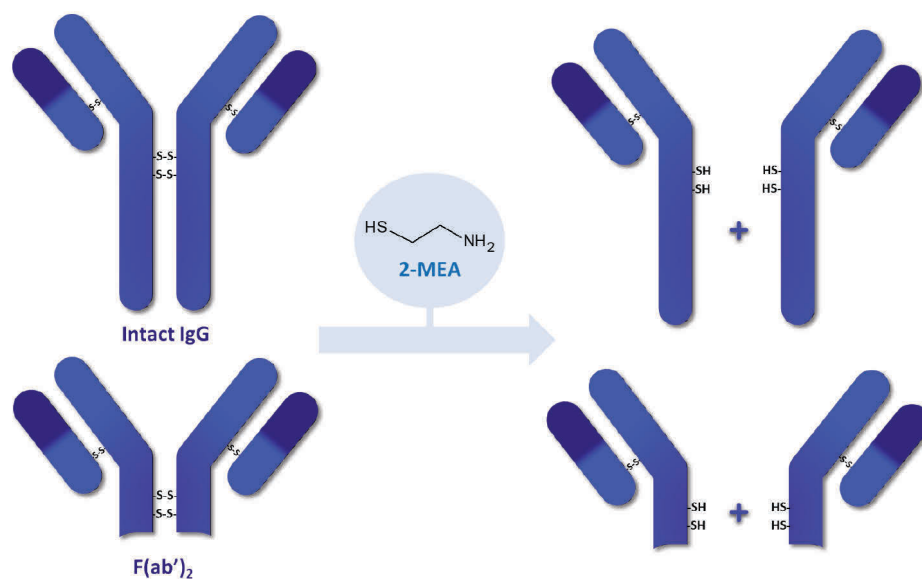
Nevertheless, no free sulfhydryl (R-SH) group is present on IgG, so its introduction can be conducted either *via* modification of (i) amine groups from lysine residues, (ii) carbohydrates groups or (iii) nucleotide binding sites or reduction of disulfide (S-S) bridges in the hinge region.<sup>52</sup> For instance, the photochemical immobilization technique (PIT) is an effective strategy to immobilize antibodies onto gold surfaces while preserving its structural and function integrities under UV irradiation.<sup>99</sup>

Under UV light ( $\sim 250$  nm), aromatic amino acids, *e.g.* tryptophan residues, first absorb UV radiation and release it through relaxation to nearby disulfide bridges leading to their cleavage and ultimately to free reactive thiol groups.

PIT is known to be selective to some cysteine-cysteine/tryptophan (Cys-Cys/Trp) residues triads.<sup>100,101</sup> Della Ventura *et al.* demonstrated that PIT was able to generate 8 reduced thiols groups in order to immobilize antibody in an oriented manner, *i.e.* end-on orientation.<sup>99</sup>

Authors also showed that PIT treated anti-IgG antibody can be immobilized on gold-coated quartz crystal microbalance (QCM) substrate and exhibited better sensitivity than non-activated antibodies.<sup>102</sup>

Furthermore, selective reduction of endogenous disulfide bonds of intact IgG or F(ab')<sub>2</sub> using 2-mercaptoethylamine (2-MEA) is another strategy to respectively create half-antibody bearing reactive sulfhydryl groups in the hinge region (**Figure 1. 7**).



**Figure 1. 7.** Disulfide bridges reduction in the hinge region using 2-mercaptoethylamine (2-MEA) from intact IgG and (Fab')<sub>2</sub> to produce antibody fragments carrying reactive thiol functions.

### 1.3.3 Antibody immobilization on modified surfaces

#### 1.3.3.1 Covalent-based strategies

Surface functionalization is a common approach to tailor the interface properties for protein adsorption like for instance strategies in anti-biofilm and antibacterial coatings<sup>103</sup> or on the other hand for immunosensor engineering. While the former mainly aims at preventing protein adsorption on surfaces, the latter focuses on increasing antibody density to improve sensing performances.

##### 1.3.3.1.1 Self-assembled monolayers (SAMs)

Self-assembled monolayers (SAMs) are one of the most investigated strategies since they offer tremendous versatility related to the nature of the anchoring organic molecules or substrates composing the SAMs. Ranging from alkanethiols on metallic surfaces (*e.g.* gold) to organosilicon on hydroxylated surfaces (*e.g.* SiO<sub>2</sub>/Si) and carboxylic acids and alkyl phosphates on oxide substrates<sup>104–106</sup>, SAMs can be employed to tether functional groups and provide robust anchorage points for antibody immobilization. In this section, we review the most investigated substrates used for immunosensor design, namely gold and oxides, and therefore we addressed the corresponding surface functionalization.

SAMs formed from alkylthiol molecules on gold surface, are one the most investigated systems on metallic surfaces since they are commercially available and are used in number of applications including biomolecules adsorption<sup>110–112</sup> and biosensors.<sup>113,114</sup>

Experimental conditions and characterization of thiolate SAMs on gold were extensively reviewed in the literature.<sup>105,115,116</sup> Briefly, thiolate SAMs are commonly formed from an ethanolic solution of thiol / disulfide in the mM range in which a gold substrate is immersed for a controlled time.

After chemisorption of the thiolate headgroup to the surface thanks to the strong coordination of sulfur to noble metal surfaces, the SAMs' alkyl chains reorganize to form a dense layer exhibiting terminal groups at the solid / air or liquid interface.

These surface functions can be used directly or undergo further modifications with crosslinking agents for antibody immobilization. Moreover, terminal groups and chain length of such molecules can be tuned in order to control surface properties such as wettability<sup>115,116</sup> for protein grafting.<sup>119–121</sup>

Modifications of hydroxyl and oxide substrates can be achieved using a wide range of organic molecules, *e.g.* catechol, carboxylate or phosphonate, yet alkyl alkoxy silanes chemisorption remains the most investigated strategy.<sup>106</sup> Organosilanes adsorption onto surfaces bearing hydroxyl groups (OH) relies on hydrolysis and condensation reactions at the liquid-solid interface to form covalent bonds with the substrate.

In contrast to thiolate SAMs on gold, organosilanes SAMs formation involves more complex reactions and requires more stringent experimental conditions. Indeed, anhydrous organic solvents, *e.g.* toluene, are often preferred to carry out the functionalization since water content influences the reaction mechanism and therefore affects the surface topography and quality of the silane layer.<sup>122</sup>

Yet similarly to thiolate SAMs, functional groups carried by organosilane molecules are useful for further biomolecules grafting with for instance the use of 3-aminopropyltriethoxysilane (APTES).<sup>123</sup>

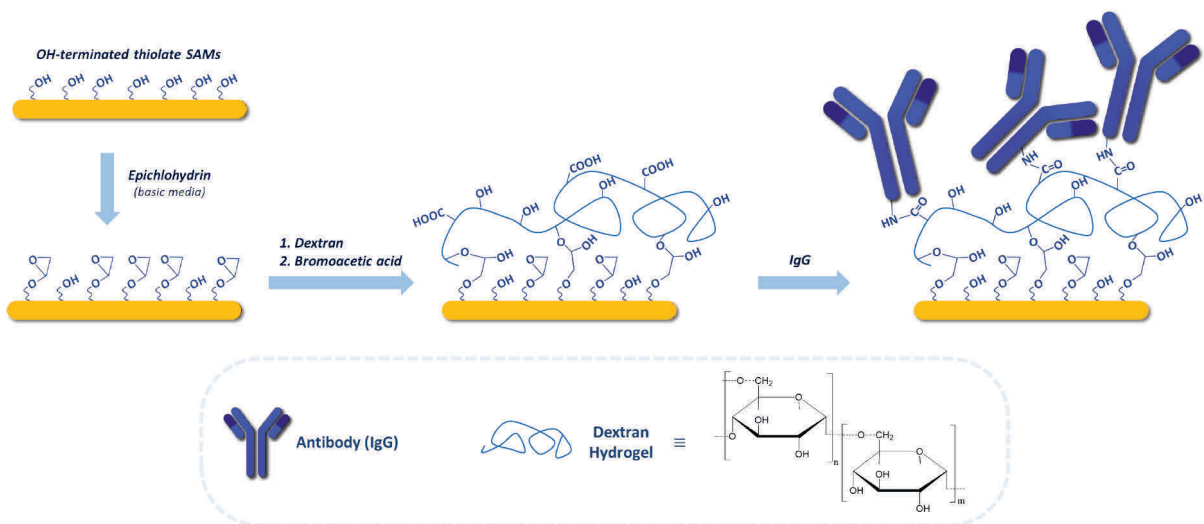
Antibody immobilization onto functionalized surfaces carrying reactive groups often relies on crosslinking agents depending on the chosen immobilization strategy, *e.g.* surfaces covered with amine, carboxylic acid or epoxy groups. On the other hand, PIT does not require such a multi-step process and has successfully been implemented for spatially oriented antibody grafting onto thiol-terminated silicon or silica surfaces.<sup>124</sup>



### 1.3.3.1.2 Polymers

Similarly, strategies using polymers were investigated to introduce reactive functional groups onto surfaces with dextran and polyethylene glycol (PEG) which are polymers composed of glucose and ethylene oxide repeating units, respectively.<sup>125,126</sup> Polymers can adopt linear or more complex structures such as branched three-dimensional (3D) arrangements, offering a higher number of anchoring points for antibody grafting. These commercial polymers are mostly hydrophilic, known to prevent non-specific adsorption of biomolecules and to provide a great variety of functional groups according to the nature of the polymer nature<sup>127</sup>, *e.g.* Dextran<sup>128–132</sup> and PEG.<sup>133–135</sup>

One of the most successful examples relying on the use of dextran over a SAM composed of 16-mercaptohexadecanol on gold chips was developed by the Biacore company for SPR chips elaboration. Briefly, the hydroxyl terminated SAMs is treated with epichlorohydrin in basic medium to generate epoxy groups which are used to covalently attach Dextran *via* its hydroxyl groups. After treatment with bromoacetic acid, the Dextran hydrogel carries in average one carboxyl group per glucose unit, used to conjugate antibody *via* its amine groups after activation (Figure 1. 8).<sup>128</sup>



**Figure 1. 8.** Schematic representation of surface functionalization strategy using thiolate SAMs on gold and carboxymethylated dextran hydrogel for IgG immobilization. Adapted from <sup>128</sup>

Tabasi *et al.* investigated immobilization of IgG1 on carboxyl (COOH) and amine (NH<sub>2</sub>) modified dextran for SPR chips design under external vertical electric field (EVEF) assisted technique.<sup>136</sup>



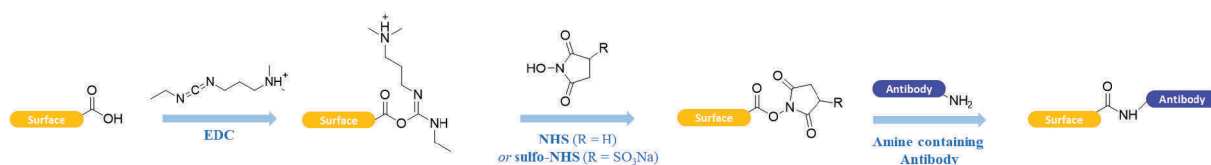
Enhanced antibody orientation and toxin detection were obtained on  $\text{NH}_2$ -terminated dextran compared to its  $\text{COOH}$ -terminated analog attributed to interaction with carboxylic groups from Fc domain. Moreover, other strategies involve molecular imprinting of polymer to form cryogels for antibody immobilization. These cryogels have been used to specifically bind IgG from human plasma<sup>137,138</sup> and for oriented immobilization antibody *via* its Fc domain using a poly(hydroxyethyl methacrylate), PHEMA cryogel.<sup>139</sup>

### 1.3.3.1.3 Crosslinking strategies

As introduced earlier in this review, strategies have been developed to introduce reactive functional groups onto surfaces to achieve antibody immobilization with the most common being carboxylic acid, amine, epoxy and sulphydryl functional groups. In this section we will discuss crosslinking strategies employed for surface reactive groups. Of course, the same approach is applicable to antibody functional groups, yet depending on the experimental conditions, *e.g.* solvent, temperature, the antibody structure and its activity can be altered, making surface modifications the preferred approach. The most widely investigated crosslinking approaches for carboxyl and amine surface groups are presented in this section.

Alternative strategies involving other chemical groups, *e.g.* hydroxyl and thiol functions are not discussed in this section and we refer to the relevant literature and references therein.<sup>89,140</sup>

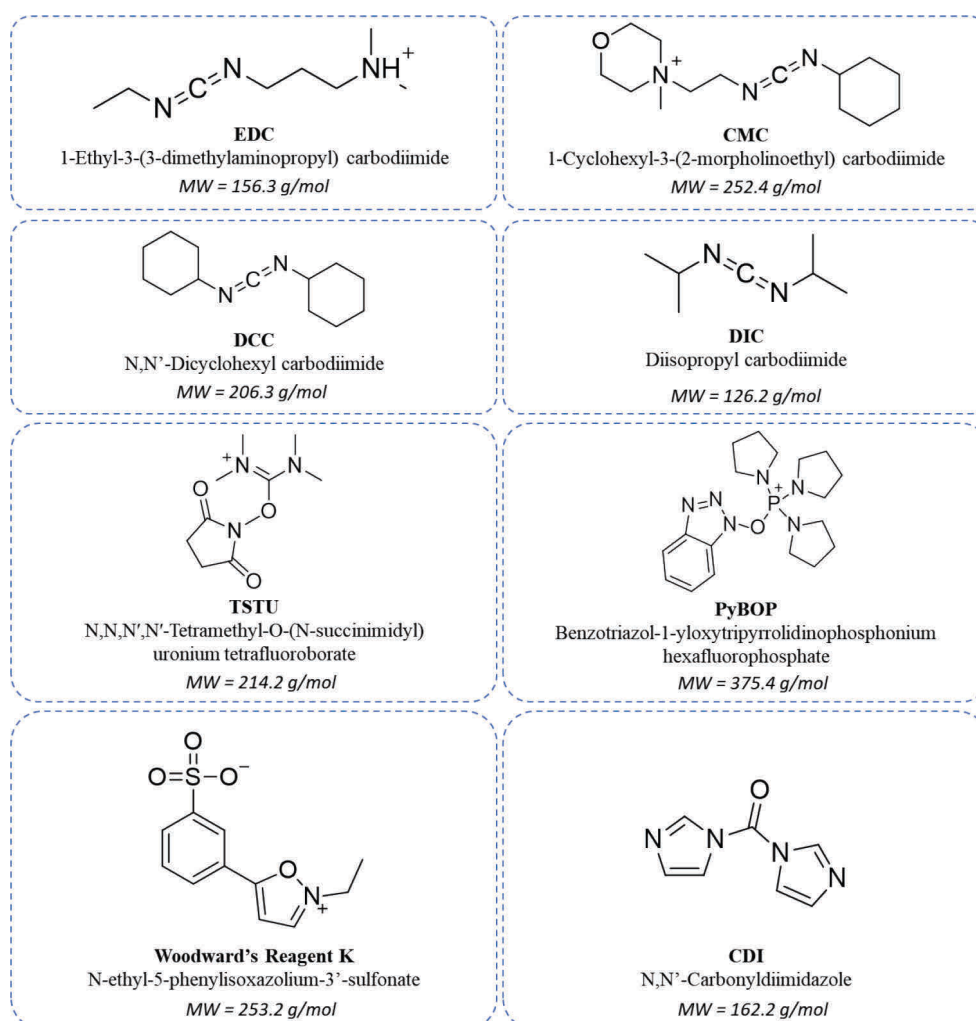
Carboxyl ( $\text{COOH}$ ) terminated surfaces are often crosslinked to amine groups carried by antibody using zero-length crosslinker which mediate amide bond formation without any additional atoms. The most widespread approach uses carbodiimide to form this amide bond with for instance 1-ethyl-3-(3-dimethylaminopropyl) carbodiimide (EDC) coupled with *N*-hydroxysuccinimide (NHS) or its water-soluble derivative sulfo-NHS (**Figure 1.9**).



**Figure 1.9.** Antibody immobilization through its amine functional groups ( $\text{NH}_2$ ) on carboxylic ( $\text{COOH}$ )-terminated surface using EDC/NHS strategy.

In the strategy using only EDC, the carbodiimide crosslinker can react with the carboxylic function to form a reactive o-acylurea intermediate which will react with the primary amine carried by the antibody to form amide bond and urea by-product.

Nevertheless, the reactive intermediate can undergo hydrolysis leading to deactivation and was also shown to react slowly with amine groups. Therefore, combination with NHS or sulfo-NHS allows to increase the yield in amide bond formation. Other carbodiimide species can be used to achieve the same goal, *i.e.* formation of strong amide bond with 1-cyclohexyl-3-(2-morpholinoethyl) carbodiimide (CMC) or in organic solvent with N,N'-dicyclohexyl carbodiimide (DCC) and diisopropyl carbodiimide (DIC) (**Figure 1. 10**). The nature of the carbodiimide crosslinking agent, its concentration and experimental conditions (solvent) are known to influence activation rate and efficiency.<sup>141,142</sup> In addition, other strategies involving Woodward's reagent K, N,N'-carbonyldiimidazole (CDI), N,N,N',N'-tetramethyl-O-(N-succinimidyl)uronium tetrafluoroborate (TSTU) or benzotriazol-1-yloxytripyrrolidinophosphonium hexafluorophosphate (PyBOP) can also be of use for COOH crosslinking and antibody immobilization *via* its amine groups.

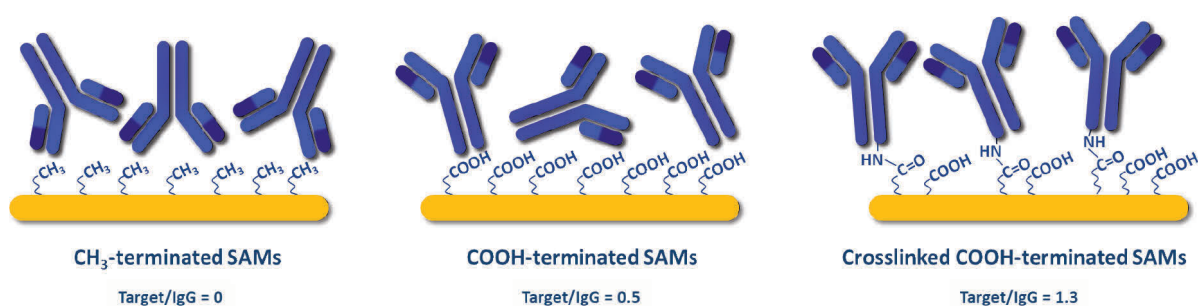


**Figure 1. 10.** Main crosslinking agents used on COOH-terminated surface

Lebec *et al.* compared IgG adsorption onto alkyl (CH<sub>3</sub>), carboxyl (COOH) and crosslinked carboxylic (COOH – EDC/NHS) terminated thiolate SAMs on gold and demonstrated that IgG orientation and sensing ability vary depending on the chosen method (**Figure 1. 11**).<sup>121</sup>

Analyses with combined ToF-SIMS and Principal Component Analysis (PCA) showed a preferential head-on orientation on the CH<sub>3</sub> layer, on the other hand IgG displayed end-on orientation on the COOH and crosslinked layer leading to accessible recognition sites (paratopes). In addition, QCM-D and infrared (IR) spectroscopy proved that a higher amount of antibodies was adsorbed on the CH<sub>3</sub>-terminated SAMs through hydrophobic interactions yet leading to nil target detection, in agreement with the determined antibody orientation.

In contrast, on the COOH-terminated SAMs, IgG adsorbed similarly but showed greater sensing ability with a 2.6-fold increased detection for IgG immobilized on crosslinked layer as determined with QCM-D and IR.

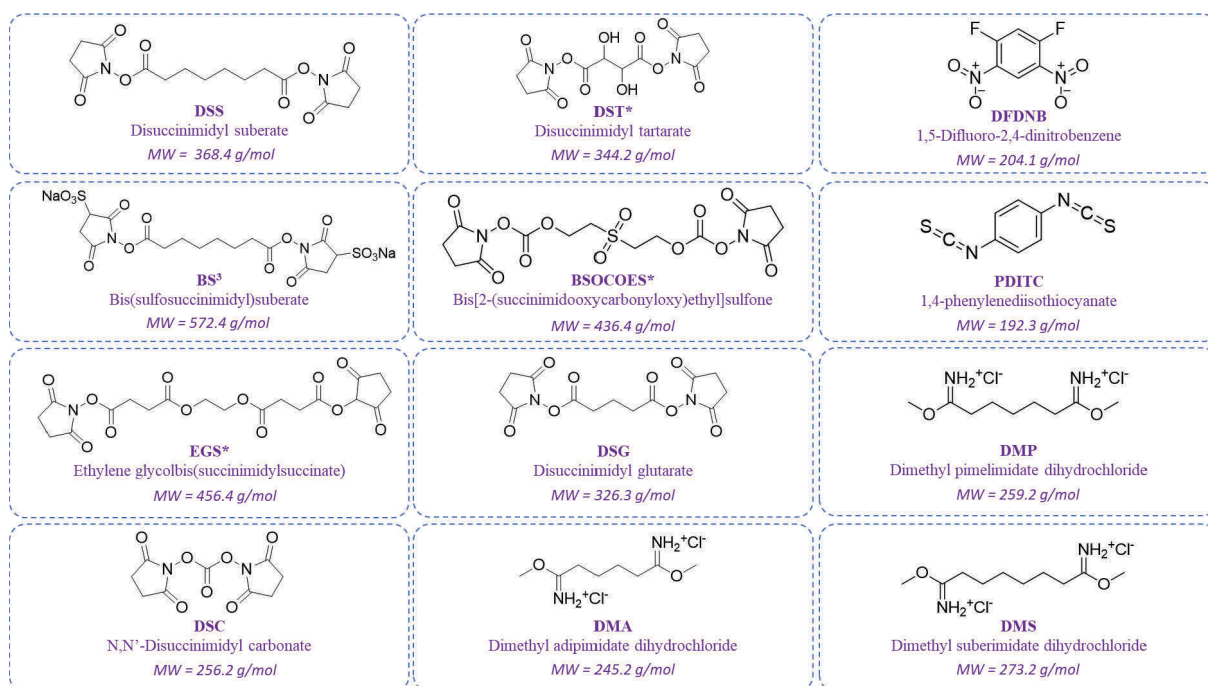


**Figure 1. 11.** Schematic representation of IgG immobilization strategies on alkane (CH<sub>3</sub>)-terminated, COOH-terminated and crosslinked (with EDC/NHS) COOH-terminated thiolate SAMs on gold. Adapted from <sup>121</sup>

Amine (NH<sub>2</sub>) terminated surfaces are also widely used for antibody immobilization and can be crosslinked to antibody NH<sub>2</sub>, or COOH functional groups as discussed earlier.

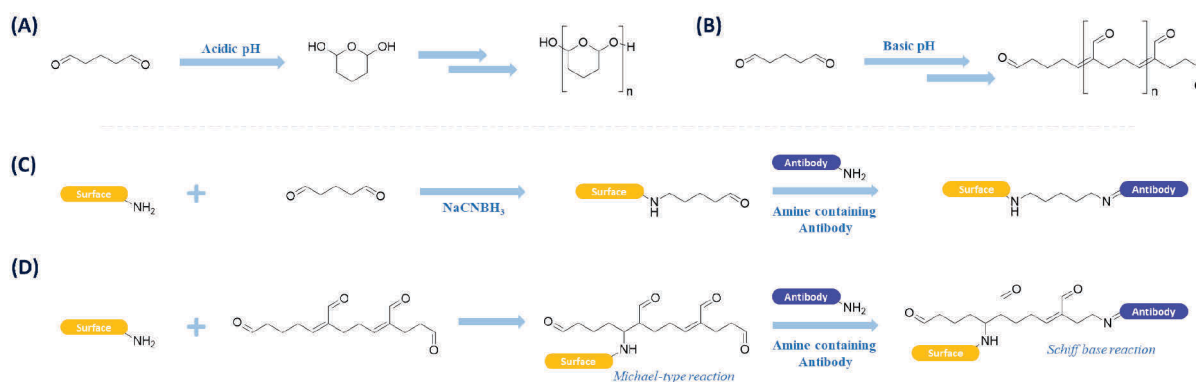
Several strategies exist using a variety of homobifunctional crosslinkers containing amine-reactive NHS ester, imidoester or isothiocyanate groups as presented in **Figure 1. 12**, *e.g.* disuccinimidyl suberate (DSS), dimethyl adipimidate (DMA) and 1,4-phenylene diisothiocyanate (PDITC).

Heterobifunctional crosslinkers and photoreactive crosslinkers are not discussed here for sake of clarity but offer other ways to couple antibodies onto planar surfaces.



**Figure 1.12.** Main homobifunctional crosslinking agents used on  $\text{NH}_2$ -terminated surface. (\*: Sulfo analogs)

Glutaraldehyde (GA) is also a well-known crosslinker used for biomolecules immobilization onto  $\text{NH}_2$ -terminated surfaces.<sup>143–145</sup> In its simplest form, GA can react with amine groups to form a Schiff base which can be further reduced with sodium cyanoborohydride ( $\text{NaCNBH}_3$ ) to form secondary amine linkage, leading GA to bear reactive aldehyde group on its other end (Figure 1.13). Yet, the latter can also react with another amine groups from the surface, offering no free reactive groups for antibody immobilization.



**Figure 1.13.** Polymerization of glutaraldehyde (GA) in aqueous solutions in (A) acidic pH and (B) basic pH. Antibody immobilization through its amine groups ( $\text{NH}_2$ ) on  $\text{NH}_2$ -terminated surface using GA (C) in its simplest linear form *via* amination reaction and *via* (D) Michael-type and amination reactions on polymerized GA.

Nevertheless, this bis-aldehyde polymer can polymerize in aqueous solution depending on the pH condition. In acidic pH, GA will tend to form polycyclic hemiacetal while in basic pH  $\alpha,\beta$ -unsaturated aldehyde polymer is formed leading to difference in crosslinking yield and to more complex structures. Indeed, amine functional groups can either interact with the aldehyde end-part or either react at points of unsaturation through Michael-type addition (Figure 1. 13D).<sup>146</sup>

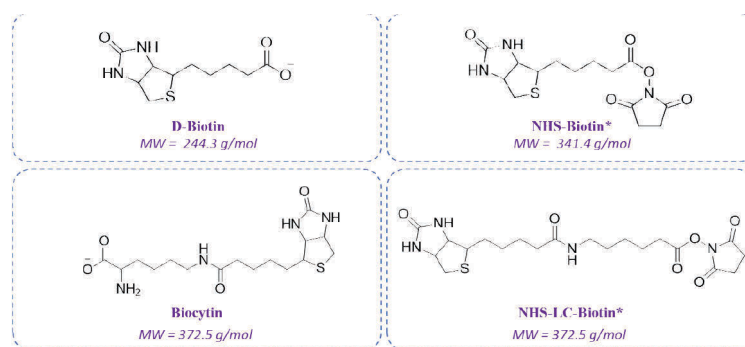
### 1.3.3.2 Affinity-based strategies

Affinity-based strategies show great advantage for antibody immobilization since they allow to orientally adsorb antibody onto surfaces. Several strategies were developed throughout the last decades for site-directed immobilization of antibody<sup>147–149</sup> using for instance Fc-binding proteins and aptamers<sup>150,151</sup> as well as DNA-directed immobilization.<sup>152,153</sup>

#### 1.3.3.2.1 Avidin-biotin strategy

One of the most investigated strategy relies on the use of (strept)avidin or neutravidin that all exhibit high affinity for biotin with a dissociation constant ( $K_d$ ) of about  $10^{-14}$ - $10^{-15}$  M.<sup>154</sup>

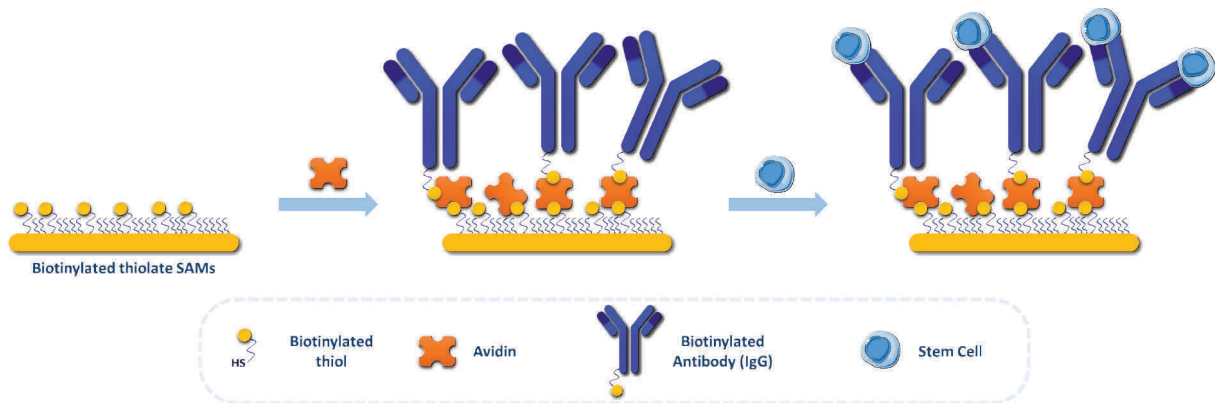
Avidin is a tetrameric glycoprotein found in egg white (66 kDa) which possesses four binding sites for biotin and which is highly basic with a pI  $\sim$  10. Despite its high affinity, avidin was shown to bind nonspecifically to other proteins *via* electrostatic interactions. Streptavidin and neutravidin ( $\sim$  60 kDa) are structural deglycosylated analogs of avidin, with lower pI around 5-6 allowing to overcome non-specific binding. For antibody immobilization *via* this affinity approach, avidin or one of its analogs is often immobilized onto surfaces using crosslinking strategies or biotin-terminated surfaces and then interacts with biotinylated antibody, *i.e.* antibody modified with a biotin tag without alteration of its structure and properties (Figure 1. 14).



**Figure 1. 14.** Amine-reactive biotinylation agents. Other biotinylation agents directed towards aldehyde or thiol antibody functional groups are not depicted herein. (\*: Sulfo analogs)

Maglio *et al.* developed a cost-effective piezoelectric immunosensor for the detection and isolation of CD34(+) stem cells using biotinylated anti-CD34 antibody (**Figure 1. 15**).

Briefly, the authors constructed mixed thiolate SAMs onto gold substrate carrying biotin end-groups, followed by avidin grafting acting as a crosslinker for biotinylated antibody immobilization.<sup>155</sup> Subsequently, the authors successfully detected CD34(+) stem cell in heterogenous cellular sample using QCM.



**Figure 1. 15.** Schematic representation of the functionalization strategy for CD34(+) stem cell immunosensing using avidin/biotin strategy. Adapted from <sup>155</sup>

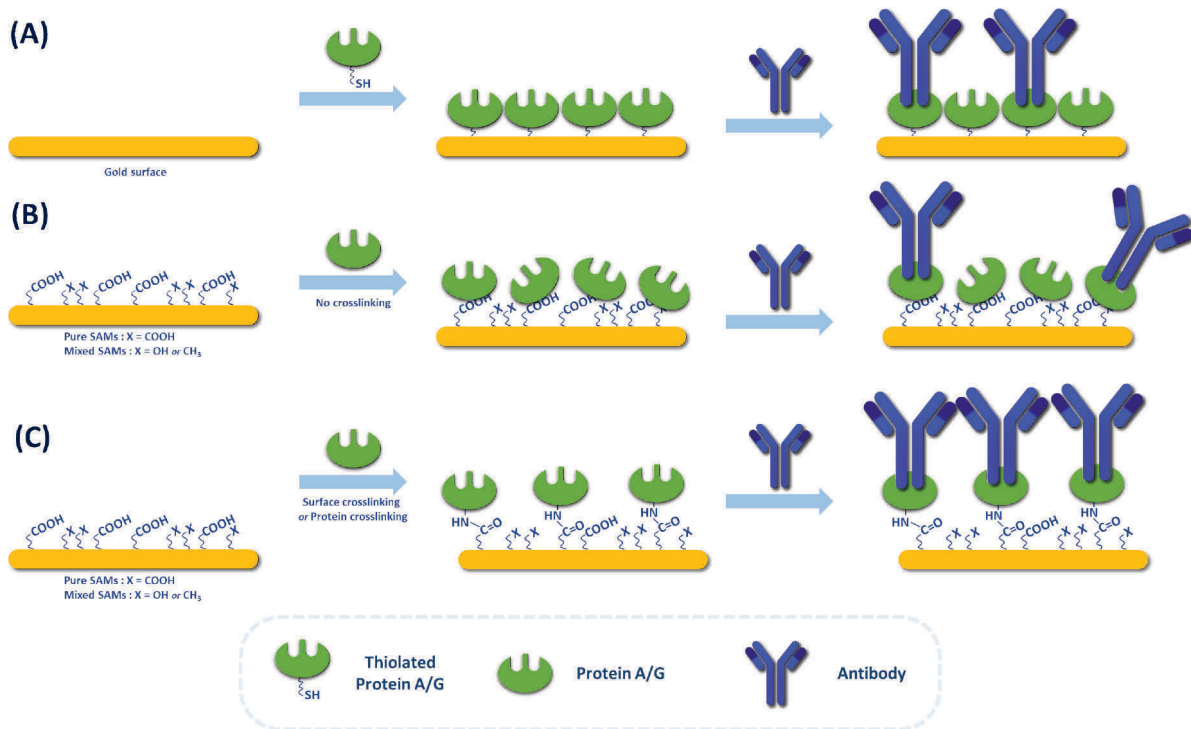
### 1.3.3.2.2 Fc-binding Protein A/G

Affinity-based strategy also involves Fc-binding proteins, *i.e.* Protein A (56 kDa) and Protein G (65 kDa), respectively produced in the cell wall of *Staphylococcus aureus* and *Streptococcal* bacteria. These proteins have been extensively used for immunosensor design with enhanced antibody orientation compared to random adsorption *via* physisorption or chemisorption using crosslinked surface.<sup>156–160</sup>

Fc-binding proteins first need to be grafted onto planar surfaces in order to achieve oriented antibody immobilization. Introduction of thiol groups using thiolation agents can be conducted in order to form self-assembled Protein A/G onto gold surfaces (**Figure 1. 16A**).

Thiolation of Protein A/G can be conducted using *N*-succinimidyl-3-(2-pyridyldithio)propionate (SPDP) and dithiothreitol (DTT)<sup>161</sup> or through modification of amine groups using Traut's reagent (2-iminothiolane) for covalent immobilization onto gold surfaces.<sup>162,163</sup>





**Figure 1. 16.** Immobilization strategies for Fc-binding Protein A/G *via* (A) thiolated Protein A/G, (B) adsorption on non-activated and (C) crosslinked SAMs. Adapted from <sup>157,160-162</sup>

Nevertheless, this approach is only applicable to gold surface, hence other strategies based on the use of crosslinked SAMs on gold and oxide surfaces were developed (**Figure 1. 16A**).

Briand *et al.* investigated Protein A grafting onto two thiolate mixed SAMs formed on gold surface comprising 11-mercaptopundecanoic acid (MUA) with either decanethiol (C<sub>9</sub>CH<sub>3</sub>) or mercaptohexanol (C<sub>6</sub>OH).<sup>164</sup>

They demonstrated that the nature of the SAM influenced the amount of immobilized Protein A, its affinity for IgG and in turn on the immunosensor sensing ability. Crosslinked MUA using EDC/NHS approach allowed Protein A immobilization with greater amount found on the MUA/C<sub>9</sub>CH<sub>3</sub> SAMs which was attributed to higher crystallinity of the SAMs with higher anchoring points as well as to additional physisorption through hydrophobic interaction.<sup>164</sup>

Tajima *et al.* also investigated immobilization of Protein A with an enzymatic coupling approach onto phospholipid polymer-coated silicon substrate *via* three strategies: (i) random physisorption of antibody on the polymer layer, (ii) partially oriented IgG on physisorbed Protein A and (iii) oriented IgG on chemisorbed Protein A using an enzymatic approach with tyrosinase. Higher orientation was obtained with the latter system, exhibiting 100-fold increased binding capacity with lower dissociation constant (K<sub>d</sub>) in the nM range.<sup>160</sup>

Tsekenis *et al.* also showed that IgG immobilization *via* Protein A/G allowed greater IgG loading on silicon nitrate (Si<sub>3</sub>N<sub>4</sub>) surface and enhanced sensing ability in comparison to random adsorption on an epoxysilane layer or using an affinity method using boronate ester chemistry.<sup>166</sup>

In the latter approach, aminophenyl-boronic-acid (APBA) reacted with epoxysilane to create reactive boronate ester groups directed towards oligosaccharide moieties of IgG's Fc domains, providing oriented IgG immobilization.

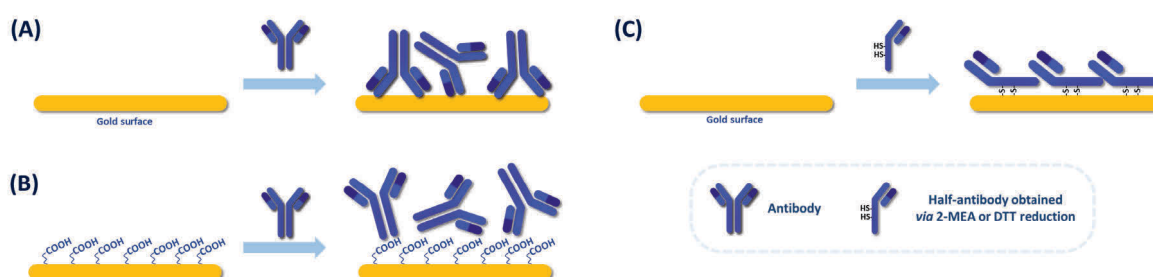
Furthermore, immunosensor development raises some fulfillment related to the biosensor field and assay conditions such as regeneration of the sensing layer for reusability purpose.<sup>167,168</sup>

Makaraviciute *et al.* developed a SPR immunosensor for repeated detection of human growth hormone in real samples using random covalent antibody immobilization and crosslinked Protein G for oriented antibody immobilization. The latter allowed repeated assays with a 3.5-fold increase in measured signal in comparison to random antibody immobilization.<sup>167</sup>

### 1.3.4 Conclusion of the section: comparison of immobilization strategies

As stated throughout this review, immunosensor design in an efficient way relies on three main features which are (i) conserved biological activity upon antibody immobilization, (ii) optimal antibody density and (iii) proper orientation. Thus, the chosen immobilization strategy is crucial to achieve the best sensing ability possible.<sup>94,148,169–171</sup>

Optimized orientation will ensure a better accessibility to the antibody paratopes for the antigen in solution or *vice versa* depending on the immunosensor format. Baniukevicius *et al.* studied oriented and random antibody immobilization methods to detect bovine leukemia virus antigen (gp51) by SPR, with random chemisorption on thiolate SAMs, physisorption and oriented immobilization with antibody fragment (Fab') as presented in **Figure 1. 17**.<sup>172</sup>



**Figure 1. 17.** Schematic representation of SPR-based immunosensor design with antibody immobilization (A) directly on gold surface, (B) adsorbed on COOH-terminated SAMs and (C) using half-antibody obtained *via* 2-MEA or DTT reduction directly on gold surface. Adapted from <sup>172</sup>



The best configuration was found with half-IgG obtained *via* DTT reduction which allowed orientation of the paratopes and enhanced detection.

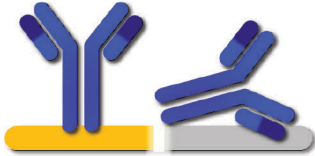

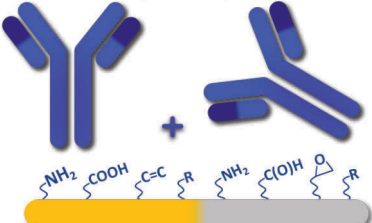
This method displayed good analytical performances, *i.e.* limit of detection (LoD) of about 0.01 mg/mL while being fully regenerable and was subsequently applied for rapid gp51 detection in blood serum.

Similarly, Bonroy *et al.* also investigated differences in sensing ability between intact IgG, F(ab')<sub>2</sub> and Fab' antibody fragments once adsorbed onto crosslinked mixed thiolate SAMs bearing COOH and OH moieties. Their results suggested a 2-fold increase of antigen binding for oriented immobilization of Fab' fragments compared to random covalent immobilization of intact IgG.<sup>173</sup> In addition, investigation of four immobilization strategies comprising this time carboxymethylated dextran was also conducted in order to decipher the impact of the chosen immobilization on the binding capacity of immunosensor.<sup>174</sup> SPR sensors were modified with random immobilization of IgG on (i) crosslinked COOH-SAMs, (ii) crosslinked carboxymethylated dextran layer, (iii) oriented immobilization of IgG on Protein G and (iv) oriented immobilization of antibody Fab' fragment directly on gold surface.

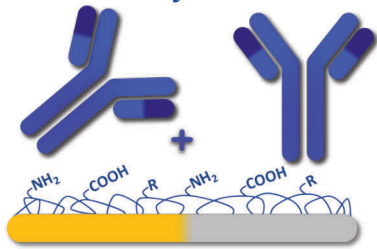
The highest IgG loading was obtained using crosslinked dextran hydrogel and maximal binding ability for human growth hormone (HGH) with intact IgG immobilized onto Protein G/COOH-SAMs. The former might be related to the higher anchoring COOH points within the 3D structure of the hydrogel. Despite the density of adsorbed IgG, this strategy remains random as opposed to Protein G approach which provides a better orientation of the IgG paratopes and therefore higher binding capacity.

Boujday *et al.* investigated three strategies for model rabbit IgG immobilization mediated by (i) Protein A, mouse monoclonal anti-IgG antibody (SAb) and neutravidin (NAV) on gold surfaces using a multi-technique approach with Polarization Modulation Reflection-Absorption Infrared Spectroscopy (PM-IRRAS) and QCM-D to study specificity, IgG accessibility and binding ability.<sup>175</sup> In addition to the already mentioned density and accessibility of adsorbed IgG, the authors provided insightful information about the impact of the sensing layer flexibility. Indeed, Protein A offered a partially covered surface onto SAMs while SAb led to monolayer formation and NAV to dense layer. Authors explained that Protein A was found to be the most efficient strategy with the highest amount of immobilized IgG and better accessibility as probed by anti-IgG antibody. All in all, several strategies offering more or less control over antibody orientation once adsorbed onto planar surfaces have been developed, *e.g.* based on (i) physisorption, (ii) antibody modification, (iii) SAMs, (iv) Polymers, (v) Avidin-biotin interactions and (vi) Fc-binding proteins (**Table 1. 1**).

**Table 1. 1.** Main characteristics of IgG immobilization strategies for immunosensor design

Immobilization strategies	Advantages	Drawbacks
<p><i>Physisorption</i></p> 	<ul style="list-style-type: none"> <li>✓ Simple one-step adsorption</li> <li>✓ No IgG modification</li> <li>✓ No surface functionalization</li> </ul>	<ul style="list-style-type: none"> <li>- Poor binding to the surface and desorption</li> <li>- Random and weak attachment</li> <li>- Nonspecific binding</li> <li>- Possible change in conformation and denaturation upon adsorption</li> <li>- Potential loss of activity</li> </ul>
<p><i>Antibody modification</i></p> 	<ul style="list-style-type: none"> <li>✓ Commercial thiolation agents</li> <li>✓ Design of IgG fragments</li> <li>✓ Well-documented modification protocols</li> <li>✓ Oriented immobilization with IgG fragments (Fab')</li> </ul>	<ul style="list-style-type: none"> <li>- IgG modification</li> <li>- Potential loss of activity</li> <li>- Random orientation of intact IgG</li> <li>- Mainly investigated on gold surface</li> </ul>
<p><i>Self-assembled monolayers (SAMs)</i></p> 	<ul style="list-style-type: none"> <li>✓ No IgG modification</li> <li>✓ Easiness of use</li> <li>✓ Application on various nature of substrates</li> <li>✓ Commercial availability of organic molecules</li> <li>✓ Tunability of functional groups</li> <li>✓ Commercial crosslinking agents</li> </ul>	<ul style="list-style-type: none"> <li>- Random orientation</li> <li>- Additional crosslinking steps</li> <li>- Crosslinked SAMs might deactivate over time (hydrolysis)</li> <li>- Free functional groups can lead to non-specific adsorption</li> </ul>

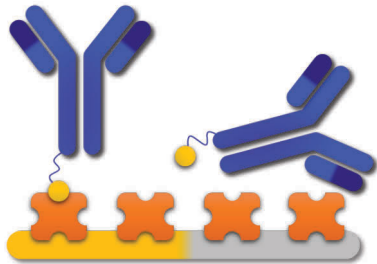
### Polymers



- ✓ No IgG modification
- ✓ Easiness
- ✓ Commercial polymers with various functional groups
- ✓ Application on various substrates
- ✓ Higher anchoring points compared to SAMs

- Crosslinked polymer chains might deactivate over time
- Additional crosslinking steps
- Free functional groups can lead to non-specific adsorption

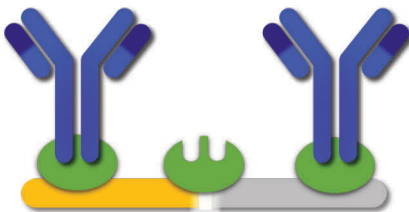
### Avidin-biotin interaction



- ✓ Oriented IgG immobilization
- ✓ Immobilization onto various SAMs
- ✓ High IgG density

- Not suitable for sandwich assay
- Additional functionalization step
- Not suitable for transduction methods with limited sensing depth
- IgG modification with biotinylating agents

### Fc-binding proteins



- ✓ Oriented IgG immobilization
- ✓ Improved sensitivity compared to random immobilization
- ✓ No IgG modification
- ✓ Direct binding to gold surface after thiolation
- ✓ Immobilization onto SAMs of various nature

- Not suitable for sandwich assay
- Additional functionalization step
- Not suitable for transduction methods with limited sensing depth

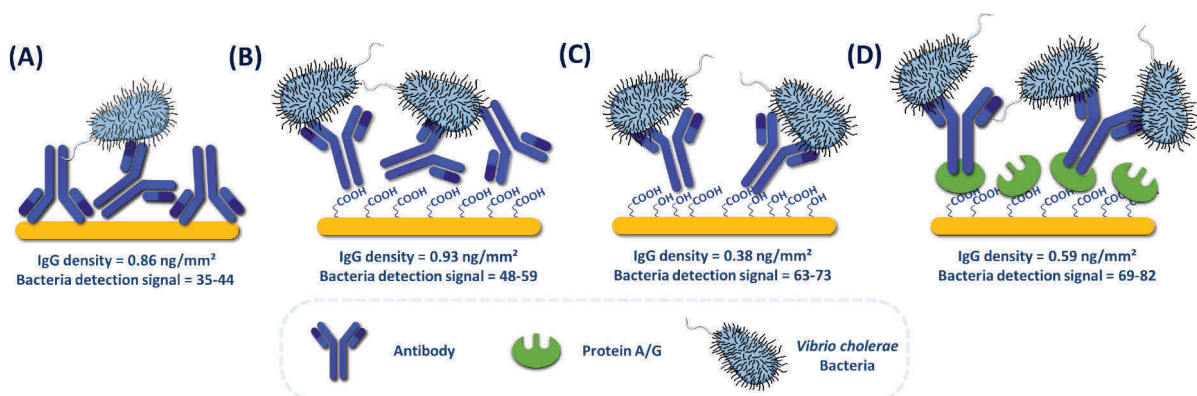
## 1.4 Specificity in functionalization to immunosensor design

When designing immunosensors, in addition to maximizing antibody loading and its accessibility upon adsorption onto planar surfaces, non-specific adsorption and specificity of the assay are crucial features to be addressed.

### 1.4.1 Mixed SAMs

Starting from the functionalization strategies, mixed SAMs can be produced by co-adsorption from solutions of mixtures of organic molecules carrying different terminal groups, *e.g.* COOH/CH<sub>3</sub>, COOH/OH, and were shown to control surface properties such as order and wettability according to molar ratio and in turn protein adsorption.<sup>157,158,164</sup> Mixed thiolate SAMs formed from a mixture of organic molecules of different chain lengths and terminal groups was shown to prevent protein denaturation and to improve its bioactivity in comparison to pure SAMs.<sup>176,177</sup> Furthermore, mixed SAMs approach was shown to increase the yield in crosslinking with EDC/NHS due to reduced steric hindrance from NHS groups and in turn affecting the efficiency of antibody immobilization.<sup>178</sup>

Taheri *et al.* compared four methods to immobilize antibody for SPR immunosensing of *Vibrio cholerae* bacteria (**Figure 1. 18**).<sup>179</sup> Amount of adsorbed IgG was found to vary with highest amount on gold surface and pure COOH-terminated SAMs.



**Figure 1. 18.** Schematic representation of IgG immobilization strategies on (A) gold surface, (B) COOH-terminated SAM, (C) mixed COOH/OH SAMs and on (D) Fc-binding Protein G. With IgG surface density and bacteria detection response in culture and spiked water media determined from SPR shifts. Adapted from<sup>179</sup>

Nevertheless, these strategies do not ensure antibody orientation and actually the best sensitivities for bacteria were found with mixed SAMs composed of 11-mercaptoundecanol/9-mercapto-1-nonanol (20/80) and Protein G strategies, the latter offering control over orientation and hence efficient detection.

## 1.4.2 Strategies to prevent non-specific adsorption in immunosensor

When designing immunosensor, one crucial parameter to be fulfilled is specificity, this can be achieved by using highly specific biorecognition elements such as (monoclonal) antibodies but also by preventing non-specific adsorption directly on the surface.<sup>180</sup> Strategies involving the use of PEG directly as part of the sensing layer, deactivation agents for reactive functional groups and blocking proteins like Bovine Serum Albumin (BSA) are discussed.

### 1.4.2.1 Polyethylene glycol (PEG) to prevent non-specific interactions

Polyethylene glycol (PEG) (also referred as polyethylene oxide (PEO)) functionalization is known to prevent protein non-specific interaction which often occurs through hydrophobic and electrostatic interaction.<sup>181,182</sup> Thus, being a hydrophilic neutral polymer and due to its tunable length, PEG can prevent adsorption on the substrate through steric repulsion. Densely packed PEG layer has been employed in immunoassays design<sup>143,183,184</sup> to prevent non-specific binding and ensure assay specificity. PEGylation of the sensor can be achieved directly by integrating a PEG component to pure or mixed SAMs layer by the dint of thiolated or silanized PEG<sup>185–188</sup> or can be done by further adsorption of a functional PEG layer onto SAMs.<sup>189–191</sup>

In addition, Mehne *et al.* demonstrated that pure or mixed self-assembled PEG monolayers onto glass substrate impact ovalbumin non-specific adsorption as well as antibody immobilization.<sup>192</sup> Yoshimoto *et al.* also showed an increase in binding ability when mixed-PEG of different lengths are immediately co-immobilized with Fab' fragment antibody onto the surface as opposed to deactivation of the paratope over time with no PEGylation.<sup>193</sup>

In addition to prevent non-specific adsorption, Haustein *et al.* co-immobilized PEG and thiol SAMs and observed an enhancement of the sensing ability in transistor-based immunosensor which measured potential shift of thyroid-stimulating hormone (TSH) detection using F(ab')<sub>2</sub> fragments.<sup>194</sup>

Combination of experimental results and analytical modeling showed that PEGylation of the sensor surface allowed to increase 3-fold the measured potential upon analyte detection.

The potential in nearby surface consisting of PEG layer was considered as constant, making detection of the analyte the only input in potential variation compared to sensing layer without PEGylation. Weimer *et al.* immobilized antibodies either directly onto glass surface or on a PEG layer *via* EDC chemistry.<sup>195</sup>

PEG strategy was shown to produce higher sensing ability than antibodies adsorbed directly onto glass substrates. Indeed, PEG provides a flexible spacer arm to extend antibody from the surface facilitating antigen detection.

### 1.4.2.2 Blocking functional groups to prevent non-specific adsorption

Upon antibody immobilization onto functionalized surface with or without crosslinking, free functional groups may remain unreacted. Hence, strategies have been developed to block free functional groups prior to sensing step using blocking agents.

Sulfo-NHS acetate and acetic or citraconic or anhydride can be used to react with free amine groups and block non-specific adsorption.

Quenching of NHS function is often performed with amine-containing blocking agents such as Tris or Ethanolamine.<sup>157,164,166</sup>

### 1.4.2.3 Adsorption of Bovine Serum Albumin (BSA) to prevent non-specific interaction

Bovine Serum Albumin (BSA) is a 66 kDa protein that is often used as a blocking agent in immunosensor development as it is known to spontaneously adsorb onto surfaces<sup>112,196</sup> occupying free remaining sites prior to target detection.<sup>159,161,197–199</sup>

Allegedly, BSA can also adsorb on functionalized substrate in order to react with remaining functional groups.

Nevertheless, in spite of being a conventional blocking agent, BSA can also induce non-specific adsorption due to its positive charge (pI = 4.7) and might suffer from inconsistencies from commercial sources from batch-to-batch leading to irreproducibility in blocking strategy.

## 1.5 Conclusion

Throughout this work, we have reviewed general features related to IgG type antibody structure and historical perspective of its applications in medicine and sensing fields.

We addressed immunosensors engineering and detection configurations available on planar gold and silica substrates. Indeed, an ideal label-free immunosensor should offer sensitive, specific and reliable detection.

Thus, IgG surface density and orientation are crucial to achieve the best sensing efficiency. Therefore, the first step towards immunosensor development relies on antibody immobilization which can be achieved *via* antibody modification or surface functionalization.

Hence, the second part of this review comprehensively covered the most investigated methodologies for antibody immobilization on planar gold and silica surfaces *via* physisorption and chemisorption. The latter involved covalent-based approaches using self-assembled monolayers (SAMs) or polymer surface functionalization and affinity-based strategies with avidin-biotin interactions and Fc-binding proteins with focus on the advantages and drawbacks of each strategy.

Chemisorption with affinity-based strategies appear as the best immobilization route as it allows oriented IgG immobilization with high surface density and often display improved sensitivity compared to random physisorption or covalent-based approaches.

The last part of this review aims to give specific features related to immunosensor development such as mixed SAMs and blocking strategies to avoid non-specific interaction and ensure high specificity of the biosensing platform.

These strategies developed on gold and silica surfaces have successfully been implemented within the last decades for label-free immunosensors using various transduction techniques such as Surface Plasmon Resonance (SPR), quartz crystal microbalance (QCM) and electrochemical methods.



## References

- (1) Narita, F.; Wang, Z.; Kurita, H.; Li, Z.; Shi, Y.; Jia, Y.; Soutis, C. A Review of Piezoelectric and Magnetostrictive Biosensor Materials for Detection of COVID-19 and Other Viruses. *Adv. Mater.* **2021**, *33* (1), 2005448.
- (2) Abid, S. A.; Ahmed Muneer, A.; Al-Kadmy, I. M. S.; Sattar, A. A.; Beshbishy, A. M.; Batiha, G. E.-S.; Hetta, H. F. Biosensors as a Future Diagnostic Approach for COVID-19. *Life Sci.* **2021**, *273*, 119117.
- (3) Taha, B. A.; Al Mashhadany, Y.; Bachok, N. N.; Ashrif A Bakar, A.; Hafiz Mokhtar, M. H.; Dzulkefly Bin Zan, M. S.; Arsad, N. Detection of COVID-19 Virus on Surfaces Using Photonics: Challenges and Perspectives. *Diagnostics* **2021**, *11* (6), 1119.
- (4) Kim, J.; Campbell, A. S.; de Avila, B. E.-F.; Wang, J. Wearable Biosensors for Healthcare Monitoring. *Nat. Biotechnol.* **2019**, *37* (4), 389–406.
- (5) Ye, S.; Feng, S.; Huang, L.; Bian, S. Recent Progress in Wearable Biosensors: From Healthcare Monitoring to Sports Analytics. *Biosensors* **2020**, *10* (12), 205.
- (6) Clark, L. C.; Lyons, C. Electrode Systems for Continuous Monitoring in Cardiovascular Surgery. *Ann. N. Y. Acad. Sci.* **1962**, *102* (1), 29–45.
- (7) Heineman, W. R.; Jensen, W. B. Leland C. Clark Jr. (1918–2005). *Biosens. Bioelectron.* **2006**, *21* (8), 1403–1404.
- (8) Tothill, I. E.; Turner, A. P. F. BIOSENSORS. In *Encyclopedia of Food Sciences and Nutrition (Second Edition)*; Caballero, B., Ed.; Academic Press: Oxford, 2003; pp 489–499.
- (9) Ali, J.; Najeeb, J.; Asim Ali, M.; Farhan Aslam, M.; Raza, A. Biosensors: Their Fundamentals, Designs, Types and Most Recent Impactful Applications: A Review. *J. Biosens. Bioelectron.* **2017**, *08* (01).
- (10) Bhalla, N.; Jolly, P.; Formisano, N.; Estrela, P. Introduction to Biosensors. *Essays Biochem.* **2016**, *60* (1), 1–8.
- (11) Sin, M. L.; Mach, K. E.; Wong, P. K.; Liao, J. C. Advances and Challenges in Biosensor-Based Diagnosis of Infectious Diseases. *Expert Rev. Mol. Diagn.* **2014**, *14* (2), 225–244.
- (12) Patel, S.; Nanda, R.; Sahoo, S.; Mohapatra, E. Biosensors in Health Care: The Milestones Achieved in Their Development towards Lab-on-Chip-Analysis. *Biochem. Res. Int.* **2016**, *2016*, 1–12.
- (13) Jayanthi, V. S. P. K. S. A.; Das, A. B.; Saxena, U. Recent Advances in Biosensor Development for the Detection of Cancer Biomarkers. *Biosens. Bioelectron.* **2017**, *91*, 15–23.
- (14) Thakur, M. S.; Ragavan, K. V. Biosensors in Food Processing. *J. Food Sci. Technol.* **2013**, *50* (4), 625–641.
- (15) Mishra, G.; Barfidokht, A.; Tehrani, F.; Mishra, R. Food Safety Analysis Using Electrochemical Biosensors. *Foods* **2018**, *7* (9), 141.
- (16) García Lozano, M.; Peña García, Y.; Silva Gonzalez, J. A.; Ochoa Bañuelos, C. V.; Luevanos Escareño, M. P.; Balagurusamy, N. Biosensors for Food Quality and Safety Monitoring: Fundamentals and Applications. In *Enzymes in Food Biotechnology*; Elsevier, 2019; pp 691–709.
- (17) Long, F.; Zhu, A.; Shi, H. Recent Advances in Optical Biosensors for Environmental Monitoring and Early Warning. *Sensors* **2013**, *13* (10), 13928–13948.
- (18) Hayat, A.; Marty, J. Disposable Screen Printed Electrochemical Sensors: Tools for Environmental Monitoring. *Sensors* **2014**, *14* (6), 10432–10453.
- (19) Justino, C.; Duarte, A.; Rocha-Santos, T. Recent Progress in Biosensors for Environmental Monitoring: A Review. *Sensors* **2017**, *17* (12), 2918.
- (20) Lippa, P. B.; Sokoll, L. J.; Chan, D. W. Immunosensors—Principles and Applications to Clinical Chemistry. *Clin. Chim. Acta* **2001**, *314* (1–2), 1–26.
- (21) Mohammed, M.-I.; Desmulliez, M. P. Y. Lab-on-a-Chip Based Immunosensor Principles and Technologies for the Detection of Cardiac Biomarkers: A Review. *Lab Chip* **2011**, *11* (4), 569–595.
- (22) Lim, Y. C.; Kouzani, A. Z.; Duan, W. Aptasensors: A Review. *J. Biomed. Nanotechnol.* **2010**, *6* (2), 93–105.



- (23) Walter, J.-G.; Heilkenbrinker, A.; Austerjost, J.; Timur, S.; Stahl, F.; Schepe, T. Aptasensors for Small Molecule Detection. *Z. Für Naturforschung B* **2012**, *67* (10), 976–986.
- (24) Yan, S.-R.; Foroughi, M. M.; Safaei, M.; Jahani, S.; Ebrahimpour, N.; Borhani, F.; Rezaei Zade Baravati, N.; Aramesh-Boroujeni, Z.; Foong, L. K. A Review: Recent Advances in Ultrasensitive and Highly Specific Recognition Aptasensors with Various Detection Strategies. *Int. J. Biol. Macromol.* **2020**, *155*, 184–207.
- (25) Ispas, C. R.; Crivat, G.; Andreescu, S. Review: Recent Developments in Enzyme-Based Biosensors for Biomedical Analysis. *Anal. Lett.* **2012**, *45* (2–3), 168–186.
- (26) Kumar, H.; Neelam. Enzyme-Based Electrochemical Biosensors for Food Safety: A Review. *Nanobiosensors Dis. Diagn.* **2016**, *29*.
- (27) Kucherenko, I. S.; Soldatkin, O. O.; Kucherenko, D. Yu.; Soldatkina, O. V.; Dzyadevych, S. V. Advances in Nanomaterial Application in Enzyme-Based Electrochemical Biosensors: A Review. *Nanoscale Adv.* **2019**, *1* (12), 4560–4577.
- (28) Nguyen, H. H.; Lee, S. H.; Lee, U. J.; Fermin, C. D.; Kim, M. Immobilized Enzymes in Biosensor Applications. *Materials* **2019**, *12* (1), 121.
- (29) Naseri, M.; Mohammadniaei, M.; Sun, Y.; Ashley, J. The Use of Aptamers and Molecularly Imprinted Polymers in Biosensors for Environmental Monitoring: A Tale of Two Receptors. *Chemosensors* **2020**, *8* (2), 32.
- (30) Lowdon, J. W.; Diliën, H.; Singla, P.; Peeters, M.; Cleij, T. J.; van Grinsven, B.; Eersels, K. MIPs for Commercial Application in Low-Cost Sensors and Assays – An Overview of the Current Status Quo. *Sens. Actuators B Chem.* **2020**, *325*, 128973.
- (31) Turner, A.; Karube, I.; Wilson, G. S. *Biosensors: Fundamentals and Applications*; Oxford University Press, 1987.
- (32) Mehrotra, P. Biosensors and Their Applications – A Review. *J. Oral Biol. Craniofacial Res.* **2016**, *6* (2), 153–159.
- (33) Fechner, P.; Bleher, O.; Ewald, M.; Freudenberger, K.; Furin, D.; Hilbig, U.; Kolarov, F.; Krieg, K.; Leidner, L.; Markovic, G.; Proll, G.; Pröll, F.; Rau, S.; Riedt, J.; Schwarz, B.; Weber, P.; Widmaier, J. Size Does Matter! Label-Free Detection of Small Molecule–Protein Interaction. *Anal. Bioanal. Chem.* **2014**, *406* (17), 4033–4051.
- (34) Boujday, S.; Chapelle, M.; Srajer, J.; Knoll, W. Enhanced Vibrational Spectroscopies as Tools for Small Molecule Biosensing. *Sensors* **2015**, *15* (9), 21239–21264.
- (35) Sassolas, A.; Leca-Bouvier, B. D.; Blum, L. J. DNA Biosensors and Microarrays. *Chem. Rev.* **2008**, *108* (1), 109–139.
- (36) Leca-Bouvier, B.; Blum, L. J. Biosensors for Protein Detection: A Review. *Anal. Lett.* **2005**, *38* (10), 1491–1517.
- (37) Ribeiro, B. V.; Cordeiro, T. A. R.; Oliveira e Freitas, G. R.; Ferreira, L. F.; Franco, D. L. Biosensors for the Detection of Respiratory Viruses: A Review. *Talanta Open* **2020**, *2*, 100007.
- (38) Saylan, Y.; Erdem, Ö.; Ünal, S.; Denizli, A. An Alternative Medical Diagnosis Method: Biosensors for Virus Detection. *Biosensors* **2019**, *9* (2), 65.
- (39) Gupta, N.; Renugopalakrishnan, V.; Liepmann, D.; Paulmurugan, R.; Malhotra, B. D. Cell-Based Biosensors: Recent Trends, Challenges and Future Perspectives. *Biosens. Bioelectron.* **2019**, *141*, 111435.
- (40) Chen, C.; Wang, J. Optical Biosensors: An Exhaustive and Comprehensive Review. *The Analyst* **2020**, *145* (5), 1605–1628.
- (41) Chen, Y.-T.; Lee, Y.-C.; Lai, Y.-H.; Lim, J.-C.; Huang, N.-T.; Lin, C.-T.; Huang, J.-J. Review of Integrated Optical Biosensors for Point-of-Care Applications. *Biosensors* **2020**, *10* (12), 209.
- (42) Ronkainen, N. J.; Halsall, H. B.; Heineman, W. R. Electrochemical Biosensors. *Chem. Soc. Rev.* **2010**, *39* (5), 1747.
- (43) Cho, I.-H.; Kim, D. H.; Park, S. Electrochemical Biosensors: Perspective on Functional Nanomaterials for on-Site Analysis. *Biomater. Res.* **2020**, *24* (1), 6.
- (44) Pohanka, M. Overview of Piezoelectric Biosensors, Immunosensors and DNA Sensors and Their Applications. *Materials* **2018**, *11* (3), 448.
- (45) Wu, A. H. B. A Selected History and Future of Immunoassay Development and Applications in Clinical Chemistry. *Clin. Chim. Acta* **2006**, *369* (2), 119–124.

- (46) Lequin, R. M. Enzyme Immunoassay (EIA)/Enzyme-Linked Immunosorbent Assay (ELISA). *Clin. Chem.* **2005**, *51* (12), 2415–2418.
- (47) Aydin, S. A Short History, Principles, and Types of ELISA, and Our Laboratory Experience with Peptide/Protein Analyses Using ELISA. *Peptides* **2015**, *72*, 4–15.
- (48) O’Farrell, B. Evolution in Lateral Flow–Based Immunoassay Systems. In *Lateral Flow Immunoassay*; Wong, R., Tse, H., Eds.; Humana Press: Totowa, NJ, 2009; pp 1–33.
- (49) Di Nardo, F.; Chiarello, M.; Cavallera, S.; Baggiani, C.; Anfossi, L. Ten Years of Lateral Flow Immunoassay Technique Applications: Trends, Challenges and Future Perspectives. *Sensors* **2021**, *21* (15), 5185.
- (50) Lara, S.; Perez-Potti, A. Applications of Nanomaterials for Immunosensing. *Biosensors* **2018**, *8* (4), 104.
- (51) Loiseau, A.; Asila, V.; Boitel-Aullen, G.; Lam, M. Silver-Based Plasmonic Nanoparticles for and Their Use in Biosensing. **2019**, 39.
- (52) Zhang, L.; Mazouzi, Y.; Salmain, M.; Liedberg, B.; Boujday, S. Antibody-Gold Nanoparticle Bioconjugates for Biosensors: Synthesis, Characterization and Selected Applications. *Biosens. Bioelectron.* **2020**, *165*, 112370.
- (53) Pellas, V.; Hu, D.; Mazouzi, Y.; Mimoun, Y.; Blanchard, J.; Guibert, C.; Salmain, M.; Boujday, S. Gold Nanorods for LSPR Biosensing: Synthesis, Coating by Silica, and Bioanalytical Applications. *Biosensors* **2020**, *10* (10), 146.
- (54) Schroeder, H. W.; Cavacini, L. Structure and Function of Immunoglobulins. *J. Allergy Clin. Immunol.* **2010**, *125* (2), S41–S52.
- (55) Fischer, E. Einfluss der Configuration auf die Wirkung der Enzyme. *Berichte Dtsch. Chem. Ges.* **1894**, *27* (3), 2985–2993.
- (56) Lemieux, R. U.; Spohr, U. How Emil Fischer Was Led to the Lock and Key Concept for Enzyme Specificity. *Adv. Carbohydr. Chem. Biochem.* **1994**, *50*, 1–20.
- (57) Padlan, E. A. Anatomy of the Antibody Molecule. *Mol. Immunol.* **1994**, *31* (3), 169–217.
- (58) Holliger, P.; Hudson, P. J. Engineered Antibody Fragments and the Rise of Single Domains. *Nat. Biotechnol.* **2005**, *23* (9), 1126–1136.
- (59) Zeng, X.; Shen, Z.; Mernaugh, R. Recombinant Antibodies and Their Use in Biosensors. *Anal. Bioanal. Chem.* **2012**, *402* (10), 3027–3038.
- (60) Bates, A.; Power, C. A. David vs. Goliath: The Structure, Function, and Clinical Prospects of Antibody Fragments. *Antibodies* **2019**, *8* (2), 28.
- (61) Pavlou, A. K.; Belsey, M. J. The Therapeutic Antibodies Market to 2008. *Eur. J. Pharm. Biopharm.* **2005**, *59* (3), 389–396.
- (62) Lu, R.-M.; Hwang, Y.-C.; Liu, I.-J.; Lee, C.-C.; Tsai, H.-Z.; Li, H.-J.; Wu, H.-C. Development of Therapeutic Antibodies for the Treatment of Diseases. *J. Biomed. Sci.* **2020**, *27* (1), 1.
- (63) Perez, H. L.; Cardarelli, P. M.; Deshpande, S.; Gangwar, S.; Schroeder, G. M.; Vite, G. D.; Borzilleri, R. M. Antibody–Drug Conjugates: Current Status and Future Directions. *Drug Discov. Today* **2014**, *19* (7), 869–881.
- (64) Baah, S.; Laws, M.; Rahman, K. M. Antibody–Drug Conjugates—A Tutorial Review. *Molecules* **2021**, *26* (10), 2943.
- (65) van Bebring, E. The Mechanism of Immunity in Animals to Diphtheria and Tetanus. 3.
- (66) The Nobel Prize in Physiology or Medicine 1901 <https://www.nobelprize.org/prizes/medicine/1901/behring/biographical/> (accessed 2021 -09 -13).
- (67) Coons, A. H. The Beginnings of Immunofluorescence. *J. Immunol.* **1961**, *87* (5), 499–503.
- (68) Porter, R. R. The Hydrolysis of Rabbit Y-Globulin and Antibodies with Crystalline Papain. 9.
- (69) The Nobel Prize in Physiology or Medicine 1972 <https://www.nobelprize.org/prizes/medicine/1972/summary/> (accessed 2021 -09 -13).
- (70) Wilson, I. A.; Stanfield, R. L. 50 Years of Structural Immunology. *J. Biol. Chem.* **2021**, *296*, 100745.
- (71) Harris, L. J. *et al.* Crystallographic Structure of an Intact IgG1 Monoclonal Antibody. 12.
- (72) Harris, L. J.; Larson, S. B.; Hasel, K. W.; McPherson, A. Refined Structure of an Intact IgG2a Monoclonal Antibody†. 17.

- (73) Sapphire, E. O. Crystal Structure of a Neutralizing Human IgG Against HIV-1: A Template for Vaccine Design. *Science* **2001**, *293* (5532), 1155–1159.
- (74) Yalow, R. S.; Berson, S. A. Assay of Plasma Insulin in Human Subjects by Immunological Methods. *Nature* **1959**, *184* (4699), 1648–1649.
- (75) The Nobel Prize in Physiology or Medicine 1977 <https://www.nobelprize.org/prizes/medicine/1977/summary/> (accessed 2021 -09 -13).
- (76) Engvall, E.; Perlmann, P. Enzyme-Linked Immunosorbent Assay (ELISA) Quantitative Assay of Immunoglobulin G. *Immunochemistry* **1971**, *8* (9), 871–874.
- (77) Van Weemen, B. K.; Schuurs, A. H. W. M. Immunoassay Using Antigen-Enzyme Conjugates. *FEBS Lett.* **1971**, *15* (3), 232–236.
- (78) Engvall, E.; Perlmann, P. Enzyme-Linked Immunosorbent Assay, Elisa: III. Quantitation of Specific Antibodies by Enzyme-Labeled Anti-Immunoglobulin in Antigen-Coated Tubes. *J. Immunol.* **1972**, *109* (1), 129–135.
- (79) Köhler, G.; Milstein, C. Continuous Cultures of Fused Cells Secreting Antibody of Predefined Specificity. *Nature* **1975**, *256* (5517), 495–497.
- (80) The Nobel Prize in Physiology or Medicine 1984 <https://www.nobelprize.org/prizes/medicine/1984/summary/> (accessed 2021 -09 -13).
- (81) Horisberger, M.; Rosset, J.; Bauer, H. Colloidal Gold Granules as Markers for Cell Surface Receptors in the Scanning Electron Microscope. *Experientia* **1975**, *31* (10), 1147–1149.
- (82) Horisberger, M.; Rosset, J. Colloidal Gold, a Useful Marker for Transmission and Scanning Electron Microscopy. *J. Histochem. Cytochem.* **1977**, *25* (4), 295–305.
- (83) Demey, J.; Moeremans, M.; Geuens, G.; Nuydens, R.; Debrabander, M. High Resolution Light and Electron Microscopic Localization of Tubulin with the IGS (Immuno Gold Staining) Method. *Cell Biol. Int. Rep.* **1981**, *5* (9), 889–899.
- (84) Tokuyasu, K. T. Visualization of Longitudinally-Oriented Intermediate Filaments in Frozen Sections of Chicken Cardiac Muscle by a New Staining Method. *J. Cell Biol.* **1983**, *97* (2), 562–565.
- (85) Aizawa, M.; Morioka, A.; Matsuoka, H.; Suzuki, S.; Nagamura, Y.; Shinohara, R.; Ishiguro, I. An Enzyme Immunosensor for IgG. *J. Solid-Phase Biochem.* **1976**, *1* (4), 319–328.
- (86) Aizawa, M.; Thomas, J. D. R.; Higgins, I. J.; Albery, W. J.; Akhtar, M.; Lowe, C. R.; Higgins, I. J. Immunosensors. *Philos. Trans. R. Soc. Lond. B Biol. Sci.* **1987**, *316* (1176), 121–134.
- (87) Karube, I.; Matsunaga, T.; Suzuki, S.; Asano, T.; Itoh, S. Immobilized Antibody-Based Flow Type Enzyme Immunosensor for Determination of Human Serum Albumin. *J. Biotechnol.* **1984**, *1* (5–6), 279–286.
- (88) Ecker, D. M.; Jones, S. D.; Levine, H. L. The Therapeutic Monoclonal Antibody Market. *mAbs* **2015**, *7* (1), 9–14.
- (89) Steen Redeker, E.; Ta, D. T.; Cortens, D.; Billen, B.; Guedens, W.; Adriaensens, P. Protein Engineering For Directed Immobilization. *Bioconjug. Chem.* **2013**, *24* (11), 1761–1777.
- (90) Pei, X.; Zhang, B.; Tang, J.; Liu, B.; Lai, W.; Tang, D. Sandwich-Type Immunosensors and Immunoassays Exploiting Nanostructure Labels: A Review. *Anal. Chim. Acta* **2013**, *758*, 1–18.
- (91) Homola, J. Surface Plasmon Resonance Sensors for Detection of Chemical and Biological Species. *Chem. Rev.* **2008**, *108* (2), 462–493.
- (92) Sharma, S.; Byrne, H.; O’Kennedy, R. J. Antibodies and Antibody-Derived Analytical Biosensors. *Essays Biochem.* **2016**, *60* (1), 9–18.
- (93) Li, Z.; Chen, G.-Y. Current Conjugation Methods for Immunosensors. *Nanomaterials* **2018**, *8* (5), 278.
- (94) Trilling, A. K.; Beekwilder, J.; Zuilhof, H. Antibody Orientation on Biosensor Surfaces: A Minireview. *The Analyst* **2013**, *138* (6), 1619.
- (95) Chen, S.; Liu, L.; Zhou, J.; Jiang, S. Controlling Antibody Orientation on Charged Self-Assembled Monolayers. *Langmuir* **2003**, *19* (7), 2859–2864.
- (96) Wang, H.; Castner, D. G.; Ratner, B. D.; Jiang, S. Probing the Orientation of Surface-Immobilized Immunoglobulin G by Time-of-Flight Secondary Ion Mass Spectrometry. *Langmuir* **2004**, *20* (5), 1877–1887.

- (97) Gajos, K.; Szafraniec, K.; Petrou, P.; Budkowski, A. Surface Density Dependent Orientation and Immunological Recognition of Antibody on Silicon: TOF-SIMS and Surface Analysis of Two Covalent Immobilization Methods. *Appl. Surf. Sci.* **2020**, *518*, 146269.
- (98) Wiseman, M. E.; Frank, C. W. Antibody Adsorption and Orientation on Hydrophobic Surfaces. *Langmuir* **2012**, *28* (3), 1765–1774.
- (99) Della Ventura, B.; Banchelli, M.; Funari, R.; Illiano, A.; De Angelis, M.; Taroni, P.; Amoresano, A.; Matteini, P.; Velotta, R. Biosensor Surface Functionalization by a Simple Photochemical Immobilization of Antibodies: Experimental Characterization by Mass Spectrometry and Surface Enhanced Raman Spectroscopy. *The Analyst* **2019**, *144* (23), 6871–6880.
- (100) Ioerger, T. R.; Du, C.; Linthicum, D. S. Conservation of Cys–Cys Trp Structural Triads and Their Geometry in the Protein Domains of Immunoglobulin Superfamily Members. *Mol. Immunol.* **1999**, *36* (6), 373–386.
- (101) Neves-Petersen, M. T.; Gryczynski, Z.; Lakowicz, J.; Fojan, P.; Pedersen, S.; Petersen, E.; Bjørn Petersen, S. High Probability of Disrupting a Disulphide Bridge Mediated by an Endogenous Excited Tryptophan Residue. *Protein Sci. Publ. Protein Soc.* **2002**, *11* (3), 588–600.
- (102) Della Ventura, B.; Schiavo, L.; Altucci, C.; Esposito, R.; Velotta, R. Light Assisted Antibody Immobilization for Bio-Sensing. *Biomed. Opt. Express* **2011**, *2* (11), 3223.
- (103) Humblot, V.; Pradier, C. Adsorption of Proteins and Anti-biofilm Strategies. In *Surface and Interface Science*; Wandelt, K., Ed.; Wiley, 2020; pp 197–227.
- (104) Ulman, A. PART THREE - SELF-ASSEMBLED MONOLAYERS. In *An Introduction to Ultrathin Organic Films*; Ulman, A., Ed.; Academic Press: San Diego, 1991; pp 237–304.
- (105) Love, J. C.; Estroff, L. A.; Kriebel, J. K.; Nuzzo, R. G.; Whitesides, G. M. Self-Assembled Monolayers of Thiolates on Metals as a Form of Nanotechnology. *Chem. Rev.* **2005**, *105* (4), 1103–1170.
- (106) Pujari, S. P.; Scheres, L.; Marcelis, A. T. M.; Zuilhof, H. Covalent Surface Modification of Oxide Surfaces. *Angew Chem Int Ed* **2014**, *35*.
- (107) Zamborini, F. P.; Crooks, R. M. Corrosion Passivation of Gold by *n*-Alkanethiol Self-Assembled Monolayers: Effect of Chain Length and End Group. *Langmuir* **1998**, *14* (12), 3279–3286.
- (108) Cao, Z.; Xiao, Z.; Gu, N.; Gong, F.; Yang, D.; Zhu, Z. Corrosion Behaviors on Polycrystalline Gold Substrates in Self-Assembled Processes of Alkanethiol Monolayers. *Anal. Lett.* **2005**, *38* (8), 1289–1304.
- (109) Cao, Z.; Xiao, Z. L.; Gu, N.; Shimada, S.; Fukuda, T.; Matsuda, H. Corrosion Behaviors Studied in Self-Assembled Processes of Alkanethiol Monolayers on Polycrystalline Gold Substrates. *Solid State Phenom.* **2007**, *121–123*, 385–388.
- (110) Mrksich, M.; Sigal, G. B.; Whitesides, G. M. Surface Plasmon Resonance Permits in Situ Measurement of Protein Adsorption on Self-Assembled Monolayers of Alkanethiolates on Gold. *Langmuir* **1995**, *11* (11), 4383–4385.
- (111) Arima, Y.; Iwata, H. Effect of Wettability and Surface Functional Groups on Protein Adsorption and Cell Adhesion Using Well-Defined Mixed Self-Assembled Monolayers. *Biomaterials* **2007**, *28* (20), 3074–3082.
- (112) Vallée, A.; Humblot, V.; Al Housseiny, R.; Boujday, S.; Pradier, C.-M. BSA Adsorption on Aliphatic and Aromatic Acid SAMs: Investigating the Effect of Residual Surface Charge and Sublayer Nature. *Colloids Surf. B Biointerfaces* **2013**, *109*, 136–142.
- (113) Thébault, P.; Boujday, S.; Sénéchal, H.; Pradier, C.-M. Investigation of an Allergen Adsorption on Amine- and Acid-Terminated Thiol Layers: Influence on Their Affinity to Specific Antibodies. *J. Phys. Chem. B* **2010**, *114* (32), 10612–10619.
- (114) Ben Haddada, M.; Salmain, M.; Boujday, S. Gold Colloid-Nanostructured Surfaces for Enhanced Piezoelectric Immunosensing of Staphylococcal Enterotoxin A. *Sens. Actuators B Chem.* **2018**, *255*, 1604–1613.
- (115) Vericat, C.; Vela, M. E.; Benitez, G.; Carro, P.; Salvarezza, R. C. Self-Assembled Monolayers of Thiols and Dithiols on Gold: New Challenges for a Well-Known System. *Chem. Soc. Rev.* **2010**, *39* (5), 1805.



- (116) Vericat, C.; Vela, M. E.; Corthey, G.; Pensa, E.; Cortés, E.; Fonticelli, M. H.; Ibañez, F.; Benitez, G. E.; Carro, P.; Salvarezza, R. C. Self-Assembled Monolayers of Thiolates on Metals: A Review Article on Sulfur-Metal Chemistry and Surface Structures. *RSC Adv* **2014**, *4* (53), 27730–27754.
- (117) Colorado, R.; Lee, T. R. Wettabilities of Self-Assembled Monolayers on Gold Generated from Progressively Fluorinated Alkanethiols. *Langmuir* **2003**, *19* (8), 3288–3296.
- (118) Chinwangso, P.; Lee, H. J.; Jamison, A. C.; Marquez, M. D.; Park, C. S.; Lee, T. R. Structure, Wettability, and Thermal Stability of Organic Thin-Films on Gold Generated from the Molecular Self-Assembly of Unsymmetrical Oligo(Ethylene Glycol) Spiroalkanedithiols. *Langmuir* **2017**, *33* (8), 1751–1762.
- (119) Lebec, V.; Landoulsi, J.; Boujday, S.; Poleunis, C.; Pradier, C.-M.; Delcorte, A. Probing the Orientation of  $\beta$ -Lactoglobulin on Gold Surfaces Modified by Alkyl Thiol Self-Assembled Monolayers. *J. Phys. Chem. C* **2013**, *117* (22), 11569–11577.
- (120) Bedford, E. E.; Boujday, S.; Humblot, V.; Gu, F. X.; Pradier, C.-M. Effect of SAM Chain Length and Binding Functions on Protein Adsorption:  $\beta$ -Lactoglobulin and Apo-Transferrin on Gold. *Colloids Surf. B Biointerfaces* **2014**, *116*, 489–496.
- (121) Lebec, V.; Boujday, S.; Poleunis, C.; Pradier, C.-M.; Delcorte, A. Time-of-Flight Secondary Ion Mass Spectrometry Investigation of the Orientation of Adsorbed Antibodies on SAMs Correlated to Biorecognition Tests. *J. Phys. Chem. C* **2014**, *118* (4), 2085–2092.
- (122) Aissaoui, N.; Bergaoui, L.; Landoulsi, J.; Lambert, J.-F.; Boujday, S. Silane Layers on Silicon Surfaces: Mechanism of Interaction, Stability, and Influence on Protein Adsorption. *Langmuir* **2012**, *28* (1), 656–665.
- (123) Vashist, S. K.; Lam, E.; Hrapovic, S.; Male, K. B.; Luong, J. H. T. Immobilization of Antibodies and Enzymes on 3-Aminopropyltriethoxysilane-Functionalized Bioanalytical Platforms for Biosensors and Diagnostics. *Chem. Rev.* **2014**, *114* (21), 11083–11130.
- (124) Neves-Petersen, M. T. Photonic Activation of Disulfide Bridges Achieves Oriented Protein Immobilization on Biosensor Surfaces. *Protein Sci.* **2006**, *15* (2), 343–351.
- (125) Szychalska, K.; Zając, D.; Baluta, S.; Halicka, K.; Cabaj, J. Functional Polymers Structures for (Bio)Sensing Application—A Review. *Polymers* **2020**, *12* (5), 1154.
- (126) Chiodi, E.; Marn, A. M.; Geib, M. T.; Ünlü, M. S. The Role of Surface Chemistry in the Efficacy of Protein and DNA Microarrays for Label-Free Detection: An Overview. *Polymers* **2021**, *13* (7), 1026.
- (127) Hosseini, S.; Ibrahim, F.; Djordjevic, I.; Koole, L. H. Recent Advances in Surface Functionalization Techniques on Polymethacrylate Materials for Optical Biosensor Applications. *The Analyst* **2014**, *139* (12), 2933.
- (128) Löfås, S.; Johnsson, B. A Novel Hydrogel Matrix on Gold Surfaces in Surface Plasmon Resonance Sensors for Fast and Efficient Covalent Immobilization of Ligands. *J. Chem. Soc. Chem Commun* **1990**, No. 21, 1526–1528.
- (129) Karlsson, R.; Michaelsson, A.; Mattsson, L. Kinetic Analysis of Monoclonal Antibody-Antigen Interactions with a New Biosensor Based Analytical System. *J. Immunol. Methods* **1991**, *145* (1–2), 229–240.
- (130) Johnsson, B.; Löfås, S.; Lindquist, G.; Edström, Å.; Hillgren, R.-M. M.; Hansson, A. Comparison of Methods for Immobilization to Carboxymethyl Dextran Sensor Surfaces by Analysis of the Specific Activity of Monoclonal Antibodies. *J. Mol. Recognit.* **1995**, *8* (1–2), 125–131.
- (131) Howell, S.; Kenmore, M.; Kirkland, M.; Badley, R. A. High-density Immobilization of an Antibody Fragment to a Carboxymethylated Dextran-linked Biosensor Surface. *J. Mol. Recognit.* **1998**, *11*, 4.
- (132) Jung, S.-H.; Jung, J.-W.; Suh, I.-B.; Yuk, J. S.; Kim, W.-J.; Choi, E. Y.; Kim, Y.-M.; Ha, K.-S. Analysis of C-Reactive Protein on Amide-Linked *N*-Hydroxysuccinimide–Dextran Arrays with a Spectral Surface Plasmon Resonance Biosensor for Serodiagnosis. *Anal. Chem.* **2007**, *79* (15), 5703–5710.
- (133) Yuan, Y.; Zhang, J.; Yin, M.; Liu, C. Plasma-Mediated Immobilization of Antibody with PEG as Spacer for Enhanced Endothelial Cell Adhesion and Proliferation. *Adv. Biomater.* **2014**, *2014*, 1–8.

- (134) Huebner, M. Layer-by-Layer Generation of PEG-Based Regenerable Immunosensing Surfaces for Small-Sized Analytes. *Biosens. Bioelectron.* **2015**, *8*.
- (135) Ben Haddada, M.; Huebner, M.; Casale, S.; Knopp, D.; Niessner, R.; Salmain, M.; Boujday, S. Gold Nanoparticles Assembly on Silicon and Gold Surfaces: Mechanism, Stability, and Efficiency in Diclofenac Biosensing. *J. Phys. Chem. C* **2016**, *120* (51), 29302–29311.
- (136) Tabasi, O.; Falamaki, C. Controlled Immobilization of IgG1 on Carboxymethyl and Amino-Dextran SPR Chips under External Vertical Electric Fields. *Appl. Surf. Sci.* **2019**, *490*, 251–259.
- (137) Bakhshpour, M.; Idil, N.; Perçin, I.; Denizli, A. Biomedical Applications of Polymeric Cryogels. *Appl. Sci.* **2019**, *9* (3), 553.
- (138) Perçin, I.; Idil, N.; Denizli, A. Molecularly Imprinted Poly(N-Isopropylacrylamide) Thermosensitive Based Cryogel for Immunoglobulin G Purification. *Process Biochem.* **2019**, *80*, 181–189.
- (139) Bereli, N.; Ertürk, G.; Tümer, M. A.; Say, R.; Denizli, A. Oriented Immobilized Anti-HlgG via F<sub>c</sub> Fragment-Imprinted PHEMA Cryogel for IgG Purification: Oriented Immobilized Anti-HlgG via Fc Fragments. *Biomed. Chromatogr.* **2013**, *27* (5), 599–607.
- (140) Vashist, S. K.; Luong, J. H. T. Antibody Immobilization and Surface Functionalization Chemistries for Immunodiagnosics. In *Handbook of Immunoassay Technologies*; Elsevier, 2018; pp 19–46.
- (141) Palazon, F.; Montenegro Benavides, C.; Léonard, D.; Souteyrand, É.; Chevolut, Y.; Cloarec, J.-P. Carbodiimide/NHS Derivatization of COOH-Terminated SAMs: Activation or Byproduct Formation? *Langmuir* **2014**, *30* (16), 4545–4550.
- (142) Tricase, A.; Blasi, D.; Favia, A.; Stefanachi, A.; Leonetti, F.; Colafemmina, G.; Torsi, L.; Scamarcio, G. Surface Composition of Mixed Self-Assembled Monolayers on Au by Infrared Attenuated Total Reflection Spectroscopy. *Appl. Surf. Sci.* **2021**, *559*, 149883.
- (143) Boujday, S.; Méthivier, C.; Beccard, B.; Pradier, C.-M. Innovative Surface Characterization Techniques Applied to Immunosensor Elaboration and Test: Comparing the Efficiency of Fourier Transform–Surface Plasmon Resonance, Quartz Crystal Microbalance with Dissipation Measurements, and Polarization Modulation–Reflection Absorption Infrared Spectroscopy. *Anal Biochem* **2009**, *8*.
- (144) Betancor, L.; López-Gallego, F.; Hidalgo, A.; Alonso-Morales, N.; Mateo, G. D.-O. C.; Fernández-Lafuente, R.; Guisán, J. M. Different Mechanisms of Protein Immobilization on Glutaraldehyde Activated Supports: Effect of Support Activation and Immobilization Conditions. *Enzyme Microb. Technol.* **2006**, *39* (4), 877–882.
- (145) López-Gallego, F.; Guisán, J. M.; Betancor, L. Glutaraldehyde-Mediated Protein Immobilization. In *Immobilization of Enzymes and Cells: Third Edition*; Guisan, J. M., Ed.; Methods in Molecular Biology; Humana Press: Totowa, NJ, 2013; pp 33–41.
- (146) Migneault, I.; Dartiguenave, C.; Bertrand, M. J.; Waldron, K. C. Glutaraldehyde: Behavior in Aqueous Solution, Reaction with Proteins, and Application to Enzyme Crosslinking. *BioTechniques* **2004**, *37* (5), 790–802.
- (147) Liu, Y.; Yu, J. Oriented Immobilization of Proteins on Solid Supports for Use in Biosensors and Biochips: A Review. *Microchim. Acta* **2016**, *183* (1), 1–19.
- (148) Welch, N. G.; Scoble, J. A.; Muir, B. W.; Pigram, P. J. Orientation and Characterization of Immobilized Antibodies for Improved Immunoassays (Review). *Biointerphases* **2017**, *12* (2), 02D301.
- (149) Shen, M.; Rusling, J. F.; Dixit, C. K. Site-Selective Orientated Immobilization of Antibodies and Conjugates for Immunodiagnosics Development. *Methods* **2017**, *116*, 95–111.
- (150) Jung, Y.; Kang, H. J.; Lee, J. M.; Jung, S. O.; Yun, W. S.; Chung, S. J.; Chung, B. H. Controlled Antibody Immobilization onto Immunoanalytical Platforms by Synthetic Peptide. *Anal Biochem* **2008**, *7*.
- (151) Bashth, O. S.; Elkhodiry, M. A.; Laroche, G.; Hoesli, C. A. Surface Grafting of Fc-Binding Peptides as a Simple Platform to Immobilize and Identify Antibodies That Selectively Capture Circulating Endothelial Progenitor Cells. *Biomater. Sci.* **2020**, *8* (19), 5465–5475.
- (152) Boozer, C.; Ladd, J.; Chen, S.; Jiang, S. DNA-Directed Protein Immobilization for Simultaneous Detection of Multiple Analytes by Surface Plasmon Resonance Biosensor. *Anal. Chem.* **2006**, *78* (5), 1515–1519.

- (153) Meyer, R.; Giselbrecht, S.; Rapp, B. E.; Hirtz, M.; Niemeyer, C. M. Advances in DNA-Directed Immobilization. *Curr. Opin. Chem. Biol.* **2014**, *18*, 8–15.
- (154) Jain, A.; Cheng, K. The Principles and Applications of Avidin-Based Nanoparticles in Drug Delivery and Diagnosis. *J. Controlled Release* **2017**, *245*, 27–40.
- (155) Maglio, O.; Costanzo, S.; Cercola, R.; Zambrano, G.; Mauro, M.; Battaglia, R.; Ferrini, G.; Nistri, F.; Pavone, V.; Lombardi, A. A Quartz Crystal Microbalance Immunosensor for Stem Cell Selection and Extraction. *Sensors* **2017**, *17* (12), 2747.
- (156) Attili, B. S.; Suleiman, A. A. A Piezoelectric Immunosensor for the Detection of Cocaine. *Microchem. J.* **1996**, *54* (2), 174–179.
- (157) Briand, E.; Salmain, M.; Compère, C.; Pradier, C.-M. Immobilization of Protein A on SAMs for the Elaboration of Immunosensors. *Colloids Surf. B Biointerfaces* **2006**, *53* (2), 215–224.
- (158) Briand, E.; Salmain, M.; Compère, C.; Pradier, C.-M. Anti-Rabbit Immunoglobulin G Detection in Complex Medium by PM-RAIRS and QCM. *Biosens. Bioelectron.* **2007**, *22* (12), 2884–2890.
- (159) Salmain, M.; Ghasemi, M.; Boujday, S.; Spadavecchia, J.; Técher, C.; Val, F.; Le Moigne, V.; Gautier, M.; Briandet, R.; Pradier, C.-M. Piezoelectric Immunosensor for Direct and Rapid Detection of Staphylococcal Enterotoxin A (SEA) at the Ng Level. *Biosens. Bioelectron.* **2011**, *29* (1), 140–144.
- (160) Tajima, N.; Takai, M.; Ishihara, K. Significance of Antibody Orientation Unraveled: Well-Oriented Antibodies Recorded High Binding Affinity. *Anal. Chem.* **2011**, *83* (6), 1969–1976.
- (161) Lee, W.; Oh, B.-K.; Min Bae, Y.; Paek, S.-H.; Hong Lee, W.; Choi, J.-W. Fabrication of Self-Assembled Protein A Monolayer and Its Application as an Immunosensor. *Biosens. Bioelectron.* **2003**, *19* (3), 185–192.
- (162) Oh, B.-K.; Lee, W.; Kim, Y.-K.; Lee, W. H.; Choi, J.-W. Surface Plasmon Resonance Immunosensor Using Self-Assembled Protein G for the Detection of Salmonella Paratyphi. *J. Biotechnol.* **2004**, *111* (1), 1–8.
- (163) Fowler, J. M.; Stuart, M. C.; Wong, D. K. Y. Self-Assembled Layer of Thiolated Protein G as an Immunosensor Scaffold. *Anal. Chem.* **2007**, *79* (1), 350–354.
- (164) Briand, E.; Salmain, M.; Herry, J.-M.; Perrot, H.; Compère, C.; Pradier, C.-M. Building of an Immunosensor: How Can the Composition and Structure of the Thiol Attachment Layer Affect the Immunosensor Efficiency? *Biosens. Bioelectron.* **2006**, *22* (3), 440–448.
- (165) Schroeder, B.; Le Xuan, H.; Völzke, J. L.; Weller, M. G. Preactivation Crosslinking: An Efficient Method for the Oriented Immobilization of Antibodies. *Methods Protoc.* **2019**, *2* (2), 35.
- (166) Tsekenis, G.; Chatzipetrou, M.; Massauti, M.; Zergioti, I. Comparative Assessment of Affinity-Based Techniques for Oriented Antibody Immobilization towards Immunosensor Performance Optimization. *J. Sens.* **2019**, *2019*, 1–10.
- (167) Makaraviciute, A.; Ramanavicius, A.; Ramanaviciene, A. Development of a Reusable Protein G Based SPR Immunosensor for Direct Human Growth Hormone Detection in Real Samples. *Anal. Methods* **2015**, *7* (23), 9875–9884.
- (168) Yoo, H.; Shin, J.; Sim, J.; Cho, H.; Hong, S. Reusable Surface Plasmon Resonance Biosensor Chip for the Detection of H1N1 Influenza Virus. *Biosens. Bioelectron.* **2020**, *168*, 112561.
- (169) Makaraviciute, A.; Ramanaviciene, A. Site-Directed Antibody Immobilization Techniques for Immunosensors. *Biosens. Bioelectron.* **2013**, *50*, 460–471.
- (170) Vashist, S. K.; Dixit, C. K.; MacCraith, B. D.; O’Kennedy, R. Effect of Antibody Immobilization Strategies on the Analytical Performance of a Surface Plasmon Resonance-Based Immunoassay. *The Analyst* **2011**, *136* (21), 4431.
- (171) Gao, S.; Guisán, J. M.; Rocha-Martin, J. Oriented Immobilization of Antibodies onto Sensing Platforms - A Critical Review. *Anal. Chim. Acta* **2021**, 338907.
- (172) Baniukevic, J.; Kirlyte, J.; Ramanavicius, A.; Ramanaviciene, A. Application of Oriented and Random Antibody Immobilization Methods in Immunosensor Design. *Sens. Actuators B Chem.* **2013**, *189*, 217–223.
- (173) Bonroy, K.; Frederix, F.; Reekmans, G.; Dewolf, E.; De Palma, R.; Borghs, G.; Declerck, P.; Goddeeris, B. Comparison of Random and Oriented Immobilisation of Antibody Fragments on Mixed Self-Assembled Monolayers. *J. Immunol. Methods* **2006**, *312* (1–2), 167–181.

- (174) Kausaite-Minkstimiene, A.; Ramanaviciene, A.; Kirlyte, J.; Ramanavicius, A. Comparative Study of Random and Oriented Antibody Immobilization Techniques on the Binding Capacity of Immunosensor. *Anal. Chem.* **2010**, *82* (15), 6401–6408.
- (175) Boujday, S.; Bantegnie, A.; Briand, E.; Marnet, P.-G.; Salmain, M.; Pradier, C.-M. In-Depth Investigation of Protein Adsorption on Gold Surfaces: Correlating the Structure and Density to the Efficiency of the Sensing Layer. *J. Phys. Chem. B* **2008**, *112* (21), 6708–6715.
- (176) Frederix, F.; Bonroy, K.; Laureyn, W.; Reekmans, G.; Campitelli, A.; Dehaen, W.; Maes, G. Enhanced Performance of an Affinity Biosensor Interface Based on Mixed Self-Assembled Monolayers of Thiols on Gold. *Langmuir* **2003**, *19* (10), 4351–4357.
- (177) Lee, J. W.; Sim, S. J.; Cho, S. M.; Lee, J. Characterization of a Self-Assembled Monolayer of Thiol on a Gold Surface and the Fabrication of a Biosensor Chip Based on Surface Plasmon Resonance for Detecting Anti-GAD Antibody. *Biosens. Bioelectron.* **2005**, *20* (7), 1422–1427.
- (178) Ataman Sadik, D.; Eksi-Kocak, H.; Ertaş, G.; Boyacı, İ. H.; Mutlu, M. Mixed-Monolayer of N-Hydroxysuccinimide-Terminated Crosslinker and Short Alkanethiol to Improve the Efficiency of Biomolecule Binding for Biosensing. *Surf. Interface Anal.* **2018**, *50* (9), 866–878.
- (179) Taheri, R. A.; Rezayan, A. H.; Rahimi, F.; Mohammadnejad, J.; Kamali, M. Comparison of Antibody Immobilization Strategies in Detection of *Vibrio Cholerae* by Surface Plasmon Resonance. *Biointerphases* **2016**, *11* (4), 041006.
- (180) Choi, S.; Chae, J. Methods of Reducing Non-Specific Adsorption in Microfluidic Biosensors. *J. Micromechanics Microengineering* **2010**, *20* (7), 075015.
- (181) Xiao, X.-F.; Jiang, X.-Q.; Zhou, L.-J. Surface Modification of Poly Ethylene Glycol to Resist Nonspecific Adsorption of Proteins. *Chin. J. Anal. Chem.* **2013**, *41* (3), 445–453.
- (182) Wang, F.; Anderson, M.; Bernards, M.; Hunt, H. PEG Functionalization of Whispering Gallery Mode Optical Microresonator Biosensors to Minimize Non-Specific Adsorption during Targeted, Label-Free Sensing. *Sensors* **2015**, *15* (8), 18040–18060.
- (183) Charles, P.; Stubbs, V.; Soto, C.; Martin, B.; White, B.; Taitt, C. Reduction of Non-Specific Protein Adsorption Using Poly(Ethylene) Glycol (PEG) Modified Polyacrylate Hydrogels In Immunoassays for Staphylococcal Enterotoxin B Detection. *Sensors* **2009**, *9* (1), 645–655.
- (184) Im, H.; Shao, H.; Park, Y. I.; Peterson, V. M.; Castro, C. M.; Weissleder, R.; Lee, H. Label-Free Detection and Molecular Profiling of Exosomes with a Nano-Plasmonic Sensor. *Nat. Biotechnol.* **2014**, *32* (5), 490–495.
- (185) Gobi, K. V.; Iwasaka, H.; Miura, N. Self-Assembled PEG Monolayer Based SPR Immunosensor for Label-Free Detection of Insulin. *Biosens. Bioelectron.* **2007**, *22* (7), 1382–1389.
- (186) Gobi, K. V.; Matsumoto, K.; Toko, K.; Miura, N. Highly Regenerable and Storageable All-Chemical Based PEG-Immunosensor Chip for SPR Detection of Ppt Levels of Fragrant
- (187) Kawaguchi, T.; Shankaran, D.; Kim, S.; Gobi, K.; Matsumoto, K.; Toko, K.; Miura, N. Fabrication of a Novel Immunosensor Using Functionalized Self-Assembled Monolayer for Trace Level Detection of TNT by Surface Plasmon Resonance. *Talanta* **2007**, *72* (2), 554–560.
- (188) Anderson, A. S.; Dattelbaum, A. M.; Montañó, G. A.; Price, D. N.; Schmidt, J. G.; Martinez, J. S.; Grace, W. K.; Grace, K. M.; Swanson, B. I. Functional PEG-Modified Thin Films for Biological Detection. *Langmuir* **2008**, *24* (5), 2240–2247.
- (189) Piehler, J.; Brecht, A.; Valiokas, R.; Liedberg, B.; Gauglitz, G. A High-Density Poly(Ethylene Glycol) Polymer Brush for Immobilization on Glass-Type Surfaces. *Biosens. Bioelectron.* **2000**, *15* (9–10), 473–481.
- (190) Hou, S.; Ma, Z.; Meng, H.; Xu, Y.; He, Q. Ultrasensitive and Green Electrochemical Immunosensor for Mycotoxin Ochratoxin A Based on Phage Displayed Mimotope Peptide. *Talanta* **2019**, *194*, 919–924.
- (191) Mazouzi, Y.; Miche, A.; Loiseau, A.; Beito, B.; Méthivier, C.; Knopp, D.; Salmain, M.; Boujday, S. Design and Analytical Performances of a Diclofenac Biosensor for Water Resources Monitoring. *ACS Sens.* **2021**, accsensors.1c01607.
- (192) Mehne, J.; Markovic, G.; Pröll, F.; Schweizer, N.; Zorn, S.; Schreiber, F.; Gauglitz, G. Characterisation of Morphology of Self-Assembled PEG Monolayers: A Comparison of Mixed and Pure Coatings Optimised for Biosensor Applications. *Anal. Bioanal. Chem.* **2008**, *391* (5), 1783–1791.



- (193) Yoshimoto, K.; Nishio, M.; Sugasawa, H.; Nagasaki, Y. Direct Observation of Adsorption-Induced Inactivation of Antibody Fragments Surrounded by Mixed-PEG Layer on a Gold Surface. *J. Am. Chem. Soc.* **2010**, *132* (23), 7982–7989.
- (194) Hausteiner, N.; Gutiérrez-Sanz, Ó.; Tarasov, A. Analytical Model To Describe the Effect of Polyethylene Glycol on Ionic Screening of Analyte Charges in Transistor-Based Immunosensing. *ACS Sens.* **2019**, *4* (4), 874–882.
- (195) Horiguchi, Y.; Miyachi, S.; Nagasaki, Y. High-Performance Surface Acoustic Wave Immunosensing System on a PEG/Aptamer Hybridized Surface. *Langmuir* **2013**, *29* (24), 7369–7376.
- (196) Jeyachandran, Y. L.; Mielczarski, J. A.; Mielczarski, E.; Rai, B. Efficiency of Blocking of Non-Specific Interaction of Different Proteins by BSA Adsorbed on Hydrophobic and Hydrophilic Surfaces. *J. Colloid Interface Sci.* **2010**, *341* (1), 136–142.
- (197) Sakai, G.; Ogata, K.; Uda, T.; Miura, N.; Yamazoe, N. A Surface Plasmon Resonance-Based Immunosensor for Highly Sensitive Detection of Morphine. *Sens. Actuators B Chem.* **1998**, *49* (1–2), 5–12.
- (198) Zhang, L.; Salmain, M.; Liedberg, B.; Boujday, S. Naked Eye Immunosensing of Food Biotoxins Using Gold Nanoparticle-Antibody Bioconjugates. *ACS Appl. Nano Mater.* **2019**, *2* (7), 4150–4158.
- (199) Salmain, M.; Ghasemi, M.; Boujday, S.; Pradier, C.-M. Elaboration of a Reusable Immunosensor for the Detection of Staphylococcal Enterotoxin A (SEA) in Milk with a Quartz Crystal Microbalance. *Sens. Actuators B Chem.* **2012**, *173*, 148–156.





---

**Chapter 2. An experimental study of chain length and terminal group effects on the organization of thiolate Self-Assembled Monolayers (SAMs) onto gold surfaces**

---



## 2.1 Introduction

Self-assembled monolayers (SAMs) are more or less ordered assemblies of organic molecules that form spontaneously on surfaces.<sup>1</sup> One of the most studied system relies on the adsorption of alkylthiols molecules on gold metallic surfaces with several literature reviews dedicated to its features.<sup>2-4</sup>

Alkylthiol molecules exhibits a large variety of functional groups allowing to tailor the surface properties in agreement to the envisioned applications, notably for electronics<sup>5,6</sup>, corrosion protection<sup>7-9</sup>, biomolecules adsorption,<sup>10-12</sup> and biosensors.<sup>13,14</sup> Furthermore, terminal groups and chain length have been shown to influence surface properties such as wettability<sup>15,16</sup> and protein grafting.<sup>17-19</sup> Bhadra *et al.* investigated effects of chain length ( $n_{CH_2} = 2, 3, 6, 11, 16$ ) in COOH-terminated thiolate SAMs on gold and their impact on antibody-antigen binding efficiency. They found that packing density influence antibody density and orientation with the lowest response for “flat-on” antibody on poorly ordered SAMs ( $n_{CH_2} \leq 3$ ) in contrast to “side-on” antibody on denser packed SAMs ( $n_{CH_2} \geq 11$ ).<sup>20</sup> In addition, Bao *et al.* showed that chain length also influences the kinetics of immunoreaction using an *in-situ* approach with Attenuated Total Reflection Surface-Enhanced Infrared Absorption Spectroscopy (ATR-SEIRAS), with faster reaction obtained for longer chains ( $n_{CH_2} \geq 11$ ).<sup>21</sup>

Furthermore in the past decades more investigations have been devoted to deeply understand the alkylthiol formation on gold, with a focus on the nature of the thiol-gold interface using theoretical and experimental strategies.<sup>22-25</sup> Adsorption of short ( $n_{CH_2} = 2$ ) and long ( $n_{CH_2} = 11$ ) chains aminothiols on gold surface demonstrated theoretically and experimentally that a surface reconstruction related to molecular adsorption occurs for shorter chain while for longer chain length backbone interaction are sufficient to obtain better organized system with higher crystallinity.<sup>26</sup>

In this context, we investigated the formation of alkylthiol self-assembled monolayers on gold surface while studying the contributions of both chain length and terminal group on the order of the SAM and on the coordination mode of sulfur to gold. Thus, functionalization was performed using thiol molecules of increasing chain length, *i.e.* number of methylene groups in the backbone, exhibiting alkane (CH<sub>3</sub>) and carboxylic acid (COOH) terminal groups.

Furthermore, we also study the influence of the pH of functionalization of ethanolic solution and found that all investigated features influence the SAMs crystallinity as well as the S-Au interface. Investigations relied on complementary surface characterization techniques, *i.e.* Water Contact Angle (WCA), Polarization Modulation InfraRed Reflection Absorption Spectroscopy (PM-IRRAS) and X-Ray Photoelectron Spectroscopy (XPS). WCA results showed that hydrophobic CH<sub>3</sub>-SAMs were formed in contrast to hydrophilic COOH-SAMs and that wettability evolved with chain length.

Furthermore, terminal groups and chain length were shown to influence the order of the SAMs as well as the coordination mode of sulfur to gold with for instance the presence of multi-coordinated sulfur at low binding energy in XPS.

## **2.2 Experimental procedure**

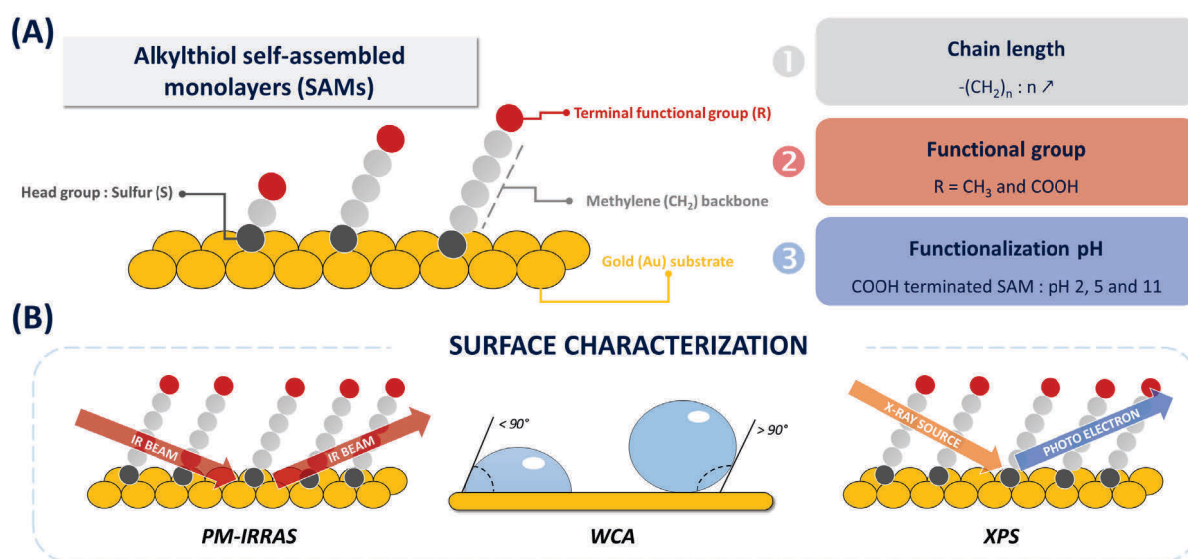
Experiments were carried out under ambient conditions on glass substrates (11 mm x 11 mm) successively coated with a  $2.5 \pm 1.5$  nm thick layer of chromium and a  $250 \pm 50$  nm thick layer of gold (Arrandee, Germany). Prior to functionalization, the gold-coated substrates were rinsed in absolute ethanol for 15 min, dried with a nitrogen flow, cleaned with UV/ozone for 30 min and annealed in a butane/propane flame to ensure good crystallinity of the gold topmost layers. Gold-coated substrates were immersed in thiol solutions in ethanol (1 mM) and left-covered for 24 hours under gentle agitation. The substrates were then washed once with ethanol for 5 min, ultrasonicated for 1 min in ethanol and washed twice for 5 min with ethanol. Functionalization and rinsing in ethanol at pH 2 were conducted using concentrated HCl. Functionalization and the two first rinsing steps in ethanol at pH 11 were performed using TMAOH, a third rinsing step was performed with an aqueous NaOH solution (1 mM).

All substrates were dried with a gentle nitrogen flow prior to further surface characterizations. Experiments were conducted in triplicate at least and data presented herein were selected as representative of the study.

More detailed information concerning materials and methods is given in the Supplementary Information at the end of this chapter.

## 2.3 Results and discussion

In this work, we studied alkylthiol self-assembled monolayers (SAMs) on gold surface and investigated the influence of (1) chain length, (2) functional group and (3) pH of functionalization on the order of the prepared SAM and on the coordination mode of sulfur to gold surface (**Figure 2. 1**). The SAMs were analyzed with appropriate characterization techniques, namely Polarization Modulation Infrared Reflection Absorption Spectroscopy (PM-IRRAS), Water Contact Angle (WCA) and X-ray Photoelectron Spectroscopy (XPS).

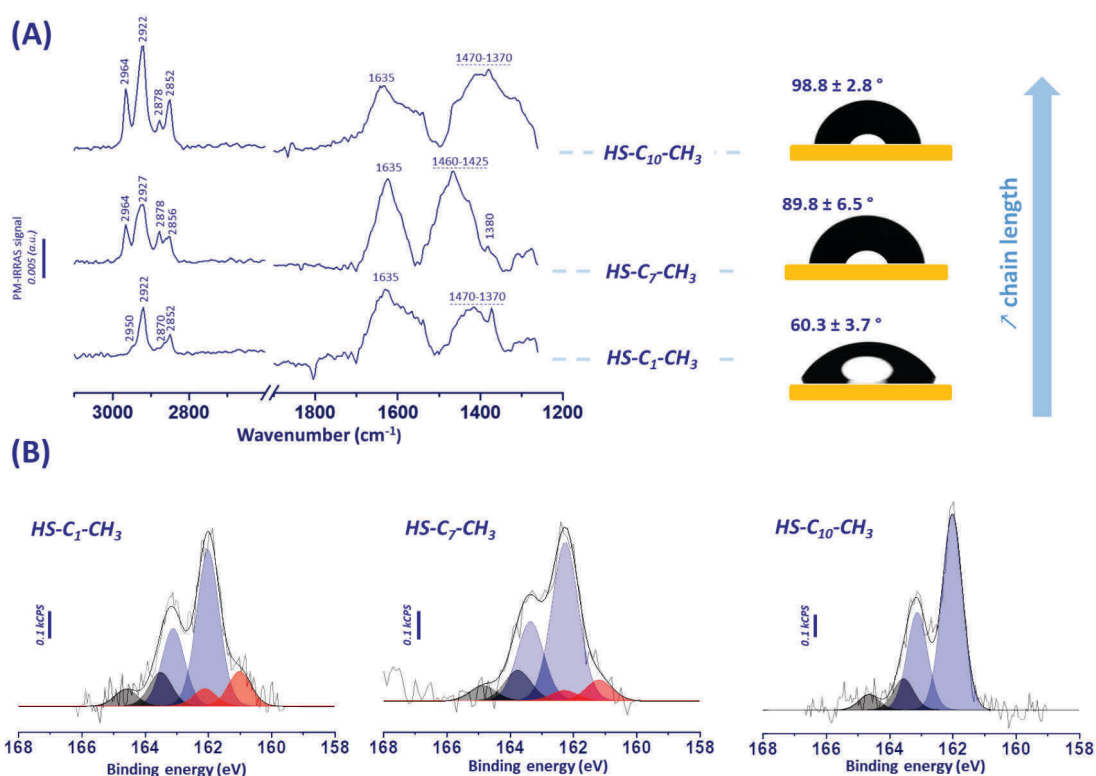


**Figure 2. 1.** (A) Overview of experimental strategy for the formation of alkylthiol SAMs on gold with investigated features: ❶ chain length, ❷ functional group and ❸ functionalization pH. (B) The prepared SAMs were analyzed using the following surface characterization techniques Polarization Modulation Infrared Reflection Absorption Spectroscopy (PM-IRRAS), Water contact angle (WCA) and X-ray photoelectron spectroscopy (XPS).

### 2.3.1 Effect of chain length

First and foremost, alkanethiol (CH<sub>3</sub>) SAMs formation on gold was investigated in order to evaluate chain length influence on the order of the SAM by PM-IRRAS and WCA, as well as on the coordination mode of sulfur atoms to gold by XPS (**Figure 2. 2**). CH<sub>3</sub>-SAMs of increasing chain length were studied, with short chain (HS-C<sub>1</sub>-CH<sub>3</sub>), mid chain (HS-C<sub>7</sub>-CH<sub>3</sub>) and long chain HS-C<sub>10</sub>-CH<sub>3</sub> molecules. Independently of the chain length, bands located at 1470 and 1380 cm<sup>-1</sup> assigned to CH<sub>2</sub> scissors and CH<sub>3</sub> symmetric vibrations were spotted on IR spectra. A broad band also observed on non-functionalized substrate was spotted at 1635 cm<sup>-1</sup> and was attributed to possible adsorbed water onto the surface (**Table S2. 1**).





**Figure 2. 2.** (A) Baseline corrected PM-IRRAS spectra with corresponding water contact angle results and (B) background subtracted high-resolution XPS S<sub>2p</sub> spectra of CH<sub>3</sub>-SAM of increasing chain length.

Characteristic bands of alkyl chains were also observed at higher wavenumber with notably the presence of asymmetric and symmetric CH<sub>3</sub> stretching vibrations centered at 2960 and 2880 cm<sup>-1</sup>, respectively. Bands in the region of 2920-2850 cm<sup>-1</sup>, attributed to asymmetric and symmetric CH<sub>2</sub> stretching vibrations, were found to switch with increasing chain length with values at 2922 cm<sup>-1</sup> for HS-C<sub>1/10</sub>-CH<sub>3</sub> and 2927 cm<sup>-1</sup> for HS-C<sub>7</sub>-CH<sub>3</sub> (Table S2. 2).

Several studies showed that while increasing chain length, interactions between methylene (CH<sub>2</sub>) groups in the backbone are more important and translate into higher intensities and smaller  $\nu_{CH_2}^{asymm}$  values, the latter being related to a more ordered SAMs with better crystallinity with for instance a value of 2918 cm<sup>-1</sup> for solid-like SAM.<sup>27,28,26</sup>

The position of  $\nu_{CH_2}^{asymm}$  band for the shorter chain was found to be lower than the one expected for non-ordered layer. Porter *et al.* suggested, that short chains SAM ( $n_{CH_2} \leq 5$ ) may adopt a more tilted configuration leading to smaller value of the asymmetric CH<sub>2</sub> band despite its poor crystallinity.<sup>29</sup>

In addition, smaller intensity of the CH<sub>3</sub> stretching band (~2960 cm<sup>-1</sup>) for shorter chain was also observed and attributed to smaller surface coverage leading to less intense signal in IR spectra and to difference in chain orientation.

WCA analysis was also conducted in order to confirm functionalization of the gold substrate and to investigate effect of chain length on surface wettability (**Figure 2. 2A**).

Starting from a hydrophilic surface for cleaned gold substrate ( $32.1 \pm 2.6^\circ$ ), SAMs adsorption led to less hydrophilic ( $60.3 \pm 3.7^\circ$ ) to hydrophobic surfaces ( $98.8 \pm 2.8^\circ$ ), for the shorter and longer CH<sub>3</sub>-SAMs, respectively. Indeed, increasing chain length (*i.e.* number of CH<sub>2</sub> groups in the backbone) results in higher proportion of nonpolar groups and consequently to hydrophobic behavior.<sup>30,31</sup> Recent work from Amara *et al.* dedicated to the impacts of chain length ( $n_{CH_2} = 6 - 19$ ) and odd-even effects on the formation of CH<sub>3</sub>-SAM on gold showed a similar behavior.<sup>32</sup> In addition to a better organization while increasing chain length, SAMs of  $n_{\text{odd}}$  exhibit more gauche defects than SAMs of  $n_{\text{even}}$  leading to variation in surface hydrophobicity. Moreover, CH<sub>3</sub>-SAM were found to undergo phase transition on gold surface based on wettability and Atomic Force Microscopy (AFM) experiments with regimes ranging from pseudo-forming to solid-like phases, respectively from short ( $n_{CH_2} \leq 3$ ) to longer chain length ( $n_{CH_2} \geq 14$ ) SAMs.<sup>33</sup> For more detailed discussion on odd-even effects in organic SAMs we refer to a review from Tao *et al.*<sup>34</sup>

**Table 2. 1.** XPS atomic percentages and S<sub>2p</sub> photopeak decompositions corrected by Scofield factors for CH<sub>3</sub>-SAMs on gold.

	HS-C <sub>1</sub> -CH <sub>3</sub>	HS-C <sub>7</sub> -CH <sub>3</sub>	HS-C <sub>10</sub> -CH <sub>3</sub>
Au <sub>4f</sub>	60.98	55.94	45.79
O <sub>1s</sub>	10.49	5.77	6.41
C <sub>1s</sub>	25.73	35.09	45.34
S <sub>2p</sub>	2.80	3.21	2.46
<i>S<sub>2p</sub> photopeak decomposition: Relative S% (absolute S%)</i>			
S-H	15.06 (0.44)	11.67 (0.38)	13.8 (0.34)
S-Au <sub>162</sub>	69.41 (1.94)	83.14 (2.67)	86.2 (2.12)
S-Au <sub>161</sub>	15.53 (0.42)	5.19 (0.16)	-
S-Au/nm <sup>2</sup>	2.6 ± 0.2	2.9 ± 0.5	3.4 ± 0.5

XPS measurements on CH<sub>3</sub>-SAM showed the presence of gold, oxygen, carbon and sulfur atoms (**Table 2. 1**). The presence of carbon and oxygen in excess on the SAMs was systematically observed and is often attributed to contamination from the deposition method at the solid-liquid interface. Work conducted on amine-terminated alkanethiols SAMs showed that oxygen content was most likely coming from co-adsorbates such as bound water molecules.<sup>35</sup>

As presented in **Table 2. 1**, with increasing chain length we observed a decrease of the Au<sub>4f</sub> signal which is consistent with the increased backbone length and to an attenuation from the substrate signal.<sup>36,37</sup> The high-resolution XPS S<sub>2p</sub> spectra from the alkanethiol SAMs on gold presented in **Figure 2. 2B** showed different contributions for the sulfur atoms.

Two main S<sub>2p<sub>3/2</sub></sub> contributions attributed to sulfur bound to gold (S-Au<sub>162</sub>) and free thiol (S-H), respectively at 162.3 and 163.8 eV, were observed independently of the chain length. In spite of the washing and sonication steps during the experimental procedure, free thiol molecules remained on the surface. In addition, the proportion of free thiol molecules for short chain was found to be higher (22 ± 6 %) in comparison to mid and longer chain lengths (~ 12 ± 2 %), showing that increasing the lateral chain stabilization between thiols backbones leads to a decrease of free molecules on the surface (**Table S2. 3**).

Another contribution of chemisorbed thiol molecules at lower binding energy (S-Au<sub>161</sub>) was observed for short and mid chain length CH<sub>3</sub>-SAM. Bedford *et al.* attributed this coordination mode to molecular adsorption of thiol molecules on the surface with a multi-coordinated sulfur atom on the surface for short amine thiol SAM.<sup>26</sup>

Furthermore, according to **Table S2. 3**, this S-Au<sub>161</sub> contribution decrease from 15.2 ± 4.7 to 7.4 ± 2.4 % while increasing chain length and is not observed for longer chain length, suggesting that chain length contribution influence the coordination mode of the sulfur to gold. Therefore, contrary to what IR results suggested, based on the  $\nu_{CH_2}^{asymm}$  values, a difference in SAMs organization was observed with respect to its chain length.

Indeed, while IR showed the same degree of organization for the shorter and longer chains, XPS demonstrated that shorter chain SAMs adopt a different mode of coordination to gold substrate with the presence of multi-coordinated sulfur (S-Au<sub>161</sub>) and also lower surface coverage (S-Au/nm<sup>2</sup>) in contrast to longer SAMs. Hence, XPS results illustrate in a more accurate way the effect of chain length on CH<sub>3</sub> SAMs formation.

Furthermore, we observed the presence of oxidized sulfur ( $\text{SO}_x$ ) at higher binding energy ( $\sim 170$  eV) for shorter thiol molecules ( $\text{HS-C}_1\text{-CH}_3$ ) as presented in **Figure S2. 1**, in that way the value presented herein are corrected from this contribution. Oxidized sulfur contribution in XPS is occasionally observed in the literature and was attributed to the deposition method at the liquid-solid interface and related to penetration of atmospheric oxygen to the gold interface.<sup>35</sup> Furthermore, work from Willey *et al.* investigated the degradation of alkanethiol SAMs on gold under ambient laboratory conditions.<sup>38</sup> They showed that exposure to air led to the appearance of oxidized sulfur, increased content in oxygen as well as a decrease in carbon and sulfur bound to gold contributions, which were related to thiol desorption. Hence in this work, the timeframe between the end of functionalization and surface characterizations was reduced to the minimum.

The number of sulfur atoms bound to gold surface ( $\text{S-Au}/\text{nm}^2$ ), comprising  $\text{S-Au}_{161}$  and  $\text{S-Au}_{162}$  contributions, for  $\text{CH}_3$ -SAMs of increasing chain length is presented in **Table 2. 1** (detailed calculation is presented in Supplementary Information). We noticed that increasing chain length led to a slight increase in the number of sulfur atoms bound to gold with values ranging from  $2.6 \pm 0.2$  to  $3.4 \pm 0.5$   $\text{S-Au}/\text{nm}^2$ , respectively for  $\text{HS-C}_1\text{-CH}_3$  and  $\text{HS-C}_{10}\text{-CH}_3$ .

Increasing stabilization from methylene groups through Van der Waals forces leads to more intermolecular interactions and to increased packing and denser SAMs on the surface with value closer to a complete monolayer ( $4.5$   $\text{S-Au}/\text{nm}^2$ ).<sup>2,39</sup> Furthermore, we noticed that the surface coverage calculated for the shorter chain is mainly attributed to sulfur atoms bound to gold for ordered molecules ( $\text{S-Au}_{162}/\text{nm}^2 = 2.1$ ) rather than multi-coordinated sulfur atoms related to molecular adsorption on the surface ( $\text{S-Au}_{161}/\text{nm}^2 = 0.5$ ).

### 2.3.2 Effect of terminal group and pH of functionalization

Subsequently, in order to investigate both chain length and terminal groups contributions we studied the formation of carboxylic acid terminated ( $\text{COOH}$ ) SAMs of increasing chain length (**Figure 2. 3**). Previous works showed that rinsing  $\text{COOH}$ -SAMs with aqueous solutions of different pH influence the protonation states of surface moieties and the order of the monolayer.<sup>12,40</sup> Nevertheless, to our knowledge no work has been conducted on the influence of the pH of functionalization on the order of SAMs and on the nature of the  $\text{S-Au}$  interface.

The main difference between  $\text{CH}_3$  and  $\text{COOH}$  terminated SAMs is the presence of characteristic bands from the carbonyl ( $\text{C=O}$ ) and carboxylates ( $\text{COO}^-$ ) moieties, respectively at  $1715$  and  $1620/1415$   $\text{cm}^{-1}$  (asymmetric and symmetric vibrations, respectively).

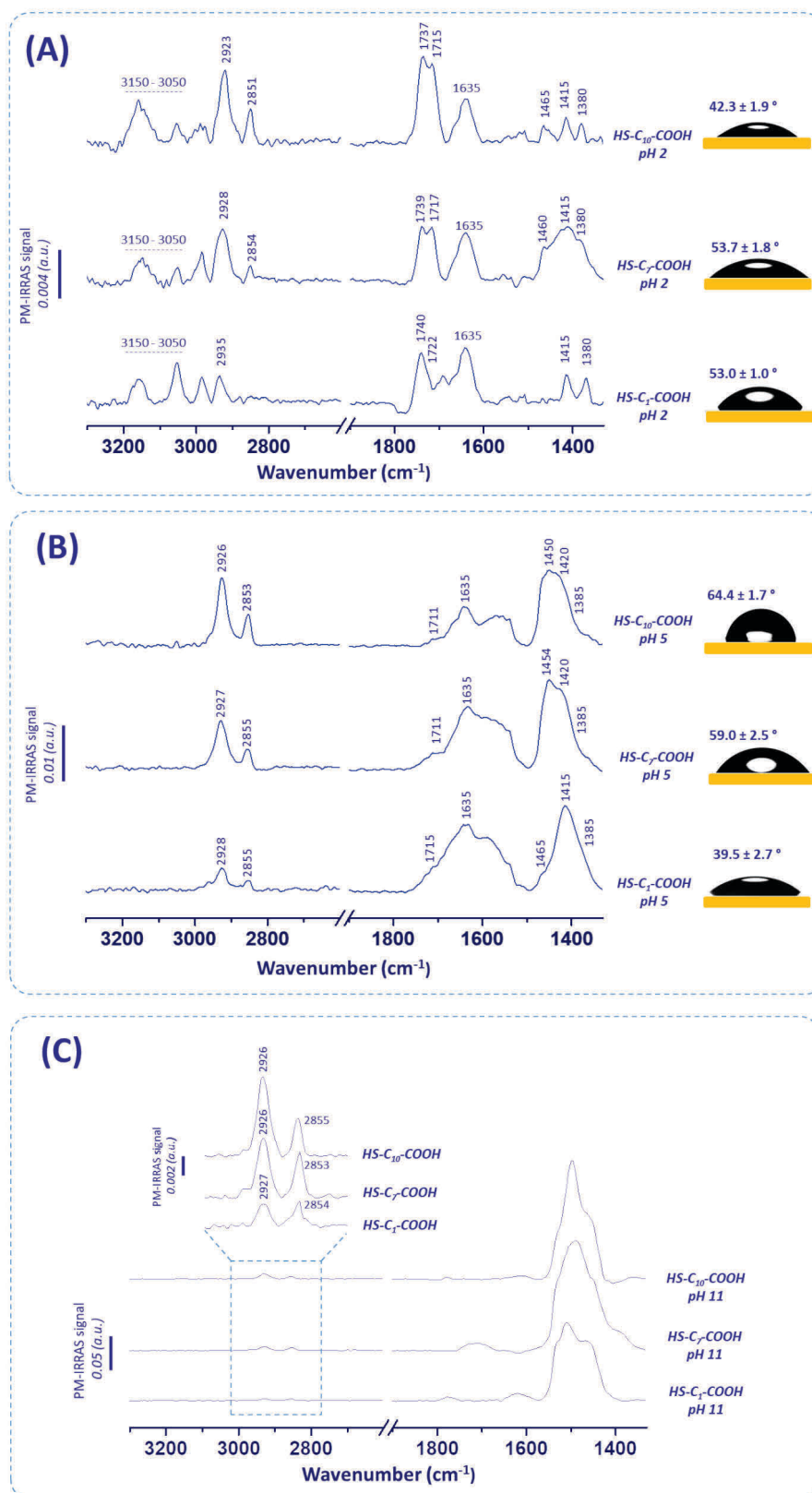
At pH 5, both protonated and deprotonated species should coexist on the surface since the  $pK_a$  of the carboxylic acid group is close to the working pH conditions, *i.e.* with theoretical  $pK_a$  values ranging from 4.2 to 5.05. Note that the  $pK_a$  of such molecules was shown to evolve with regards to several parameters: (1) with chain length and surface coverage<sup>41,42</sup>, (2) once adsorbed on a gold surface compared to free molecules in solution<sup>43-45</sup> and (3) depending on surface's curvature if immobilized on gold nanoparticle (AuNP).<sup>46</sup>

IR spectra show a small shoulder around  $1715\text{ cm}^{-1}$  most likely coming from carbonyl function on the surface as well as more intense bands at  $1415\text{ cm}^{-1}$  attributed to the symmetric stretching of carboxylates functions, suggesting indeed that both C=O and COO<sup>-</sup> moieties are present on the surface. These observations are consistent with previous work from Méthivier *et al.* demonstrating that terminal group of a HS-C<sub>10</sub>-COOH SAMs undergo deprotonation while immersed in ethanolic solution.<sup>40</sup> The observation of a band around  $1620\text{ cm}^{-1}$  corresponding to the asymmetric stretching of carboxylates functions was made difficult due to the presence of a large band possibly coming from adsorbed water ( $\sim 1635\text{ cm}^{-1}$ ).

At acidic pH, we observed a stronger signal for the carbonyl function with two contributions from the free C=O and H-bonded carboxylic acid stretching vibrations, respectively at  $1740$  and  $1715\text{ cm}^{-1}$ . Bands at higher wavenumbers ( $3150\text{-}3050\text{ cm}^{-1}$ ) were only encountered at acidic pH and were attributed to OH vibrations (**Table S2. 1**).

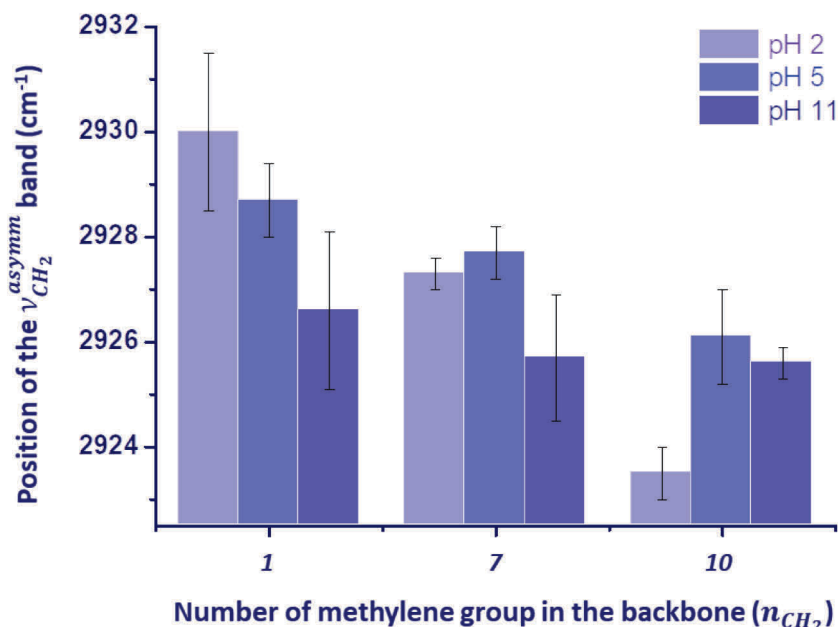
After functionalization in TMAOH and washing with an aqueous NaOH solution, the IR spectra showed intense signal at lower wavenumbers making assignment difficult in this region, thus we focused on the higher wavenumber region. In order to check if some residual salts remained on the surface, which would interfere with further surface characterizations, the surface was immersed in milli-Q water for 5 minutes.

We observed a drastic decrease of these IR bands (**Figure S2. 2**), indicating removal of adsorbed salts onto the surface, as well as a shift of the  $\nu_{CH_2}^{asymm}$  band with increased intensity, suggesting SAM reorganization on the surface.



**Figure 2. 3.** Baseline corrected PM-IRRAS spectra and corresponding WCA results of COOH-SAMs of increasing chain lengths on gold at different pH of functionalization: (A) pH 2, (B) pH 5 and (C) pH 11.

The position of the asymmetric CH<sub>2</sub> stretching ( $\nu_{CH_2}^{asymm}$ ) band was plotted for all chain length and pH of functionalization and is given in **Figure 2. 4**.



**Figure 2. 4.** Position of the asymmetric CH<sub>2</sub> stretching ( $\nu_{CH_2}^{asymm}$ ) vibration band from PM-IRRAS results for the COOH-SAMs of different chain length at pH of functionalization of 2, 5 and 11.

Globally for all pH values, increasing the chain length led to a decrease in the position of the  $\nu_{CH_2}^{asymm}$  band. Moreover, we observed that the presence of the carboxylic acid terminal group, able to interact with the neighboring molecules through H-bonding, does not necessarily conduct to a more ordered layer as compared to CH<sub>3</sub>-SAMs. Techane *et al.* found that most alkanethiol SAMs tend to form slightly more ordered layers than the corresponding carboxylic acid terminated SAMs and attributed it to steric hindrance from the COOH group as well as H-bonding leading to more disordered SAMs.<sup>36</sup>

At pH 5, increasing the chain length led to slightly more ordered SAMs as shown in **Figure 2. 4** and **Table S2. 4**. However, the COOH-SAMs appear to be less ordered than the CH<sub>3</sub>-SAMs for short and mid chain length adsorbates, in spite of the ability of terminal groups interactions *via* H-bonding. For longer chain length, a value of  $2925.7 \pm 0.6 \text{ cm}^{-1}$  was obtained and suggest the formation of an ordered layer on the gold surface.



We did not observe any improvement for the short and mid chain length SAMs at pH 2 neither with a highest degree of disorder for the shorter chain. Nevertheless, for the long chain SAM a position of  $2923.5 \pm 0.5 \text{ cm}^{-1}$  was found for the  $\nu_{\text{CH}_2}^{\text{assym}}$  band. Hence, at acidic pH we observed the contributions from both chain length and terminal group on the order of the SAMs.

At basic pH, the surface moieties should predominantly be  $\text{COO}^-$  groups leading to electrostatic repulsion from the terminal groups during functionalization and therefrom to less ordered SAMs. Surprisingly, we obtained similar results to the ones at pH 5 with slightly improved order while increasing chain length (**Figure 2. 4**) despite of the expected disorder for such system as previously reported in the literature.<sup>12,27</sup>

Results of WCA at pH values of 2 and 5 were similar as shown in **Figure 2. 3** and the surface remained hydrophilic even for increased chain length, as opposed to what was observed for  $\text{CH}_3$ -SAMs. Therefore, terminal groups do influence the surface wettability due to the polar nature of its surface moieties, *i.e.*  $\text{COOH}$  and  $\text{COO}^-$  groups.<sup>47,48</sup>

We also noticed a less significative influence of the chain length on the wettability of those surface in comparison to the  $\text{CH}_3$ -SAMs as not so much change is observed while increasing chain length, suggesting that terminal group contribution overweight the one of chain length for  $\text{COOH}$ -SAMs.

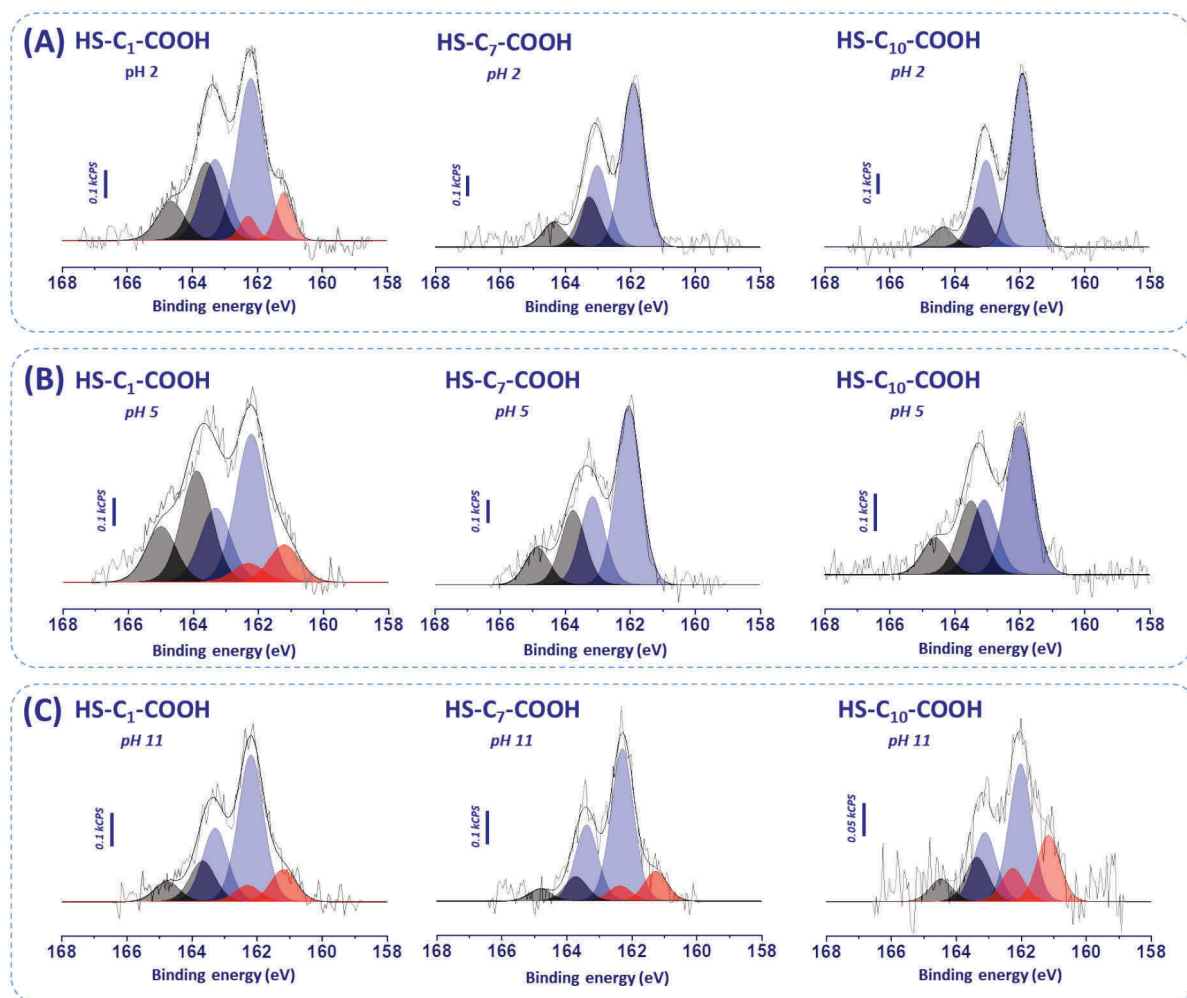
For SAMs prepared at basic pH the water droplet immediately spread on the surface after deposition making WCA analysis impossible. However, we do not attribute this to a superhydrophilic behavior but rather to the presence of some remaining salts, as suggested earlier in the discussion.

High-resolution XPS  $\text{S}_{2p}$  spectra for  $\text{COOH}$ -SAMs of increasing chain length at different pH of functionalization are presented in **Figure 2. 5** and corresponding elemental composition is provided in **Table S2. 5**.

For functionalization conducted at pH values of 2 and 5, both chain length and terminal groups appeared to influence the coordination behavior of sulfur to gold since we did not observe the  $\text{S-Au}_{161}$  contribution for the mid chain length SAMs ( $\text{HS-C}_7\text{-COOH}$ ), in opposition to what was obtained for  $\text{CH}_3$ -SAMs. As presented in **Figure 2. 5C**, conducting the functionalization at pH 11 led to less ordered SAMs even for those of longer chain length.

Without stabilization from H-bonding and considering electrostatic repulsion from the terminal groups, molecular adsorption ( $\text{S-Au}_{161}$ ) was observed independently of the chain length.

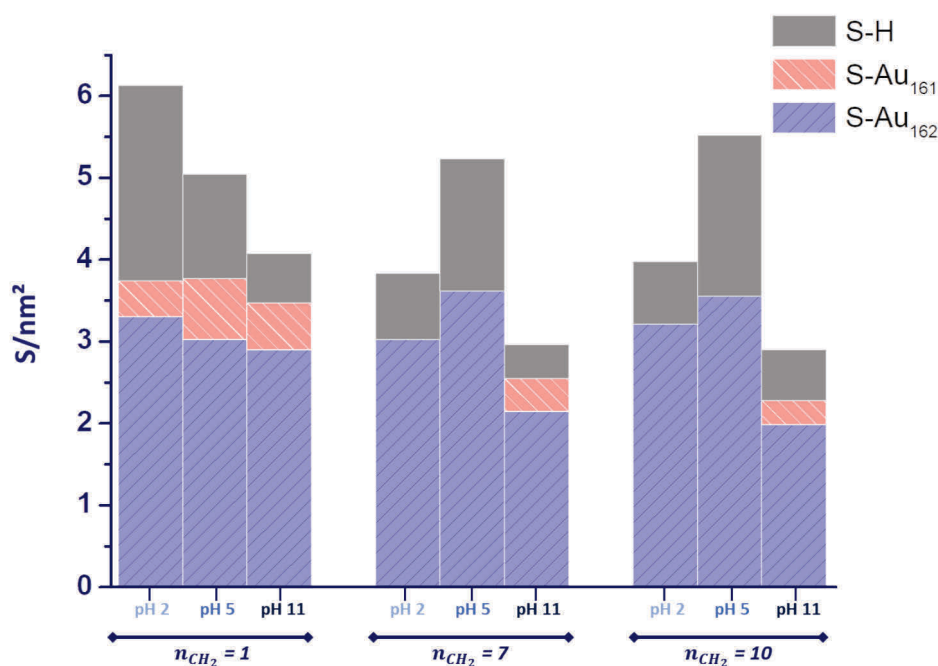




**Figure 2. 5.** Background subtracted high-resolution XPS  $S_{2p}$  spectra of COOH-SAMs of increasing chain length adsorbed on gold at different pH of functionalization: (A) pH 2, (B) pH 5 and (C) pH 11.

As presented in **Figure 2. 6**, the number of sulfur atoms bound to gold ( $S\text{-Au}/\text{nm}^2$ ) for COOH-SAMs was determined following the same procedure presented in Supporting Information and the number of free thiol molecules ( $\text{SH}/\text{nm}^2$ ) was calculated from the relative percentages presented in **Table S2. 6**.

Globally, chemisorption on gold was higher at pH values of 2 and 5 showing that terminal group interaction, typically H-bonding, allow to form denser monolayer on the surface ( $\sim 4 S\text{-Au}/\text{nm}^2$ ). At basic pH, *i.e* beyond  $pK_a$  value, most surface moieties are  $\text{COO}^-$  groups, thus electrostatic repulsion between terminal groups led to smaller molecules adsorption. Nevertheless, we acknowledge that functionalization in such complex media, *e.g.* presence of more species than just the solvent and the thiol molecules, might lead to adsorption of contaminants and ultimately to less dense monolayers.



**Figure 2. 6.** Total amount of sulfur molecules adsorbed onto gold ( $S/nm^2$ ) during the formation of COOH-SAMs of increasing chain length at different pH of functionalization: *i.e.* 2, 5 and 11. With the number of S atoms bound to gold ( $S-Au/nm^2$ ) and free thiol molecules ( $S-H/nm^2$ ) determined from XPS analysis. With  $S-Au_{162}$  and  $S-Au_{161}$  corresponding to sulfur atoms bound to gold and to multi-coordinated sulfur atoms, respectively.

At pH 5, the proportion of free thiol molecules ( $S-H$ ) was greater than the one of  $CH_3$ -SAMs (Table S2. 3 and Table S2. 6) and increased moderately with chain length, thus this can be attributed to more physisorbed molecules on the surface through electrostatic interaction and H-bonding. At acidic pH, chain length appeared to influence the presence of free molecules onto the surface. Indeed, shorter chain SAM exhibited the highest number of free molecules and while increasing chain length this contribution decreased from 2.4 to  $\sim 0.8$   $S-H/nm^2$ , respectively (Figure 2. 6). As stated from IR results, lateral stabilization from  $CH_2$  groups through Van der Waals interactions, might not be sufficient to counterweight H-bonding for shorter chain and to obtained ordered layer.

Independently of the chain length, conducting the functionalization at basic pH led to less free thiol as expected from the presence of  $COO^-$  groups with values of  $\sim 0.5$   $S-H/nm^2$ . Furthermore, these values were found to be similar to the one obtained for  $CH_3$ -SAMs indicating that preventing H-bonding between terminal groups led the same behavior as the one observed for  $CH_3$ -SAMs. Multi-coordinated sulfur to gold atoms ( $S-Au_{161}$ ) was observed for the shorter COOH-SAM ( $HS-C_1-COOH$ ) at all pH values.

As presented in **Figure 2. 6**, this contribution increased with pH, thus less H-binding led to more molecular adsorption, *i.e.* SAM disorder (**Table S2. 5**).

In addition, conducting the functionalization at basic pH led to molecular adsorption for all chain length, illustrating the influence of terminal group on the coordination mode of S to gold surface. To investigate if washing at basic pH led to a modification of the coordination mode of sulfur to gold, the following control experiment was conducted.

Functionalization of HS-C<sub>7</sub>-COOH was performed at pH 5, followed by washing steps in ethanolic TMAOH and aqueous NaOH solutions. Similar result to the one for functionalization at pH 5 was obtained with no molecular adsorption of thiol molecules (**Figure S2. 3**), indicating that rinsing at basic pH did not modify the S-Au interface.

Furthermore, we investigated the formation of alternatives short chain length COOH-SAMs ( $n_{CH_2} = 2,3,5$ ) on gold at pH values of 5 and 11, whom characterizations are presented in **Figure S2. 4** and **Figure S2. 5**. Complementary IR results did not provide more insightful information but no multi-coordinated sulfur to gold contribution was observed at pH 5 for XPS results (**Figure S2. 5** and **Table S2. 7**), suggesting that two carbon atoms in the backbone are sufficient to avoid molecular adsorption for COOH-SAMs on gold.

In addition, the presence of multi-coordinated sulfur to gold was observed on all chain length at pH 11 (**Figure S2. 5B**), confirming that deprotonation of the carboxylic acid groups leads to less ordered monolayers. Furthermore, compiled results of WCA illustrate the progressive decrease of surface hydrophilicity with increasing chain length and above all the presence of three regimes for (i)  $n_{CH_2} = 1$ , (ii)  $n_{CH_2} = 2 - 7$  and (iii)  $n_{CH_2} = 10$  (**Figure S2. 6**).

Previous investigation related to the engineering of CH<sub>3</sub>-SAMs on gold showed a similar evolution with SAMs ranging from pseudo-forming for  $n_{CH_2} < 3$ , to liquid-like for  $n_{CH_2} = 4 - 8/9$ , to wax-like for  $n_{CH_2} = 9/10 - 13$  and finally to solid-like for  $n_{CH_2} > 14$ .<sup>33</sup>

Hence, we attributed a similar behavior to what we observed on COOH-SAMs yet a slight decrease of WCA was observed for  $n_{CH_2} = 10$  and was not observed for CH<sub>3</sub>-SAMs.

This would suggest a supplementary effect from COOH/COO<sup>-</sup> terminal groups that drive the system to increased hydrophilicity after a certain chain length threshold, in order to confirm this observation more work on longer SAMs could be envisioned.

## 2.4 Conclusion

Alkylthiol self-assembled monolayers (SAMs) bearing alkane (CH<sub>3</sub>) and carboxylic acid (COOH) functions with increasing chain length were formed on gold substrate and characterized using Polarization Modulation Infrared Reflection Absorption Spectroscopy (PM-IRRAS), Water Contact Angle (WCA) and X-ray Photoelectron Spectroscopy (XPS).

Main results on CH<sub>3</sub>-SAMs showed that increasing chain length led to the formation of hydrophobic SAMs and to a modification of the coordination mode of sulfur to gold substrate while IR results were quite similar between all investigated samples based on the position of the  $\nu_{CH_2}^{assym}$  band. Indeed, XPS outcome for short and mid chain length CH<sub>3</sub>-SAMs ( $n_{CH_2} = 1,7$ ) revealed the presence of multi-coordinated sulfur at low binding energy (S-Au<sub>161</sub>) related to molecular adsorption of molecules on the surfaces and to less ordered monolayers, yet this feature was not observed for longer SAMs.

Furthermore, COOH-SAMs of increasing chain length were also investigated to illustrate effect of terminal groups in comparison to CH<sub>3</sub>-SAMs. SAMs bearing COOH terminal groups are able to interact with neighboring molecules through H-bonding and led hydrophilic monolayers with overall better organization as suggested from IR analysis and also to the absence of molecular adsorption for mid length COOH-SAMs ( $n_{CH_2} = 7$ ).

In addition, effect of the pH of functionalization, *i.e.* protonation states of the terminal groups, was investigated. Our study suggests that deprotonation of the terminal groups (COO<sup>-</sup>) leads to less ordered SAMs with the appearance of multi-coordinated even for longer chain length SAMs ( $n_{CH_2} = 7, 10$ ) in spite of the low position for the  $\nu_{CH_2}^{assym}$  band in IR results.

In that way, we acknowledged that IR analysis is not sufficient to deeply describe SAMs order and XPS appeared to give a more insightful probing of SAMs features such as number of adsorbed species and environment of the chemisorbed thiols molecules with contribution from self-assembly (S-Au<sub>162</sub>) and molecular adsorption (S-Au<sub>161</sub>).

Further investigations will focus on the understanding of the evolution of the surface charge of COOH-SAMs, and other terminal groups, and its impacts on protein adsorption.

## References

- (1) Ulman, A. Formation and Structure of Self-Assembled Monolayers. *Chem. Rev.* **1996**, *96* (4), 1533–1554.
- (2) Love, J. C.; Estroff, L. A.; Kriebel, J. K.; Nuzzo, R. G.; Whitesides, G. M. Self-Assembled Monolayers of Thiolates on Metals as a Form of Nanotechnology. *Chem. Rev.* **2005**, *105* (4), 1103–1170.
- (3) Vericat, C.; Vela, M. E.; Benitez, G. A.; Gago, J. A. M.; Torrelles, X.; Salvarezza, R. C. Surface Characterization of Sulfur and Alkanethiol Self-Assembled Monolayers on Au(111). *J. Phys. Condens. Matter* **2006**, *18* (48), R867–R900.
- (4) Vericat, C.; Vela, M. E.; Benitez, G.; Carro, P.; Salvarezza, R. C. Self-Assembled Monolayers of Thiols and Dithiols on Gold: New Challenges for a Well-Known System. *Chem. Soc. Rev.* **2010**, *39* (5), 1805.
- (5) Singh, M.; Kaur, N.; Comini, E. The Role of Self-Assembled Monolayers in Electronic Devices. *J. Mater. Chem. C* **2020**, *8* (12), 3938–3955.
- (6) Kim, S.; Yoo, H. Self-Assembled Monolayers: Versatile Uses in Electronic Devices from Gate Dielectrics, Dopants, and Biosensing Linkers. *Micromachines* **2021**, *12* (5), 565.
- (7) Zamborini, F. P.; Crooks, R. M. Corrosion Passivation of Gold by *n*-Alkanethiol Self-Assembled Monolayers: Effect of Chain Length and End Group. *Langmuir* **1998**, *14* (12), 3279–3286.
- (8) Cao, Z.; Xiao, Z.; Gu, N.; Gong, F.; Yang, D.; Zhu, Z. Corrosion Behaviors on Polycrystalline Gold Substrates in Self-Assembled Processes of Alkanethiol Monolayers. *Anal. Lett.* **2005**, *38* (8), 1289–1304.
- (9) Cao, Z.; Xiao, Z. L.; Gu, N.; Shimada, S.; Fukuda, T.; Matsuda, H. Corrosion Behaviors Studied in Self-Assembled Processes of Alkanethiol Monolayers on Polycrystalline Gold Substrates. *Solid State Phenom.* **2007**, *121–123*, 385–388.
- (10) Mrksich, M.; Sigal, G. B.; Whitesides, G. M. Surface Plasmon Resonance Permits in Situ Measurement of Protein Adsorption on Self-Assembled Monolayers of Alkanethiolates on Gold. *Langmuir* **1995**, *11* (11), 4383–4385.
- (11) Arima, Y.; Iwata, H. Effect of Wettability and Surface Functional Groups on Protein Adsorption and Cell Adhesion Using Well-Defined Mixed Self-Assembled Monolayers. *Biomaterials* **2007**, *28* (20), 3074–3082.
- (12) Vallée, A.; Humblot, V.; Al Housseiny, R.; Boujday, S.; Pradier, C.-M. BSA Adsorption on Aliphatic and Aromatic Acid SAMs: Investigating the Effect of Residual Surface Charge and Sublayer Nature. *Colloids Surf. B Biointerfaces* **2013**, *109*, 136–142.
- (13) Thébault, P.; Boujday, S.; Sénéchal, H.; Pradier, C.-M. Investigation of an Allergen Adsorption on Amine- and Acid-Terminated Thiol Layers: Influence on Their Affinity to Specific Antibodies. *J. Phys. Chem. B* **2010**, *114* (32), 10612–10619.
- (14) Ben Haddada, M.; Salmain, M.; Boujday, S. Gold Colloid-Nanostructured Surfaces for Enhanced Piezoelectric Immunosensing of Staphylococcal Enterotoxin A. *Sens. Actuators B Chem.* **2018**, *255*, 1604–1613.
- (15) Colorado, R.; Lee, T. R. Wettabilities of Self-Assembled Monolayers on Gold Generated from Progressively Fluorinated Alkanethiols. *Langmuir* **2003**, *19* (8), 3288–3296.
- (16) Chinwangso, P.; Lee, H. J.; Jamison, A. C.; Marquez, M. D.; Park, C. S.; Lee, T. R. Structure, Wettability, and Thermal Stability of Organic Thin-Films on Gold Generated from the Molecular Self-Assembly of Unsymmetrical Oligo(Ethylene Glycol) Spiroalkanedithiols. *Langmuir* **2017**, *33* (8), 1751–1762.
- (17) Lebec, V.; Landoulsi, J.; Boujday, S.; Poleunis, C.; Pradier, C.-M.; Delcorte, A. Probing the Orientation of  $\beta$ -Lactoglobulin on Gold Surfaces Modified by Alkyl Thiol Self-Assembled Monolayers. *J. Phys. Chem. C* **2013**, *117* (22), 11569–11577.
- (18) Bedford, E. E.; Boujday, S.; Humblot, V.; Gu, F. X.; Pradier, C.-M. Effect of SAM Chain Length and Binding Functions on Protein Adsorption:  $\beta$ -Lactoglobulin and Apo-Transferrin on Gold. *Colloids Surf. B Biointerfaces* **2014**, *116*, 489–496.



- (19) Lebec, V.; Boujday, S.; Poleunis, C.; Pradier, C.-M.; Delcorte, A. Time-of-Flight Secondary Ion Mass Spectrometry Investigation of the Orientation of Adsorbed Antibodies on SAMs Correlated to Biorecognition Tests. *J. Phys. Chem. C* **2014**, *118* (4), 2085–2092.
- (20) Bhadra, P.; Shajahan, M. S.; Bhattacharya, E.; Chadha, A. Studies on Varying N-Alkanethiol Chain Lengths on a Gold Coated Surface and Their Effect on Antibody–Antigen Binding Efficiency. *RSC Adv.* **2015**, *5* (98), 80480–80487.
- (21) Bao, W.-J.; Li, J.; Cao, T.-Y.; Li, J.; Xia, X.-H. Chain-Length Dependent Interfacial Immunoreaction Kinetics on Self-Assembled Monolayers Revealed by Surface-Enhanced Infrared Absorption Spectroscopy. *Talanta* **2018**, *176*, 124–129.
- (22) Vericat, C.; Vela, M. E.; Corthey, G.; Pensa, E.; Cortés, E.; Fonticelli, M. H.; Ibañez, F.; Benitez, G. E.; Carro, P.; Salvarezza, R. C. Self-Assembled Monolayers of Thiolates on Metals: A Review Article on Sulfur-Metal Chemistry and Surface Structures. *RSC Adv* **2014**, *4* (53), 27730–27754.
- (23) Guo, Q.; Li, F. Self-Assembled Alkanethiol Monolayers on Gold Surfaces: Resolving the Complex Structure at the Interface by STM. *Phys. Chem. Chem. Phys.* **2014**, *16* (36), 19074.
- (24) Guesmi, H.; Luque, N. B.; Santos, E.; Tielens, F. Does the S–H Bond Always Break after Adsorption of an Alkylthiol on Au(111)? *Chem. - Eur. J.* **2017**, *23* (6), 1402–1408.
- (25) Truyens, A.-J.; Vekeman, J.; Tielens, F. A Subtle Balance between Interchain Interactions and Surface Reconstruction at the Origin of the Alkylthiol/Au(111) Self-Assembled Monolayer Geometry. *Surf. Sci.* **2020**, *696*, 121597.
- (26) Bedford, E.; Humblot, V.; Méthivier, C.; Pradier, C.-M.; Gu, F.; Tielens, F.; Boujday, S. An Experimental and Theoretical Approach to Investigate the Effect of Chain Length on Aminothiols Adsorption and Assembly on Gold. *Chem. - Eur. J.* **2015**, *21* (41), 14555–14561.
- (27) Nuzzo, R. G.; Dubois, L. H.; Allara, D. L. Fundamental Studies of Microscopic Wetting on Organic Surfaces. 1. Formation and Structural Characterization of a Self-Consistent Series of Polyfunctional Organic Monolayers. 12.
- (28) Briand, E.; Salmain, M.; Herry, J.-M.; Perrot, H.; Compère, C.; Pradier, C.-M. Building of an Immunosensor: How Can the Composition and Structure of the Thiol Attachment Layer Affect the Immunosensor Efficiency? *Biosens. Bioelectron.* **2006**, *22* (3), 440–448.
- (29) Porter, M. D.; Bright, T. B.; Allara, D. L.; Chidsey, C. E. D. Spontaneously Organized Molecular Assemblies. 4. Structural Characterization of n-Alkyl Thiol Monolayers on Gold by Optical Ellipsometry, Infrared Spectroscopy, and Electrochemistry. *J. Am. Chem. Soc.* **1987**, *109* (12), 3559–3568.
- (30) Folkers, J. P.; Laibinis, P. E. Self-Assembled Monolayers of Alkanethiols on Gold: The Adsorption and Wetting Properties of Monolayers Derived from Two Components with Alkane Chains of Different Lengths. 16.
- (31) Laibinis, P. E.; Parikh, A. N.; Nuzzo, R. G. Comparison of the Structures and Wetting Properties of Self-Assembled Monolayers of n-Alkanethiols on the Coinage Metal Surfaces, Cu, Ag, Au'. 16.
- (32) Amara, F. B.; Dionne, E. R.; Kassir, S.; Pellerin, C.; Badia, A. Molecular Origin of the Odd–Even Effect of Macroscopic Properties of n-Alkanethiolate Self-Assembled Monolayers: Bulk or Interface? *J Am Chem Soc* **2020**, *11*.
- (33) Chen, J.; Chang, B.; Oyola-Reynoso, S.; Wang, Z.; Thuo, M. Quantifying Gauche Defects and Phase Evolution in Self-Assembled Monolayers through Sessile Drops. *ACS Omega* **2017**, *13*.
- (34) Tao, F.; Bernasek, S. L. Understanding Odd–Even Effects in Organic Self-Assembled Monolayers. 46.
- (35) Baio, J. E.; Weidner, T.; Brison, J.; Graham, D. J.; Gamble, L. J.; Castner, D. G. Amine Terminated SAMs: Investigating Why Oxygen Is Present in These Films. *J. Electron Spectrosc. Relat. Phenom.* **2009**, *172* (1–3), 2–8.
- (36) Techane, S. D.; Gamble, L. J.; Castner, D. G. Multitechnique Characterization of Self-Assembled Carboxylic Acid-Terminated Alkanethiol Monolayers on Nanoparticle and Flat Gold Surfaces. *J. Phys. Chem. C* **2011**, *10*.

- (37) Singhana, B.; Jamison, A. C.; Hoang, J.; Lee, T. R. Self-Assembled Monolayer Films Derived from Tridentate Cyclohexyl Adsorbates with Alkyl Tailgroups of Increasing Chain Length. **2013**, 9.
- (38) Willey, T. M.; Vance, A. L.; van Buuren, T.; Bostedt, C.; Terminello, L. J.; Fadley, C. S. Rapid Degradation of Alkanethiol-Based Self-Assembled Monolayers on Gold in Ambient Laboratory Conditions. *Surf. Sci.* **2005**, 576 (1–3), 188–196.
- (39) Dubois, L. H.; Nuzzo, R. G. Synthesis, Structure, and Properties of Model Organic Surfaces. *Annu. Rev. Phys. Chem.* **1992**, 43 (1), 437–463.
- (40) Méthivier, C.; Beccard, B.; Pradier, C. M. In Situ Analysis of a Mercaptoundecanoic Acid Layer on Gold in Liquid Phase, by PM-IRAS. Evidence for Chemical Changes with the Solvent. *Langmuir* **2003**, 19 (21), 8807–8812.
- (41) Sugihara, K.; Teranishi, T.; Shimazu, K.; Uosaki, K. Structure Dependence of the Surface pKa of Mercaptoundecanoic Acid SAM on Gold. *Electrochemistry* **1999**, 67 (12), 1172–1174.
- (42) ShimazuKatsuaki; TeranishiTadashi; SugiharaKouki; UosakiKohei. Surface Mass Titrations of Self-Assembled Monolayers of  $\omega$ -Mercaptoalkanoic Acids on Gold. *Chem. Lett.* **2003**.
- (43) Zhao, J.; Luo, L.; Yang, X.; Wang, E.; Dong, S. Determination of Surface PKa of SAM Using an Electrochemical Titration Method. **1999**, No. 15, 4.
- (44) Hale, P. S.; Gooding, J. J.; Maddox, L.; Shapter, J. G. Surface PKa of Self-Assembled Monolayers. 3.
- (45) Lin, W.-C.; Lee, S.-H.; Karakachian, M.; Yu, B.-Y.; Chen, Y.-Y.; Lin, Y.-C.; Kuo, C.-H.; Shyue, J.-J. Tuning the Surface Potential of Gold Substrates Arbitrarily with Self-Assembled Monolayers with Mixed Functional Groups. *Phys. Chem. Chem. Phys.* **2009**, 11 (29), 6199.
- (46) Wang, D.; Nap, R. J.; Han, S.; Grzybowski, B. A.; Szeleifer, I. How and Why Nanoparticle's Curvature Regulates the Apparent PKa of the Coating Ligands. *J. Am. Chem. Soc.* **2011**, 6.
- (47) Laibinis, P. E.; Whitesides, G. M. ..Omega.-Terminated Alkanethiolate Monolayers on Surfaces of Copper, Silver, and Gold Have Similar Wettabilities. *J. Am. Chem. Soc.* **1992**, 114 (6), 1990–1995.
- (48) Hajiraissi, R.; Hanke, M.; Yang, Y.; Duderija, B.; Orive, A. G.; Grundmeier, G.; Keller, A. Adsorption and Fibrillization of Islet Amyloid Polypeptide at Self-Assembled Monolayers Studied by QCM-D, AFM, and PM-IRRAS. **2018**, 8.

## 2.5 Supporting Information

### 2.5.1 Experimental section

#### 2.5.1.1 Materials

Ethanethiol (HS-C<sub>1</sub>-CH<sub>3</sub>), 1-octanethiol (HS-C<sub>7</sub>-CH<sub>3</sub>), 1-undecanethiol (HS-C<sub>10</sub>-CH<sub>3</sub>), 3-mercaptopropionic acid (HS-C<sub>2</sub>-COOH), 4-mercaptopbutyric acid (HS-C<sub>3</sub>-COOH), 6-mercaphohexanoic acid (HS-C<sub>5</sub>-COOH), 8-mercaphooctanoic acid (HS-C<sub>7</sub>-COOH), 11-mercaphoundecanoic acid (HS-C<sub>10</sub>-COOH), hydrochloric acid (HCl, 37%), sodium hydroxide (NaOH) pellets and tetramethylammonium hydroxide (TMAOH, 25 wt.% in water) were purchased from Sigma Aldrich (Saint-Quentin Fallavier, France). Thioglycolic acid (HS-C<sub>1</sub>-COOH) was purchased from Fluka. The pH of the ethanolic solutions for functionalization was adjusted to pH 2 with concentrated HCl and to pH 11 by adding TMAOH and monitored using pH papers (Lyphan). All solvents and reagents were used without any further purification.

#### 2.5.1.2 Techniques

##### 2.5.1.2.1 PM-IRRAS (Polarization Modulation InfraRed Reflection Absorption Spectroscopy)

PM-IRRAS spectra were recorded on a commercial Thermo-scientific Nicolet Nexus 5700 spectrometer. The external beam was focused on the sample with a mirror, at an optical incident angle of 85°. A ZnSe grid polarizer and a ZnSe photoelastic modulator, modulating the incident beam between p- and s- polarizations (HINDS Instruments, PEM 90, modulation frequency of 37 kHz), were placed prior to the sample. The light reflected at the sample was then focused onto a liquid nitrogen-cooled MCT detector. The PM-IRRAS signal is given by the differential reflectivity  $\Delta R/R = (R_p - R_s)/(R_p + R_s)$ . The presented infrared (IR) spectra result from the acquisition of 1024 scans recorded at 8 cm<sup>-1</sup> resolution. Position for the asymmetric methylene stretching vibration was fitted on baseline corrected spectra using Origin Software.



### 2.5.1.2.2 WCA (Water Contact Angle)

Static water contact angles were measured at room temperature using the sessile drop method and image analysis of the drop profile. The instrument, which uses a CCD camera and an image analysis processor, was purchased from Krüss (Germany). The water (Milli-Q) droplet volume was 1  $\mu\text{L}$  and the contact angle ( $\theta$ ) was measured 5 s after the drop was deposited on the sample. Experiments were conducted in triplicate and the reported values are the average of three droplets at different locations of each sample's surface.

### 2.5.1.2.3 XPS (X-Ray Photoelectron Spectroscopy)

XPS analysis were performed on a Scienta Omicron Argus X-ray photoelectron spectrometer, using a monochromated  $\text{AlK}\alpha$  ( $h\nu = 1486.6 \text{ eV}$ ) radiation source having a 280 W electron beam power. The emission of photoelectrons from the sample was analyzed at a takeoff angle of  $45^\circ$  under ultra-high vacuum conditions ( $1 \times 10^{-9} \text{ Pa}$ ).

XPS spectra were collected at pass energy of 100 eV for the survey scan and 20 eV for the  $\text{C}_{1s}$ ,  $\text{O}_{1s}$ ,  $\text{N}_{1s}$ ,  $\text{Cl}_{2p}$ ,  $\text{Na}_{1s}$ ,  $\text{Au}_{4f}$ ,  $\text{S}_{2p}$  core XPS levels. The energy resolution for  $\text{S}_{2p}$  acquisition was adjusted from 0.1 to 0.05 eV. The peak areas were determined after subtraction of a Shirley background, except for  $\text{S}_{2p}$  contribution for which a linear background was applied.

The spectra were fitted using Casa XPS software and applying a Gaussian/ Lorentzian ratio (G/L) equal to 70/30 and binding energies were calibrated against the  $\text{Au}_{4f_{7/2}}$  at 84 eV.

### 2.5.1.3 Results and discussion

**Table S2. 1.** Characteristic Infrared vibrational modes of alkane (CH<sub>3</sub>) and carboxylic acid (COOH) terminated thiol SAMs. <sup>1-7</sup>

Vibrational assignment		
3150 – 3050	OH	O-H stretching vibration, intermolecular H-bonded
2960	$\nu_{CH_3}^{asymm}$	Asymmetric CH <sub>3</sub> stretching
2930 - 2920	$\nu_{CH_2}^{asymm}$	Asymmetric CH <sub>2</sub> stretching
2880	$\nu_{CH_3}^{symm}$	Symmetric CH <sub>3</sub> stretching
2855 - 2850	$\nu_{CH_2}^{symm}$	Symmetric CH <sub>2</sub> stretching
1740-1780	$\nu_{C=O}$	free C=O stretching
1715	$\nu_{C=O}$	H-bonded carboxylic acid stretching
1620	$\nu_{COO^-}^{asymm}$	Asymmetric COO <sup>-</sup> stretching
1635	H <sub>2</sub> O	Adsorbed water
1470 - 1440	$\delta_{CH_2}$	CH <sub>2</sub> scissors bending
1415	$\nu_{COO^-}^{symm}$	Symmetric COO <sup>-</sup> stretching
1380	$\delta_{CH_3}^{symm}$	Symmetric CH <sub>3</sub> bending

**Table S2. 2.** Position of the asymmetric CH<sub>2</sub> stretching bands (in cm<sup>-1</sup>) for CH<sub>3</sub>-SAMs of increasing chain length on gold for experiments performed at least in triplicate.

HS-C <sub>1</sub> -CH <sub>3</sub>	HS-C <sub>7</sub> -CH <sub>3</sub>	HS-C <sub>10</sub> -CH <sub>3</sub>
2921.6	2925.3	2922.8
2920.0	2925.2	2921.8
2919.8	2923.8	2920.9
2920.2	2926.7	2922.9
2920.4 ± 0.8	2925.3 ± 1.2	2921.7 ± 1.2

### Estimation of the number of sulfur atoms bound to gold

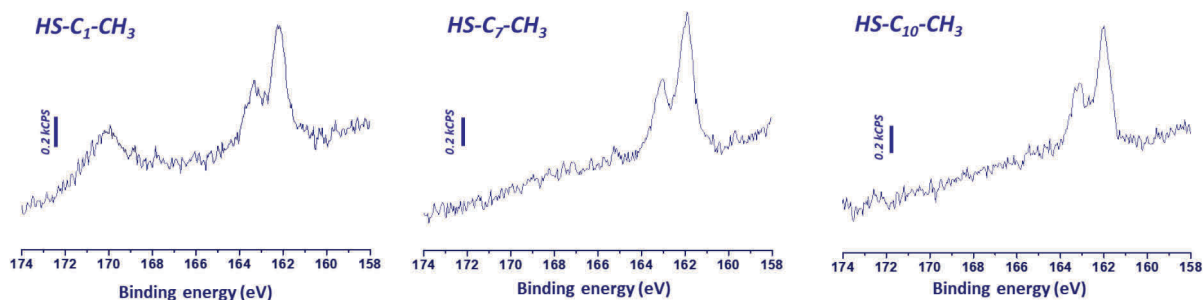
The number of sulfur atoms bound to gold per unit area (S-Au/nm<sup>2</sup>) was determined using the following equation with the ratio between the area of sulfur ( $I_S$ ) and the raw area of gold ( $I_{Au}$ ):

$$n_{sd} = \cos(\theta) * \frac{I_S \rho_{Au} \sigma_{Au} \lambda_{Au}^{Au}}{I_{Au} M_{Au} \sigma_S} * 10^{-21} * N_A$$

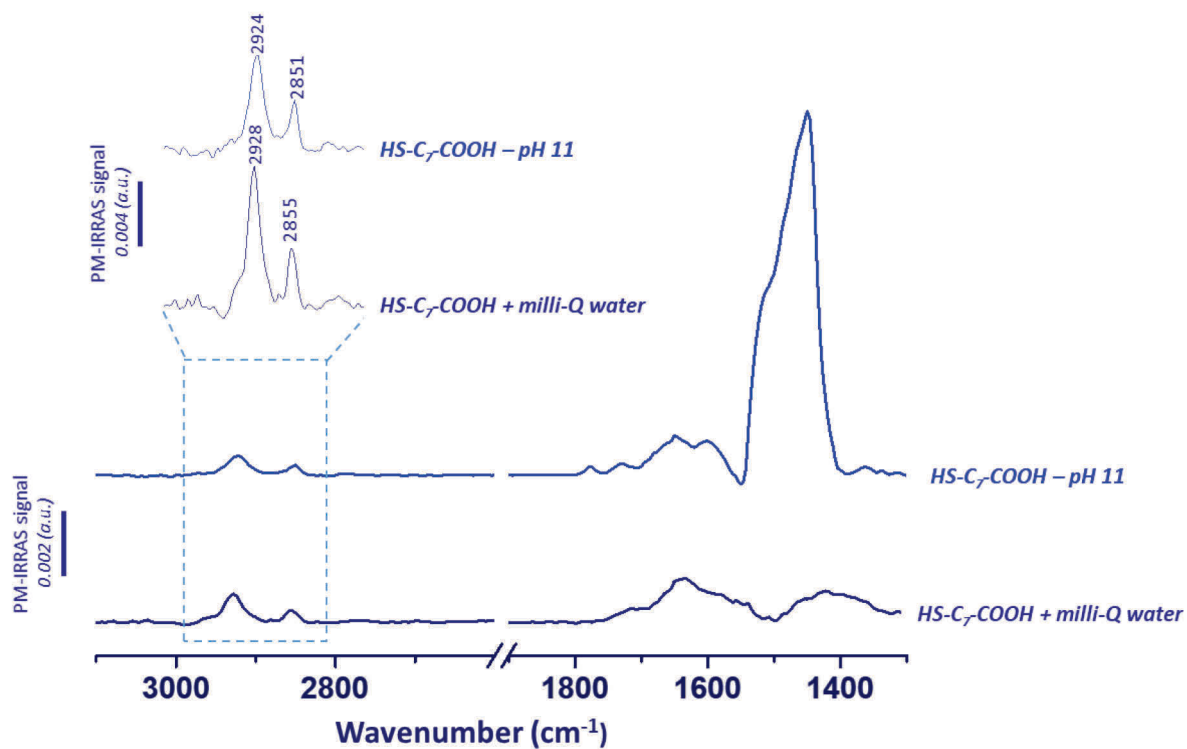
In this equation,  $n_{sd}$  is the number of sulfur atoms bound to gold surface (S-Au/nm<sup>2</sup>),  $\theta$  is the photoelectron collection angle (45°),  $\rho_{Au}$  is the volumic mass of gold (19.3 g/cm<sup>3</sup>),  $M_{Au}$  is the molar mass of gold (197 g/mol) and  $N_A$  is the Avogadro number (6.022\*10<sup>23</sup> mol<sup>-1</sup>). The Scofield photoionization cross sections  $\sigma$  are 14.34 for Au<sub>4f</sub> and 1.67 for S<sub>2p</sub>.<sup>8</sup> The electron inelastic mean free paths  $\lambda$  were calculated using the Quases program based on the TPP2M formula, with  $\lambda_{Au}^{Au} = 1.6$  nm.<sup>9</sup>

**Table S2. 3.** S2p photopeak decompositions and corresponding surface coverage calculated from XPS measurements for CH<sub>3</sub>-SAMs of increasing chain length. Binding energies (B.E.) were calibrated against the  $Au_{4f_{7/2}}$  at 84 eV. Experiments were conducted in triplicate at least.

	S-Au <sub>161</sub>		S-Au <sub>162</sub>		S-H		
	B.E. (eV)	%S-Au <sub>161</sub>	B.E. (eV)	%S-Au <sub>162</sub>	B.E. (eV)	%S-H	S-Au/nm <sup>2</sup>
HS-C <sub>1</sub> -CH <sub>3</sub>	161.0	15.5	162.0	69.4	163.5	15.1	2.51
	161.1	10.4	162.0	63.8	163.8	25.9	2.88
	161.2	19.8	162.1	55.7	163.5	24.5	2.42
	161.1 ± 0.1	15.2 ± 4.7	162.0 ± 0.1	62.9 ± 6.9	163.6 ± 0.2	21.8 ± 5.9	2.60 ± 0.24
HS-C <sub>7</sub> -CH <sub>3</sub>	161.0	7.1	162.0	82.2	163.6	10.7	2.37
	161.0	5.2	162.0	83.1	163.7	11.7	3.21
	161.2	9.9	162.3	75.5	163.8	14.6	3.12
	161.1 ± 0.1	7.4 ± 2.4	162.1 ± 0.2	80.3 ± 4.2	163.7 ± 0.1	12.31 ± 2.02	2.9 ± 0.5
HS-C <sub>10</sub> -CH <sub>3</sub>	-	-	162.0	86.2	163.5	13.8	2.97
	-	-	162.0	86.5	163.6	13.5	3.00
	-	-	161.6	90.4	163.2	9.6	3.89
	-	-	161.9	89.6	163.3	10.4	3.55
			161.9 ± 0.2	88.2 ± 2.1	163.4 ± 0.2	11.8 ± 2.1	3.35 ± 0.45



**Figure S2. 1.** High-resolution XPS  $S_{2p}$  spectra of  $CH_3$ -SAMs of increasing chain length on gold surface showing the presence of oxidized sulfur ( $SO_x \sim 170$  eV) for shorter chain length ( $HS-C_1-CH_3$ ).



**Figure S2. 2.** Baseline corrected PM-IRRAS spectra of mid chain length COOH-SAM ( $HS-C_7-COOH$ ) on gold obtained at pH 11 (top curve) and after rinsing in milli-Q water (bottom curve).

**Table S2. 4.** Position of the asymmetric CH<sub>2</sub> stretching band (in cm<sup>-1</sup>) for COOH-SAMs of increasing chain length on gold at different pH of functionalization. Experiments were conducted in triplicate at least.

	HS-C <sub>1</sub> -COOH	HS-C <sub>7</sub> -COOH	HS-C <sub>10</sub> -COOH
pH 2	2930.1	2927.2	2923.9
	2931.4	2927.7	2922.9
	2928.5	2927.2	2923.7
	2930.0 ± 1.5	2927.3 ± 0.3	2923.5 ± 0.5
pH 5	2928.2	2927.1	2925.1
	2928.4	2927.9	2926.3
	2929.6	2927.9	2925.7
	2928.7 ± 0.7	2927.7 ± 0.5	2925.7 ± 0.6
pH 11	2927.6	2924.7	2925.3
	2925.5	2925.5	2925.8
	2925.7	2926.9	2925.8
	2926.6 ± 1.5	2925.7 ± 1.2	2925.6 ± 0.3

**Table S2. 5.** XPS atomic percentages and S<sub>2p</sub> photopeak decompositions corrected by Scofield factors for COOH-SAMs of increasing chain length on gold at different pH of functionalization corresponding to the results presented in **Figure 2. 5**. The number of sulfur atoms bound to gold per surface area in nm<sup>2</sup> includes contributions from both S-Au<sub>161</sub> and S-Au<sub>162</sub>.

pH 2	HS-C <sub>1</sub> -COOH	HS-C <sub>7</sub> -COOH	HS-C <sub>10</sub> -COOH
Au <sub>4f</sub>	52.57	49.20	40.15
O <sub>1s</sub>	11.99	10.23	10.15
C <sub>1s</sub>	29.97	37.43	46.90
S <sub>2p</sub>	5.46	3.14	2.80
<i>S<sub>2p</sub> photopeak decomposition: Relative S% (absolute S%)</i>			
S-H	42.40 (2.32)	26.25 (0.82)	23.93 (0.67)
S-Au <sub>162</sub>	53.01 (2.89)	73.75 (2.32)	76.07 (2.13)
S-Au <sub>161</sub>	4.59 (0.25)	-	-
S-Au/nm <sup>2</sup>	3.73 ± 0.02	3.01 ± 0.12	3.20 ± 0.40

Table S2.5. (continued)

<b>pH 5</b>	<b>HS-C<sub>1</sub>-COOH</b>	<b>HS-C<sub>7</sub>-COOH</b>	<b>HS-C<sub>10</sub>-COOH</b>
Au <sub>4f</sub>	47.31	32.41	25.47
O <sub>1s</sub>	18.14	18.94	19.41
C <sub>1s</sub>	31.62	45.79	52.87
S <sub>2p</sub>	2.93	2.86	2.24
<i>S<sub>2p</sub> photopeak decomposition: Relative S% (absolute S%)</i>			
S-H	18.32 (0.54)	29.64 (0.85)	37.67 (0.84)
S-Au <sub>162</sub>	66.53 (1.95)	70.36 (2.01)	62.33 (1.40)
S-Au <sub>161</sub>	15.15 (0.44)	-	-
S-Au/nm <sup>2</sup>	3.76 ± 1.36	3.61 ± 0.72	3.54 ± 0.43
<b>pH 11</b>	<b>HS-C<sub>1</sub>-COOH</b>	<b>HS-C<sub>7</sub>-COOH</b>	<b>HS-C<sub>10</sub>-COOH</b>
Au <sub>4f</sub>	32.69	32.24	25.54
O <sub>1s</sub>	20.76	14.15	21.23
C <sub>1s</sub>	40.30	49.62	47.64
S <sub>2p</sub>	1.93	1.58	1.05
N <sub>1s</sub>	-	-	-
Na <sub>1s</sub>	4.32	2.41	4.53
<i>S<sub>2p</sub> photopeak decomposition: Relative S% (absolute S%)</i>			
S-H	13.31 (0.26)	11.74 (0.19)	13.63 (0.14)
S-Au <sub>162</sub>	76.13 (1.47)	73.84 (1.17)	57.82 (0.61)
S-Au <sub>161</sub>	10.56 (0.20)	14.42 (0.22)	28.55 (0.3)
S-Au/nm <sup>2</sup>	3.46 ± 0.59	2.54 ± 0.63	2.27 ± 0.24

**Table S2. 6.** S<sub>2p</sub> photopeak decompositions and corresponding surface coverage calculated from XPS measurements for COOH-SAMs of increasing chain length at different pH of functionalization. Binding energies (B.E.) were calibrated against the Au<sub>4f<sub>7/2</sub></sub> at 84 eV. Experiments were conducted in triplicate at least.

	S-Au <sub>161</sub>		S-Au <sub>162</sub>		S-H		
	B.E. (eV)	%S-Au <sub>161</sub>	B.E. (eV)	%S-Au <sub>162</sub>	B.E. (eV)	%S-H	S-Au/nm <sup>2</sup>
<b>HS-C<sub>1</sub>-COOH</b> pH 2	160.9	5.8	162.1	48.2	163.4	45.9	3.72
	161	4.6	162.1	53.0	164.5	42.4	3.72
	161.2	10.9	162.2	60.1	163.6	28.9	3.76
	161.0 ± 0.2	7.1 ± 3.4	162.1 ± 0.1	53.8 ± 6.0	163.6 ± 0.2	39.1 ± 9.0	3.73 ± 0.02
<b>HS-C<sub>7</sub>-COOH</b> pH 2	-	-	161.9	76.6	163.3	23.4	3.15
	-	-	161.8	73.8	163.1	26.3	2.93
	-	-	162.0	86.2	163.6	13.8	2.94
			161.9 ± 0.1	78.9 ± 6.5	163.3 ± 0.2	21.2 ± 6.5	3.01 ± 0.12
<b>HS-C<sub>10</sub>-COOH</b> pH 2	-	-	161.9	81.4	163.3	18.6	3.39
	-	-	161.9	76.1	163.3	23.9	3.47
	-	-	162.1	82.3	163.5	17.8	3.63
	-	-	162.0	84.6	163.7	15.4	2.74
		161.9 ± 0.2	80.7 ± 4.3	163.4 ± 0.3	19.3 ± 4.3	3.20 ± 0.40	

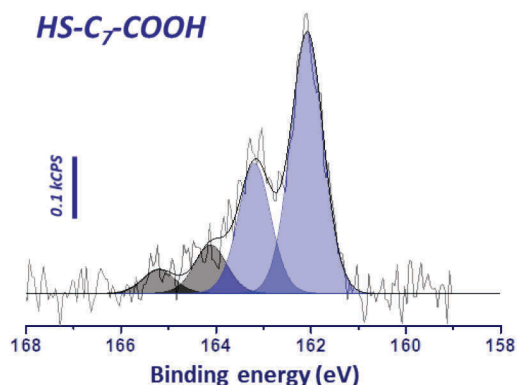


**Table S2. 6.** (continued)

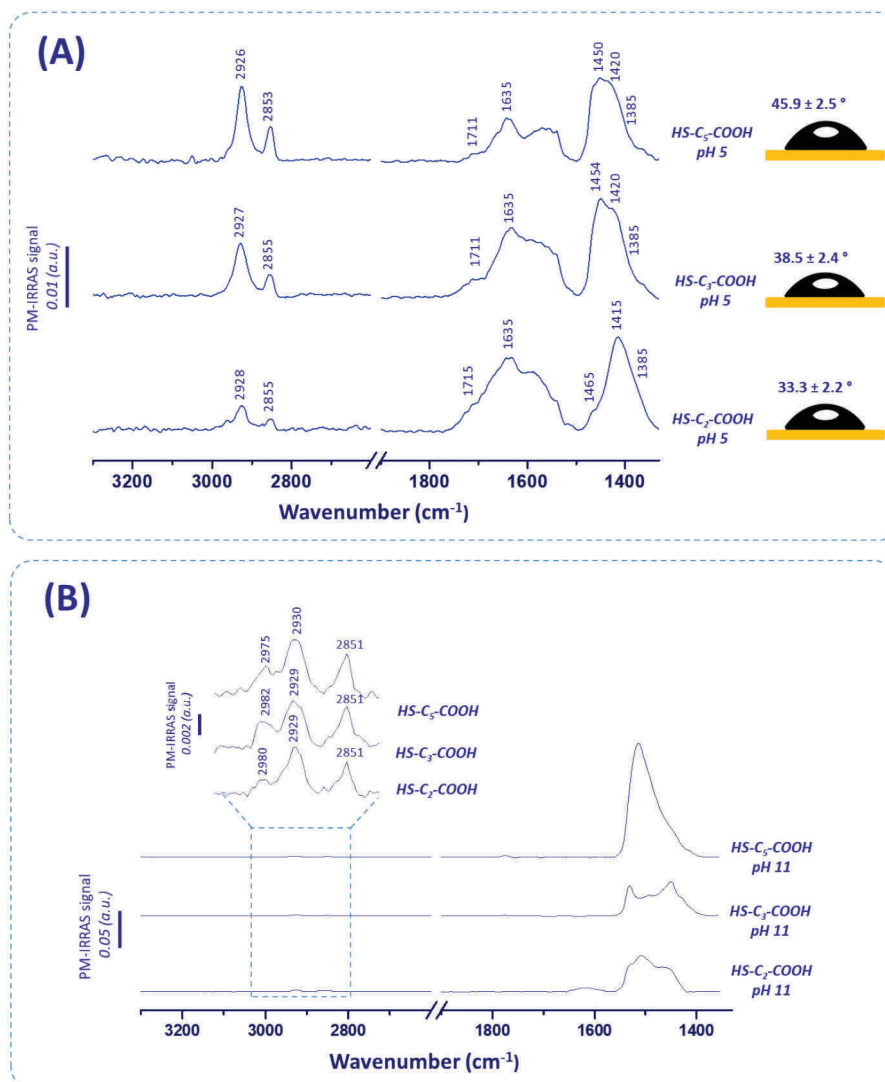
	160.8	15.2	161.8	66.5	163.3	18.3	3.23
<b>HS-C<sub>1</sub>-COOH</b> pH 5	160.7	17.3	161.7	62.2	163.6	20.5	2.75
	161.2	12.4	162.2	50.2	163.9	37.5	5.31
	160.9 ± 0.3	14.9 ± 2.5	162.1 ± 0.1	59.6 ± 8.5	163.6 ± 0.3	25.4 ± 10.5	3.76 ± 1.36
	-	-	162.1	70.4	163.7	29.6	3.93
<b>HS-C<sub>7</sub>-COOH</b> pH 5	-	-	162.1	64.5	163.8	35.5	4.47
	-	-	160.8	59.4	162.4	40.7	2.96
	-	-	161.9	72.5	163.4	27.5	3.06
			161.7 ± 0.6	69.1 ± 4.1	163.3 ± 0.7	30.9 ± 4.1	3.61 ± 0.72
	-	-	162.0	63.7	163.8	36.3	3.64
<b>HS-C<sub>10</sub>-COOH</b> pH 5	-	-	162.1	62.3	164.0	37.7	3.07
	-	-	162.0	66.9	163.5	33.1	3.92
			162.0 ± 0.1	64.3 ± 2.4	163.8 ± 0.3	35.7 ± 2.4	3.54 ± 0.43

**Table S2. 6.** (continued)

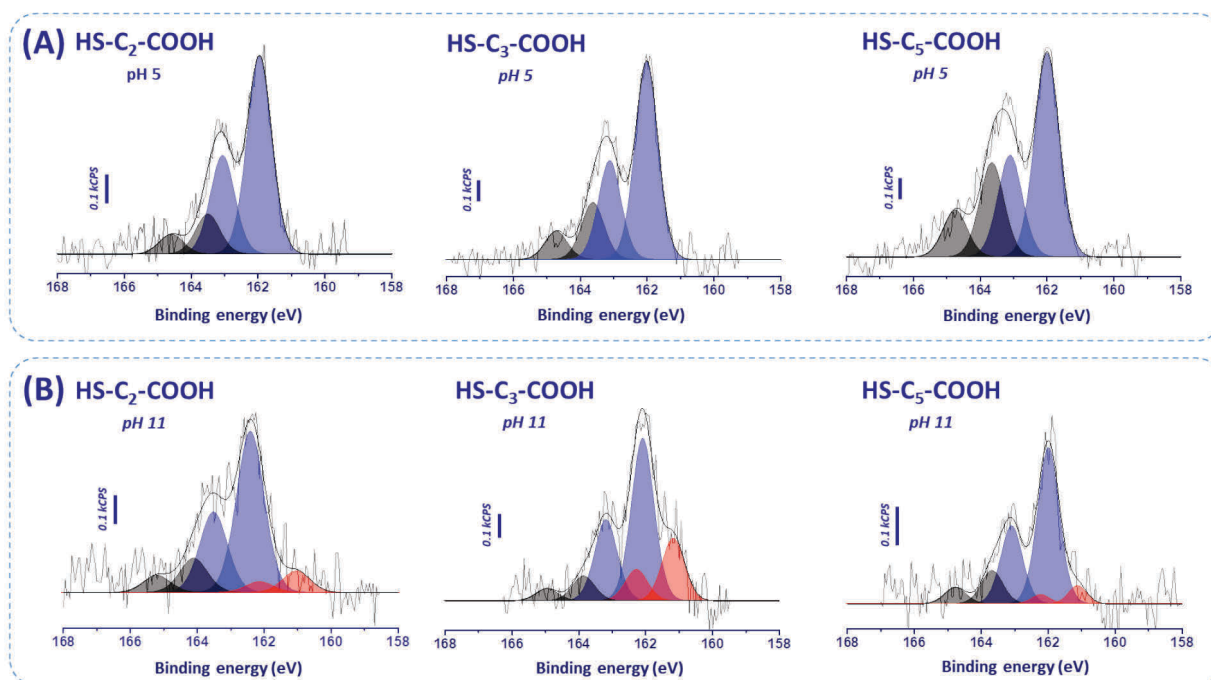
	161.5	15.1	162.6	72.7	163.9	12.1	3.15
<b>HS-C<sub>1</sub>-COOH</b> pH 11	160.9	12.4	162.1	76.1	163.7	13.3	3.08
	161.2	14.6	162.2	66.9	163.7	18.5	4.14
	161.2 ± 0.3	14.0 ± 1.5	162.3 ± 0.3	71.3 ± 4.7	163.6 ± 0.3	14.7 ± 3.4	3.46 ± 0.59
<b>HS-C<sub>7</sub>-COOH</b> pH 11	160.3	14.4	161.3	73.8	162.7	11.7	2.76
	161.1	18.6	161.9	66.1	163.1	15.3	1.83
	161.0	8.3	162.0	77.5	163.6	14.3	3.04
	160.8 ± 0.4	13.8 ± 5.2	161.7 ± 0.4	72.4 ± 5.8	163.2 ± 0.5	13.8 ± 1.8	2.54 ± 0.63
<b>HS-C<sub>10</sub>-COOH</b> pH 11	161.0	13.9	162.1	68.2	163.3	17.8	2.50
	160.9	28.6	162.0	57.8	164.0	13.6	2.10
	161.2	26.8	162.0	55.5	163.4	17.8	2.53
	161.1 ± 0.1	23.1 ± 8.0	162.0 ± 0.1	60.5 ± 6.8	163.6 ± 0.4	16.4 ± 2.4	2.27 ± 0.24



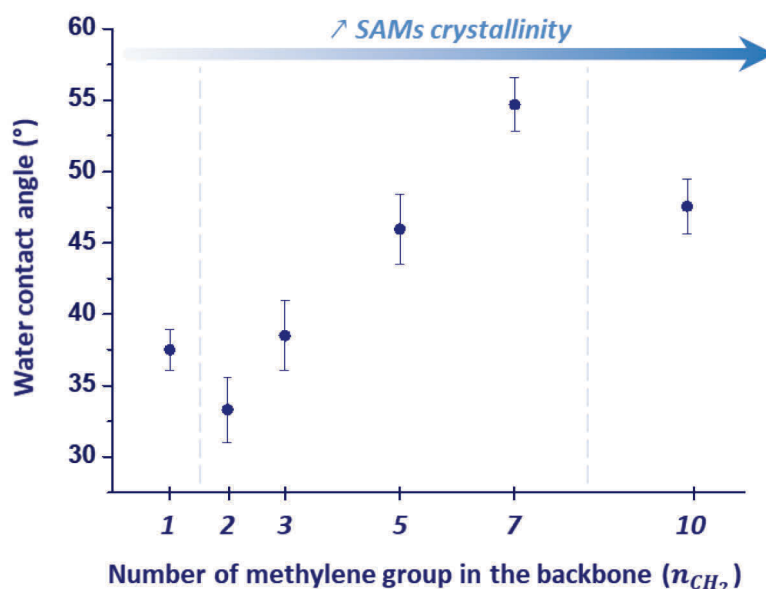
**Figure S2. 3.** Background subtracted high-resolution  $S_{2p}$  XPS photopeak for mid chain length COOH-SAM on gold (HS-C<sub>7</sub>-COOH). Functionalization was performed at pH 5 and followed with rinsing at basic pH using TMAOH and NaOH solutions.



**Figure S2. 4.** Baseline corrected PM-IRRAS spectra and corresponding WCA (only at pH 5) results of COOH-SAMs of increasing chain lengths on gold at different pH of functionalization: (A) pH 5 and (B) pH 11.



**Figure S2. 5.** Background subtracted high-resolution XPS  $S_{2p}$  spectra of COOH-SAMs of increasing chain length adsorbed on gold at different pH of functionalization: (A) pH 5 and (B) pH 11.



**Figure S2. 6.** Water contact angle (WCA) values for COOH-SAMs of increasing chain length adsorbed on gold surfaces at pH 5.

**Table S2. 7.** S2p photopeak decompositions and corresponding surface coverage calculated from XPS measurements for COOH-SAMs of increasing chain length at different pH of functionalization. Binding energies (B.E.) were calibrated against the  $Au_{4f_{7/2}}$  at 84 eV.

	S-Au <sub>161</sub>		S-Au <sub>162</sub>		S-H		S-Au/nm <sup>2</sup>
	B.E. (eV)	%S-Au <sub>161</sub>	B.E. (eV)	%S-Au <sub>162</sub>	B.E. (eV)	%S-H	
<b>HS-C<sub>2</sub>-COOH</b> <b>pH 5</b>	-	-	161.7	71.2	163.2	28.8	4.1
	-	-	161.7	85.8	163.1	14.2	2.6
	-	-	161.9	83.1	163.5	16.8	3.8
			$161.8 \pm 0.2$	$80.0 \pm 7.8$	$163.3 \pm 0.2$	$19.9 \pm 7.8$	$3.5 \pm 0.8$
<b>HS-C<sub>3</sub>-COOH</b> <b>pH 5</b>	-	-	161.9	62.4	163.5	37.6	4.4
	-	-	161.9	68.5	163.5	31.5	3.1
	-	-	162.0	77.6	163.6	22.4	3.8
			$161.9 \pm 0.1$	$69.5 \pm 7.7$	$163.6 \pm 0.1$	$30.5 \pm 7.7$	$3.7 \pm 0.7$
<b>HS-C<sub>5</sub>-COOH</b> <b>pH 5</b>	-	-	161.9	68.4	163.6	31.6	3.9
	-	-	161.9	76.0	163.4	24	3.0
	-	-	161.9	79.5	163.5	20.5	2.7
			$161.9 \pm 0.1$	$74.6 \pm 5.6$	$163.5 \pm 0.1$	$25.4 \pm 5.6$	$3.2 \pm 0.6$

**Table S2. 7. (continued)**

<b>HS-C<sub>2</sub>-COOH</b> pH 11	161.0	9.9	162.4	74.3	164.1	15.8	2.8
	161.2	5.9	162.1	77.8	164.8	16.3	3.8
	161.1 ± 0.1	7.9 ± 2.9	162.3 ± 0.2	76.1 ± 2.5	164.5 ± 0.5	16.0 ± 0.3	3.3 ± 0.7
<b>HS-C<sub>3</sub>-COOH</b> pH 11	161.2	25.0	162.1	64.9	163.8	9.9	1.9
	160.9	17.0	162.1	63.9	162.5	19.1	1.8
	161.1 ± 0.1	21.0 ± 5.6	162.1 ± 0.1	64.5 ± 0.8	163.2 ± 0.9	14.5 ± 6.4	1.8 ± 0.1
<b>HS-C<sub>5</sub>-COOH</b> pH 11	160.9	12.8	162.1	66.8	163.6	20.4	2.8
	161.1	8.6	162.0	75.2	163.7	16.2	2.8
	161.1 ± 0.2	10.7 ± 3.0	162.0 ± 0.1	71.0 ± 5.9	163.7 ± 0.1	18.3 ± 2.9	2.8 ± 0.0

## References

- (1) Rodriguez, K. R.; Shah, S.; Williams, S. M.; Teeters-Kennedy, S.; Coe, J. V. Enhanced Infrared Absorption Spectra of Self-Assembled Alkanethiol Monolayers Using the Extraordinary Infrared Transmission of Metallic Arrays of Subwavelength Apertures. 6.
- (2) Porter, M. D.; Bright, T. B.; Allara, D. L.; Chidsey, C. E. D. Spontaneously Organized Molecular Assemblies. 4. Structural Characterization of n-Alkyl Thiol Monolayers on Gold by Optical Ellipsometry, Infrared Spectroscopy, and Electrochemistry. *J. Am. Chem. Soc.* **1987**, *109* (12), 3559–3568.
- (3) Nuzzo, R. G.; Dubois, L. H.; Allara, D. L. Fundamental Studies of Microscopic Wetting on Organic Surfaces. 1. Formation and Structural Characterization of a Self-Consistent Series of Polyfunctional Organic Monolayers. 12.
- (4) Frey, B. L.; Corn, R. M. Covalent Attachment and Derivatization of Poly(L-Lysine) Monolayers on Gold Surfaces As Characterized by Polarization-Modulation FT-IR Spectroscopy. *Anal. Chem.* **1996**, *68* (18), 3187–3193.
- (5) Briand, E.; Salmain, M.; Herry, J.-M.; Perrot, H.; Compère, C.; Pradier, C.-M. Building of an Immunosensor: How Can the Composition and Structure of the Thiol Attachment Layer Affect the Immunosensor Efficiency? *Biosens. Bioelectron.* **2006**, *22* (3), 440–448.
- (6) Vallée, A.; Humblot, V.; Al Housseiny, R.; Boujday, S.; Pradier, C.-M. BSA Adsorption on Aliphatic and Aromatic Acid SAMs: Investigating the Effect of Residual Surface Charge and Sublayer Nature. *Colloids Surf. B Biointerfaces* **2013**, *109*, 136–142.
- (7) Socrates, G. Infrared Characteristic Group Frequencies: Tables and Charts, 2nd Ed. 2nd Ed.; John Wiley and Sons: 1994.
- (8) Scofield, J. H. Hartree-Slater Subshell Photoionization Cross-Sections at 1254 and 1487 eV. *J. Electron Spectrosc. Relat. Phenom.* **1976**, *8* (2), 129–137.
- (9) Tanuma, S.; Powell, C. J.; Penn, D. R. Calculations of Electron Inelastic Mean Free Paths. V. Data for 14 Organic Compounds over the 50-2000 eV Range. *Surf. Interface Anal.* **1993**, *21* (3), 165–176.







---

---

**Chapter 3. Surface charge of acid-terminated thiolate  
SAMs on gold**

---

---



### 3.1 Introduction

At the fundamental level, all interactions can be seen as electrostatic ones, ranging from matter cohesion to molecules formation. This consideration is now greatly examined when adsorbing small molecules at oxide surfaces as exemplified when studying transition metal complexes adsorption on oxide surfaces, that proved to be mainly governed by electrostatic interaction at least during the first stages.<sup>1,2</sup> When the substrate is a functionalized metallic surface, the impact of the solvent, and particularly the surface charge of the functionalized material, is often forgotten including when investigating proteins adsorption onto these surfaces in aqueous media. Indeed, proteins interactions with planar surfaces have been investigated throughout decades for numerous applications including anti-biofilm strategies<sup>3</sup>, protein adsorption<sup>4,5</sup> and immunosensor design.<sup>6-8</sup> Proteins are three-dimensional (3D) arrangements of polypeptide chains composed themselves of amino acids sequences that fold according to their nature through electrostatic, Van der Waals, ionic or covalent interactions.<sup>9</sup> Furthermore, depending on their structure and composition, proteins possess a global net charge, often simplified to their isoelectric point (IP), while still displaying charged domains which can interact with a functionalized material surface. Self-assembled monolayers (SAMs) formation is one of the most widespread strategies for surface functionalization and allow to tether surfaces features thanks to great variety of organic molecules with various chain length and functional groups, most commonly amine (NH<sub>2</sub>) and carboxylic (COOH) ones.<sup>10-12</sup> Moreover, chain length and surface terminal groups have proved to modulate surface wettability and in turn protein adsorption.<sup>13-15</sup>

However, in most papers dealing with protein adsorption, the latter is performed in PBS buffer without any further consideration towards the impact of this solvent. PBS is a rightful contributor as much as the adsorbate and the adsorbent on both surfaces charges of the proteins and the functionalized material. Indeed, very few studies consider the surface charge of the functionalized surface and often assume that it is driven solely by the pK<sub>a</sub> of the assembled molecules.

Yet, the surface charge of molecules was shown to change once adsorbed onto a substrate compared to free molecules in solution<sup>16-18</sup> and also depending on the surface's curvature if immobilized on gold nanoparticles.<sup>19</sup> For a same terminal group, the surface charge was also dependent from the chain length and surface coverage of adsorbed species.<sup>20-22</sup> Strategies involving mixed SAMs were also employed to modulate the surface charge of planar surfaces with for instance mixed

COOH/NH<sub>2</sub> thiolate SAMs on gold<sup>18,23,24</sup> or NH<sub>2</sub>/thiol (SH) silane SAMs on silica<sup>25</sup> substrates. As expected when assembling mixed NH<sub>2</sub>/COOH and OH/CH<sub>3</sub> thiolate SAMs, increasing COOH amount led to a general decrease in surface wettability and increase in surface isoelectric point (IEP).<sup>26</sup> The resulting SAMs were applied to osteopontin adsorption and cell adhesion studies, and the amount of adsorbed osteopontin was found to depend on surface wettability with poor binding on OH/CH<sub>3</sub> mixed layer in comparison to the NH<sub>2</sub>/COOH one and also on surface charge with the greater density on the mixed SAMs displaying the highest IEP.

Beyond the pH influence on the assembly, we previously demonstrated, when investigating Bovine Serum Albumin (BSA) adsorption onto COOH-terminated thiolate SAMs that the pH used to wash the functionalized substrate had a considerable influence on BSA adsorption, even if this adsorption is carried out in ultrapure water without any further control of the local pH during the interaction.<sup>27</sup> Rinsing at three pH values, *i.e.* 2, 5.5 and 11, had indeed impacted the SAM order and hydrophilicity, and the surfaces immersed in ultrapure water showed to exhibit a memory effect during the interaction with the negatively charged BSA. All these findings highlight the crucial effect of the pH on the various steps included in protein/functionalized surface interaction.

In the work presented herein, we investigated the impact of chain length on surface charges by forming COOH-terminated thiolate SAMs of increasing chain length ( $n_{CH_2} = 1,7,10$ ) on gold surfaces. These surfaces were analyzed using Water Contact Angle (WCA), Polarization Modulation InfraRed Reflection Absorption Spectroscopy (PM-IRRAS), X-Ray Photoelectron Spectroscopy (XPS) and electrokinetic measurements. The electrokinetic measurements suggest that adsorption could affect the pK<sub>a</sub> values of COOH-terminated thiols in contrast to the ones of free molecules in the bulk phase. In addition, chain length was shown to influence the measured zeta potential and resultant surface IEP of COOH-terminated thiolate SAMs on gold.

### 3.2 Experimental procedure

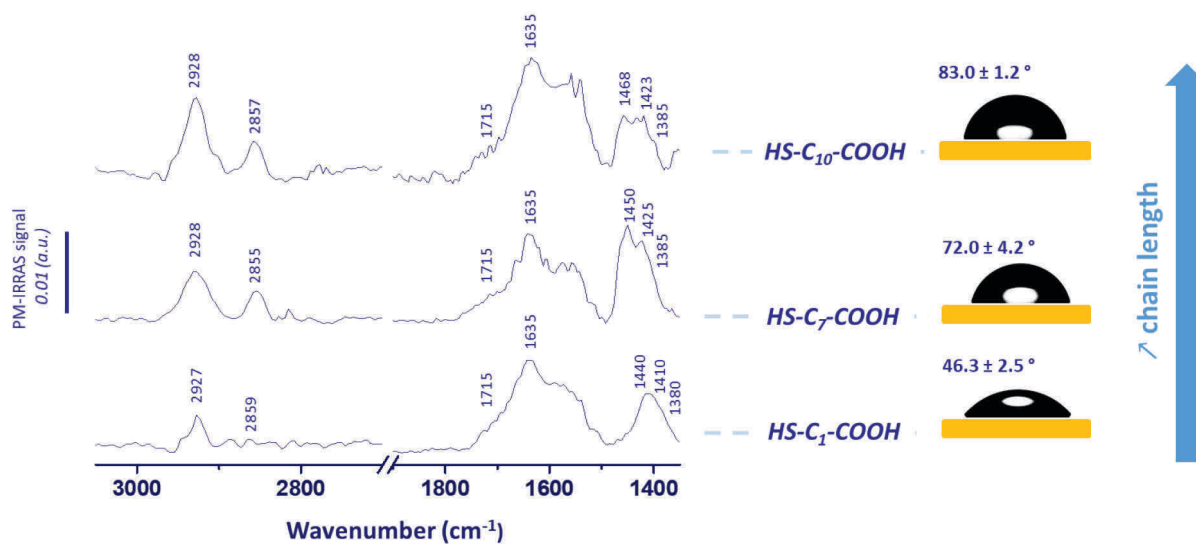
We applied the same surface functionalization procedure presented in our previous paper to form COOH-terminated SAMs on gold surfaces. Briefly, gold-coated substrates were immersed in thiol solutions in ethanol (1 mM) and left-covered for 24 hours under gentle agitation.

The substrates were then washed once with ethanol for 5 min, ultrasonicated for 1 min in ethanol and washed twice for 5 min with ethanol. All substrates were dried with a gentle nitrogen flow prior to further surface characterizations.

### 3.3 Results and discussion

#### 3.3.1 Surface characterization

Similar PM-IRRAS and WCA results to those presented in our previous investigation were obtained (**Figure 3. 1**). Briefly, the same infrared (IR) signatures were observed with typical bands attributed to carbonyl (C=O) and carboxylates (COO<sup>-</sup>) groups respectively at 1715 and 1620/1415 cm<sup>-1</sup> and methylene (CH<sub>2</sub>) bands of in the 2930-2850 cm<sup>-1</sup> region.



**Figure 3. 1.** Baseline corrected PM-IRRAS spectra with corresponding water contact angle results of COOH-SAMs of increasing chain length ( $n_{CH_2} = 1, 7, 10$ ).

The position of the asymmetric bands ( $\nu_{CH_2}^{asymm}$ ) is characteristic of the order of the SAMs with values typically ranging from 2930 to 2918 cm<sup>-1</sup>, with the latter being attributed to a solid-like monolayer.<sup>9,26</sup>

Furthermore, chain length have been shown to influence the overall order through increased Van der Waals interactions between methylene groups of the backbone.<sup>27-29</sup>

Nevertheless,  $\nu_{CH_2}^{asymm}$  values reported herein exhibited a different behavior than the one described in our previous study. Indeed, chain length moderately influenced the position of this band, with values around 2928  $cm^{-1}$  (**Table 3. 1**).

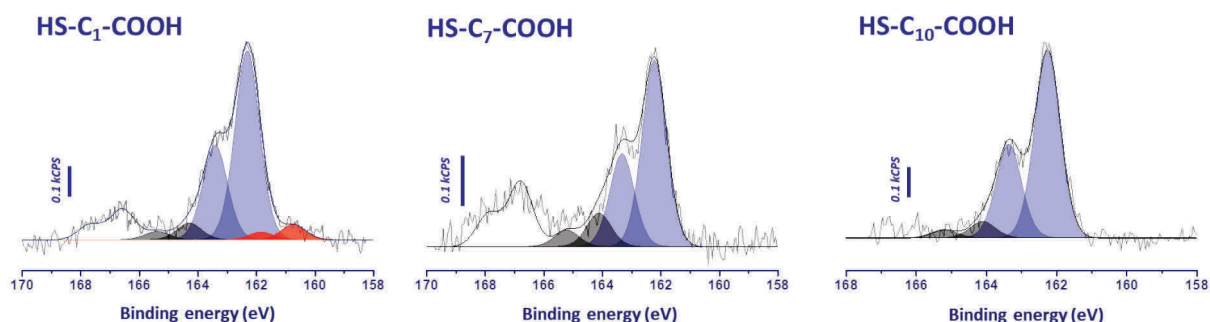
**Table 3. 1.** Position of the asymmetric  $CH_2$  stretching bands (in  $cm^{-1}$ ) for COOH-SAMs of increasing chain length on gold for experiments performed in duplicate.

HS-C <sub>1</sub> -COOH	HS-C <sub>7</sub> -COOH	HS-C <sub>10</sub> -COOH
2927.4	2928.3	2928.5
2927.4	2928.0	2928.3
2927.4	2928.2 ± 0.2	2928.4 ± 0.1

Moreover, WCA results suggested less hydrophilic SAMs in comparison to those prepared on commercial gold substrates in our previous study which might correlate with less ordered SAMs, with respectively values of  $46.3 \pm 2.5^\circ$ ,  $72.0 \pm 4.2^\circ$  and  $83.0 \pm 1.2^\circ$  for HS-C<sub>1</sub>-COOH, HS-C<sub>7</sub>-COOH and HS-C<sub>10</sub>-COOH. Indeed, experiments were carried out using prepared in-house substrates that could not withstand the same experimental conditions, *i.e.* annealing procedure. Specific dimensions for the gold substrates were mandatory to carry out the electrokinetic experiments. Thus, we expect differences in the gold layer such as lower crystallinity of the substrates, that could affect the thiolate SAMs formation and lead to overall more disordered SAMs and higher WCA values. Furthermore, XPS results showed the presence of gold, oxygen, carbon and sulfur atoms as expected in the formation of thiolate SAMs on gold (**Table 3. 1**) and confirmed functionalization with notably the presence of chemisorbed thiolate molecules (**Figure 3. 2**).

**Table 3. 2.** XPS atomic percentages for COOH-SAMs of increasing chain length on gold.

	HS-C <sub>1</sub> -COOH	HS-C <sub>7</sub> -COOH	HS-C <sub>10</sub> -COOH
O <sub>1s</sub>	56.12	51.88	48.07
C <sub>1s</sub>	41.0	45.82	49.78
S <sub>2p</sub>	2.88	2.31	2.15



**Figure 3. 2.** Representative background subtracted high-resolution XPS  $S_{2p}$  spectra of COOH-SAMs of increasing chain length on gold. Experiments were performed in duplicate.

### 3.3.2 Electrokinetic measurements

Subsequently, we measured the surface zeta potential through electrokinetic measurements using a cell with an adjustable gap. Streaming current measurements allowed to determine the zeta potential and isoelectric point (IEP) of the functionalized substrate by using the Helmholtz-Smoluchowski equation:

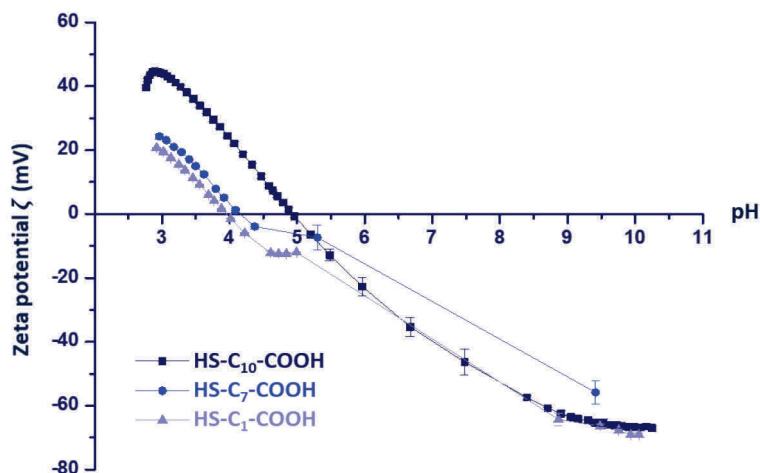
$$\zeta = \frac{dI_{str}}{dp} * \frac{\eta}{\varepsilon * \varepsilon_0} * \frac{L}{A}$$

,where  $\zeta$  is the zeta potential,  $dI_{str}/dp$  is the slope of the streaming current *versus* pressure,  $\eta$  is the electrolyte viscosity,  $\varepsilon$  is the dielectric constant of the electrolyte,  $\varepsilon_0$  is the vacuum permittivity, L and A are respectively the length and cross-section of the streaming channel.

Titration curves for COOH-terminated SAMs of increasing chain length on gold are presented in **Figure 3. 3**. Titrations were conducted in a NaCl electrolyte solution (1 M) using HCl (0.1 M) and NaOH (0.1 M) aqueous solutions to respectively acidic ( $\sim 3$ ) and basic ( $\sim 10$ ) pH values.

The isoelectric points (IEP) of functionalized sensors, *i.e.* pH values at which zeta potential is zero, were also determined in duplicate at least and representative data are given in **Figure 3. 3** and **Table 3. 3**.





**Figure 3. 3.** Zeta potential measurements obtained on functionalized COOH-terminated thiolate SAMs of increasing length ( $n_{CH_2} = 1,7,10$ ) on gold surfaces.

The presented zeta potential values are the sum of four individual measurements and the titration curves were constructed along titration process by adding either acid or base to the electrolyte solution. At the IEP value, the surface charge is globally neutral with equilibrium of the protonated and deprotonated surface moieties concentrations. Below the IEP, the surface is positively charged with zeta potential value up to 40 mV and inversely beyond this value the surface is negatively charged with values around  $-80$  mV. Furthermore, we observed at extreme pH value for the HS-C<sub>10</sub>-COOH sample, *i.e.*  $pH \leq 3.5$ , a drop in zeta potential values that was previously attributed to high conductivity of the electrolyte.<sup>20</sup>

**Table 3. 3.** Theoretical  $pK_a$  values and experimental IEP determined through electrokinetic measurements for COOH-terminated SAMs of increasing chain length on gold. Theoretical values were determined with the ChemAxon software.<sup>31,32</sup>

	HS-C <sub>1</sub> -COOH	HS-C <sub>7</sub> -COOH	HS-C <sub>10</sub> -COOH
<i>Theoretical <math>pK_a</math></i>	4.20	5.05	4.95
<i>Experimental IEP</i>	4.0	4.2	4.8
	4.2	3.8	4.9
	3.9	-	4.9
	$4.1 \pm 0.1$	$4.0 \pm 0.2$	$4.9 \pm 0.1$

\* Calculated using the ChemAxon software.<sup>31,32</sup>

Furthermore, chain length of COOH-terminated thiolate molecules is known to influence the  $pK_a$  value of its functional groups. Theoretical values presented in **Table 3. 3** were calculated using the ChemAxon software which calculates  $pK_a$  values based on partial charge distribution.<sup>30,31</sup>

Measured IEP of functionalized substrates also showed an influence of chain length over the surface charge, *i.e.* zeta potential and IEP values. Indeed, almost identical IEP values were obtained for the short and long chain length SAMs while a higher one was measured for the mid SAMs with a difference of one pH unit (**Table 3. 3**).

In contrast, we observed discrepancies between the surface IEP and the  $pK_a$  value of free molecules for the mid chain length SAMs, *i.e.* HS-C<sub>7</sub>-COOH, as previously observed in the literature.<sup>18-20</sup>

Shimazu *et al.* carried out a surface mass titration of COOH-terminated thiolate SAMs on gold using quartz crystal microbalance (QCM) and measured the difference in frequency shift upon titrations.<sup>15</sup>

This shift was attributed to deprotonation of the surface moieties to carboxylate groups associated with sodium cation and linked to the number of adsorbed functional groups and surface  $pK_a$  which were higher than the ones of free molecules in solution.

Accordingly, work from Dai *et al.* on increasing chain length thiolate SAMs on gold ( $n_{CH_2} = 1,2,10,15$ ) determined higher  $pK_a$  values using electrochemical titration.<sup>32</sup>

The authors found that the surface  $pK_a$  evolved with chain length when  $n_{CH_2} > 2$ , increasing chain length led to denser SAMs through Van der Waals interactions and to higher electron-donating ability from the methylene groups. The given  $pK_a$  values were higher than these from the bulk phase and explained it by the ability to form hydrogen bonding between carbonyl and carboxylate groups once adsorbed on a substrate.

Furthermore, Vezenov *et al.* used chemical force microscopy (CFM) and adhesion force titrations on COOH-terminated surface and determined a surface  $pK_a$  of 5.5, close to the one of free molecules in the bulk phase.<sup>33</sup>

All in all, there exists discrepancies in the determined  $pK_a$  for adsorbed thiolate molecules in contrast to the one from the solution phase which could originate from the different ionic strength and determination methods employed in the literature.

### 3.4 Conclusion

In this study, we studied the adsorption of COOH-terminated thiols onto gold surfaces and measured the impact of chain length on the surface charge, *i.e.* isoelectric point (IEP).

We have shown that the nature of the gold substrate appeared to influence the order of the SAMs and wettability of the designed monolayers with overall less ordered monolayers with decreased hydrophilicity. Furthermore, electrokinetic measurements were carried out on COOH-terminated thiolate SAMs on gold of increasing chain length.

Results suggested that chain length influenced the measured zeta potential as well as the IEP values for these SAMs. Finally, discrepancies between the surface IEP *versus* the  $pK_a$  of the free molecule in the bulk phase were observed and previously documented in the literature.

## References

- (1) Hervier, A.; Blanchard, J.; Costentin, G.; Regalbuto, J.; Louis, C.; Boujday, S. The Genesis of a Heterogeneous Catalyst: In Situ Observation of a Transition Metal Complex Adsorbing onto an Oxide Surface in Solution. *Chem. Commun.* **2014**, 50 (19), 2409–2411.
- (2) Blanchard, J.; Hervier, A.; Costentin, G.; Regalbuto, J.; Louis, C.; Boujday, S. In-Situ Monitoring of Transition Metal Complex Adsorption on Oxide Surfaces during the First Stages of Supported Metal Catalyst Preparation. *Catal. Today* **2014**, 235, 245–249.
- (3) Humblot, V.; Pradier, C. Adsorption of Proteins and Anti-biofilm Strategies. In *Surface and Interface Science*; Wandelt, K., Ed.; Wiley, 2020; pp 197–227.
- (4) Mrksich, M.; Sigal, G. B.; Whitesides, G. M. Surface Plasmon Resonance Permits in Situ Measurement of Protein Adsorption on Self-Assembled Monolayers of Alkanethiolates on Gold. *Langmuir* **1995**, 11 (11), 4383–4385.
- (5) Arima, Y.; Iwata, H. Effect of Wettability and Surface Functional Groups on Protein Adsorption and Cell Adhesion Using Well-Defined Mixed Self-Assembled Monolayers. *Biomaterials* **2007**, 28 (20), 3074–3082.
- (6) Briand, E.; Salmain, M.; Compère, C.; Pradier, C.-M. Immobilization of Protein A on SAMs for the Elaboration of Immunosensors. *Colloids Surf. B Biointerfaces* **2006**, 53 (2), 215–224.
- (7) Briand, E.; Salmain, M.; Compère, C.; Pradier, C.-M. Anti-Rabbit Immunoglobulin G Detection in Complex Medium by PM-RAIRS and QCM. *Biosens. Bioelectron.* **2007**, 22 (12), 2884–2890.
- (8) Salmain, M.; Ghasemi, M.; Boujday, S.; Spadavecchia, J.; Técher, C.; Val, F.; Le Moigne, V.; Gautier, M.; Briandet, R.; Pradier, C.-M. Piezoelectric Immunosensor for Direct and Rapid Detection of Staphylococcal Enterotoxin A (SEA) at the Ng Level. *Biosens. Bioelectron.* **2011**, 29 (1), 140–144.
- (9) Stollar, E. J.; Smith, D. P. Uncovering Protein Structure. *Essays Biochem.* **2020**, 64 (4), 649–680.
- (10) Love, J. C.; Estroff, L. A.; Kriebel, J. K.; Nuzzo, R. G.; Whitesides, G. M. Self-Assembled Monolayers of Thiolates on Metals as a Form of Nanotechnology. *Chem. Rev.* **2005**, 105 (4), 1103–1170.
- (11) Vericat, C.; Vela, M. E.; Benitez, G.; Carro, P.; Salvarezza, R. C. Self-Assembled Monolayers of Thiols and Dithiols on Gold: New Challenges for a Well-Known System. *Chem. Soc. Rev.* **2010**, 39 (5), 1805.
- (12) Vericat, C.; Vela, M. E.; Corthey, G.; Pensa, E.; Cortés, E.; Fonticelli, M. H.; Ibañez, F.; Benitez, G. E.; Carro, P.; Salvarezza, R. C. Self-Assembled Monolayers of Thiolates on Metals: A Review Article on Sulfur-Metal Chemistry and Surface Structures. *RSC Adv* **2014**, 4 (53), 27730–27754.
- (13) Lebec, V.; Landoulsi, J.; Boujday, S.; Poleunis, C.; Pradier, C.-M.; Delcorte, A. Probing the Orientation of  $\beta$ -Lactoglobulin on Gold Surfaces Modified by Alkyl Thiol Self-Assembled Monolayers. *J. Phys. Chem. C* **2013**, 117 (22), 11569–11577.
- (14) Bedford, E. E.; Boujday, S.; Humblot, V.; Gu, F. X.; Pradier, C.-M. Effect of SAM Chain Length and Binding Functions on Protein Adsorption:  $\beta$ -Lactoglobulin and Apo-Transferrin on Gold. *Colloids Surf. B Biointerfaces* **2014**, 116, 489–496.
- (15) Lebec, V.; Boujday, S.; Poleunis, C.; Pradier, C.-M.; Delcorte, A. Time-of-Flight Secondary Ion Mass Spectrometry Investigation of the Orientation of Adsorbed Antibodies on SAMs Correlated to Biorecognition Tests. *J. Phys. Chem. C* **2014**, 118 (4), 2085–2092.
- (16) Zhao, J.; Luo, L.; Yang, X.; Wang, E.; Dong, S. Determination of Surface PKa of SAM Using an Electrochemical Titration Method. *Electroanalysis* **1999**, 11 (15), 1108–1113.
- (17) Gooding, J. J.; Hale, P. S.; Maddox, L. M.; Shapter, J. G. Surface PKa of Self-Assembled Monolayers. *J. Chem. Educ.* **2005**, 82 (5), 779.

- (18) Lin, W.-C.; Lee, S.-H.; Karakachian, M.; Yu, B.-Y.; Chen, Y.-Y.; Lin, Y.-C.; Kuo, C.-H.; Shyue, J.-J. Tuning the Surface Potential of Gold Substrates Arbitrarily with Self-Assembled Monolayers with Mixed Functional Groups. *Phys. Chem. Chem. Phys.* **2009**, *11* (29), 6199.
- (19) Wang, D.; Nap, R. J.; Han, S.; Grzybowski, B. A.; Szeleifer, I. How and Why Nanoparticle's Curvature Regulates the Apparent PKa of the Coating Ligands. *J. Am. Chem. Soc.* **2011**, *6*.
- (20) Shimazu, K.; Teranishi, T.; Sugihara, K.; Uosaki, K. Surface Mass Titrations of Self-Assembled Monolayers of  $\omega$ -Mercaptoalkanoic Acids on Gold. *Chem. Lett.* **1998**, *27* (7), 669–670.
- (21) Sugihara, K.; Teranishi, T.; Shimazu, K.; Uosaki, K. Structure Dependence of the Surface pKa of Mercaptoundecanoic Acid SAM on Gold. *Electrochemistry* **1999**, *67* (12), 1172–1174.
- (22) Marmisolé, W. A.; Capdevila, D. A.; de la Llave, E.; Williams, F. J.; Murgida, D. H. Self-Assembled Monolayers of NH<sub>2</sub>-Terminated Thiolates: Order, pK<sub>a</sub>, and Specific Adsorption. *Langmuir* **2013**, *29* (17), 5351–5359.
- (23) Chang, H.-Y.; Huang, C.-C.; Lin, K.-Y.; Kao, W.-L.; Liao, H.-Y.; You, Y.-W.; Lin, J.-H.; Kuo, Y.-T.; Kuo, D.-Y.; Shyue, J.-J. Effect of Surface Potential on NIH3T3 Cell Adhesion and Proliferation. *J. Phys. Chem. C* **2014**, *118* (26), 14464–14470.
- (24) Besharat, Z.; Wakeham, D.; Johnson, C. M.; Luengo, G. S.; Greaves, A.; Odnevall Wallinder, I.; Göthelid, M.; Rutland, M. W. Mixed Monolayers of Alkane Thiols with Polar Terminal Group on Gold: Investigation of Structure Dependent Surface Properties. *J. Colloid Interface Sci.* **2016**, *484*, 279–290.
- (25) Kuo, C.-H.; Chang, H.-Y.; Liu, C.-P.; Lee, S.-H.; You, Y.-W.; Shyue, J.-J. Effect of Surface Chemical Composition on the Surface Potential and Iso-Electric Point of Silicon Substrates Modified with Self-Assembled Monolayers. *Phys. Chem. Chem. Phys.* **2011**, *13* (9), 3649.
- (26) Hao, L.; Li, T.; Yang, F.; Zhao, N.; Cui, F.; Shi, X.; Du, C.; Wang, Y. The Correlation between Osteopontin Adsorption and Cell Adhesion to Mixed Self-Assembled Monolayers of Varying Charges and Wettability. *Biomater. Sci.* **2017**, *5* (4), 800–807.
- (27) Vallée, A.; Humblot, V.; Al Housseiny, R.; Boujday, S.; Pradier, C.-M. BSA Adsorption on Aliphatic and Aromatic Acid SAMs: Investigating the Effect of Residual Surface Charge and Sublayer Nature. *Colloids Surf. B Biointerfaces* **2013**, *109*, 136–142.
- (28) Nuzzo, R. G.; Dubois, L. H.; Allara, D. L. Fundamental Studies of Microscopic Wetting on Organic Surfaces. 1. Formation and Structural Characterization of a Self-Consistent Series of Polyfunctional Organic Monolayers. *J. Am. Chem. Soc.* **1990**, *112* (2), 558–569.
- (29) Briand, E.; Salmain, M.; Herry, J.-M.; Perrot, H.; Compère, C.; Pradier, C.-M. Building of an Immunosensor: How Can the Composition and Structure of the Thiol Attachment Layer Affect the Immunosensor Efficiency? *Biosens. Bioelectron.* **2006**, *22* (3), 440–448.
- (30) Bedford, E.; Humblot, V.; Méthivier, C.; Pradier, C.-M.; Gu, F.; Tielens, F.; Boujday, S. An Experimental and Theoretical Approach to Investigate the Effect of Chain Length on Amino-thiol Adsorption and Assembly on Gold. *Chem. - Eur. J.* **2015**, *21* (41), 14555–14561.
- (31) Szegezdi, J.; Csizmadia, F. A Method for Calculating the PKa Values of Small and Large Molecules. 2.
- (32) Szegezdi, J.; Csizmadia, F. Prediction of Dissociation Constant Using Microconstants. 2.
- (33) Dai, Z.; Ju, H. Effect of Chain Length on the Surface Properties of  $\omega$ -Carboxy Alkanethiol Self-Assembled Monolayers. *Phys. Chem. Chem. Phys.* **2001**, *3* (17), 3769–3773.
- (34) Vezenov, D. V.; Noy, A.; Rozsnyai, L. F.; Lieber, C. M. Force Titrations and Ionization State Sensitive Imaging of Functional Groups in Aqueous Solutions by Chemical Force Microscopy. *J. Am. Chem. Soc.* **1997**, *119* (8), 2006–2015.

## 3.5 Supplementary Information

### 3.5.1 Experimental section

#### 3.5.1.1 Materials

8-mercaptooctanoic acid (HS-C<sub>7</sub>-COOH) and 11-mercaptoundecanoic acid (HS-C<sub>10</sub>-COOH) were purchased from Sigma Aldrich (Saint-Quentin Fallavier, France). Thioglycolic acid (HS-C<sub>1</sub>-COOH) was purchased from Fluka. All solvents and reagents were used without any further purification. Experiments were carried out under ambient conditions on glass substrates (9 mm x 9 mm) successively coated with a 5-6 nm thick layer of chromium and a 210-220 nm thick layer of gold. Prior to functionalization, the gold-coated substrates were rinsed in absolute ethanol for 15 min, dried with a nitrogen flow, cleaned with UV/ozone for 30 min and annealed in a butane/propane flame to ensure good crystallinity of the gold topmost layers.

#### 3.5.1.2 Techniques

##### 3.5.1.2.1 PM-IRRAS (Polarization Modulation InfraRed Reflection Absorption Spectroscopy)

PM-IRRAS spectra were recorded on a commercial Thermo-scientific Nicolet Nexus 5700 spectrometer. The external beam was focused on the sample with a mirror, at an optical incident angle of 85°. A ZnSe grid polarizer and a ZnSe photoelastic modulator, modulating the incident beam between p- and s- polarizations (HINDS Instruments, PEM 90, modulation frequency of 37 kHz), were placed prior to the sample. The light reflected at the sample was then focused onto a liquid nitrogen-cooled MCT detector. The PM-IRRAS signal is given by the differential reflectivity  $\Delta R/R = (R_p - R_s)/(R_p + R_s)$ . The presented infrared (IR) spectra result from the acquisition of 1024 scans recorded at 8 cm<sup>-1</sup> resolution. Position for the asymmetric methylene stretching vibration was fitted on baseline corrected spectra using Origin Software.

### 3.5.1.2.2 WCA (Water Contact Angle)

Static water contact angles were measured at room temperature using the sessile drop method and image analysis of the drop profile. The instrument, which uses a CCD camera and an image analysis processor, was purchased from Krüss (Germany). The water (Milli-Q) droplet volume was 1  $\mu\text{L}$  and the contact angle ( $\theta$ ) was measured 5 s after the drop was deposited on the sample. Experiments were conducted in duplicate and the reported values are the average of three droplets at different locations of each sample's surface.

### 3.5.1.2.3 XPS (X-Ray Photoelectron Spectroscopy)

XPS analysis were performed on a Scienta Omicron Argus X-ray photoelectron spectrometer, using a monochromated  $\text{AlK}\alpha$  ( $h\nu = 1486.6 \text{ eV}$ ) radiation source having a 280 W electron beam power. The emission of photoelectrons from the sample was analyzed at a takeoff angle of  $45^\circ$  under ultra-high vacuum conditions ( $1 \times 10^{-9} \text{ Pa}$ ). XPS spectra were collected at pass energy of 100 eV for the survey scan and 20 eV for the  $\text{C}_{1s}$ ,  $\text{O}_{1s}$ ,  $\text{N}_{1s}$ ,  $\text{Cl}_{2p}$ ,  $\text{Na}_{1s}$ ,  $\text{Au}_{4f}$ ,  $\text{S}_{2p}$  core XPS levels. The energy resolution for  $\text{S}_{2p}$  acquisition was adjusted from 0.1 to 0.05 eV. The peak areas were determined after subtraction of a Shirley background. The spectra were fitted using Casa XPS software and applying a Gaussian/ Lorentzian ratio (G/L) equal to 70/30.

### 3.5.1.2.4 Electrokinetic measurements

The zeta ( $\zeta$ ) potential of functionalized gold substrates were determined by measuring the streaming current between two planar substrates using a cell with an adjustable gap, comprised between 100-150  $\mu\text{m}$ , using an electrokinetic analyzer (SurPass, Anton Paar GmbH, Austria).

The measurements were carried out by flowing a 1 mM NaCl electrolyte solution through the micro-channel with syringe pumps under a pressure ramp of 0 to 200 mbar. The aqueous solutions were immediately purged with nitrogen after preparation to avoid dissolution of atmospheric carbon dioxide ( $\text{CO}_2$ ). Surface titrations were conducted to acidic pH ( $\sim 3$ ) and basic pH ( $\sim 11$ ) using 0.1 M HCl or NaOH aqueous solutions, respectively.

The Helmholtz–Smoluchowski equation was used to convert measured streaming currents to zeta potential values with as well determination of the isoelectric point (IEP) which is the pH for which the zeta potential is nil.







---

**Chapter 4. Design and analytical performances of a  
diclofenac biosensor for water resources monitoring**

---



## 4.1 Introduction

Diclofenac (DCF), a non-steroidal anti-inflammatory drug (NSAID), is one of the most consumed pain killers worldwide with, for instance, 80 to 100 tons/year consumed in Germany and 40 to 60 ton/year in France.<sup>1</sup> As a result, and because of inefficient waste water treatment processes, DCF is considered as an emerging water pollutant and was listed in the first watch list of ten organic molecules to be monitored and reported.<sup>2,3</sup> DCF is suspected to be hazardous to the aquatic environment<sup>4</sup> and in turn to human health. In 2019, the French agency for food safety and environment (ANSES) published a notice on the possible sanitary consequences of the presence of DCF in surface water and edited a guide value of 0.4 µg/L.<sup>5</sup>

Chromatographic methods are routinely used to quantify DCF residues in surface and ground water.<sup>6,7</sup> Alternatively, label-based immunochemical assays allow to quantify DCF in water samples with sensitivities from the µg/L down to the sub ng/L range, depending on the detection method.<sup>8-17</sup> Although these methods are selective and sensitive, they are not easily amenable to on-site detection. In this context, various biosensing set ups have been implemented using antibodies,<sup>18</sup> aptamers<sup>19,20</sup> or even whole cells<sup>21-23</sup> as bioreceptors coupled to electrochemical<sup>24-26</sup> or optical<sup>27,28</sup> signal transduction. With such set ups, DCF could be quantified in various matrices with variable sensitivities.

DCF being a small molecule, the only possible assay format is of the competitive type, thus requiring to build up a sensing platform at the surface of the transducer comprising an analog of the analyte that will compete with the analyte in solution to bind the antibody.

Previously, we had introduced a reliable strategy to generate a sensing layer comprising DCF molecules at the surface of planar and nanostructured gold and silica substrates and its ability to bind a polyclonal anti-DCF antibody.<sup>29,30</sup>

This led to the implementation of an automated, flow-through, enzyme-based competitive immunoassay of DCF using chemiluminescence readout with good analytical performances and shelf-life.<sup>29</sup>

In this work, we rely on this strategy to develop a label-free and fully regenerable piezoelectric immunosensor for the quantification of DCF in water samples.

The sensing layer was carefully constructed at the surface of silica-coated QCM-D sensors with a slight modification regarding DCF immobilization thanks to an optimized activation process. Binding of a monoclonal highly affine anti-DCF antibody (mAb) developed by some of us<sup>15</sup> to silica-coated quartz sensors functionalized by DCF was monitored in real time by quartz crystal microbalance with dissipation (QCM-D) measurement and by an original simultaneous combination of QCM-D and Localized Surface Plasmon Resonance (LSPR). This allowed to estimate the coverage and the hydration level of the formed monolayer; mAb appeared to form a highly hydrated monolayer.

The competitive QCM-D immunosensing device to which we aspired in our previous studies, was built and tested in buffer media. For this sensor, the response is expressed as frequency shift,  $\Delta F$ , inversely related to the concentration of DCF in solution. We determined the analytical performances of our QCM-D immunosensor in terms of dynamic range (DR), limit of detection (LoD) and limit of quantification (LoQ). Eventually, this biosensor was employed to quantify DCF in river water samples collected at different spots in the Seine and Marne rivers in France.

## 4.2 Experimental procedure

Materials, surface functionalization protocols and characterization techniques are presented in Supporting Information (**Figure S4. 1-2** and **Table S4. 1**).

### 4.2.1 Anti-diclofenac antibody binding test and regeneration

Functionalized sensors were mounted in the QCM-D chambers and the following measurement cycle was applied. After signal stabilization in running buffer (0), mAb solution (1) was flown over the sensor substrate for approximately 120 min.

Then, the sensor was rinsed with running buffer to remove unbound antibody. For reuse purpose, the regeneration buffer (2) was injected for 15 min prior to re-equilibration in running buffer for another 15 min. Antibody concentration optimization was conducted by injecting increasing solutions ranging from 0.05 to 5 mg/L at a flow rate of 50  $\mu\text{L}/\text{min}$ . Flow rate impact on antibody binding was investigated by injecting anti-DCF antibody (1 mg/L) at 25 and 50  $\mu\text{L}/\text{min}$ .

#### 4.2.2 Combined QCM-D and LSPR measurements

For combined QCM-D and Localized Surface Plasmon Resonance (LSPR) measurements, the same experimental protocol was followed, except that mAb solution (5 mg/L) was injected for approximately 110 min and the flow rate was set to 25  $\mu\text{L}/\text{min}$ .

#### 4.2.3 Competitive assay for diclofenac detection in buffer

For diclofenac immunosensing, the competitive format was employed with DCF covalently immobilized onto the sensor surface *via* the PyBOP procedure. Samples containing known concentrations of DCF ranging from 0 to 333.2 nM were pre-incubated with mAb (5 mg/L) during 60 min at 37 °C in either PBS or PBS/EtOH 9:1. The preincubated samples were flown over the substrate surface for 60 min at a flow rate of 25  $\mu\text{L}/\text{min}$  and rinsed with running buffer for 15 min.

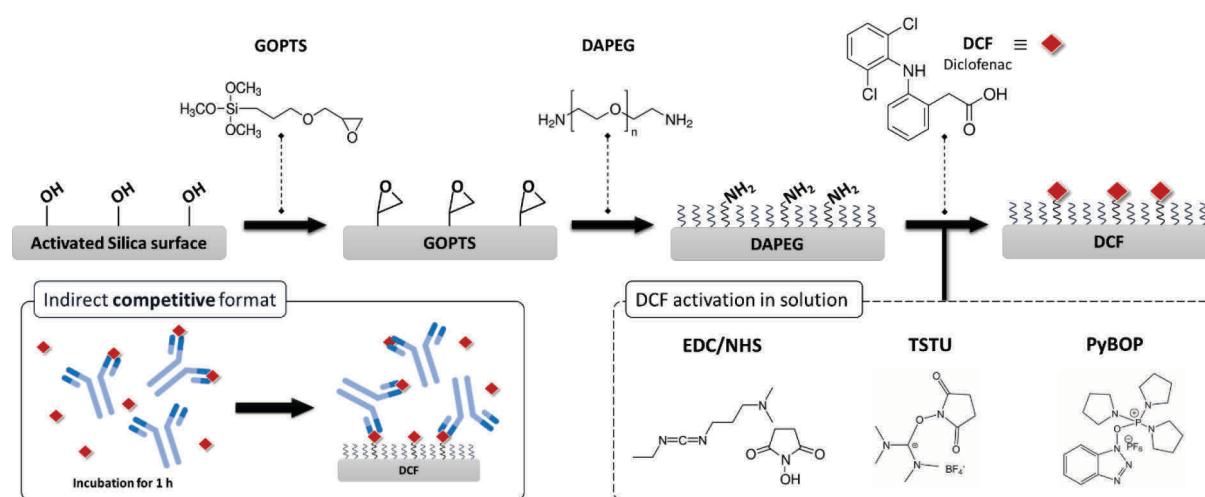
#### 4.2.4 Quantification of diclofenac in surface water samples

Surface water samples (500 mL) were filtered through a 0.22  $\mu\text{m}$  cellulose ester membrane filter (Millipore) to remove suspended matter and were kept in the dark at 4 °C until solid phase extraction (SPE). DCF were extracted following a modified procedure using Oasis HLB 3cc cartridge (Waters) without pH adjustment.<sup>15</sup> The cartridge was preconditioned with 1 mL of methanol followed by 1 mL of ultrapure water. The surface water sample was loaded onto the cartridge followed by washing with 1 mL of water/MeOH 95/5 (v/v). The cartridge was dried for 10 min under vacuum, and DCF was eluted with 1 mL of methanol and kept in the dark at 4 °C. Prior to QCM-D measurement, the extracts were dried under vacuum and the residues reconstituted with 5 mL of PBS. A 100-fold concentration factor was therefore obtained, assuming total recovery during SPE procedure. The water samples were preincubated with mAb (5 mg/L) during 60 min at 37 °C and then were flown over the substrate surface for 60 min at a flow rate of 25  $\mu\text{L}/\text{min}$  and rinsed with running buffer for 15 min. Considering sample preconcentration, antibody incubation and frequency readout, the total assay time is close to 3 hours. The frequency readout step can be reduced to 10 min, thus lowering the total assay time to ca. 2h.

### 4.3 Results and discussion

#### 4.3.1 Surface functionalization.

A sensing layer comprising a PEG layer bearing terminal amine functions, was built up on planar and nanostructured silica-coated quartz sensors as schematized in **Figure 4. 1**, following a previously reported surface functionalization protocol.<sup>29</sup>

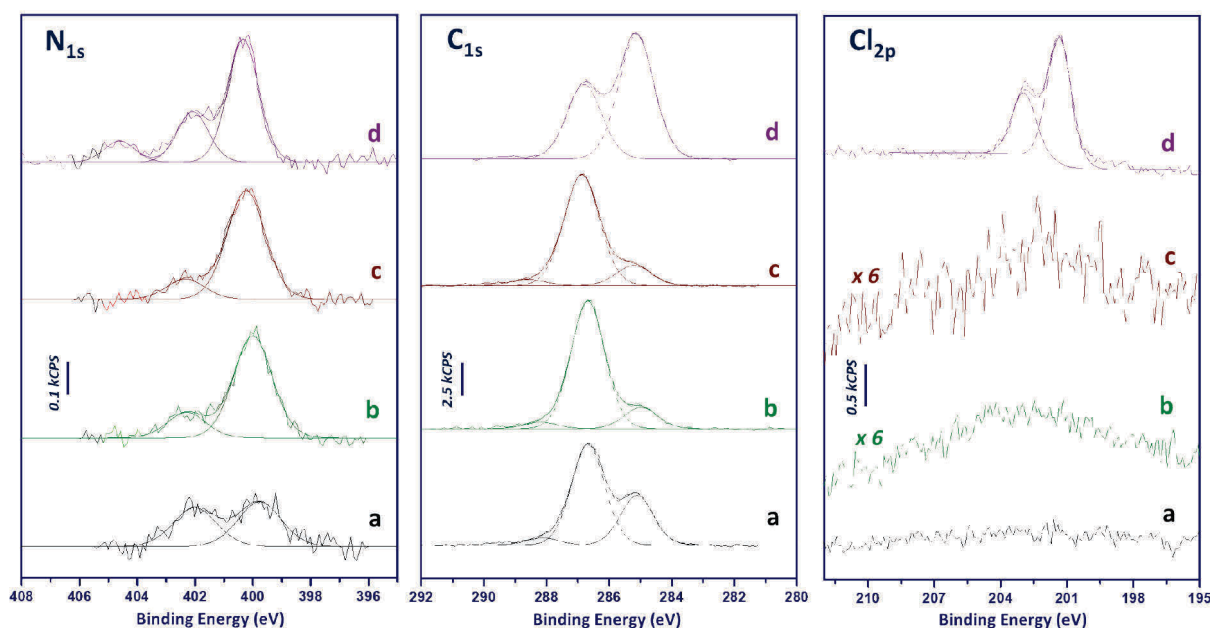


**Figure 4. 1.** Formation of diclofenac sensing layer by step-by-step functionalization of silica / silicon surfaces and schematic representation of competitive assay format.

Experimental details and surface characterizations by ATR-IR, WCA and XPS are given in the supplementary information. Conjugation of DCF to the primary amine group of DAPEG requires preliminary activation of its carboxylic acid function.

This was performed with three activation reagents, namely EDC/NHS, TSTU or PyBOP (**Figure S4. 3**) with the objective of comparing the coupling efficiency and optimizing the number of analytes on the surface and, therefore, the sensing efficiency.

The presence of DCF at the surface of the sensors was investigated by XPS, taking advantage of the two chlorine atoms of DCF, possibly resulting in a chlorine Cl<sub>2p</sub> photopeak at 200 eV. The resulting spectra and the corresponding atomic compositions are shown in **Figure 4. 2** and **Table S4. 2**, respectively.



**Figure 4. 2.**  $N_{1s}$ ,  $C_{1s}$  and  $Cl_{2p}$  XPS spectra of Si substrates sequentially treated by (a) GOPTS and DAPEG; then by DCF activated *via* (b) EDC/NHS, (c) TSTU and (d) PyBOP.

For the three methods  $N_{1s}$  showed a change in contribution balance previously assigned to amide bonds formation.<sup>29</sup>  $Cl_{2p}$  and  $C_{1s}$  photopeaks showed differences between the activation reagents. First, the  $Cl_{2p}$  photopeak was barely detectable for EDC/NHS and TSTU but not for the PyBOP activation strategy, possibly due to a DCF surface concentration under the limit of detection of XPS in the two first cases. Second, the  $C_{1s}$  photopeak for PyBOP strategy was strongly modified: PEG contribution at 286.9 eV was attenuated while the aliphatic contribution at 285.2 eV increased in agreement with DCF grafting.

The PyBOP strategy was further explored by analyzing the XPS peak intensities (**Figure S4. 4**). The surface density in DCF was estimated to 2.3 molecules/nm<sup>2</sup> (detailed calculation is presented in Supporting Information).

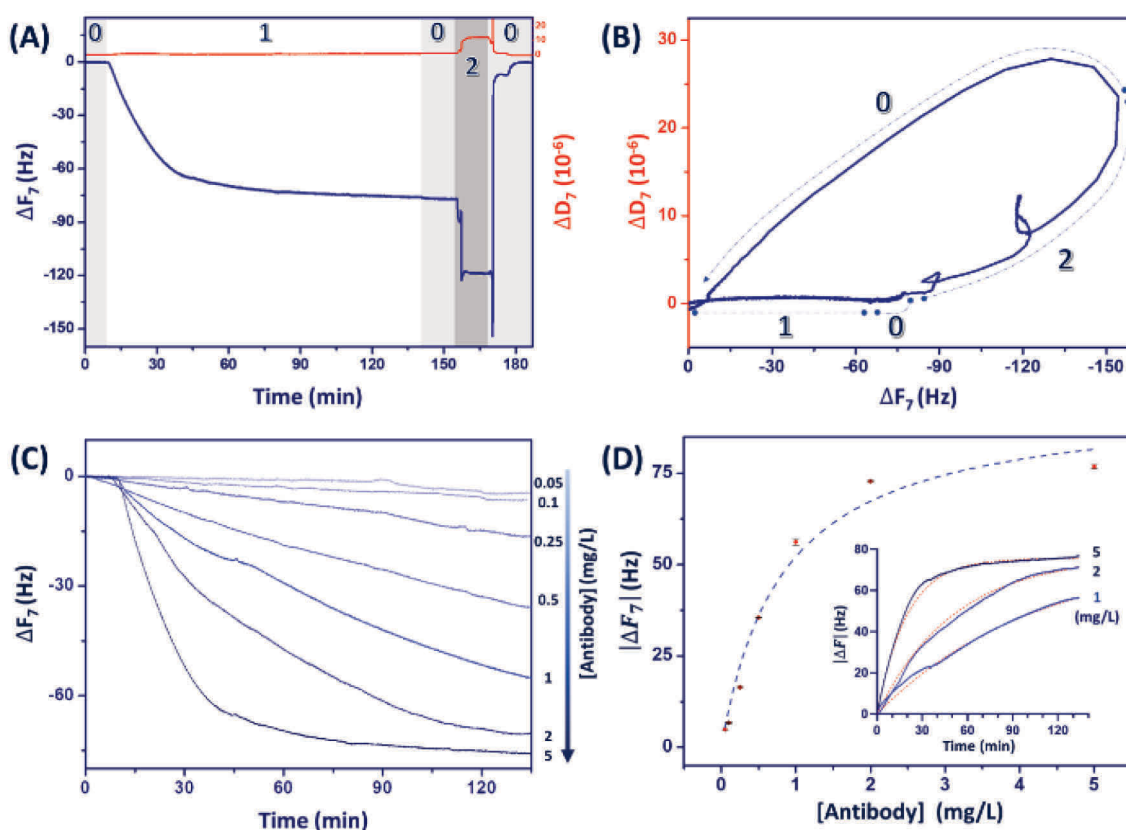
This value is slightly high and may result from excess physisorbed DAPEG and DCF.

Indeed we followed by XPS analysis the removal of DCF when adding a sonication step and observed significant decrease of the  $Cl_{2p}$  signal (**Figure S4. 5**). We further investigated the efficiency of the three activation reagents by comparing, by QCM-D, the binding of mAb to DCF-coated quartz sensors (**Figure S4. 6**). We observed that regardless of the chosen activation reagent, mAb binding led to similar frequency shifts. This result and the observation of Chlorine XPS signal led us to select PyBOP for the following studies.



### 4.3.2 Biosensor design and regeneration.

First, the ability of the DCF-coated quartz sensor *via* PyBOP strategy to bind a monoclonal anti-DCF antibody (mAb) was investigated by QCM-D in flow-through mode (**Figure 4. 3A**). Prior to antibody injection, stabilization was performed by flowing degassed PBS/EtOH 9:1. Then, mAb solution (5 mg/L) was injected at 50  $\mu\text{L}/\text{min}$  for ca. 120 min after which the running buffer was flown again. Within this time frame, signal saturation was reached and the frequency and dissipation energy values shifted by -77 Hz and  $\sim 1 \times 10^{-6}$ , respectively. The frequency shift was much higher in comparison to previous experiments conducted with a polyclonal anti-DCF antiserum for which a  $\Delta F$  of -12 Hz shift was observed.<sup>29</sup> After flowing regeneration and rinsing buffers, the frequency and dissipation returned to their initial values. This shows the complete removal of bound antibody from the DCF sensing layer and a successful surface regeneration process.



**Figure 4. 3.** (A) QCM-D frequency and dissipation shifts upon injection of mAb solution (5 mg/L) to DCF modified quartz sensor at 50  $\mu\text{L}/\text{min}$  and (B) the corresponding D-F plot. (0) running buffer, (1) mAb adsorption, (2) regeneration. (C) QCM-D frequency and dissipation shifts upon injection of mAb solution (0.05 - 5 mg/L) at 50  $\mu\text{L}/\text{min}$  and (D) the corresponding saturation curve. QCM data used for the fit were added as an inset.

One way to represent QCM-D data is by plotting the dissipation versus frequency, also referred as D-F plot (**Figure 4. 3B**). This representation removes time as an explicit parameter and reveals  $\Delta D$ - $\Delta F$  relationship since it shows how much dissipation is induced by a frequency change. Antibody binding (step 1 in **Figure 4. 3B**) was characterized by a linear relationship between dissipation and frequency shifts with a small slope of  $\sim 30 \times 10^{-9} \text{ Hz}^{-1}$  indicative of the formation of a rigid antibody layer.<sup>31</sup> Upon flowing buffer and regeneration solutions, large variations in both dissipation and frequency shifts can be observed.

Through this data representation, full regeneration is illustrated by a loop going back to its starting point. This experiment was repeated with mAb solutions ranging from 0.05 to 5 mg/L in running buffer as shown in **Figure 4. 3C**.

These solutions were flowed at 50  $\mu\text{L}/\text{min}$  for  $\sim 120$  min, followed by a washing step for 15 min. The absolute value of frequency shifts were plotted as a function of mAb concentration (**Figure 4. 3D**). We have chosen to work at constant time rather than waiting for equilibrium which was reached at different times, depending on antibody concentrations. This allows us to be more rigorous in the evaluation of the analytical performances.

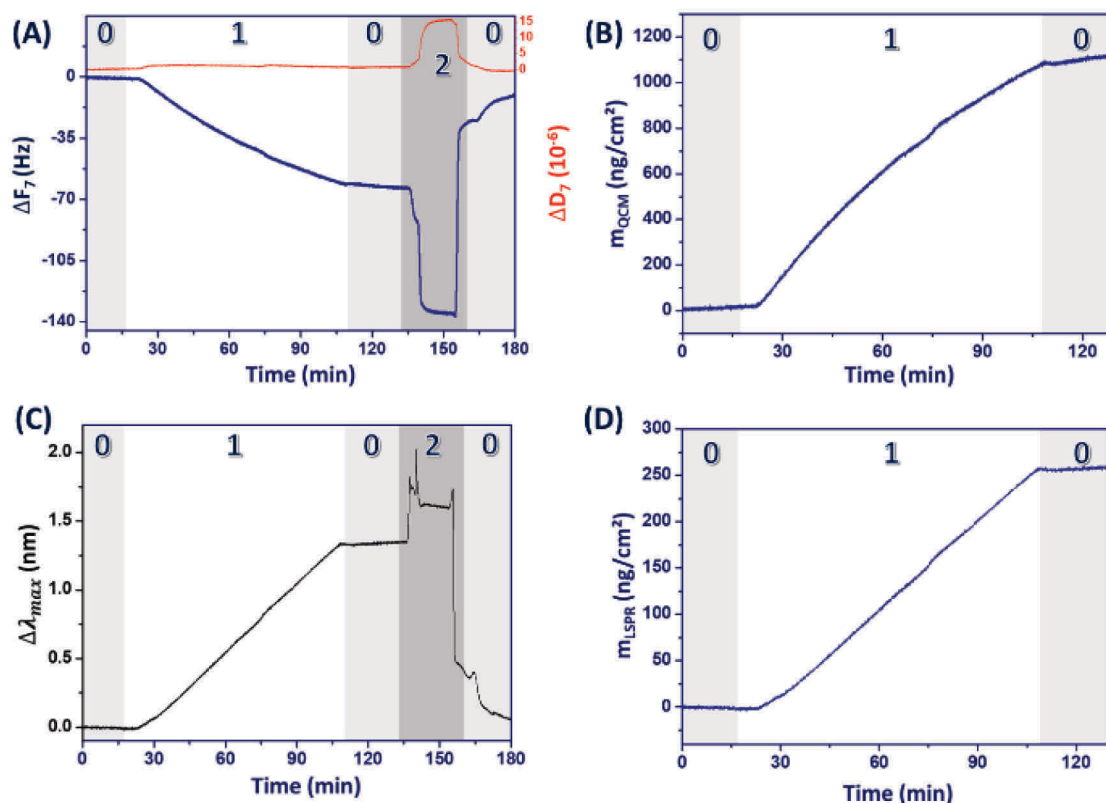
The determination of the kinetic parameters, *i.e.* association ( $k_{\text{on}}$ ) and dissociation ( $k_{\text{off}}$ ) rate constants and the dissociation constant ( $K_{\text{D}}$ ), was performed by curve fitting according to the following equation during the antibody association phase (inset in **Figure 4. 3D**).<sup>32</sup>

$$\Delta F(t) = \frac{\Delta F_{\text{max}} \times [\text{Antibody}]}{K_{\text{D}} + [\text{Antibody}]} \times \left( 1 - \frac{1}{e^{(k_{\text{on}} \times [\text{Antibody}] + k_{\text{off}})t}} \right)$$

The detailed fit parameters are summarized in **Table S4. 3**. From the data fit,  $k_{\text{on}}$  and  $k_{\text{off}}$  rate constants were obtained, and a  $K_{\text{D}}$  of 0.23 nM was calculated. This latter value is close to the one determined by Surface Plasmon Resonance (SPR) measurement in a previous work although the surface chemistry used for DCF immobilization was different in this experiment (0.15 nM).<sup>15</sup> With a flowrate of 25  $\mu\text{L}/\text{min}$ , the frequency shift measured after 120 min of antibody injection at 1 mg/L was of -74 Hz (**Figure S4. 7**). The following QCM-D experiments were conducted at this flowrate, also allowing to reduce mAb consumption.

### 4.3.3 Combined QCM-D & LSPR measurements

Binding of mAb to the sensing layer was also investigated on nanostructured sensors, allowing combined piezoelectric and optical transduction of the binding event by QCM-D and LSPR, respectively. This simultaneous real-time measurement, under the same experimental conditions and on the same surface, provides complementary information as both changes in acoustic ( $m_{QCM-D}$ ) and optical mass ( $m_{LSPR}$ ) uptakes. The nanostructured sensors consist in silica-coated QCM-D sensors comprising, beneath the silica layer, randomly distributed gold nanodisks, thus allowing to use the same surface chemistry than above. The resulting combined measurement data for QCM-D (frequency and dissipation shifts) and LSPR (LSPR peak position shift) are shown in **Figure 4. 4**. Before mAb injection, stabilization was performed by flowing running buffer at 25  $\mu\text{L}/\text{min}$ . Injection of mAb (5 mg/L) led to a decrease in the frequency and a slight increase in dissipation energy values, respectively -62 Hz and  $0.9 \times 10^{-6}$  after 120 min (**Figure 4. 4A**). Simultaneous LSPR measurement led to a  $\Delta\lambda_{\text{max}}$  red-shift of around 1.40 nm upon antibody recognition (**Figure 4. 4C**).



**Figure 4. 4.** Adsorption of mAb (5 mg/L) by DCF-modified nanostructured quartz sensor at 25  $\mu\text{L}/\text{min}$ : (A) QCM-D frequency and dissipation shifts and (B) the corresponding acoustic mass obtained from the Sauerbrey equation. (C) LSPR peak shift  $\Delta\lambda_{\text{max}}$  simultaneously recorded on the same substrate and (D) the corresponding optical mass calculated from LSPR measurement. (0) running buffer, (1) mAb adsorption, (2) regeneration.

The acoustic mass uptake (mAb and coupled solvent) was estimated from QCM-D data by applying the Sauerbrey equation, which reached ca. 1120 ng/cm<sup>2</sup> after 120 min (**Figure 4. 4B**). On the other hand, the optical mass uptake was calculated from LSPR signal shift, and plateaued around 260 ng/cm<sup>2</sup> as shown in **Figure 4. 4D** (detailed calculation is presented in Supporting Information). The optical mass uptake is considered as more representative of the real surface coverage as it only considers the antibody mass without interference from solvent molecules trapped with the protein layer. This experimental surface coverage value is consistent with the formation of a monolayer of antibodies with a head-on orientation.<sup>33,34</sup> Performing the measurement on the same surface and in identical experimental conditions allows an accurate comparison of both acoustic and optical mass uptakes.

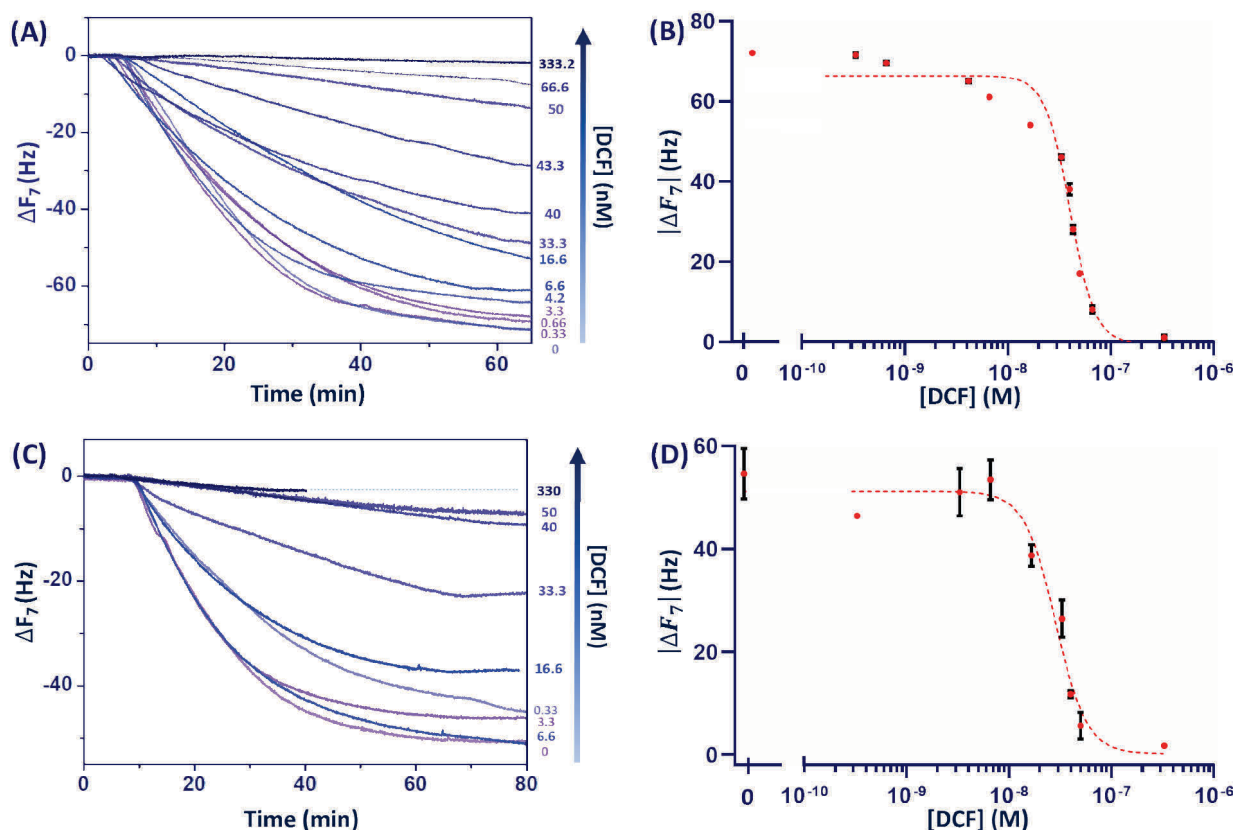
Hence, the percentage of coupled water to the antibody layer was calculated, giving a hydration value of ~ 77% from data presented in Figure 5. This result is consistent with values found in the literature for proteins adsorption onto planar surfaces<sup>35,36</sup> or colloidal systems.<sup>37</sup>

$$\%coupled\ water = \left( \frac{m_{QCM-D} - m_{LSPR}}{m_{QCM-D}} \right) * 100$$

Unlike the previous systems, nanostructured sensors regeneration could not be achieved (the frequency did not return to its initial value and stabilized around -10 Hz while LSPR signal returned to its baseline level), see **Figure 4. 4**. Several attempts were conducted by flowing successively the regeneration and running buffers onto a DCF-functionalized nanostructured substrate (**Figure S4. 8**). No return to the baseline level was observed after the first, second and third cycles of regeneration which might be attributed to a reorganization of the PEG layer on the nanostructured surface. Consequently, at this stage combined QCM-D and LSPR measurements could not be used for DCF biosensing and we focus in what follows on QCM-D.

#### 4.3.4 DCF Biosensing in buffers

The principle of detection of DCF relies on a competitive assay for which binding of high affinity mAb to the DCF-containing sensing layer is inhibited by DCF in solution. To this purpose, standard solutions of DCF (0 – 333.2 nM) in running buffer were mixed with mAb (5 mg/L), incubated during one hour and then flowed over the DCF functionalized sensor for 60 min followed by a 15 min washing step with running buffer (**Figure 4. 5A**). Upon injection of the mixtures of DCF and mAb, the free antibodies interacted with the immobilized DCF and generated a frequency decrease inversely related to the concentration of DCF in solution.



**Figure 4. 5.** Competitive immunoassay established from frequency shifts measured during injection of mixtures of mAb (5 mg/L) and DCF (0 -333.2 nM) at flow rate of 25  $\mu$ L/min (A) in PBS/EtOH with (B) corresponding calibration curve; (C) in PBS with (D) corresponding calibration curve. QCM-D values are summarized in **Table S4. 6** and fitting parameters are detailed in **Table S4. 4**.

Indeed, when the concentration was small, there was no significant impact on the frequency shift. Conversely, injection of mixture of anti-DCF and a high concentration of DCF (333.2 nM) did not result in any change of frequency, indicating complete inhibition of antibody binding to the surface and absence of non-specific response. A calibration curve for which the frequency shift measured between 0 and 60 min is plotted as a function of the DCF concentration in logarithmic scale is shown in **Figure 4. 5B**. Non-linear regression of data was performed with a four-parameter logistic curve according to the following equation:

$$F = B + \frac{(T - B)}{1 + \left(\frac{IC_{50}}{[DCF]}\right)^{HS}}$$

, where F is the signal response at DCF concentration [DCF], and B (bottom) and T (top) are the asymptotic ends corresponding to the signal at nil and infinite DCF concentrations.

The inflection point of the sigmoid curve ( $IC_{50}$ ) defined as the DCF concentration yielding a 50% signal decrease was  $40 \pm 2.4$  nM ( $12 \pm 0.7$   $\mu\text{g/L}$ ). Other fitting parameters are summed in **Table S4. 4**. The limit of detection (LoD), the limit of quantitation (LoQ) and dynamic range (DR) of the assay were calculated from the calibration curve presented in **Figure S4. 9**.

This calibration curve was produced by normalizing the QCM-D data to blank sample response ( $\Delta F_0$ ). The LoD and LoQ values respectively represent the  $IC_{90}$  and  $IC_{80}$ , which are the DCF concentrations for which the QCM-D signal is 90 and 80 % of the one obtained for the blank sample in a competitive assay. The dynamic range (DR) is defined as the DCF concentration values for which the sensor signal is 20 and 80 % ( $IC_{80}$  and  $IC_{20}$ ) of  $\Delta F/\Delta F(0)$ .

This experiment was also conducted with standard solutions of DCF in PBS (0 – 330 nM) with each sample analyzed in triplicate (*i.e.* three different sensor chips). QCM-D data and the resulting calibration curve from average  $\Delta F$  values are respectively presented in **Figure 4. 5C-D**. The individual calibration curves and fitting parameters are presented in **Figure S4. 10A** and **Table S4. 4**, respectively. An  $IC_{50}$  of  $28.22 \pm 0.49$  nM ( $8.36 \pm 0.15$   $\mu\text{g/L}$ ) was determined by fitting the data with the four-parameter logistic curve. The determined analytical parameters for both assays performed in PBS/EtOH and PBS are summarized in **Table 4. 1**. The LoD was lower in PBS/EtOH while in PBS we obtained a lower LoQ and a DR centered on lower DCF concentrations. Therefore, in what follows PBS will be preferred as buffer for water resources analysis.

**Table 4. 1.** Limit of detection (LoD), limit of quantification (LoQ) and dynamic range (DR) for the competitive assay of DCF in PBS/EtOH and PBS.

	PBS/EtOH	PBS
LoD (nM)	6.9	9.5
LoD ( $\mu\text{g/L}$ )	2.0	2.8
LoQ (nM)	24.4	15.3
LoQ ( $\mu\text{g/L}$ )	7.2	4.5
DR (nM)	24.4 – 56.1	15.3 – 46.1
DR ( $\mu\text{g/L}$ )	7.2 – 16.6	4.5 – 13.6

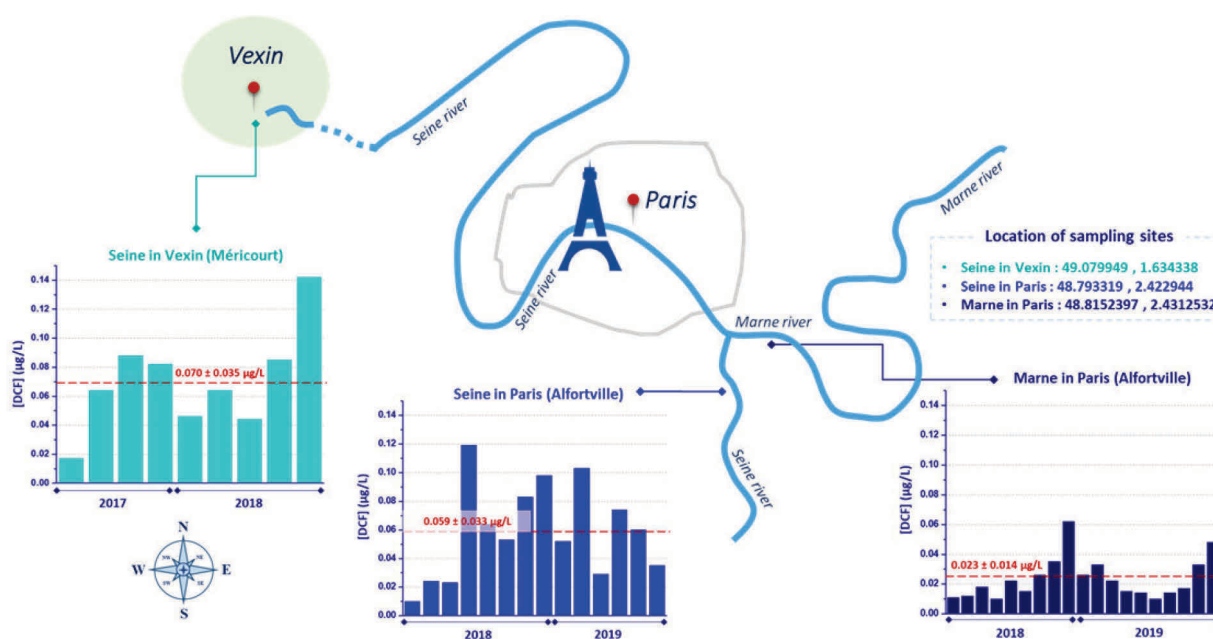
The LoD obtained here are in the same range, even slightly lower, that those obtained by advanced chromatographic methods, HPLC-MS (3  $\mu\text{g/L}$ ).<sup>6</sup>



In addition, the analytical performances of the piezoelectric immunosensor compare favorably with previously reported label-free immunoassays. Steinke *et al.* developed an optical immunoassay, using the same mAb, which presented a detection range in the  $\mu\text{g/L}$  window.<sup>18</sup> Rau *et al.* proposed another optical immunoassay for DCF with a LoD of  $0.2842 \mu\text{g/L}$  and a LoQ of  $0.4933 \mu\text{g/L}$  in buffer.<sup>27</sup> This better sensitivity might be due to the use of aceclofenac instead of DCF as a less competitive immobilized ligand. More detailed information on the analytical performances of biosensors already reported for diclofenac quantification in various media are gathered in **Table S4. 8**.

#### 4.3.5 DCF quantification in surface water samples.

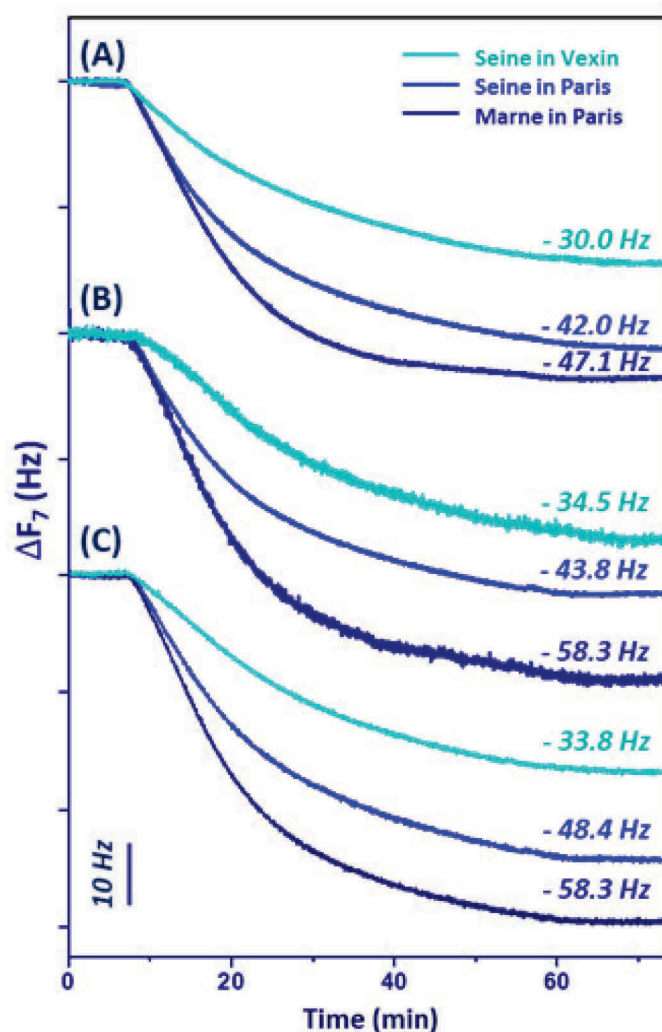
The competitive immunoassay was applied to the quantification of DCF in surface water samples collected in the Seine river at two locations (Paris and Vexin, France) and the Marne river in Paris as presented in **Figure 4. 6**.



**Figure 4. 6.** Sampling sites of surface water collected in the Marne river in Paris and the Seine river in Paris and Vexin; and corresponding DCF concentrations determined by eaufrance agency<sup>38</sup> with average values.

Prior to the analysis, the collected samples were concentrated 100-fold by solid phase extraction (SPE) following a procedure described in the experimental section.

All samples were analyzed in triplicate (*i.e.* three different sensor chips) and the corresponding sensorgrams are presented in **Figure 4. 7** and summarized in **Table 4. 2** with average values. Upon analysis of surface water samples and using the individual calibration curves established from DCF standards in PBS (Figure S10), DCF concentrations of  $23.2 \pm 1.5$  nM ( $6.9 \pm 0.5$   $\mu\text{g/L}$ ) and  $14.4 \pm 0.2$  nM ( $4.27 \pm 0.06$   $\mu\text{g/L}$ ) were calculated for the Seine river in Vexin and Paris, respectively. DCF concentration in Marne water was found below the calculated LoD of the analytical system.



**Figure 4. 7.** QCM-D frequency shifts for the competitive immunoassay of DCF in surface water samples performed by flowing mAb (5 mg/L) in PBS buffer at 25  $\mu\text{L}/\text{min}$  for (A) sensor 1, (B) sensor 2 and (C) sensor 3. QCM-D data are summarized in **Table S4. 8**.



Considering the pre-concentration by 100-fold and assuming no loss during SPE procedure, the DCF concentration in the Seine water would be of  $0.0687 \pm 0.0049 \mu\text{g/L}$  and  $0.0427 \pm 0.0006 \mu\text{g/L}$  for the Seine river in Vexin and Paris, respectively. These values are consistent with data provided by eaufrance agency<sup>38</sup> (Figure 4. 6) and are also lower than the guide value given by ANSES ( $0.4 \mu\text{g/L}$ ).<sup>5</sup> Attempts to assay the same pre-concentrated river samples by RP-HPLC were unsuccessful (Figure S4. 11).

**Table 4. 2.** DCF concentration in three different surface water samples as calculated from the calibration curve established in PBS and shown in Figure S10.

	Seine in Vexin		Seine in Paris		Marne in Paris	
	[DCF] (nM)	[DCF] ( $\mu\text{g/L}$ )	[DCF] (nM)	[DCF] ( $\mu\text{g/L}$ )	[DCF] (nM)	[DCF] ( $\mu\text{g/L}$ )
<i>Sensor 1</i>	23.8	7.1	14.2	4.2	< LoD	< LoD
<i>Sensor 2</i>	21.4	6.3	14.5	4.3	< LoD	< LoD
<i>Sensor 3</i>	24.3	7.2	14.6	4.3	< LoD	< LoD
Average values	$23.2 \pm 1.5$	$6.9 \pm 0.5$	$14.4 \pm 0.2$	$4.27 \pm 0.06$		

## 4.4 Conclusion

In this work, we designed a competitive piezoelectric immunosensor to assay diclofenac in water resources. A sensing layer comprising diclofenac as competitor was built up layer-by-layer by a wet chemistry process on silica-coated quartz sensor chips.

Diclofenac immobilization to the amine-terminated PEG layer was investigated using three different activation strategies and the PyBOP chemistry was selected for further experiments. Binding of a highly affine monoclonal antibody to immobilized diclofenac was investigated by combining, in real time, QCM-D and LSPR.

These measurements allowed to calculate a dissociation constant  $K_D$  of 0.24 nM and an optical mass uptake of 260 ng/cm<sup>2</sup> upon antibody binding, in excellent agreement with the formation of a monolayer of antibodies in a head-on orientation. A hydration percentage of ca. 75% was determined for the antibody layer.

A competitive QCM-D assay was then set up for the detection of diclofenac for which binding of antibody to the DCF-containing sensing layer is inhibited by DCF in solution.

The sensor response expressed as frequency shift  $\Delta F$  was inversely related to the concentration of DCF in solution with a dynamic range of 15 – 46 nM and a limit of detection of 9.5 nM (2.8 µg/L) in PBS.

Finally, this piezoelectric immunosensor was applied to the analysis of surface water samples taken at three locations in the rivers Seine and Marne.

The calculated concentration of DCF in these samples was in good agreement with data published by eaufrance agency which collection requires extremely heavy protocols. These finding pave the way for a rapid and easy to implement assay of small pollutants in river water.

## References

- (1) Bregoli, F.; Acuña, V.; Barceló, D.; Corominas, L.; Ginebreda, A.; Petrovic, M.; Rodríguez-Roda, I.; Sabater, S.; Marcé, R. The fate of pharmaceuticals in freshwaters: a new global model for decision making | IHE Delft Institute for Water Education <https://www.un-ihe.org/news/fate-pharmaceuticals-freshwaters-new-global-model-decision-making> (accessed 2020 -12 -21).
- (2) Vella, K. *Commission Implementing Decision (EU) 2015/495 of 20 March 2015 Establishing a Watch List of Substances for Union-Wide Monitoring in the Field of Water Policy Pursuant to Directive 2008/105/EC of the European Parliament and of the Council (Notified under Document C(2015) 1756) Text with EEA Relevance*; 2015; Vol. 078.
- (3) Sousa, J. C. G.; Ribeiro, A. R.; Barbosa, M. O.; Pereira, M. F. R.; Silva, A. M. T. A Review on Environmental Monitoring of Water Organic Pollutants Identified by EU Guidelines. *J. Hazard. Mater.* **2018**, *344*, 146–162.
- (4) Lonappan, L.; Brar, S. K.; Das, R. K.; Verma, M.; Surampalli, R. Y. Diclofenac and Its Transformation Products: Environmental Occurrence and Toxicity - A Review. *Environ. Int.* **2016**, *96*, 127–138.
- (5) ANSES. Site | Anses - Agence nationale de sécurité sanitaire de l'alimentation, de l'environnement et du travail <https://www.anses.fr/fr/search/site/EAUX2016SA0135?iso1=fr&iso2=en> (accessed 2020 -12 -21).
- (6) Schmidt, S.; Hoffmann, H.; Garbe, L.-A.; Schneider, R. J. Liquid Chromatography–Tandem Mass Spectrometry Detection of Diclofenac and Related Compounds in Water Samples. *J. Chromatogr. A* **2018**, *1538*, 112–116.
- (7) Kafeenah, H. I. S.; Osman, R.; Bakar, N. K. A. Disk Solid-Phase Extraction of Multi-Class Pharmaceutical Residues in Tap Water and Hospital Wastewater, Prior to Ultra-Performance Liquid Chromatographic-Tandem Mass Spectrometry (UPLC-MS/MS) Analyses. *RSC Adv.* **2018**, *8* (70), 40358–40368.
- (8) Raysyan, A.; Moerer, R.; Coesfeld, B.; Eremin, S. A.; Schneider, R. J. Fluorescence Polarization Immunoassay for the Determination of Diclofenac in Wastewater. *Anal. Bioanal. Chem.* **2021**, *413* (4), 999–1007.
- (9) Yang, X.; Wang, Y.; Yang, J.; Sun, Z.; Chu, C.; Yue, Z.; Li, L.; Hu, X. Development of an Immunochromatographic Lateral Flow Strip Test for the Rapid Detection of Diclofenac in Medicinal Wine. *Food Agric. Immunol.* **2020**, *31* (1), 205–216.
- (10) Carl, P.; Sarma, D.; Gregório, B. J. R.; Hoffmann, K.; Lehmann, A.; Rurack, K.; Schneider, R. J. Wash-Free Multiplexed Mix-and-Read Suspension Array Fluorescence Immunoassay for Anthropogenic Markers in Wastewater. *Anal. Chem.* **2019**, *91* (20), 12988–12996.
- (11) Deng, D.; Yang, H.; Liu, C.; Zhao, K.; Li, J.; Deng, A. Ultrasensitive Detection of Diclofenac in Water Samples by a Novel Surface-Enhanced Raman Scattering (SERS)-Based Immunochromatographic Assay Using AgMBA@SiO<sub>2</sub>-Ab as Immunoprobe. *Sensor Actuat. B-Chem.* **2019**, *283*, 563–570.
- (12) Wang, C.; Jiang, T.; Zhao, K.; Deng, A.; Li, J. A Novel Electrochemiluminescent Immunoassay for Diclofenac Using Conductive Polymer Functionalized Graphene Oxide as Labels and Gold Nanorods as Signal Enhancers. *Talanta* **2019**, *193*, 184–191.
- (13) Hlaváček, A.; Peterek, M.; Farka, Z.; Mickert, M. J.; Prechtel, L.; Knopp, D.; Gorris, H. H. Rapid Single-Step Upconversion-Linked Immunosorbent Assay for Diclofenac. *Microchim. Acta* **2017**, *184* (10), 4159–4165.
- (14) Hlaváček, A.; Farka, Z.; Hübner, M.; Horňáková, V.; Němeček, D.; Niessner, R.; Skládal, P.; Knopp, D.; Gorris, H. H. Competitive Upconversion-Linked Immunosorbent Assay for the Sensitive Detection of Diclofenac. *Anal. Chem.* **2016**, *88* (11), 6011–6017.
- (15) Huebner, M.; Weber, E.; Niessner, R.; Boujday, S.; Knopp, D. Rapid Analysis of Diclofenac in Freshwater and Wastewater by a Monoclonal Antibody-Based Highly Sensitive ELISA. *Anal. Bioanal. Chem.* **2015**, *407* (29), 8873–8882.

- (16) Kaewwonglom, N.; Oliver, M.; Cocovi-Solberg, D. J.; Zirngibl, K.; Knopp, D.; Jakmune, J.; Miro, M. Reliable Sensing Platform for Plasmonic Enzyme-Linked Immunosorbent Assays Based on Automatic Flow-Based Methodology. *Anal. Chem.* **2019**, *91* (20), 13260–13267.
- (17) Shi, J.; Xu, M.; Tang, Q.; Zhao, K.; Deng, A.; Li, J. Highly Sensitive Determination of Diclofenac Based on Resin Beads and a Novel Polyclonal Antibody by Using Flow Injection Chemiluminescence Competitive Immunoassay. *Spectrochim. Acta. A. Mol. Biomol. Spectrosc.* **2018**, *191*, 1–7.
- (18) Steinke, N.; Döring, S.; Wuchrer, R.; Kroh, C.; Gerlach, G.; Härtling, T. Plasmonic Sensor for On-Site Detection of Diclofenac Molecules. *Sensor Actuat. B-Chem.* **2019**, *288*, 594–600.
- (19) Kassahun, G. S.; Griveau, S.; Juillard, S.; Champavert, J.; Ringuedé, A.; Bresson, B.; Tran, Y.; Bedioui, F.; Slim, C. Hydrogel Matrix-Grafted Impedimetric Aptasensors for the Detection of Diclofenac. *Langmuir* **2020**, *36* (4), 827–836.
- (20) Shi, T.; Wen, Z.; Ding, L.; Liu, Q.; Guo, Y.; Ding, C.; Wang, K. Visible/near-Infrared Light Response VOPc/Carbon Nitride Nanocomposites: VOPc Sensitizing Carbon Nitride to Improve Photo-to-Current Conversion Efficiency for Fabricating Photoelectrochemical Diclofenac Aptasensor. *Sensor Actuat. B-Chem.* **2019**, *299*, 126834.
- (21) Schirmer, C.; Posseckardt, J.; Kick, A.; Rebatschek, K.; Fichtner, W.; Ostermann, K.; Schuller, A.; Rödel, G.; Mertig, M. Encapsulating Genetically Modified *Saccharomyces Cerevisiae* Cells in a Flow-through Device towards the Detection of Diclofenac in Wastewater. *J. Biotechnol.* **2018**, *284*, 75–83.
- (22) Schirmer, C.; Posseckardt, J.; Schröder, M.; Gläser, M.; Howitz, S.; Scharff, W.; Mertig, M. Portable and Low-Cost Biosensor towards on-Site Detection of Diclofenac in Wastewater. *Talanta* **2019**, *203*, 242–247.
- (23) Guenther, M.; Altenkirch, F.; Ostermann, K.; Rödel, G.; Tobehn-Steinhäuser, I.; Herbst, S.; Görlandt, S.; Gerlach, G. Optical and Impedimetric Study of Genetically Modified Cells for Diclofenac Sensing. *J. Sens. Sens. Syst.* **2019**, *8* (1), 215–222.
- (24) Nguyen, T. T. K.; Vu, T. T.; Anquetin, G.; Tran, H. V.; Reisberg, S.; Noël, V.; Mattana, G.; Nguyen, Q. V.; Dai Lam, T.; Pham, M. C.; Piro, B. Enzyme-Less Electrochemical Displacement Heterogeneous Immunosensor for Diclofenac Detection. *Biosens. Bioelectron.* **2017**, *97*, 246–252.
- (25) Azadbakht, A.; Beirvand, S. Voltammetric Aptamer-Based Switch Probes for Sensing Diclofenac Using a Glassy Carbon Electrode Modified with a Composite Prepared from Gold Nanoparticles, Carbon Nanotubes and Amino-Functionalized Fe<sub>3</sub>O<sub>4</sub> Nanoparticles. *Microchim. Acta* **2017**, *184* (8), 2825–2835.
- (26) Kashefi-Kheyraadi, L.; Mehrgardi, M. A. Design and Construction of a Label Free Aptasensor for Electrochemical Detection of Sodium Diclofenac. *Biosens. Bioelectron.* **2012**, *33* (1), 184–189.
- (27) Rau, S.; Hilbig, U.; Gauglitz, G. Label-Free Optical Biosensor for Detection and Quantification of the Non-Steroidal Anti-Inflammatory Drug Diclofenac in Milk without Any Sample Pretreatment. *Anal. Bioanal. Chem.* **2014**, *406* (14), 3377–3386.
- (28) Steinke, N.; Rio, M.; Wuchrer, R.; Schuster, C.; Ljasenko, E.; Knopp, D.; Gerlach, G.; Härtling, T. Detection of Diclofenac Molecules by Planar and Nanostructured Plasmonic Sensor Substrates. *Sensor Actuat. B-Chem.* **2018**, *254*, 749–754.
- (29) Huebner, M.; Ben Haddada, M.; Méthivier, C.; Niessner, R.; Knopp, D.; Boujday, S. Layer-by-Layer Generation of PEG-Based Regenerable Immunosensing Surfaces for Small-Sized Analytes. *Biosens. Bioelectron.* **2015**, *67*, 334–341.
- (30) Ben Haddada, M.; Huebner, M.; Casale, S.; Knopp, D.; Niessner, R.; Salmain, M.; Boujday, S. Gold Nanoparticles Assembly on Silicon and Gold Surfaces: Mechanism, Stability, and Efficiency in Diclofenac Biosensing. *J. Phys. Chem. C* **2016**, *120* (51), 29302–29311.
- (31) Höök, F.; Rodahl, M.; Brzezinski, P.; Kasemo, B. Energy Dissipation Kinetics for Protein and Antibody–Antigen Adsorption under Shear Oscillation on a Quartz Crystal Microbalance. *Langmuir* **1998**, *14* (4), 729–734.

- (32) Oshannessy, D. J.; Brighamburke, M.; Soneson, K. K.; Hensley, P.; Brooks, I. Determination of Rate and Equilibrium Binding Constants for Macromolecular Interactions Using Surface Plasmon Resonance: Use of Nonlinear Least Squares Analysis Methods. *Anal. Biochem.* **1993**, *212* (2), 457–468.
- (33) Boujday, S.; Bantegnie, A.; Briand, E.; Marnet, P.-G.; Salmain, M.; Pradier, C.-M. In-Depth Investigation of Protein Adsorption on Gold Surfaces: Correlating the Structure and Density to the Efficiency of the Sensing Layer. *J. Phys. Chem. B* **2008**, *112* (21), 6708–6715.
- (34) Zhang, L.; Mazouzi, Y.; Salmain, M.; Liedberg, B.; Boujday, S. Antibody-Gold Nanoparticle Bioconjugates for Biosensors: Synthesis, Characterization and Selected Applications. *Biosens. Bioelectron.* **2020**, *165*, 112370.
- (35) Vörös, J. The Density and Refractive Index of Adsorbing Protein Layers. *Biophys. J.* **2004**, *87* (1), 553–561.
- (36) Ray, S.; Shard, A. G. Quantitative Analysis of Adsorbed Proteins by X-Ray Photoelectron Spectroscopy. *Anal. Chem.* **2011**, *83* (22), 8659–8666.
- (37) Bell, N. C.; Minelli, C.; Shard, A. G. Quantitation of IgG Protein Adsorption to Gold Nanoparticles Using Particle Size Measurement. *Anal. Methods* **2013**, *5* (18), 4591.
- (38) Naïades. Recherche | Naïades <http://www.naiades.eaufrance.fr/acces-donnees/#/physicochimie/resultats?debut=16-11-2017&fin=16-11-2020&parametres=5349> (accessed 2020 -12 -21).

## 4.5 Supporting Information

### 4.5.1 Experimental section

#### 4.5.1.1 Materials

3-Glycidyloxypropyltrimethoxysilane (GOPTS), Poly(ethylene glycol) bis (amine) (DAPEG) with a molecular mass of 2000 g/mol, Diclofenac sodium salt (DCF), N-(3-Dimethylaminopropyl)-N'-ethylcarbodiimide hydrochloride (EDC), N-hydroxysuccinimide (NHS), Benzotriazole-1-yl-oxy-tris-pyrrolidino-phosphonium hexafluorophosphate (PyBOP), N,N,N',N'-Tetramethyl-O-(N-succinimidyl)uronium tetrafluoroborate (TSTU), N,N-Diisopropylethylamine (DIEA) and Phosphate-buffered saline (PBS) tablets were purchased from Sigma-Aldrich (France). Sodium dodecyl sulfate (SDS) was purchased from Thermo Fischer Scientific (France). Hellmanex II was purchased from Hellma Analytics (Mülheim, Germany). All solvents were reagent-grade and were used without any further purification. The monoclonal anti-DCF antibody mAb12G5 was prepared in-house.<sup>1</sup>

Silicon wafers <111> were purchased from Sigma-Aldrich (France) and cut into 1x1 cm<sup>2</sup> substrates. For QCM-D measurements, AT-cut quartz crystals coated with a thin SiO<sub>2</sub> film (thickness ~ 50 nm) were purchased from Quantum Design (Les Ulis, France).

For combined QCM-D and LSPR measurements, gold nanostructured AT-cut quartz coated with a thin SiO<sub>2</sub> layer (thickness ~ 5-10 nm) were purchased from Insplorion AB (Gothenburg, Sweden). All solutions were prepared using purified Milli-Q water (18 MΩ, Millipore, France).

#### 4.5.1.2 Surface functionalization

##### 4.5.1.2.1 Cleaning and oxidation

First, all substrates were prepared following a revised procedure.<sup>2</sup> Silicon wafers and quartz sensors were cleaned in a 2% Hellmanex solution during one hour with sonication, then under mild shaking for 12 h and finally during one hour with sonication. After rinsing with Milli-Q water, the substrates were dried under nitrogen flow. Etching step was performed for 1 h in a mixture of 37% hydrochloric acid and methanol (v/v = 1), followed with concentrated sulfuric acid treatment for 4 x 15 min.

Then, the substrates were extensively rinsed with Milli-Q water and kept in Milli-Q water for at least 72 h. Note that sonication is prohibited during the whole functionalization process for nanostructured sensors in order to preserve nanostructures integrity.

#### 4.5.1.2.2 Silanization with GOPTS

GOPTS (20  $\mu$ L) was spread on a dry oxidized substrate and covered with another substrate in a “sandwich” format. This sandwich was incubated for 3 h. Afterwards, substrates were separated and rinsed successively in ethanol, methanol and ethanol for 5 min with sonication. The surfaces were then dried under nitrogen flow for 5 min, then at 85 °C for 7 min.

#### 4.5.1.2.3 DAPEG functionalization

DAPEG (20 mg) was weighted in a 1.5 mL Eppendorf tube which was then placed in a water bath at 75 °C for 15 min. In parallel, substrates to be functionalized were heated to 98 °C. Molten DAPEG (20  $\mu$ L) was spotted on one substrate onto which another substrate was placed to form a sandwich which was heated to 98 °C for 12 h. The sandwich was separated by dipping in water, then the substrates were thoroughly rinsed twice under sonication in water during 15 min and dried under nitrogen flow.

#### 4.5.1.2.4 Grafting of diclofenac

A solution of diclofenac sodium salt (10 mM) was activated in dry dimethylformamide (DMF) during 75 min under mild shaking at room temperature using three different coupling reagents, by adding either: (i) 1.2 eq. EDC and 2.4 eq. NHS, (ii) 1 eq. TSTU and 1 eq. DIEA, (iii) 1 eq. PyBOP and 1 eq. DIEA. Then, the substrates were immersed into the activated diclofenac solution. They were shaken over night at room temperature and washed in Milli-Q water for 3 x 15 min prior to drying under nitrogen flow and storage in a desiccator.



### 4.5.1.3 Techniques

#### 4.5.1.3.1 Quartz Crystal Microbalance with dissipation (QCM-D)

Piezoelectric measurements were performed on AT-cut quartz silica-coated crystals with nominal frequency of 5 MHz (Quantum Design, France). The QCM-D (E4 model, Biolin Scientific, Sweden) was operated in the flow-through mode at 20 °C. The flow rate was adjusted to 25 or 50  $\mu\text{L}/\text{min}$  by using a peristaltic pump. Signal stabilization was carried out with PBS or degassed PBS/EtOH 9:1 (v/v). The regeneration buffer was a solution of 2 wt% SDS in water/EtOH 9:1 (v/v) adjusted to pH=2 (HCl). For the QCM-D data interpretation, the dissipation should be considered. Provided that no dissipation by energy exchange occurs with the liquid, the adsorbed layer can be considered as rigid. According to Sauerbrey equation, the measured frequency shifts are proportional to mass uptake:

$$\Delta F = -\frac{N * \Delta m}{C_f}$$

,with the mass sensitivity constant ( $C_f = 17.7 \text{ ng}/\text{cm}^2 \text{ Hz}^{-1}$  at  $f=5 \text{ MHz}$ ) and the overtone number ( $N=7$ ).

#### 4.5.1.3.2 Combined QCM-D & NanoPlasmonic (NPS)

The combined QCM-D and NPS measurements were carried out using the Q-Sense E1 module with Q-Sense sapphire window module (Biolin Scientific, Sweden) coupled with the Insplorion Acoulyte module (Insplorion AB, Sweden). In this setup, an optical fiber connected to the Insplorion X-Nano optics unit (Insplorion AB, Sweden) is placed on top of QCM-D module which enables illumination in reflection mode. Measurements were performed on Acoulyte quartz crystal sensors which are QCM-D sensors on which silica-coated gold nanodisks (100 nm in diameter and 20 nm in height) are randomly distributed. Light interaction with gold nanodisks leads to a collective oscillation of conduction electrons known as LSPR resulting in an intense absorption band ( $\lambda_{\text{max}}$ ) around 700 nm. At the surface vicinity, refractive index changes will lead to LSPR peak position shifts, referred herein as  $\Delta\lambda_{\text{max}}$ , allowing to monitor biomolecular interactions in real time. Analysis of frequency and dissipation shifts was carried out using the QTools software, version 3.1.33.567 (Biolin Scientific, Sweden). Analysis of LSPR signals was performed using Insplorer software, version 1.3.1 (Insplorion AB, Sweden).



#### 4.5.1.3.3 Attenuated Total Reflection Infrared (ATR-IR)

ATR-IR spectra were recorded on a Tensor 27 FT-IR spectrometer (Bruker) equipped with a VariGATR™ grazing angle accessory (Harrick scientific). Each spectrum results from the accumulation of 64 scans at  $4\text{ cm}^{-1}$  spectral resolution.

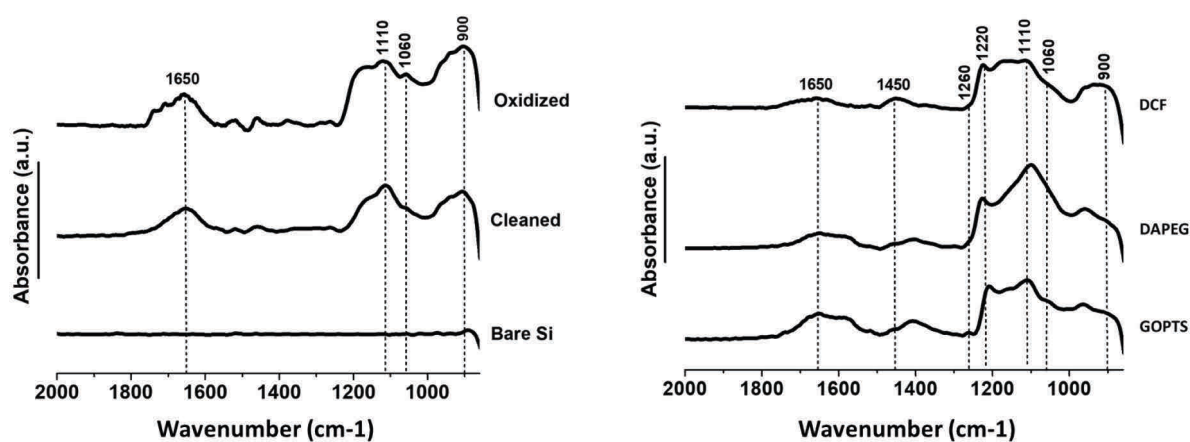
#### 4.5.1.3.4 Water Contact Angle (WCA)

Static water contact angles (WCA) were measured at room temperature using the sessile drop method and image analysis of the drop profile. The instrument, which uses a CCD camera and an image analysis processor, was purchased from Krüss (Germany). The water (Milli-Q) droplet volume was  $1\ \mu\text{L}$  and the contact angle ( $\theta$ ) was measured 5 sec after the drop was deposited on the sample. For each sample, the reported value is the average of the results obtained on three droplets and the overall accuracy in the measurements was better than  $\pm 3^\circ$ .

#### 4.5.1.3.5 X-ray Photoelectron Spectroscopy (XPS)

XPS analysis were performed on a Scienta Omicron Argus X-ray photoelectron spectrometer, using a monochromated  $\text{AlK}\alpha$  ( $h\nu= 1486.6\text{ eV}$ ) radiation source having a 280 W electron beam power. The emission of photoelectrons from the sample was analyzed at a take-off angle of  $45^\circ$  under ultra-high vacuum conditions ( $1 \times 10^{-9}\text{ Pa}$ ). XPS spectra were collected at pass energy of 100 eV for the survey scan and 20 eV for the  $\text{C}_{1s}$ ,  $\text{O}_{1s}$ ,  $\text{N}_{1s}$ ,  $\text{Cl}_{2p}$ ,  $\text{Si}_{2p}$  core XPS levels. The peak areas were determined after subtraction of a Shirley background. The spectra were fitted using Casa XPS software and applying a Gaussian/Lorentzian ratio (G/L) equal to 70:30 and binding energies were calibrated against the  $\text{Si}_{2p_{3/2}}$  at 99.4 eV.

#### 4.5.1.4 Results and discussion

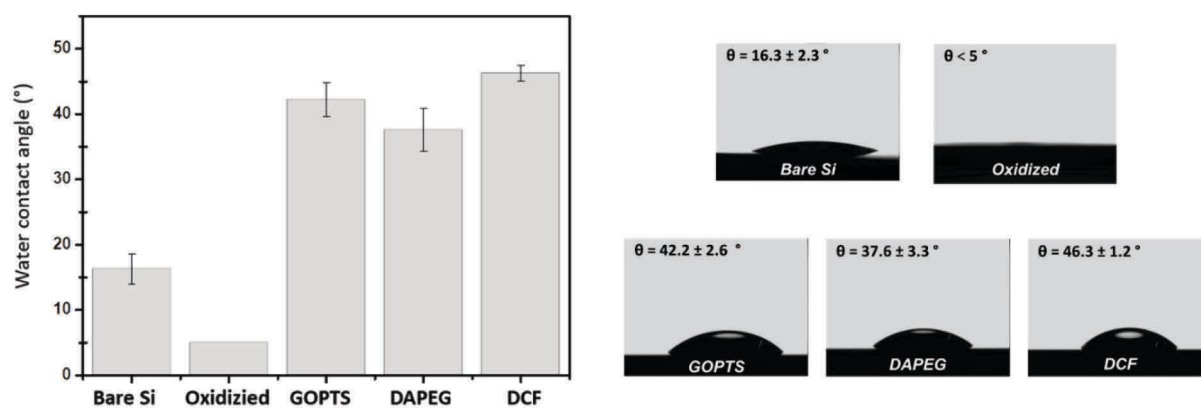


**Figure S4. 1.** Baseline corrected ATR-IR spectra of Si substrates before and after cleaning and oxidation (left panel) and after each functionalization steps (right panel)

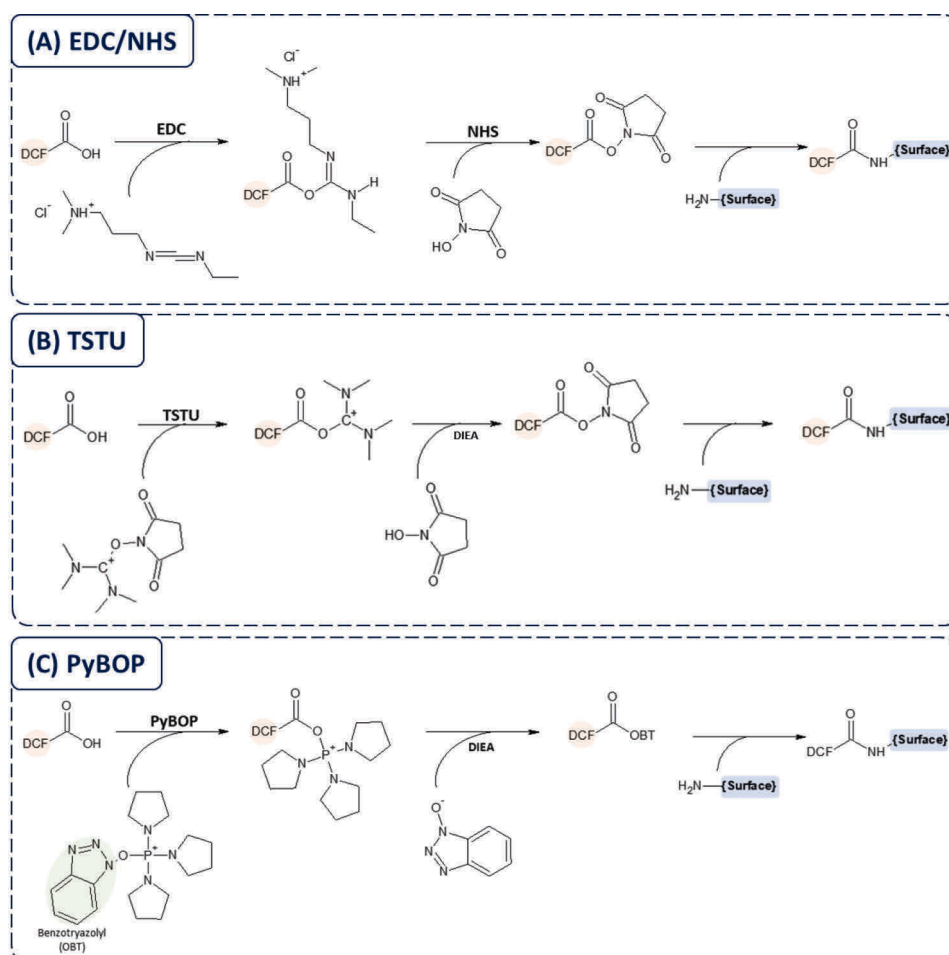
**Table S4. 1.** ATR-IR bands and assignments for each functionalization step. Corresponding baseline corrected ATR-IR spectra are presented in **Figure S4. 1**.

ATR-IR peaks (cm <sup>-1</sup> )					Assignment
<i>Cleaned Si</i>	<i>Oxidized Si</i>	<i>GOPTS</i>	<i>DAPEG</i>	<i>DCF</i>	
1650	1650	1650	1650	1650	H <sub>2</sub> O / NH <sub>2</sub> (DAPEG)
-	-	1450	1450	1450	CH <sub>2</sub>
-	-	1260	-	-	Epoxy
1220	1220	1220	1220	1220	Si-O-Si
-	-	1110	1110	1110	C-O-C
1110	1110	1110	1110	1110	Si-O-Si
1060	1060	1060	1060	1060	Si-O-Si
900	900	900	900	900	Si-OH

## Chapter 4. Design and analytical performances of a diclofenac biosensor for water resources monitoring



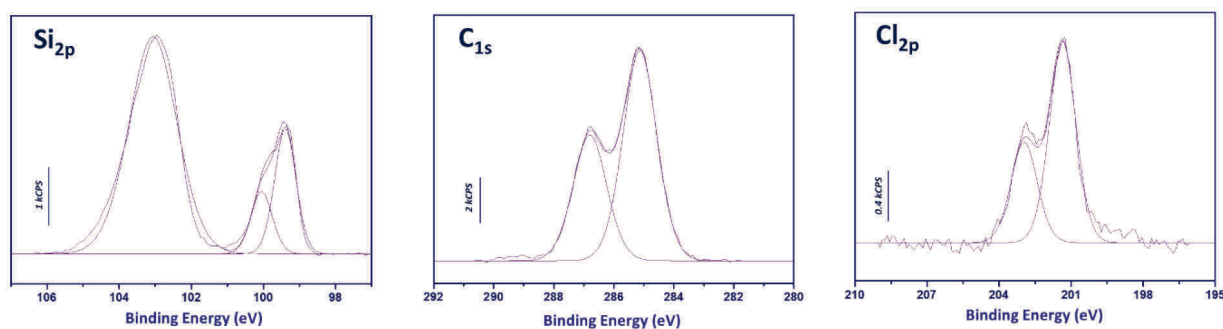
**Figure S4. 2.** Water contact angle (WCA) values and images for the different cleaning, oxidation and functionalization steps.



**Figure S4. 3.** Coupling mechanisms of DCF to the DAPEG surface via (A) EDC/NHS, (B) TSTU and (C) PyBOP chemistries. DIEA, diisopropylethylamine

**Table S4. 2.** XPS atomic composition of the Si substrates after DAPEG functionalization and DCF grafting *via* EDC/NHS, TSTU and PyBOP strategies

Binding Energy (eV)	Assignment	Peak Area (At. %)			
		DAPEG	DCF <i>via</i> EDC/NHS	DCF <i>via</i> TSTU	DCF <i>via</i> PyBOP
532.9	<b>O 1s</b>	16.64	16.19	16.90	9.38
	<b>N 1s</b>	0.27	0.45	0.46	0.50
400.1	NH/NH <sub>2</sub>	0.14	0.35	0.38	0.31
402.5	NH <sub>3</sub> <sup>+</sup>	0.13	0.10	0.08	0.13
404.6	N-O	-	-	-	0.06
	<b>C 1s</b>	60.48	61.56	59.25	77.76
288.4	C1s	2.75	2.48	2.67	0.91
286.9	C-O/C-N	38.62	50.61	47.79	28.71
285.2	C-C/C-H	19.11	8.47	8.79	48.14
	<b>Cl 2p</b>	-	-	-	0.48
201.4	Cl 2p <sub>3/2</sub>				0.30
203	Cl 2p <sub>1/2</sub>				0.18
	<b>Si 2p</b>	22.61	21.80	23.39	11.88
103.3	SiO <sub>2</sub>	8.60	7.09	7.47	8.62
100	Si 2p <sub>1/2</sub>	5.40	5.59	5.63	1.23
99.4	Si 2p <sub>3/2</sub>	8.61	9.12	10.29	2.03



**Figure S4. 4.** Si<sub>2p</sub>, C<sub>1s</sub> and Cl<sub>2p</sub> XPS spectra of Si substrates after DCF immobilization using PyBOP strategy.

Thicknesses of the oxide and organic layers were estimated by means of the XPS peak intensities of the spectra presented in Figure S4. In this approach, the oxide layer thickness ( $d_{oxide}$ ) was first determined using the following equation:

$$d_{oxide} = \lambda_{Si2p}^{SiO_2} \cos\theta \cdot \ln \left( 1 + \frac{I_{SiO_2} M_{SiO_2} \rho_{Si} \lambda_{Si2p}^{Si}}{I_{Si} M_{Si} \rho_{SiO_2} \lambda_{Si2p}^{SiO_2}} \right)$$

Subsequently, the organic layer thickness was determined from the ratio of intensities between the  $C_{1s}$  and  $Si_{2p}$  signals. The input in thickness from the organic layer was approximated to be the one of DAPEG due to its size in comparison to those of GOPTS and DCF.

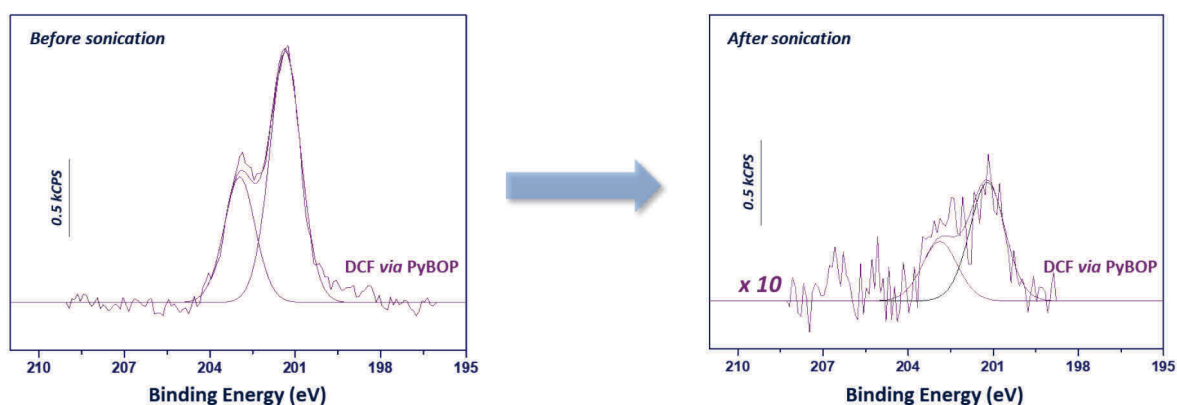
$$\frac{I_{C1s(287\text{ eV})}}{I_{Si2p(100\text{ eV})}} = \frac{44 \frac{\rho_{DAPEG}}{M_{DAPEG}} \sigma_{C1s} \lambda_{C1s}^{org} \left[ 1 - \exp\left(-\frac{d_{org}}{\lambda_{C1s}^{org} \sin\theta}\right) \right]}{\frac{\rho_{Si}}{M_{Si}} \sigma_{Si2p} \lambda_{Si2p}^{Si} \exp\left(-\frac{d_{org}}{\lambda_{Si2p}^{org} \sin\theta}\right) \exp\left(-\frac{d_{SiO_2}}{\lambda_{Si2p}^{SiO_2} \sin\theta}\right)}$$

Then, the number of chlorines was determined, considering the attenuation of its signal through the substrate, oxide and organic layers. Note that, because the DCF molecule carries two chlorine atoms, the chlorine coverage should be divided by a factor two in order to calculate surface coverage.

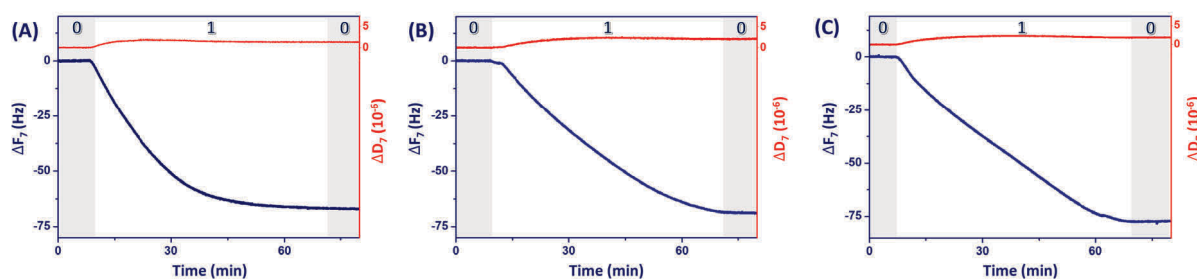
$$N_{Cl}(nm^{-2}) = \frac{I_{Cl2p} \rho_{Si} \sigma_{Si2p} \lambda_{Si2p}^{Si} \sin\theta \cdot \exp\left(-\frac{d_{org}}{\lambda_{Si2p}^{org} \sin\theta}\right) \exp\left(-\frac{d_{SiO_2}}{\lambda_{Si2p}^{SiO_2} \sin\theta}\right)}{I_{Si2p(100\text{ eV})} M_{Si} \sigma_{Cl2p}}$$

In these equations,  $d$  is the layer thickness of either the oxide layer ( $d_{oxide}$ ) or the organic layer ( $d_{org}$ ) and  $\theta$  is the photoelectron collection angle ( $45^\circ$ ). The Scofield photoionization cross sections  $\sigma$  are 1 for  $C_{1s}$ , 0.682 for  $Si_{2p}$  and 1.98 for  $Cl_{2p}$ .<sup>3</sup> The electron inelastic mean free paths  $\lambda$  were calculated using the Quases program based on the TPP2M formula, with  $\lambda_{C1s}^{org} = 3.3$  nm,  $\lambda_{Si2p}^{org} = 3.7$  nm and  $\lambda_{Si2p}^{Si} = 3.1$  nm.<sup>4</sup>

## Chapter 4. Design and analytical performances of a diclofenac biosensor for water resources monitoring



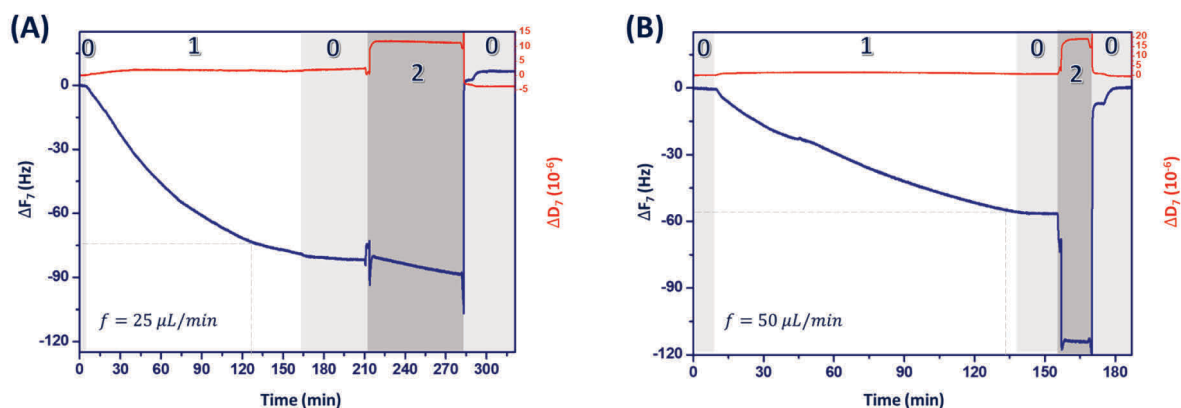
**Figure S4. 5.**  $\text{Cl}_{2p}$  XPS spectra of Si substrates after DCF functionalization *via* PyBOP strategy, before (left) and after (right) sonication.



**Figure S4. 6.** QCM-D frequency and dissipation shifts upon injection of mAb solution (5 mg/L) at 25  $\mu\text{L}/\text{min}$  on DCF-modified quartz sensor using (A) PyBOP, (B) EDC/NHS and (C) TSTU strategies. (0) running buffer, (1) mAb adsorption.

**Table S4. 3.** Fitting parameters obtained with GraphPad Prism software for the determination of the dissociation constant ( $K_D$ ) between DCF and mAb presented in **Figure 4. 3D**.

$k_{\text{off}} \times 10^{-4} \text{ (min}^{-1}\text{)}$	$k_{\text{on}} \times 10^6 \text{ (M}^{-1}\cdot\text{min}^{-1}\text{)}$	$\Delta F_{\text{max}} \text{ (Hz)}$	$K_D \text{ (nM)}$	$R^2$
$3.5 \pm 0.35$	$1.541 \pm 0.003$	$75.17 \pm 0.08$	0.23	0.994



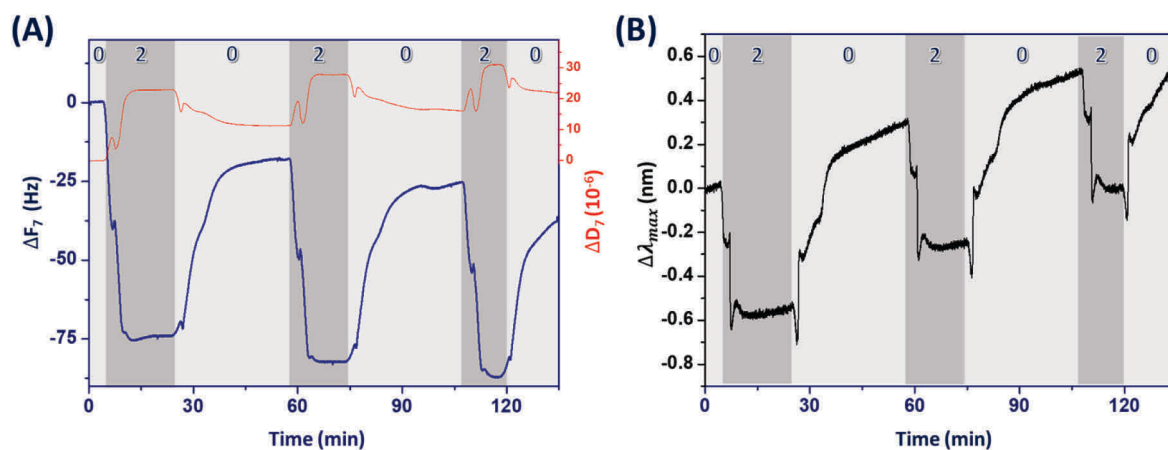
**Figure S4. 7.** QCM-D frequency and dissipation shifts for mAb binding (1 mg/L) to DCF-modified quartz sensor at flow rates of (A) 25  $\mu\text{L}/\text{min}$  and (B) 50  $\mu\text{L}/\text{min}$ . (0) running buffer, (1) mAb adsorption (2) regeneration.

The optical mass  $m_{LSPR}$  was calculated using the following equation adapted from the literature<sup>5,6</sup>:

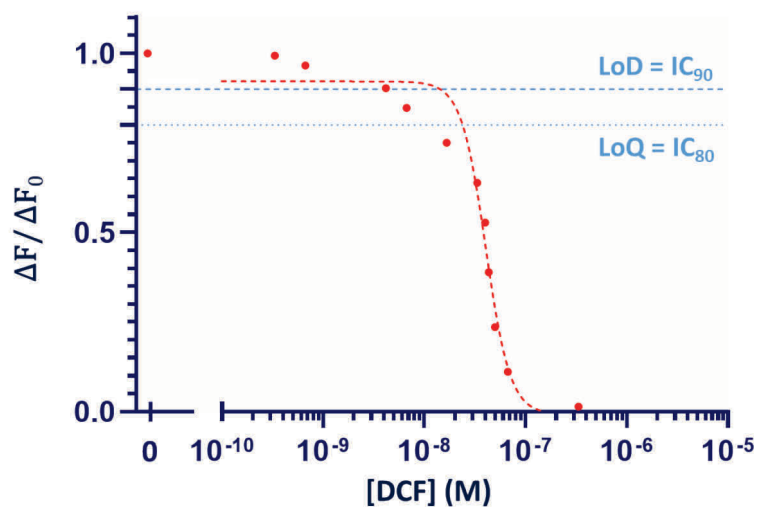
$$m_{LSPR} = d_i \frac{\Delta\lambda_{NPS}}{S_0(e^{-2d_{i-1}/L_z} - e^{-2(d_{i-1}+d_i)/L_z})dn_i/d_c}$$

where  $\Delta\lambda_{NPS}$  is the measured LSPR shift,  $dn_i/d_c$  is the refractive index increment for proteins,  $S_0$  the sensitivity of the substrate and  $d_i$  the thickness of the sample layer determined from QCM-D data and  $d_{i-1}$  is the thickness of the starting layer, *i.e.* organic layer, and was approximated to nil. The refractive index of the flowing solution (PBS/EtOH 9/1) was approximated to be the one of an aqueous PBS solution ( $n = 1.33$ )<sup>7</sup> and the refractive index increment was taken as an average value for protein ( $0.185 \text{ cm}^3/\text{g}$ )<sup>8,9</sup>.

The gold nanostructured sensors are coated with a  $\text{Si}_3\text{N}_4$  layer, which is subsequently oxidized and displays a LSPR sensitivity ( $S_0$ ) of 60 nm/RIU and an evanescent field decay length ( $L_z$ ) of 30 nm (data from the sensor manufacturer).

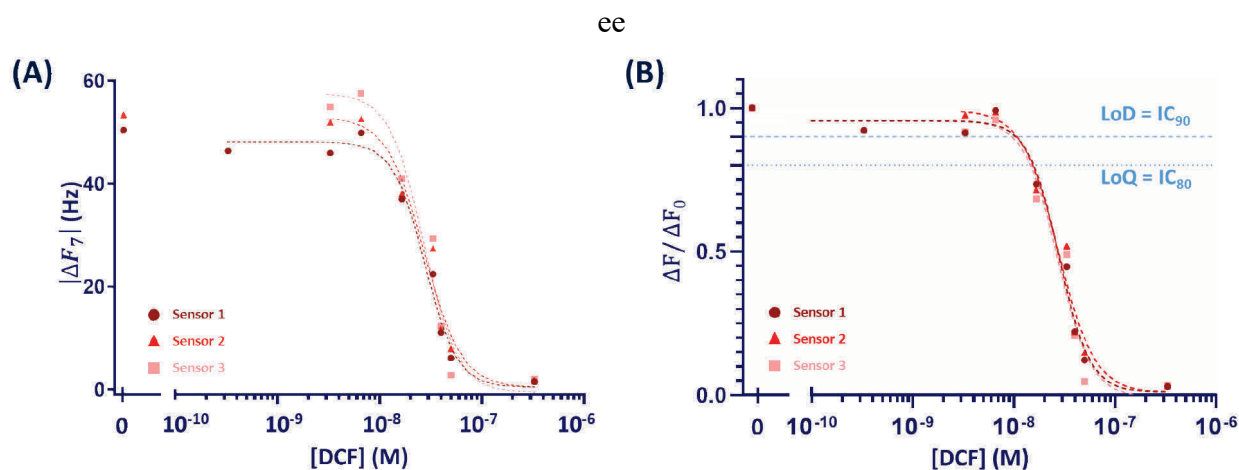


**Figure S4. 8.** Impact of the regeneration buffer on a DCF-DAPEG modified nanostructured quartz sensor at a flow rate of 25  $\mu\text{L}/\text{min}$ : (A) QCM-D frequency and dissipation shifts and (B) LSPR peak shift, simultaneously recorded on the same substrate. (0) running buffer and (2) regeneration.



**Figure S4. 9.** Calibration curve for the competitive immunoassay of DCF in PBS/EtOH with QCM-D data normalized to blank sample ( $\Delta F_0$ ), corresponding to data presented in Figure 4. 5B.





**Figure S4. 10.** (A) QCM-D calibration curves for the competitive immunoassay of DCF in PBS at 25  $\mu\text{L}/\text{min}$  and (B) the corresponding data normalized to blank sample ( $\Delta F_0$ ).

**Table S4. 4.** Fitting parameters obtained with GraphPad Prism software for the indirect competitive assay of DCF in PBS/EtOH and PBS respectively presented in **Figure 4. 5B** and **Figure S4. 9A**.

PBS/EtOH					
	Bottom (Hz)	Top (Hz)	$\text{IC}_{50}$ (nM)	Hill slope ( $\text{Hz}\cdot\text{M}^{-1}$ )	$\text{R}^2$
	0.04243	64.85	$40 \pm 2.4$	-4.005	0.969
PBS					
Sensor	Bottom (Hz)	Top (Hz)	$\text{IC}_{50}$ (nM)	Hill slope ( $\text{Hz}\cdot\text{M}^{-1}$ )	$\text{R}^2$
1	0.510	47.21	28.53	-2.965	0.985
2	0.468	52.57	27.66	-2.460	0.971
3	-0.5449	55.55	28.48	-2.880	0.957
		Average	$28.22 \pm 0.49$		

**Table S4. 5.** IC90 or limit of detection (LoD), IC80 or limit of quantification (LoQ) and IC20 obtained for the indirect competitive assay of DCF in PBS/EtOH and in PBS. Corresponding calibration curves are respectively presented in **Figure S4. 8** and **Figure S4. 9B**.

<b>PBS/EtOH</b>							
	LoD (nM)	LoD ( $\mu\text{g/L}$ )	LoQ (nM)	LoQ ( $\mu\text{g/L}$ )	IC <sub>20</sub> (nM)	IC <sub>20</sub> ( $\mu\text{g/L}$ )	$-\Delta F_0$ (Hz)
	6.86	2.03	24.44	7.24	56.10	16.61	72.0
<b>PBS</b>							
Sensor	LoD (nM)	LoD ( $\mu\text{g/L}$ )	LoQ (nM)	LoQ ( $\mu\text{g/L}$ )	IC <sub>20</sub> (nM)	IC <sub>20</sub> ( $\mu\text{g/L}$ )	$-\Delta F_0$ (Hz)
1	9.73	2.88	15.79	4.68	45.07	13.35	50.4
2	10.64	3.15	15.36	4.55	49.24	14.58	53.4
3	8.10	2.40	14.86	4.40	43.84	12.98	60.1
Average	$9.49 \pm 1.29$	$2.81 \pm 0.38$	$15.34 \pm 0.46$	$4.54 \pm 0.14$	$46.05 \pm 2.83$	$13.64 \pm 0.84$	

**Table S4. 6.** Summarized QCM-D data for the competitive immunoassay of DCF in PBS/EtOH and PBS. Mass uptakes were calculated using the Sauerbrey equation.

PBS / EtOH			
[DCF] (nM)	$-\Delta F_7$ (Hz)	$\Delta D_7$ ( $10^{-6}$ )	$\Delta m$ (ng/cm <sup>2</sup> )
0	72	1.3	1274
0.33	71.5	0.7	1266
0.66	69.5	0.8	1230
3.33	68.5	0.7	1213
4.2	65	0.5	1151
6.6	61	0.4	1080
16.6	54	0.4	956
33.3	46	1.3	814
40	38	1.3	673
43.3	28	1.3	496
50	17	0.5	301
66.6	12	0.4	212
333.2	1	< 0.1	17.7
PBS			
[DCF] (nM)	$-\Delta F_7$ (Hz)	$\Delta D_7$ ( $10^{-6}$ )	$\Delta m$ (ng/cm <sup>2</sup> )
0	50.4	1.7	892
0.33	46.4	1.2	821
3.3	46	1.5	814
6.6	49.9	1.4	883
16.6	37.7	1.1	667
33.3	22.5	1.5	398
40	11.1	0.8	197
50	6.1	0.9	108
330	1.5	0.4	27.6

**Table S4. 7.** Summarized QCM-D data for the competitive immunoassay of DCF in Seine river in Paris and Vexin and for the Marne river in Paris. Mass uptakes were calculated using the Sauerbrey equation.

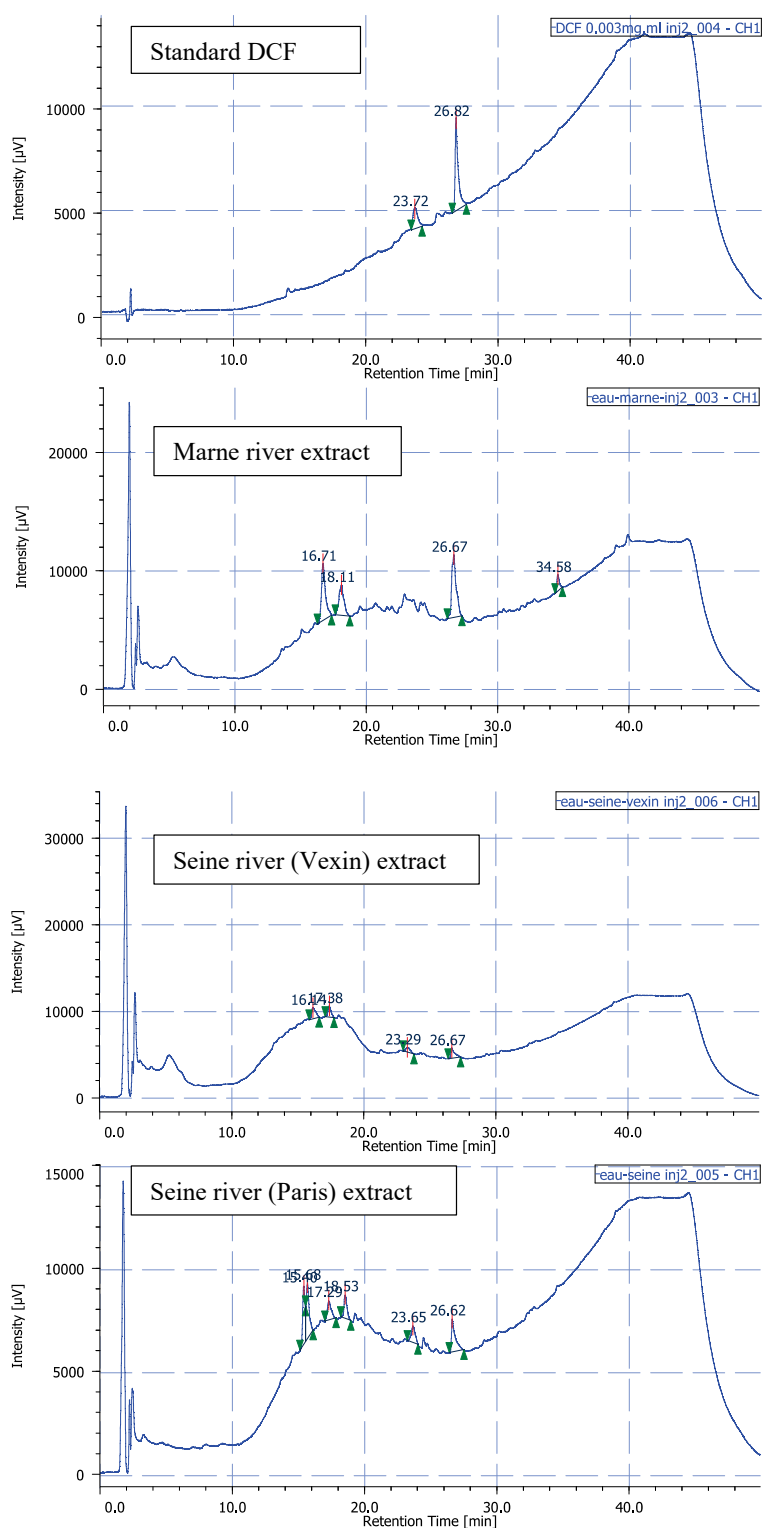
Seine in Vexin			
Sensor	$-\Delta F_7$ (Hz)	$\Delta D_7$ ( $10^{-6}$ )	$\Delta m$ (ng/cm <sup>2</sup> )
1	30.0	1.8	531
2	34.5	4.5	611
3	33.8	2.4	598
Seine in Paris			
Sensor	$-\Delta F_7$ (Hz)	$\Delta D_7$ ( $10^{-6}$ )	$\Delta m$ (ng/cm <sup>2</sup> )
1	42.0	2.6	743
2	43.8	2.7	775
3	48.4	3.2	857
Marne in Paris			
Sensor	$-\Delta F_7$ (Hz)	$\Delta D_7$ ( $10^{-6}$ )	$\Delta m$ (ng/cm <sup>2</sup> )
1	47.1	2.1	834
2	58.3	5.5	1032
3	58.7	3.2	1039

**Table S4. 8.** Analytical performances of label-free biosensors for determination of DCF in environmental and food samples

Transducer	Bioreceptor	Detection	Sample type	Sample preparation	Dynamic range	LoD	Ref.
Electrochemical	pAb <sup>1</sup>	Square wave voltammetry	tap water	no	0.025 – 25 ng/L	0.006 ng/L	10
Electrochemical	pAb	Electrochemiluminescence	tap water, lake water, wastewater	membrane filtration	0.001-1000 µg/L	0.3 ng/L	11–13
Optical	pAb	Reflectometric interference spectroscopy (RIfS)	milk	dilution with buffer	0.4 – 2.2 µg/L	0.112 µg/L	14
Optical	mAb <sup>2</sup>	plasmonic resonance	buffer	no	1 – 10 µg/l	-	15
Optical	genetically engineered yeast cells	green fluorescent protein	buffer	no	2.96 – 14.8 µg/L	-	16
Piezoelectric	mAb	quartz crystal microbalance (QCM-D)	surface water	membrane filtration followed by solid phase extraction and dilution with buffer	4.4 – 13.6 µg/L	2.8 µg/L	this work

<sup>1</sup>polyclonal anti-diclofenac antibody; <sup>2</sup>monoclonal anti-diclofenac antibody.

## Chapter 4. Design and analytical performances of a diclofenac biosensor for water resources monitoring



**Figure S4. 11.** RP-HPLC analysis of river water sample extracts. Analysis conditions: Macherey-Nagel Nucleodur C18 HD column (4.6 x 150 mm, 5 μm). Mobile phase: A: 0.1% TFA in H<sub>2</sub>O; B: 0.08% TFA in MeCN; flowrate = 1 mL/min; Elution conditions: 30 to 90% B in 30 min then 90% B for 5 min then back to initial conditions for 5 min. Injection volume: 20 μL. Detection: 254 nm.

## References

- (1) Huebner, M.; Weber, E.; Niessner, R.; Boujday, S.; Knopp, D. Rapid Analysis of Diclofenac in Freshwater and Wastewater by a Monoclonal Antibody-Based Highly Sensitive ELISA. *Anal. Bioanal. Chem.* **2015**, *407* (29), 8873–8882.
- (2) Huebner, M.; Ben Haddada, M.; Méthivier, C.; Niessner, R.; Knopp, D.; Boujday, S. Layer-by-Layer Generation of PEG-Based Regenerable Immunosensing Surfaces for Small-Sized Analytes. *Biosens. Bioelectron.* **2015**, *67*, 334–341.
- (3) Scofield, J. H. Hartree-Slater Subshell Photoionization Cross-Sections at 1254 and 1487 eV. *J. Electron Spectrosc. Relat. Phenom.* **1976**, *8* (2), 129–137.
- (4) Tanuma, S.; Powell, C. J.; Penn, D. R. Calculations of Electron Inelastic Mean Free Paths. V. Data for 14 Organic Compounds over the 50–2000 eV Range. *Surf. Interface Anal.* **1993**, *21* (3), 165–176.
- (5) Jonsson, M. P.; Jönsson, P.; Höök, F. Simultaneous Nanoplasmonic and Quartz Crystal Microbalance Sensing: Analysis of Biomolecular Conformational Changes and Quantification of the Bound Molecular Mass. *Anal. Chem.* **2008**, *80* (21), 7988–7995.
- (6) Ferhan, A. R.; Jackman, J. A.; Cho, N.-J. Integration of Quartz Crystal Microbalance-Dissipation and Reflection-Mode Localized Surface Plasmon Resonance Sensors for Biomacromolecular Interaction Analysis. *Anal. Chem.* **2016**, *88* (24), 12524–12531.
- (7) Hoang, V. T.; Stepniewski, G.; Czarnecka, K. H.; Kasztelan, R.; Long, V. C.; Xuan, K. D.; Shao, L.; Śmietana, M.; Buczyński, R. Optical Properties of Buffers and Cell Culture Media for Optofluidic and Sensing Applications. *Appl. Sci.* **2019**, *9* (6), 1145.
- (8) Theisen, A.; Johann, C.; Deacon, M. . . P.; Harding, S. . . E. *Refractive Increment Data-Book for Polymer and Biomolecular Scientists*; Nottingham University Press: Nottingham, 2000.
- (9) Vörös, J. The Density and Refractive Index of Adsorbing Protein Layers. *Biophys. J.* **2004**, *87* (1), 553–561.
- (10) Nguyen, T. T. K.; Vu, T. T.; Anquetin, G.; Tran, H. V.; Reisberg, S.; Noel, V.; Mattana, G.; Nguyen, Q. V.; Lam, T. D.; Pham, M. C.; Piro, B. Enzyme-Less Electrochemical Displacement Heterogeneous Immunosensor for Diclofenac Detection. *Biosens. Bioelectron.* **2017**, *97*, 246–252.
- (11) Wang, C.; Jiang, T.; Zhao, K.; Deng, A.; Li, J. A Novel Electrochemiluminescent Immunoassay for Diclofenac Using Conductive Polymer Functionalized Graphene Oxide as Labels and Gold Nanorods as Signal Enhancers. *Talanta* **2019**, *193*, 184–191.
- (12) Chen, W.; Zhu, Q.; Tang, Q.; Zhao, K.; Deng, A.; Li, J. Ultrasensitive Detection of Diclofenac Based on Electrochemiluminescent Immunosensor with Multiple Signal Amplification Strategy of Palladium Attached Graphene Oxide as Bioprobes and Ceria Doped Zinc Oxide as Substrates. *Sensor Actuat. B-Chem.* **2018**, *268*, 411–420.
- (13) Hu, L.; Zheng, J.; Zhao, K.; Deng, A.; Li, J. An Ultrasensitive Electrochemiluminescent Immunosensor Based on Graphene Oxide Coupled Graphite-like Carbon Nitride and Multiwalled Carbon Nanotubes-Gold for the Detection of Diclofenac. *Biosens. Bioelectron.* **2018**, *101*, 260–267.
- (14) Rau, S.; Hilbig, U.; Gauglitz, G. Label-Free Optical Biosensor for Detection and Quantification of the Non-Steroidal Anti-Inflammatory Drug Diclofenac in Milk without Any Sample Pretreatment. *Anal. Bioanal. Chem.* **2014**, *406* (14), 3377–3386.
- (15) Steinke, N.; Döring, S.; Wuchrer, R.; Kroh, C.; Gerlach, G.; Härtling, T. Plasmonic Sensor for On-Site Detection of Diclofenac Molecules. *Sensor Actuat. B-Chem.* **2019**, *288*, 594–600.
- (16) Schirmer, C.; Posseckardt, J.; Schröder, M.; Gläser, M.; Howitz, S.; Scharff, W.; Mertig, M. Portable and Low-Cost Biosensor towards on-Site Detection of Diclofenac in Wastewater. *Talanta* **2019**, *203*, 242–247.







---

**Chapter 5. A rapid and efficient method for label-free immunosensing of extracellular vesicle subtypes**

---



## 5.1 Introduction

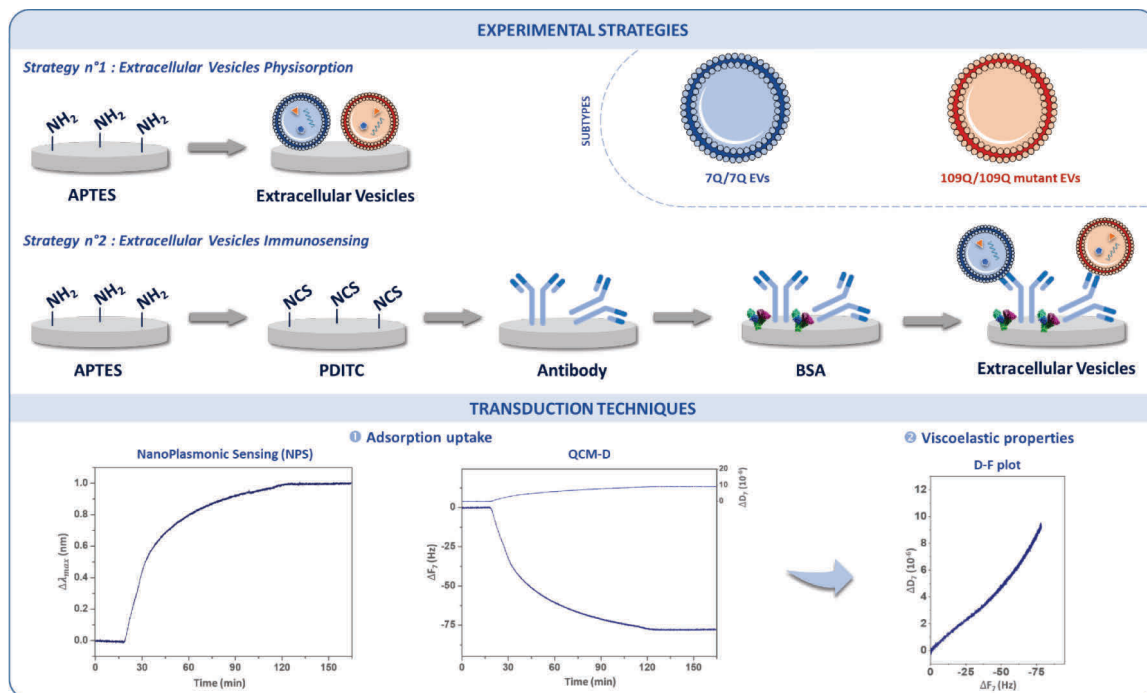
Extracellular vesicles (EVs) are nano-sized secreted particles that are surrounded by a double-layer lipid membrane and that have emerged as key modulators of a wide range of biological processes in normal and disease conditions.<sup>1-3</sup> As such, EVs are considered as promising circulating biomarkers with strong diagnostic potential to distinguish disease-associated states from normal conditions,<sup>4</sup> predict disease progression rates and clinical response to treatment.<sup>5</sup> However, EVs show highly heterogeneous features (size, density, surface proteins, cargo composition, the latter feature encompassing RNAs, DNAs, proteins and organelles), which may root in their origin in the cell (*e.g.* endosomal origin, or membrane budding) and the stage (*e.g.* differentiating or mature cells), status (*e.g.* healthy *versus* diseased) and type of secreting cells.<sup>6-8</sup> In spite of the methodological progress achieved in isolating EV subpopulations, the fast and accurate characterization of EV subpopulations remains a challenging task, regardless of secreting cells or tissues.<sup>9</sup> This task is complicated by the macromolecular structures that, in the extracellular milieu or biological fluids, have size, density and physicochemical surface properties similar to those of EVs. In addition, proteins (or protein complexes) that are part of EV membranes may also circulate in the extracellular milieu or biological fluids. The now well established usefulness of exosomes as valuable biomarkers in the context of numerous pathologies, *e.g.* cancer and neurodegenerative diseases, has prompted the development of a plethora of biosensors to quantify exosomes in biofluids as minimally invasive diagnostic tools.<sup>10-14</sup> Discrimination between EVs generated from normal physiological and pathological states or between EV subpopulations is typically achieved by screening the differences in membrane proteins composition, *i.e.* by molecular profiling. This can be achieved by multiplex (nano)plasmonic biosensors including arrays of antibody probes targeting specific antigens.<sup>15-19</sup> Alternatively, EVs produced at two different stages of myeloma have been efficiently profiled according to their difference of affinity for heparin-coated SPR sensors.<sup>20</sup> Also, exosomes were discriminated from multivesicular vesicles *via* their difference of affinity for bare gold nanoislands.<sup>21</sup> Methods to access other physico-chemical properties of EVs such as size, mass/density and viscoelasticity, each parameter being complementary to establish a specific signature of EV subpopulations, are still scarce with biosensing platforms. For instance, combination of SPR immunosensing and plasmonic microscopy recently enabled simultaneous access to size distribution, concentration and binding affinity of EVs produced by cancer cells.<sup>22</sup> However, these methods require the design

of sophisticated sensing arrays and surface functionalization. Here, we designed a label-free immunosensor to probe at high precision differences in the physicochemical properties of small EVs that may occur between normal and disease conditions. As a proof-of-concept, we used our label-free immunosensor to characterize the mass and viscoelasticity of CD63- and CD81-positive small EVs isolated from mouse striatal cells that are homozygous for normal or mutated Huntingtin (Htt), The Huntington's disease (HD) gene, namely 7Q/7Q (wild-type) and 109Q/109Q (mutated) striatal cells derived from HdhQ111 knock-in mice.<sup>23</sup> Small EVs (enriched in the 100,000g fraction) were isolated from these cells using differential ultracentrifugation (DUC). As transduction methods, we selected quartz crystal microbalance with dissipation monitoring (QCM-D) coupled to nanoplasmonic sensing (NPS). QCM-D provides information about the mass changes and the viscoelastic properties of thin films at the surface of piezoelectric quartz sensors. QCM-D is also able to characterize the interfacial structure and the binding kinetics of the adsorbed biomolecules.<sup>24</sup> The advantage of QCM-D is its ability to distinguish between the binding of EVs and artifactual phenomena from other components present in the media (proteins or other contaminants) as well as an excellent match between EV size and its sensing depth.<sup>25</sup> NPS is a label-free optical transduction method that relies on the Localized Surface Plasmon Resonance (LSPR) phenomenon. LSPR results from the confinement of collective electron charge oscillations in metallic nanostructures, here gold, induced by electromagnetic field of incident light, leading to light absorption/scattering in the visible spectral range. Biorecognition results in the LSPR band shift induced by the change of local refractive index close to the gold nanostructures.<sup>26</sup> Although NPS<sup>15,27</sup> and QCM-D<sup>25</sup> have already been used separately to monitor EVs adsorption on surfaces, their combination has yet to be exploited, and even more, their application to the sensing of different subtypes of EVs has never been demonstrated. Here, we coupled QCM-D and NPS to enable real-time simultaneous detection occurring at the same sensor surface.<sup>28</sup> Additionally, coupling QCM-D and NPS informs about the molecular dry mass and the solvation degree of molecular layers, which is not accessible by solely using QCM-D or NPS.<sup>29</sup> Finally, NPS exhibits a decay length of tens of nanometers<sup>30,31</sup> (30 nm here) while QCM-D is sensitive to a much larger sensing depth, up to several hundred nanometers (~250 nm).<sup>32,33</sup> Thus, given the average size of small EVs which is about 110 nm (and ranging from 50 to 250 nm, as inferred using nanoparticle tracking analysis (NTA), another advantage of coupling QCM-D and NPS is to broaden the window size for in-depth sensing of EV while obtaining complementary information from the two label-free transduction techniques.<sup>28,34</sup> In what follows we precisely design and test a surface-based

immunosensor for the detection and the differentiation of EV subtypes isolated by differential ultracentrifugation from knock-in mouse striatal cells expressing a mutated allele of huntingtin (Htt), the Huntington’s disease gene, referred to as “mutated” *versus* those expressing the wild-type Htt allele referred to as “normal”. Our approach has the ambition at a long-time objective to allow for the rapid and early biosensing of neurodegenerative diseases.

## 5.2 Results and discussion

To assess whether combined QCM-D and NPS may be able to precisely characterize the mechanical features of EV subtypes in normal and disease conditions, we isolated small EVs secreted by 7Q/7Q or 109Q/109Q mouse striatal cells using DUC followed by nanoparticle tracking of the 100,000g pellet (100K), the fraction enriched in small EVs with size centered around 100 nm (**Figure S5. 1**). Next, we used information on the particles concentration in the samples to detect 100K EV samples (**Figure 5. 1**).

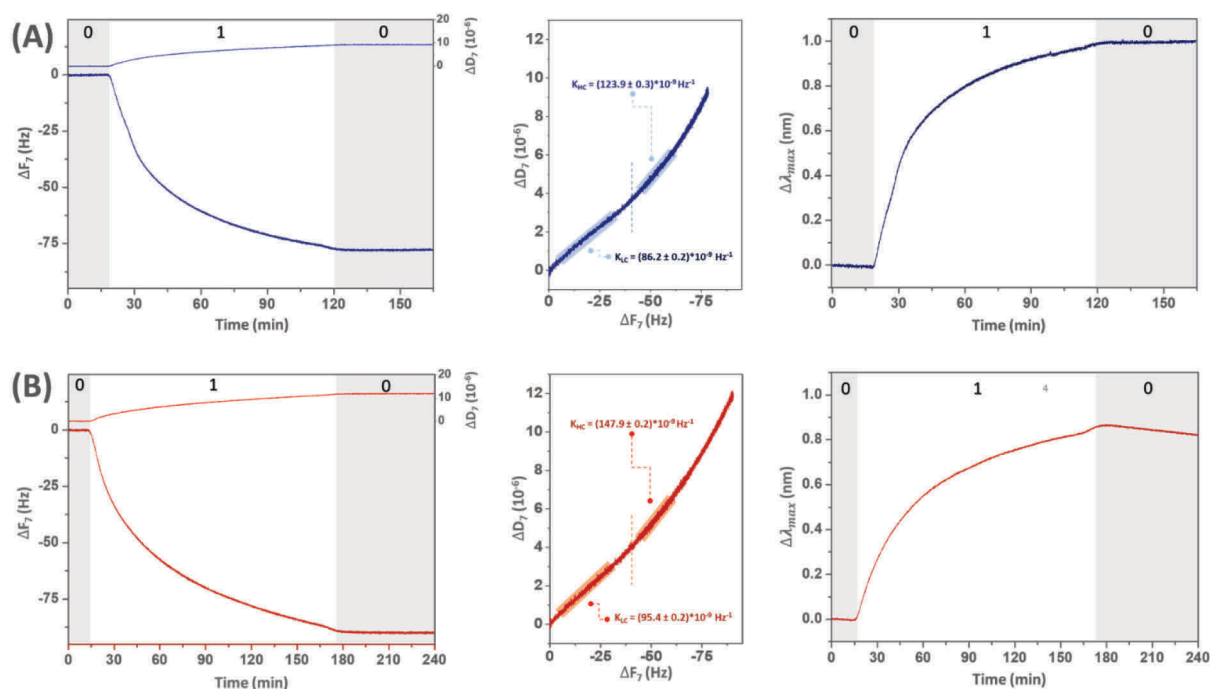


**Figure 5. 1.** Overview of experimental strategies for EV sensing. The physical characterization of EV subtypes, *i.e.* 7Q/7Q and 109Q/109Q small EVs that may be of endosomal origin (*i.e.* EVs positive for CD63 and CD81), were performed using piezoelectric and optical transduction methods to study adsorption uptakes and viscoelastic of the adsorbed material, namely NPS, a method based on localized surface plasmon resonance (LSPR) phenomena and QCM-D, a method based on piezoelectric effect.

As a preliminary experiment, interaction of the EV samples with antibody-free amine-terminated silane layer on silica-coated nanostructured sensors was investigated, whereas, in another set of experiments, we used sensors coated with anti-CD81 and anti-CD63 antibodies for immunosensing of small EVs of endosomal origin. Adsorption uptakes and investigation of the viscoelastic properties of adsorbed EVs were conducted with NPS and QCM-D as transduction methods. Surface functionalization characterizations are presented in Supplementary Information (**Figure S5. 2**, **Table S5. 1** and **Table S5. 2**).

### 5.2.1 EVs physisorption on antibody-free substrates

As a preliminary study, we first injected a solution of EVs on antibody-free silica-coated gold nanostructured quartz sensors (**Figure 5. 2**). This study was conducted on APTES-coated substrates and not directly on bare silica surface in order to avoid the rupture of vesicles and formation of supported lipid bilayer (SLB).<sup>28,35,36</sup>



**Figure 5. 2.** Representative physisorption of (A) 7Q/7Q-EVs and (B) 109Q/109Q-EVs on APTES layer on nanostructured quartz sensor with from left to right: QCM-D sensorgrams, D-F plot and NPS sensorgrams. Experiment was performed at a flow rate of 10  $\mu\text{L}/\text{min}$  at 20  $^{\circ}\text{C}$  and  $[\text{EV}] = 40 \text{ mg}/\text{L}$ . (0) DPBS, (1) EV adsorption. One independent experiment was performed for each EVs subtypes.

Real-time monitoring of EVs physisorption was performed by the combined QCM-D and NPS approach to compare their respective ability to sense EVs.

The resulting data for QCM-D (frequency  $\Delta F$  and dissipation  $\Delta D$  shifts), D-F plots and LSPR peak position shift ( $\Delta\lambda_{\max}$ ) are presented in **Figure 5. 2A** and **Figure 5. 2B**, respectively for the 7Q/7Q-EV and 109Q/109Q-EV. After stabilization in DPBS, flowing of EV samples having the same protein concentration over the sensor substrates led to similar QCM-D responses over the same injection time (100 min) with values of frequency shifts of -76.4 Hz and dissipation shifts of  $9 \times 10^{-6}$  (**Table S5. 3**).

These large variations in dissipation as well as splitting of the frequency shifts at different overtones,  $n_{\text{QCM-D}}$ , (**Figure S5. 3** and **Table S5. 4**) illustrate the viscoelastic properties of the EV layers. In addition to the high dissipation value, the monotonous variation of QCM-D response upon vesicle adsorption ruled out vesicle rupture and SLB formation,<sup>28,35</sup> rather suggesting that the vesicles remained intact all along their adsorption on the APTES layer.

Data analysis of the QCM-D signals was done using the Voigt-Voinova viscoelastic model.<sup>37,38</sup> A film thickness of  $\sim 40$  nm was determined after EV adsorption over 100 min (**Figure S5. 4** and **Table S5. 5**). The calculated thickness is smaller than the expected size of EV in solution ( $\sim 100$  nm), which is consistent with vesicles' flattening once adsorbed on surface as previously described in the literature.<sup>39</sup> Furthermore, corresponding acoustic mass uptakes of 4230 and 4430 ng/cm<sup>2</sup> were determined.

One way to compare experiments and to obtain time-independent QCM-D curves is to plot the dissipation variation as a function of the frequency shift. This representation allows investigating  $\Delta D - \Delta F$  relationship as it shows how much dissipation is caused by a frequency input. Besides, the slope of the linear portion, referred herein as K, gives information on the mechanical properties of the adsorbed layer: a small K value is observed for rigid protein layers while a greater value is related to the formation of viscoelastic ones.<sup>40,41</sup>

The corresponding D-F plots (**Figure 5. 2** - middle panel) show two linear portions with an inflection point around - 40 Hz, suggesting two EV adsorption regimes. The first portion at low coverage (LC) is characterized by a smaller value of  $K_{\text{LC}}$  ( $86.2$  and  $95.4 \times 10^{-9} \text{ Hz}^{-1}$ , respectively for 7Q/7Q-EVs and 109Q/109Q-EVs), whereas the second one at high coverage (HC) exhibits a greater value of  $K_{\text{HC}}$  ( $123.9$  and  $147.9 \times 10^{-9} \text{ Hz}^{-1}$ , respectively for the 7Q/7Q-EV and 109Q/109Q-EV). These results suggest that the layer resulting from physisorption of both EVs subtypes became less rigid with a positive deviation from linearity at higher coverage.

This might be attributed to vesicles deformation upon packing onto the surface, ultimately leading to a more viscoelastic layer on the surface.<sup>39</sup>



Furthermore, we observed that the layer of 7Q/7Q-EVs seems to be more rigid than the one formed from the physisorption of 109Q/109Q-EVs, with differences of 10.7% and 19.4% detected for LC and HC between the two populations.

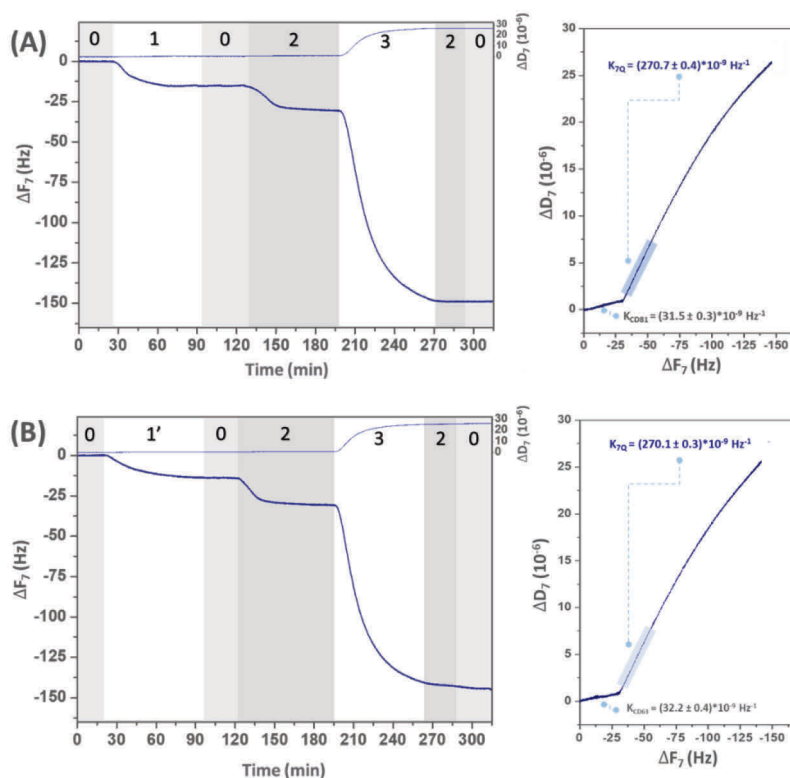
Simultaneously, the position of the LSPR band red-shifted by 0.97 nm and 0.75 nm upon flowing of 7Q/7Q-EV and 109Q/109Q-EV solutions, respectively. Since the  $\Delta\lambda_{\max}$  is not sensitive to the solvent, this difference suggests that more material is adsorbed on the surface in the case of the 7Q/7Q-EV within the sensing volume of LSPR or that more contact points are established between the 7Q/7Q-EV and the surface. In the latter case, the layer of 7Q/7Q-EV should be more rigid than that of 109Q/109Q-EV, in agreement with the lower  $K$  calculated above. Furthermore, optical mass uptakes of 431 and 364 ng/cm<sup>2</sup> respectively for the 7Q/7Q-EV and 109Q/109Q-EV were determined (detailed calculation is given in Supplementary Information). This difference between both acoustic and optical mass uptakes illustrates the high hydration and viscoelastic properties of EV (**Figure S5. 4**). In addition, we observed a 15.5% difference in the optical mass inputs determined from the respective  $\Delta\lambda_{\max}$  shifts between 7Q/7Q-EV and 109Q/109Q-EV.

### 5.2.2 Immunosensing of 7Q/7Q EVs with QCM-D

With the purpose of analyzing complex EV samples and to meet the need for a specific biorecognition element, sensors were functionalized with monoclonal antibodies against the transmembrane proteins CD63 or CD81, the combination of which is considered to be a biomarker of exosomes (EVs of endosomal origin).<sup>42</sup> For antibody immobilization, we chose not to use an oriented approach using protein A or G<sup>43,44</sup> as, owing to the limited sensing depth of NPS, the antibody needs to be as close as possible to the surface.<sup>30,31</sup> Rather, we chose to generate the sensing layer using covalent coupling of antibodies *via* silanization with APTES to generate surface amine groups, followed by reaction with the homobifunctional crosslinker PDITC to create amine-reactive isothiocyanate functions.<sup>45</sup> The sensing layer was characterized throughout all functionalization steps and results are presented in Supplementary Information. Immobilization of anti-CD81 and anti-CD63 capture antibodies onto flat silica-coated quartz sensors was monitored in real time by QCM-D (**Figure 5. 3**). Prior to antibody injection, stabilization was performed by flowing DPBS over the sensors surface at a flow rate of 10  $\mu$ L/min.

Then, anti-CD81 (**Figure 5. 3A**) and anti-CD63 (**Figure 5. 3B**) antibody solutions at a concentration of 20 mg/L in DPBS were injected until signal saturation and led to similar frequency and low dissipation shifts after rinsing (**Table S5. 6**).

A blocking step with DPBS-BSA (0.1%) was next performed in order to prevent non-specific interactions. Next, the same sample of 7Q/7Q EVs in DPBS-BSA ( $1.8 \times 10^{10}$  particles/mL as assayed by NTA) was flown over the two surfaces, resulting in large variations in both frequency and dissipation. These values were about -114 Hz and  $25 \times 10^{-6}$  with anti-CD63 as capture antibody and about -118 Hz and  $26 \times 10^{-6}$  with anti-CD81 as capture antibody (**Table S5. 6**). Covalent immobilization of anti-CD81 or anti-CD63 antibodies led to similar K values of  $30 \times 10^{-9} \text{ Hz}^{-1}$  (**Figure 5. 3**), indicating the formation of a rigid antibody layer.



**Figure 5. 3.** Representative adsorption of 7Q/7Q EV on planar surface using (A) anti-CD81 and (B) anti-CD63 as capture antibodies with from left to right: QCM-D sensorgrams and corresponding D-F plots. Experiment was performed at a flow rate of 10  $\mu\text{L}/\text{min}$  and  $[\text{EV}] = 1.8 \times 10^{10}$  particles/mL. (0): running buffer, (1) and (1'): anti-CD81 and anti-CD63 capture antibodies, (2): DPBS-BSA (0.1%), (3) EV adsorption. One independent experiment was performed for each detection strategy.

Upon adsorption of 7Q/7Q EVs, an inflection point was observed and led to a second linear portion with a much higher slope, which indicates that a second adsorption process took place. In the low surface coverage regime, a K value of  $270 \times 10^{-9} \text{ Hz}^{-1}$  was calculated by linear regression. This high value illustrates the high viscoelasticity of the 7Q/7Q EV layers formed at the sensors surface. Interestingly, K appeared to be independent of the capture antibody but rather characteristic of the 7Q/7Q-EV layers formed by affinity binding.

Slightly negative deviation from the linear trend was observed at higher surface coverage, indicative of an increased rigidity likely due to close packing of the vesicles.

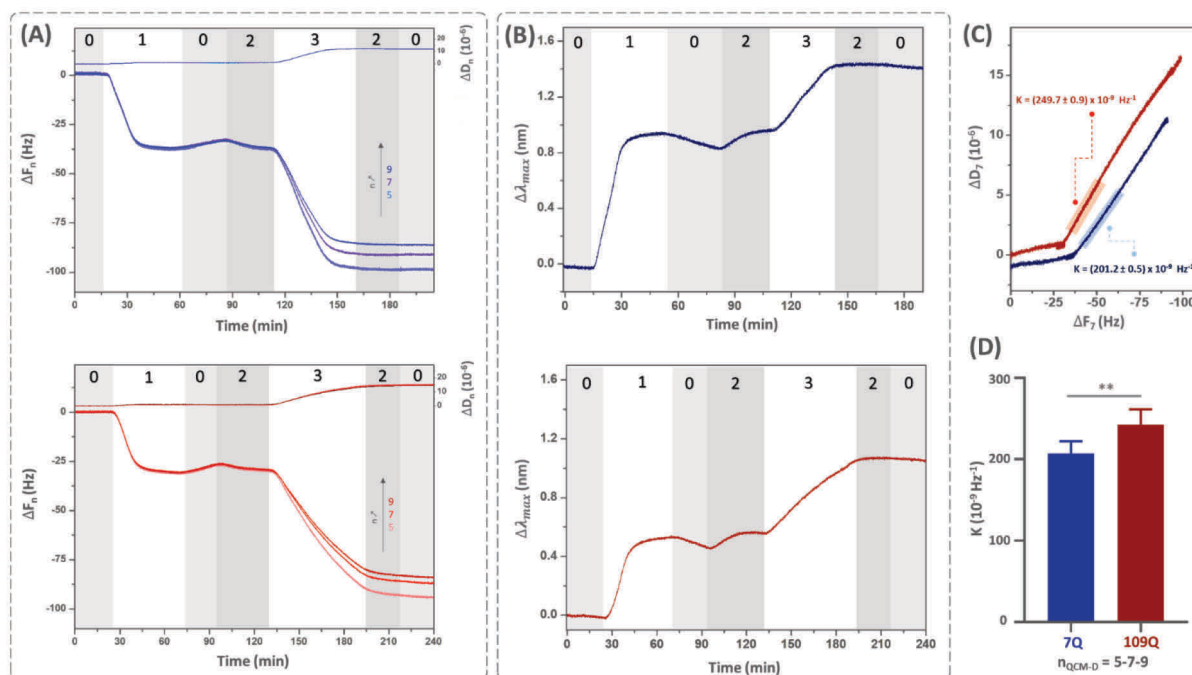
Additional evidence that the variation of frequency and high dissipation resulted from the specific capture of EV by immobilized anti-CD81 was demonstrated by further injection of anti-CD63 revelation antibody in a sandwich format. A shift of the resonance frequency of -8.2 Hz was measured, indicating that the previously captured species carry both CD81 and CD63 protein markers on their membrane (**Figure S5. 5**).

### 5.2.3 Immunosensing of EVs subtypes with combined QCM-D and NPS methods

Based on the presented sets of experiments, we wondered whether it could be possible to discriminate 7Q/7Q-EVs from 109Q/109Q-EVs samples by their distinct mechanical properties. Thus, we combined QCM-D and NPS using silica-coated gold nanostructured substrates functionalized with anti-CD81 as capture antibody. Frequency, dissipation and LSPR peak position shifts from three independent experiments are presented in **Figure 5. 4** and in Supplementary Information (**Figure S5. 5** and **Figure S5. 6**).

After stabilization in DPBS running buffer, anti-CD81 solution (20 mg/L) was flown at 10  $\mu\text{L}/\text{min}$  over the sensor until signal saturation. It led to a decrease of resonance frequency together with a slight increase of dissipation, indicating that a rigid organic film was formed at the surface of the sensor.

Simultaneously, the LSPR band was shown to progressively shift to the red by 0.5 - 0.7 nm (**Table S5. 7**). After a blocking step with DPBS-BSA (0.1%), injection of 7Q/7Q-EVs in DPBS-BSA led to a large decrease of frequency ( $-31.3 - -136.7 \text{ Hz}$ ) while the dissipation increased ( $6.2 - 24.9 \times 10^{-6}$ ), suggesting successful capture of EVs (**Figure 5. 4A**). Simultaneously, binding of EVs translated in  $\lambda_{\text{max}}$  shifts to the red (0.17 - 1.18 nm). Furthermore, although the sensing depth of NPS is much shorter than the size of the vesicles, we noticed that both QCM-D and NPS signals saturated at around the same time.



**Figure 5. 4.** (A) Representative QCM-D sensorgrams, (B) Representative NPS sensorgrams and (C) Representative D-F plots for immunosensing of 7Q/7Q-EVs (in blue) and 109Q/109Q-EVs (in red) on nanostructured sensor. (D) Summarized K values at different QCM-D overtones for immunosensing of 7Q/7-EVs and 109Q/109Q-EVs using an anti-CD81 antibody as the capture antibody. The values obtained for the 7Q/7-EVs and 109Q/109Q-EV samples were compared using QCM-D overtones 5,7 and 9. Statistical significance was analyzed by the Mann-Whitney U test (\*\* $p < 0.05$ ). Three independent experiments were performed. Experiments were conducted at a flow rate of 10  $\mu\text{L}/\text{min}$ .

Combined QCM-D and NPS immunosensing was also conducted with the 109Q/109Q-EV population (**Figure 5. 4B**). Similarly, to 7Q/7Q-EVs, injection of 109Q/109Q-EVs in DPBS-BSA led to a large decrease of frequency while the dissipation simultaneously increased and the position of the LSPR band shifted to the red (**Table S5. 7**).

To compare experiments carried out with different injection times and EVs concentrations, dissipation shift  $\Delta D$  was again plotted as a function of frequency shift  $\Delta F$  for both EV populations. The plots followed a linear trend over nearly the whole range of frequencies from which the K factor was determined by linear regression analysis.

The fitted slope K obtained for the 7Q/7Q-EV was lower than the one of 109Q/109Q-EV,  $(206.7 \pm 4.9) \times 10^{-9} \text{ Hz}^{-1}$  and  $(243.3 \pm 5.8) \times 10^{-9} \text{ Hz}^{-1}$  respectively (7<sup>th</sup> harmonic, 3 independent experiments). These results suggest that the layer formed by binding of 7Q/7Q-EVs to anti-CD81 is slightly more rigid than the one formed by 109Q/109Q-EVs with a 17.7 % difference detected between the two populations.

Statistical tests were conducted from three independent experiments and for the two EV populations using three different QCM-D overtones ( $n_{\text{QCM-D}} = 5, 7, 9$ ) to increase the number of replicates and the results are presented in Figure 4D.

We observed a statistical difference of 16.5% between 7Q/7Q-EVs and 109Q/109Q-EVs ( $n = 9, p = 0.0012$ , *Mann-Whitney U test*), suggesting that the layer of 7Q/7Q-EVs is more rigid compared to that of 109Q/109Q-EVs (**Table S5. 8**).

Thus, the QCM-D technique allows to discriminate between the two populations of EVs according to the viscoelastic properties (K value) of the films of EVs formed by interaction between the membrane CD81 biomarker and anti-CD81 immobilized at the sensor surface. Furthermore, we observed that the EV layers formed on antibody-free sensors were more rigid (compare K values) than those resulting from immunocapture, regardless of EV subtype. During physisorption, EVs might be more prone to deformation due to multiple anchoring points to the surface, revealing a different adsorption process.

The NPS signals measured upon immunocapture of EVs appeared to be less exploitable for discriminating EVs based on their respective LSPR responses. In addition, we also observed that  $\Delta F$  and  $\Delta\lambda_{\text{max}}$  were linearly correlated, regardless of the EVs subtype (**Figure S5. 8**).

This shows that the signals generated by both techniques are representative of the number of adsorbed vesicles on the surface.<sup>28</sup>

### 5.3 Conclusion

In summary, we devised an immunosensor and method based on coupling QCM-D and NPS to precisely characterize EV subtypes across conditions based on their viscoelastic properties, as suggested herein by the comparison of small EVs that are isolated from normal (7Q/7Q) and mutated (109Q/109Q) mouse striatal cells and that are positive for CD81 and CD63.

A sensing layer comprising an antibody directed against the generic exosomal marker CD81 was built up on silica-coated gold nanostructured quartz sensors, allowing label-free, simultaneous optical and gravimetric detection of binding events. Injection of EV led to a large shift of both the frequency and dissipation, as a result of the specific capture of the EV.

The  $\partial D/\partial F$  slope (K value) representing the viscoelastic properties of the layer of EV was found to discriminate small EVs that are secreted by normal or mutated mouse striatal cells. 7Q/7Q EVs were found to form a more rigid layer upon physisorption and immunosensing using an anti-CD81 capture antibody in comparison to 109Q/109Q EV.

In the case of physisorption, the higher rigidity of the 7Q-EV layer was interpreted thanks to NPS data as particles possibly creating more anchoring points with the silica surface.

Our data unveil the potential of label-free immunosensing using QCM-D and NPS as a fast and accurate approach to detect changes in the mechanical properties, *i.e.* viscoelastic properties, of EV subtypes across physiological conditions and paves the way for an early diagnosis of neurodegenerative diseases.

## References

- (1) Krämer-Albers, E.-M.; Hill, A. F. Extracellular Vesicles: Interneural Shuttles of Complex Messages. *Curr. Opin. Neurobiol.* **2016**, *39*, 101–107.
- (2) Vlassov, A. V.; Magdaleno, S.; Setterquist, R.; Conrad, R. Exosomes: Current Knowledge of Their Composition, Biological Functions, and Diagnostic and Therapeutic Potentials. *Biochim. Biophys. Acta BBA - Gen. Subj.* **2012**, *1820* (7), 940–948.
- (3) Doyle, L.; Wang, M. Overview of Extracellular Vesicles, Their Origin, Composition, Purpose, and Methods for Exosome Isolation and Analysis. *Cells* **2019**, *8* (7), 727.
- (4) Hill, A. F. Extracellular Vesicles and Neurodegenerative Diseases. *J. Neurosci. Off. J. Soc. Neurosci.* **2019**, *39* (47), 9269–9273.
- (5) Cheng, N.; Du, D.; Wang, X.; Liu, D.; Xu, W.; Luo, Y.; Lin, Y. Recent Advances in Biosensors for Detecting Cancer-Derived Exosomes. *Trends Biotechnol.* **2019**, *37* (11), 1236–1254.
- (6) Colombo, M.; Raposo, G.; Théry, C. Biogenesis, Secretion, and Intercellular Interactions of Exosomes and Other Extracellular Vesicles. *Annu. Rev. Cell Dev. Biol.* **2014**, *30*, 255–289.
- (7) van Niel, G.; D'Angelo, G.; Raposo, G. Shedding Light on the Cell Biology of Extracellular Vesicles. *Nat. Rev. Mol. Cell Biol.* **2018**, *19* (4), 213–228.
- (8) Gauthier, S. A.; Pérez-González, R.; Sharma, A.; Huang, F.-K.; Alldred, M. J.; Pawlik, M.; Kaur, G.; Ginsberg, S. D.; Neubert, T. A.; Levy, E. Enhanced Exosome Secretion in Down Syndrome Brain - a Protective Mechanism to Alleviate Neuronal Endosomal Abnormalities. *Acta Neuropathol. Commun.* **2017**, *5* (1), 65.
- (9) Théry, C. *et al.*. Minimal Information for Studies of Extracellular Vesicles 2018 (MISEV2018): A Position Statement of the International Society for Extracellular Vesicles and Update of the MISEV2014 Guidelines. *J. Extracell. Vesicles* **2018**, *7* (1), 1535750.
- (10) Im, H.; Lee, K.; Weissleder, R.; Lee, H.; Castro, C. M. Novel Nanosensing Technologies for Exosome Detection and Profiling. *Lab. Chip* **2017**, *17* (17), 2892–2898.
- (11) Xu, L.; Shoaie, N.; Jahanpeyma, F.; Zhao, J.; Azimzadeh, M.; Al-Jamal, K. T. Optical, Electrochemical and Electrical (Nano)Biosensors for Detection of Exosomes: A Comprehensive Overview. *Biosens. Bioelectron.* **2020**, *161*, 112222.
- (12) Choi, J.-H.; Lee, J.-H.; Choi, J.-W. Applications of Bionano Sensor for Extracellular Vesicles Analysis. *Materials* **2020**, *13* (17), 3677.
- (13) Kholafazad Kordasht, H.; Hasanzadeh, M. Biomedical Analysis of Exosomes Using Biosensing Methods: Recent Progress. *Anal. Methods* **2020**, *12* (22), 2795–2811.
- (14) Chin, L. K.; Son, T.; Hong, J.-S.; Liu, A.-Q.; Skog, J.; Castro, C. M.; Weissleder, R.; Lee, H.; Im, H. Plasmonic Sensors for Extracellular Vesicle Analysis: From Scientific Development to Translational Research. *ACS Nano* **2020**, *14* (11), 14528–14548.
- (15) Im, H.; Shao, H.; Park, Y. I.; Peterson, V. M.; Castro, C. M.; Weissleder, R.; Lee, H. Label-Free Detection and Molecular Profiling of Exosomes with a Nano-Plasmonic Sensor. *Nat. Biotechnol.* **2014**, *32* (5), 490–495.
- (16) Zhu, L.; Wang, K.; Cui, J.; Liu, H.; Bu, X.; Ma, H.; Wang, W.; Gong, H.; Lausted, C.; Hood, L.; Yang, G.; Hu, Z. Label-Free Quantitative Detection of Tumor-Derived Exosomes through Surface Plasmon Resonance Imaging. *Anal. Chem.* **2014**, *86* (17), 8857–8864.
- (17) Sina, A. A. I.; Vaidyanathan, R.; Dey, S.; Carrascosa, L. G.; Shiddiky, M. J. A.; Trau, M. Real Time and Label Free Profiling of Clinically Relevant Exosomes. *Sci. Rep.* **2016**, *6* (1), 30460.
- (18) Kwizera, E. A.; O'Connor, R.; Vinduska, V.; Williams, M.; Butch, E. R.; Snyder, S. E.; Chen, X.; Huang, X. Molecular Detection and Analysis of Exosomes Using Surface-Enhanced Raman Scattering Gold Nanorods and a Miniaturized Device. *Theranostics* **2018**, *8* (10), 2722–2738.
- (19) Picciolini, S.; Gualerzi, A.; Vanna, R.; Sguassero, A.; Gramatica, F.; Bedoni, M.; Masserini, M.; Morasso, C. Detection and Characterization of Different Brain-Derived Subpopulations of Plasma Exosomes by Surface Plasmon Resonance Imaging. *Anal. Chem.* **2018**, *90* (15), 8873–8880.



- (20) Di Noto, G.; Bugatti, A.; Zandrini, A.; Mazzoldi, E. L.; Montanelli, A.; Caimi, L.; Rusnati, M.; Ricotta, D.; Bergese, P. Merging Colloidal Nanoplasmonics and Surface Plasmon Resonance Spectroscopy for Enhanced Profiling of Multiple Myeloma-Derived Exosomes. *Biosens. Bioelectron.* **2016**, *77*, 518–524.
- (21) Thakur, A.; Qiu, G.; Ng, S.-P.; Guan, J.; Yue, J.; Lee, Y.; Wu, C.-M. L. Direct Detection of Two Different Tumor-Derived Extracellular Vesicles by SAM-AuNIs LSPR Biosensor. *Biosens. Bioelectron.* **2017**, *94*, 400–407.
- (22) Yang, Y.; Zhai, C.; Zeng, Q.; Khan, A. L.; Yu, H. Multifunctional Detection of Extracellular Vesicles with Surface Plasmon Resonance Microscopy. *Anal. Chem.* **2020**, *92* (7), 4884–4890.
- (23) Trettel, F.; Rigamonti, D.; Hilditch-Maguire, P.; Wheeler, V. C.; Sharp, A. H.; Persichetti, F.; Cattaneo, E.; MacDonald, M. E. Dominant Phenotypes Produced by the HD Mutation in STHdh(Q111) Striatal Cells. *Hum. Mol. Genet.* **2000**, *9* (19), 2799–2809.
- (24) Hook, F.; Rodahl, M.; Keller, C.; Glasmastar, K.; Fredriksson, C.; Dahiqvist, P.; Kasemo, B. The Dissipative QCM-D Technique: Interfacial Phenomena and Sensor Applications for Proteins, Biomembranes, Living Cells and Polymers. In *Proceedings of the 1999 Joint Meeting of the European Frequency and Time Forum and the IEEE International Frequency Control Symposium (Cat. No.99CH36313)*; 1999; Vol. 2, pp 966–972 vol.2.
- (25) Suthar, J.; Parsons, E. S.; Hoogenboom, B. W.; Williams, G. R.; Guldin, S. Acoustic Immunosensing of Exosomes Using a Quartz Crystal Microbalance with Dissipation Monitoring. *Anal. Chem.* **2020**, *92* (5), 4082–4093.
- (26) Sepúlveda, B.; Angelomé, P. C.; Lechuga, L. M.; Liz-Marzán, L. M. LSPR-Based Nanobiosensors. *Nano Today* **2009**, *4* (3), 244–251.
- (27) Raghu, D.; Christodoulides, J. A.; Christophersen, M.; Liu, J. L.; Anderson, G. P.; Robitaille, M.; Byers, J. M.; Raphael, M. P. Nanoplasmonic Pillars Engineered for Single Exosome Detection. *PLOS ONE* **2018**, *13* (8), e0202773.
- (28) Ferhan, A. R.; Jackman, J. A.; Cho, N.-J. Integration of Quartz Crystal Microbalance-Dissipation and Reflection-Mode Localized Surface Plasmon Resonance Sensors for Biomacromolecular Interaction Analysis. *Anal. Chem.* **2016**, *88* (24), 12524–12531.
- (29) Larsson, E. M.; Edvardsson, M. E. M.; Langhammer, C.; Zorić, I.; Kasemo, B. A Combined Nanoplasmonic and Electrodeless Quartz Crystal Microbalance Setup. *Rev. Sci. Instrum.* **2009**, *80* (12), 125105.
- (30) Mazzotta, F.; Johnson, T. W.; Dahlin, A. B.; Shaver, J.; Oh, S.-H.; Höök, F. Influence of the Evanescent Field Decay Length on the Sensitivity of Plasmonic Nanodisks and Nanoholes. *ACS Photonics* **2015**, *2* (2), 256–262.
- (31) Ferhan, A. R.; Jackman, J. A.; Cho, N.-J. Probing Spatial Proximity of Supported Lipid Bilayers to Silica Surfaces by Localized Surface Plasmon Resonance Sensing. *Anal. Chem.* **2017**, *89* (7), 4301–4308.
- (32) Keiji Kanazawa, K.; Gordon, J. G. The Oscillation Frequency of a Quartz Resonator in Contact with Liquid. *Anal. Chim. Acta* **1985**, *175*, 99–105.
- (33) Johannsmann, D.; Reviakine, I.; Richter, R. P. Dissipation in Films of Adsorbed Nanospheres Studied by Quartz Crystal Microbalance (QCM). *Anal. Chem.* **2009**, *81* (19), 8167–8176.
- (34) Dahlin, A. B.; Jönsson, P.; Jonsson, M. P.; Schmid, E.; Zhou, Y.; Höök, F. Synchronized Quartz Crystal Microbalance and Nanoplasmonic Sensing of Biomolecular Recognition Reactions. *ACS Nano* **2008**, *2* (10), 2174–2182.
- (35) Reimhult, E.; Höök, F.; Kasemo, B. Vesicle Adsorption on SiO<sub>2</sub> and TiO<sub>2</sub>: Dependence on Vesicle Size. *J. Chem. Phys.* **2002**, *117* (16), 7401–7404.
- (36) Reimhult, E.; Höök, F.; Kasemo, B. Intact Vesicle Adsorption and Supported Biomembrane Formation from Vesicles in Solution: Influence of Surface Chemistry, Vesicle Size, Temperature, and Osmotic Pressure †. *Langmuir* **2003**, *19* (5), 1681–1691.
- (37) Kanazawa, K.; Cho, N.-J. Quartz Crystal Microbalance as a Sensor to Characterize Macromolecular Assembly Dynamics. *J. Sens.* **18**.
- (38) Ohlsson, G.; Tigerström, A.; Höök, F.; Kasemo, B. Phase Transitions in Adsorbed Lipid Vesicles Measured Using a Quartz Crystal Microbalance with Dissipation Monitoring. *Soft Matter* **2011**, *7* (22), 10749.



- (39) Ferhan, A. R.; Jackman, J. A.; Cho, N.-J. Investigating How Vesicle Size Influences Vesicle Adsorption on Titanium Oxide: A Competition between Steric Packing and Shape Deformation. *Phys. Chem. Chem. Phys.* **2017**, *19* (3), 2131–2139.
- (40) Höök, F.; Rodahl, M.; Brzezinski, P.; Kasemo, B. Energy Dissipation Kinetics for Protein and Antibody–Antigen Adsorption under Shear Oscillation on a Quartz Crystal Microbalance. *Langmuir* **1998**, *14* (4), 729–734.
- (41) Hook, F.; Rodahl, M.; Kasemo, B.; Brzezinski, P. Structural Changes in Hemoglobin during Adsorption to Solid Surfaces: Effects of PH, Ionic Strength, and Ligand Binding. *Proc. Natl. Acad. Sci.* **1998**, *95* (21), 12271–12276.
- (42) Andreu, Z.; Yanez-Mo, M. Tetraspanins in Extracellular Vesicle Formation and Function. *Front. Immunol.* **2014**, *5*.
- (43) Salmain, M.; Ghasemi, M.; Boujday, S.; Spadavecchia, J.; Técher, C.; Val, F.; Le Moigne, V.; Gautier, M.; Briandet, R.; Pradier, C.-M. Piezoelectric Immunosensor for Direct and Rapid Detection of Staphylococcal Enterotoxin A (SEA) at the Ng Level. *Biosens. Bioelectron.* **2011**, *29* (1), 140–144.
- (44) Welch, N. G.; Scoble, J. A.; Muir, B. W.; Pigram, P. J. Orientation and Characterization of Immobilized Antibodies for Improved Immunoassays (Review). *Biointerphases* **2017**, *12* (2), 02D301.
- (45) Zhang, L.; Salmain, M.; Liedberg, B.; Boujday, S. Naked Eye Immunosensing of Food Biotoxins Using Gold Nanoparticle-Antibody Bioconjugates. *ACS Appl. Nano Mater.* **2019**, *2* (7), 4150–4158.

## 5.4 Supplementary Information

Culture of mouse striatal cell lines, isolation of extracellular vesicles by differential ultracentrifugation and measurements of particles sizes were performed by the Brain C-lab (Institut de Biologie de Paris Seine, IPBS) with which we collaborate.

### 5.4.1 Culture of mouse striatal cell lines

Low passage (< 10) 7Q/7Q and 109Q/109Q cells established from HdhQ111 knock-in mice<sup>1</sup> were cultured in DMEM (Sigma) supplemented with 10% fetal bovine serum, Pen-Strep (10,000 U/ml, 10,000 µg/ml), and 1 mm l-glutamine and grown at 33°C with 5% CO<sub>2</sub>.

### 5.4.2 Isolation of extracellular vesicles by differential ultracentrifugation

We used homozygous striatal cells expressing normal (7Q/7Q) and mutant (109Q/109Q) *Htt* derived from HdhQ111 knock-in mice and handled them as previously described.<sup>1</sup> For extracellular vesicles (EV) isolation, low-passage (P9-P11) cells were cultured in 150 mm<sup>2</sup> dishes. After 48h, cells were washed in DPBS (Life technologies) and further cultured in 20 ml of medium supplemented with 10% EV-depleted fetal bovine serum (FBS) (Life technologies). To obtain FBS EV-depleted medium, DMEM medium supplemented with 20% FBS was centrifugated 18 hours at  $100\,000 \times g$  (31 200 rpm) in a Type 70Ti rotor (Beckman) and subsequently filtered through at 0.2 µm aPES bottle filter (Thermo Fisher Nalgene filter unit). EVs were isolated from conditioned medium 48h after media exchange, when cells had reached 90% confluence (around  $12\text{-}15 \times 10^6$  cells per 150 mm<sup>2</sup> dish). EVs were isolated by differential ultracentrifugation (dUC). Briefly, conditioned medium was centrifuged at  $300 \times g$  for 10 min at 4 °C to remove dead cells and cellular debris. Supernatant was centrifuged at  $2,000 \times g$  for 20 min at 4 °C (2K pellet), transferred to new tubes, and centrifuged in a Type 70Ti rotor (Beckman) for 50 min at  $10\,000 \times g$  (10K pellet). Finally, the supernatant was centrifuged for 100 min at  $100,000 \times g$  (100K pellet). The 2K, 10K and 100K pellets were washed in 20 mL of PBS and re-centrifuged at the same speed before being suspended in 50 µL of sterile DPBS and kept at -80°C for further analysis. Cells were recovered from dishes using 0.25% Trypsin-EDTA (Life technologies) and counted using light microscopy.

### 5.4.3 Particle concentration and size distribution

EVs concentration and size distribution were determined using Zetaview PMX 120 particle tracking analyzer (Particle Metrix, Germany) equipped with CMOS camera. The 100K fractions were diluted 1:10 000 or 1:20 000 in 0.2  $\mu\text{m}$ -filtered DPBS to achieve a concentration of 150-200 particles per frame. All the measurements were carried out at 20°C using the following camera settings: sensitivity 75 and shutter of 75. For each measurement, 11 cell positions were scanned (5 cycles per position) capturing 30 frames per position. After capture, the videos were analyzed by the ZetaView Software 8.04.02 with the following parameters: Maximum particle size 500, Minimum particle size 5, Minimum particle brightness: 20. Before each session, a calibration of instrument is performed using size standard beads (Polystyrene latex (PSL) beads, 102 nm). Size distribution data are presented as mean  $\pm$  SEM. Statistical analyses (Two-way ANOVA) were performed with GraphPad Prism 7 (CA, USA).

### 5.4.4 Materials for sensing EVs

(3-Aminopropyl)triethoxysilane (APTES), p-Phenylenediisothiocyanate (PDITC) were purchased from Sigma-Aldrich (France). Purified anti-mouse/rat CD81 and purified anti-mouse CD63 antibodies were purchased Biolegend (ref 104902 and 143902). BSA was purchased from Euromedex (ref 04-100-812-C).

Silicon wafers <111> were purchased from Sigma-Aldrich (France) and cut into 1x1 cm<sup>2</sup> substrates. For QCM-D measurements, AT-cut quartz crystals coated with a thin SiO<sub>2</sub> film (thickness  $\sim$  50 nm) were purchased from Quantum Design (Les Ulis, France).

Combined QCM-D and LSPR measurements were performed with gold nanostructured AT-cut quartz sensors coated with a thin SiO<sub>2</sub> layer (thickness  $\sim$  5-10 nm) purchased from Insplorion AB (Gothenburg, Sweden). All solutions were prepared using purified Milli-Q water (18 M $\Omega$ , Millipore, France).

### 5.4.5 Surface functionalization

#### 5.4.5.1 Cleaning and oxidation

Silicon wafers and silica coated quartz sensors were prepared following an previously optimized protocol.<sup>2</sup> Briefly, they were cleaned in a 2% Hellmanex solution under mild shaking for 15 h. After rinsing with Milli-Q water, the substrates were dried under nitrogen flow for 5 min. Note that sonication must be avoided to preserve the nanostructures' integrity for combined QCM-D and NPS experiments.

Oxidation was performed for 1 h in a mixture of 37% hydrochloric acid and methanol (v/v = 1), followed with concentrated sulfuric acid treatment for 4 x 15 min.

Then, the substrates were extensively rinsed with Milli-Q water and kept in Milli-Q water for at least 72 h. Prior to further functionalization steps, the substrates were dried under nitrogen flow for 5 min.

#### 5.4.5.2 Silanization with APTES

Amine-terminated surfaces were prepared by the following protocol.<sup>3</sup> Oxidized substrates were immersed in APTES solution (2% v/v in anhydrous toluene) at 90°C for 1 h under argon atmosphere. After the silanization step, the samples were washed with anhydrous toluene twice, dried under nitrogen and heated at 100°C for 1 h.

#### 5.4.5.3 PDITC crosslinking

PDITC crosslinking was performed immediately after APTES functionalization on Si substrates. The sensors were immersed in a freshly prepared solution of PDITC (200 mg/L) in a 9:1 mixture of dimethylformamide (DMF) and pyridine.<sup>3,4</sup> After 1 h, the sensors were removed from the solution and washed once in DMF, twice in ethanol and dried under nitrogen flow. The substrates were kept in a desiccator prior to further experiments.

#### 5.4.5.4 Immunosensor construction

Antibody immobilization was first investigated *ex-situ* using ATR-IR: a 150  $\mu$ L droplet of a solution of antibody (20 mg/L in DPBS) was deposited on an activated silicon wafer for 90 min, washed with DPBS twice and washed with milli-Q water prior to analysis.

For *in-situ* antibody immobilization, an activated sensor was mounted in the QCM-D module and a solution of antibody (20 mg/L in DPBS) was flowed for 40-60 min at 10  $\mu$ L/min. After a washing step with DPBS, non-specific binding was blocked with a solution of DPBS-BSA (0.1%).

#### 5.4.5.5 Extracellular vesicle biosensing

Activated sensors were mounted in the QCM-D chambers and the following measurement cycle was applied. After signal stabilization in DPBS buffer (0), anti-CD81 (1) (or anti-CD63 (1')) antibody was flown over the sensor surface for  $\sim$  45 min. After rinsing with running buffer for 30 min, DPBS-BSA (2) at 0.1% w/v was injected for 30 min to block remaining free adsorption sites. Sensing of EV in DPBS-BSA (3) was performed for 30 to 60 min until reaching signal stabilization, followed by a rinsing step with DPBS-BSA for 30 min.

#### 5.4.5.6 Techniques

#### 5.4.5.7 Quartz Crystal Microbalance with dissipation (QCM-D)

Piezoelectric measurements were performed on AT-cut quartz silica-coated crystals with nominal frequency of 5 MHz (Quantum Design, France). The QCM-D (E4 model, Biolin Scientific, Sweden) was operated in the flow-through mode at 20 °C. The flow rate was adjusted to 10  $\mu$ L/min by using a peristaltic pump. Signal stabilization was carried out with DPBS.

#### 5.4.5.8 Combined Quartz Crystal Microbalance with dissipation (QCM-D) and NanoPlasmonic Sensing (NPS)

The combined QCM-D and NPS measurements were carried out using the Q-Sense E1 module with Q-Sense sapphire window module (Biolin Scientific, Sweden) coupled with the Insplorion Acoulyte module (Insplorion AB, Sweden). In this setup, an optical fiber connected to the Insplorion X-Nano optics unit (Insplorion AB, Sweden) is placed on top of QCM-D module which enables illumination in reflection mode. Measurements were performed on Acoulyte quartz crystal sensors which are QCM-D sensors on which silica-coated gold nanodisks (100 nm in diameter and 20 nm in high) are randomly distributed.

Light interaction with gold nanodisks leads to a collective oscillation of conduction electrons known as Localized Surface Plasmon Resonance (LSPR) resulting in an intense absorption band ( $\lambda_{\max}$ ) localized around 700 nm. At the surface vicinity, refractive index changes will lead to LSPR peak position shifts, referred herein as  $\Delta\lambda_{\max}$ , allowing to monitor biomolecular interactions in real time. Analysis of frequency and dissipation shifts was carried out using the QTools software, version 3.1.33.567 (Biolin Scientific, Sweden). Analysis of LSPR signals was performed using Insploer software, version 1.3.1 (Insploer AB, Sweden).

#### 5.4.5.9 Attenuated Total Reflection-InfraRed (ATR-IR)

ATR-IR spectra were recorded on a Tensor 27 FT-IR spectrometer (Bruker) equipped with a VariGATR™ grazing angle accessory (Harrick scientific). Each spectrum results from the accumulation of 64 scans at 4  $\text{cm}^{-1}$  spectral resolution with baseline correction and  $\text{CO}_2$  correction performed with OPUS software.

#### 5.4.5.10 Water Contact Angle (WCA)

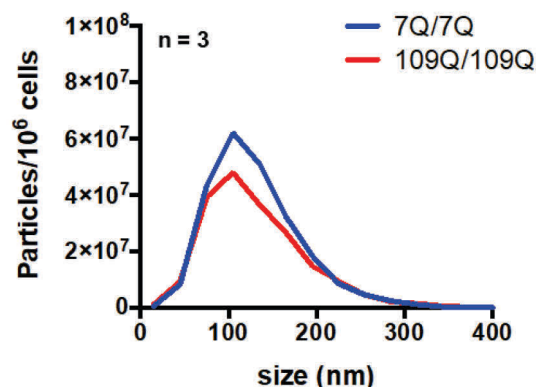
Static water contact angles were measured at room temperature using the sessile drop method and image analysis of the drop profile using Drop Shape Analysis software. The instrument, which uses a CCD camera and an image analysis processor, was purchased from Krüss (Germany). The water (Milli-Q) droplet volume was 1  $\mu\text{L}$  and the contact angle ( $\theta$ ) was measured 5 sec after the drop was deposited on the substrate. For each sample, the reported value is the average of the results obtained on three droplets.

#### 5.4.5.11 X-Ray Photoelectron Spectroscopy (XPS)

XPS analysis were performed on a Scienta Omicron Argus X-ray photoelectron spectrometer, using a monochromated  $\text{AlK}\alpha$  ( $h\nu = 1486.6 \text{ eV}$ ) radiation source having a 280 W electron beam power. The emission of photoelectrons from the sample was analyzed at a takeoff angle of  $45^\circ$  under ultra-high vacuum conditions ( $1 \times 10^{-9} \text{ Pa}$ ). XPS spectra were collected at pass energy of 100 eV for the survey scan and 20 eV for the C1s, O1s, N1s, Si 2p core XPS levels. The peak areas were determined after subtraction of a Shirley background. The spectra were fitted using Casa XPS software and applying a Gaussian/ Lorentzian ratio (G/L) equal to 70:30 and binding energies were calibrated against the  $\text{Si}2\text{p}_{3/2}$  at 99.4 eV.

## 5.4.6 Results and discussion

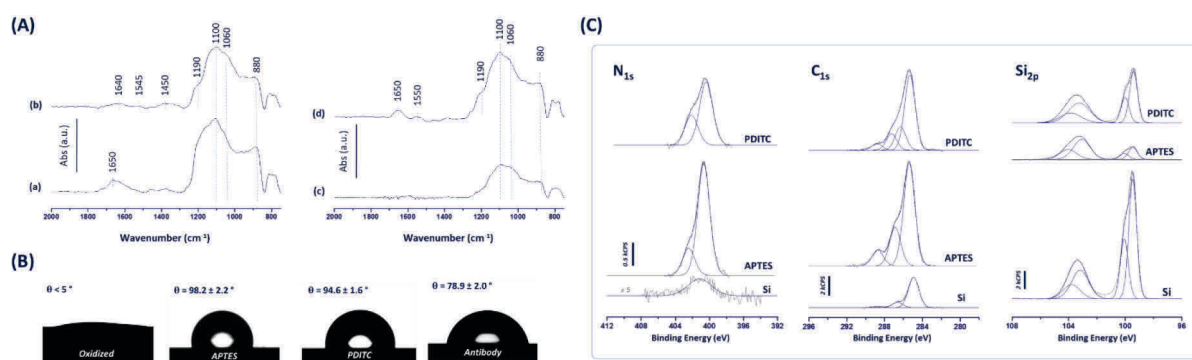
### 5.4.6.1 EV related results



**Figure S5. 1.** (A) Representative size distribution of EVs isolated from 7Q/7Q and 109Q/109Q mouse striatal cells in the 100,000 g fraction upon differential ultracentrifugation and nanoparticle tracking analysis (NTA).

### 5.4.6.2 Surface functionalization

The sensing layer was obtained by sequential treatment of silicon surfaces with (3-aminopropyl)triethoxysilane (APTES) and 1,4-phenylenediisothiocyanate (PDITC) to generate amine-reactive functions for antibody immobilization. Capture layer construction steps were performed ex-situ and monitored by ATR-IR, water contact angle and XPS techniques (**Figure S5. 2**).



**Figure S5. 2.** (A) Baseline-corrected ATR-IR spectra of (a) oxidized Si substrate sequentially treated with (b) APTES, (c) PDITC and (d) antibody and corresponding (B) water contact angle results. (C)  $N_{1s}$ ,  $C_{1s}$  and  $Si_{2p}$  XPS spectra of bare Si substrate, sequentially treated with APTES and PDITC.

In **Table S5. 1** are summarized the ATR-IR bands and assignments for each functionalization step, the corresponding baseline-corrected ATR-IR spectra are presented in **Figure S5. 2**. After cleaning and oxidation procedures, the bands at 1110 and 1060  $\text{cm}^{-1}$  were assigned to a continuous layer of Si-O-Si and the band at 880  $\text{cm}^{-1}$  was attributed to silanol groups. The Si substrates were kept in water in order to increase the number of silanol groups, hence the broad band at 1650  $\text{cm}^{-1}$  was assigned to water adsorbed at the surface. Upon functionalization with APTES, bands were spotted at 1640, 1545 and 1450  $\text{cm}^{-1}$  and were assigned to the terminal amine group, besides a decrease in the silanol band at 880  $\text{cm}^{-1}$  was observed indicating consumption of the surface hydroxyl groups. After crosslinking with PDITC, bands corresponding to the imine group ( $-\text{C}=\text{N}$ ) and to the isothiocyanate function ( $-\text{N}=\text{C}=\text{S}$ ) were not observed. Antibody immobilization was evidenced by the presence of bands at 1660  $\text{cm}^{-1}$  and 1550  $\text{cm}^{-1}$ , attributed to amide I and amide II modes, respectively.

**Table S5. 1.** ATR-IR peaks and assignments for each functionalization step. Corresponding baseline corrected ATR-IR are presented in **Figure S5. 2**.

ATR-IR peaks ( $\text{cm}^{-1}$ )				Assignment
<i>Oxidized Si</i>	<i>APTES</i>	<i>PDITC</i>	<i>Antibody</i>	
1650	-	-	-	H <sub>2</sub> O
-	-	-	1650-1550	Amide I & II
-	1640	-	-	NH <sub>2</sub>
-	1545	-	-	NH <sub>2</sub>
-	1450	-	-	NH <sub>2</sub>
-	1190	-	-	CH <sub>2</sub>
1110	1110	1110	1110	Si-O-Si
1060	1060	1060	1060	Si-O-Si
880	880	880	880	Si-OH



Water contact angle measurement was used to follow changes in surface wettability and properties after each functionalization step, results are shown in **Figure S5. 2**. After cleaning and oxidation, the value for water contact angle was less than  $5^\circ$  indicating a highly hydrophilic surface. Subsequently, grafting of APTES led to an increase in the contact angle value from less than  $5^\circ$  to  $98.2 \pm 2.2^\circ$ , attributed to the formation of APTES layer on the surface.<sup>3,5</sup> After crosslinking with PDITC to generate reactive imine function the water contact angle value was found to be slightly more hydrophilic ( $94.6 \pm 1.6^\circ$ ). Antibody grafting on the surface led to a more hydrophilic surface with decrease in water contact angle with a value of  $78.9 \pm 2.0^\circ$ .

XPS spectra of the subsequent functionalization steps are presented in **Figure S5. 2** and the corresponding atomic compositions are given in **Table S5. 2** with notably the presence of carbon, oxygen, nitrogen and silicon elements.

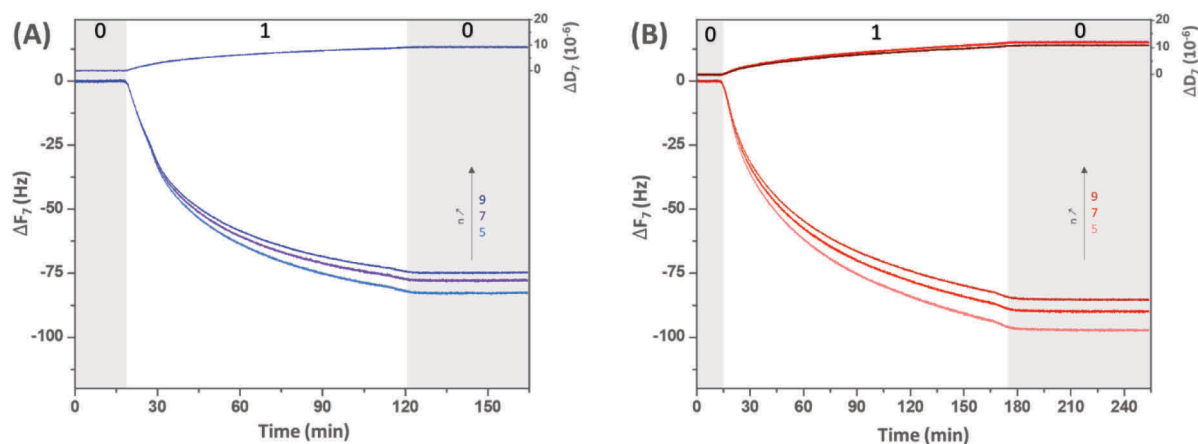
**Table S5. 2.** XPS atomic percentages on bare Si substrate and sequentially functionalized with APTES and PDITC.

Binding energy (eV)	Assignment	Peak Area (At. %)		
		Si	APTES	PDITC
532.8	<b>O 1s</b>	<b>31.9</b>	<b>20.6</b>	<b>23.1</b>
	<b>N 1s</b>	<b>0.3</b>	<b>6.8</b>	<b>4.6</b>
400.6	NH/NH <sub>2</sub>	-	5.5	3.1
402.3	NH <sub>3</sub> <sup>+</sup>	-	1.3	1.5
	<b>C 1s</b>	<b>10.1</b>	<b>52.3</b>	<b>36.3</b>
288.4	-	-	5.3	2.4
286.9	C-N	1.7	12.8	8.2
285.4	C-C / C-H	8.4	34.2	25.7
	<b>Si 2p</b>	<b>57.7</b>	<b>20.3</b>	<b>36.0</b>
103.3	SiO <sub>2</sub>	19.5	16.1	<b>18.5</b>
100	Si 2p <sub>1/2</sub>	12.8	1.6	<b>5.8</b>
99.4	Si 2p <sub>3/2</sub>	25.4	3.2	<b>11.7</b>

**Table S5. 3.** Values for non-specific adsorption of 7Q/7Q-EVs and 109Q/109Q-EVs (40 mg/L) on APTES-coated nanostructured quartz sensors monitored by QCM-D and NPS. Corresponding sensorgrams are presented in **Figure 5. 2**. K values were determined by linear regression of the D-F plots using Origin software.

	7Q/7Q-EVs	109Q/109Q-EVs
$\Delta F_7$ (Hz) *	- 76.5	- 76.3
$\Delta D_7$ ( $10^{-6}$ ) *	8.9	9.1
$\Delta \lambda_{\max}$ (nm)*	0.97	0.75
$K_{LC}$ ( $10^{-9}$ Hz $^{-1}$ )	$86.2 \pm 0.2$	$95.4 \pm 0.2$
$R^2$	0.992	0.992
$K_{HC}$ ( $10^{-9}$ Hz $^{-1}$ )	$123.9 \pm 0.3$	$147.9 \pm 0.2$
$R^2$	0.987	0.992

\*: values were taken after 100 min of injection



**Figure S5. 3.** QCM-D sensorgrams at multiple overtones ( $n_{QCM-D} = 5, 7$  and  $9$ ) for the physisorption of (A) 7Q/7Q EVs and (B) 109Q/109Q EVs on APTES-coated sensor at a flow rate of  $10 \mu\text{L}/\text{min}$ . (0) : DPBS, (1) EV at  $40 \text{ mg}/\text{L}$  in DPBS.

**Table S5. 4.** Frequency and dissipation shifts at different overtones ( $n_{\text{QCM-D}} = 5, 7$  and  $9$ ) measured during physisorption of 7Q/7Q EVs and 109Q/109Q EVs (40 mg/L) on APTES-coated sensors. Corresponding sensorgrams are presented in **Figure S5. 3**.

	7Q/7Q EVs	109Q/109Q EVs
$\Delta F_5$ (Hz) *	- 81.4	- 81.1
$\Delta D_5$ ( $10^{-6}$ ) *	9.1	9.3
$\Delta F_7$ (Hz) *	- 76.5	- 76.3
$\Delta D_7$ ( $10^{-6}$ ) *	8.9	9.1
$\Delta F_9$ (Hz) *	- 73.6	-73.6
$\Delta D_9$ ( $10^{-6}$ ) *	8.8	8.6

\*: values were taken after 100 min of injection

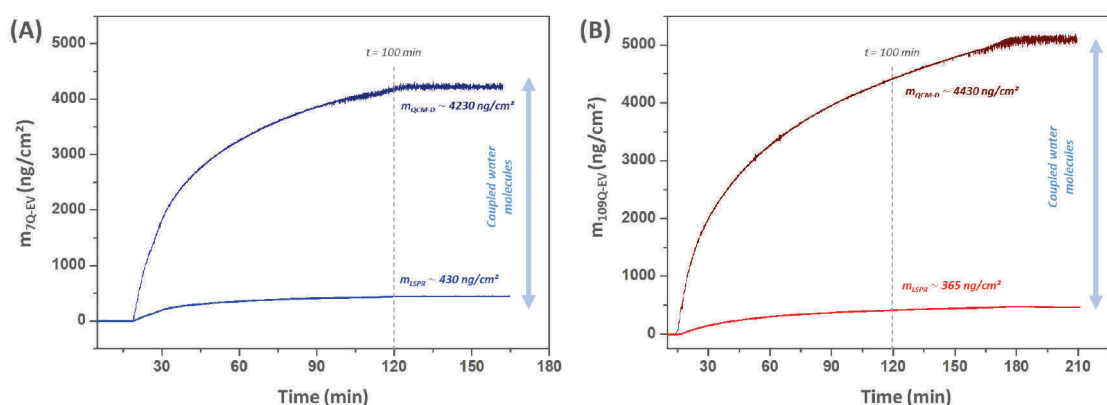
QCM-D data modeling was performed using the Voigt-Voinova model<sup>6,7</sup> included in the Q-Tools software (Biolin Scientific). For the model fitting, the thickness and acoustic mass ( $m_{\text{QCM-D}}$ ) of the adsorbed vesicle layer were calculated using values for the film density of  $1000 \text{ kg/m}^3$  and the viscosity of the bulk aqueous solution of  $0.001 \text{ kg/ms}$ .<sup>8</sup>

The optical mass ( $m_{\text{LSPR}}$ ) was calculated using the following equation adapted from the literature<sup>8,9</sup>:

$$m_{\text{LSPR}} = d_i \frac{\Delta \lambda_{\text{NPS}}}{S_0 (e^{-2d_{i-1}/L_z} - e^{-2(d_{i-1}+d_i)/L_z}) dn_i/d_c}$$

where  $\Delta \lambda_{\text{NPS}}$  is the measured LSPR shift,  $dn_i/d_c$  is the refractive index increment for proteins,  $S_0$  the sensitivity of the substrate,  $d_i$  the thickness of the sample layer determined from QCM-D data and  $d_{i-1}$  is the thickness of the starting layer, *i.e.* APTES layer, and was approximated to nil. The refractive index of the flowing solution (DPBS) was approximated to be the one of an aqueous solution ( $n = 1.33$ ) and the refractive index increment was taken as an average value for lipid vesicles ( $0.16 \text{ cm}^3/\text{g}$ ).<sup>10,11</sup>

The gold nanostructured sensors are coated with a Si<sub>3</sub>N<sub>4</sub> layer, which is subsequently oxidized and displays a LSPR sensitivity ( $S_0$ ) of 60 nm/RIU and an evanescent field decay length ( $L_z$ ) of 30 nm (data provided by the sensor manufacturer).



**Figure S5. 4.** Acoustic mass ( $m_{\text{QCM-D}}$ ) from QCM-D measurement, as determined by Voigt-Voinova modeling and optical mass ( $m_{\text{LSPR}}$ ) calculated from NPS measurement obtained for the adsorption of (A) 7Q/7Q-EVs and (B) 109Q/109Q-EVs on an APTES layer on silica-coated gold nanostructured sensor.

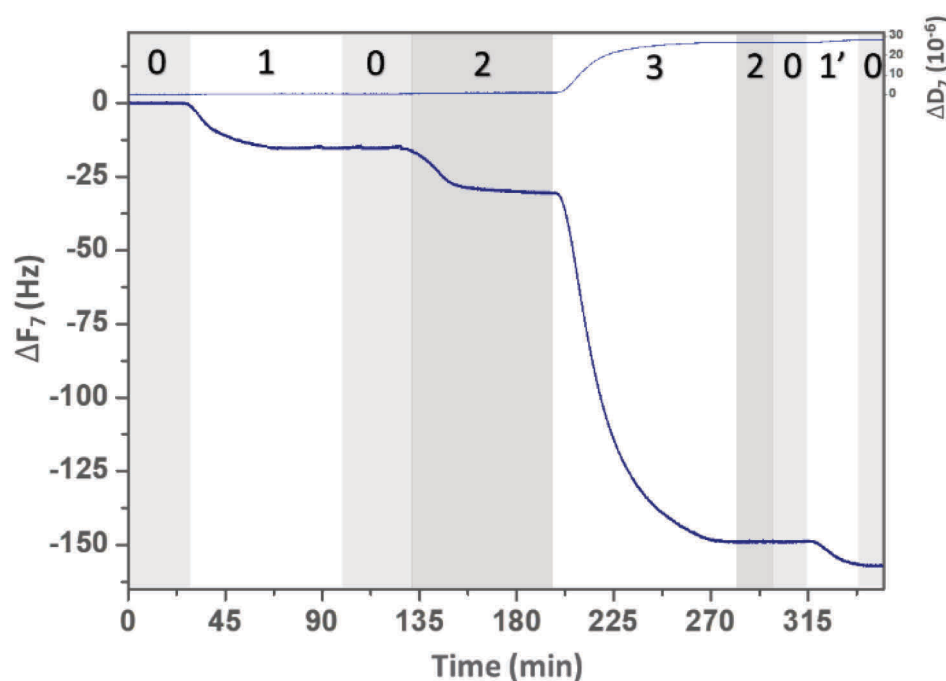
**Table S5. 5.** Values of thicknesses and acoustic masses from QCM-D measurement, as determined by Voigt-Voinova modeling and LSPR peak shifts and corresponding optical masses from NPS measurement for 7Q/7Q-EVs and 109Q/109Q-EVs at 100 min and saturation point for adsorptions of 7Q/7Q-EVs and 109Q/109Q-EVs.

	7Q/7Q-EV		109Q/109Q-EV	
	t = 100min	Saturation	t = 100min	Saturation
Thickness (nm)	36.9	42.7	44.2	51.1
$m_{\text{QCM-D}}$ (ng/cm <sup>2</sup> )	4230	4267	4430	5105
$\Delta\lambda$ (nm)	0.97	1.00	0.75	0.82
$m_{\text{LSPR}}$ (ng/cm <sup>2</sup> )	431	472	364	451

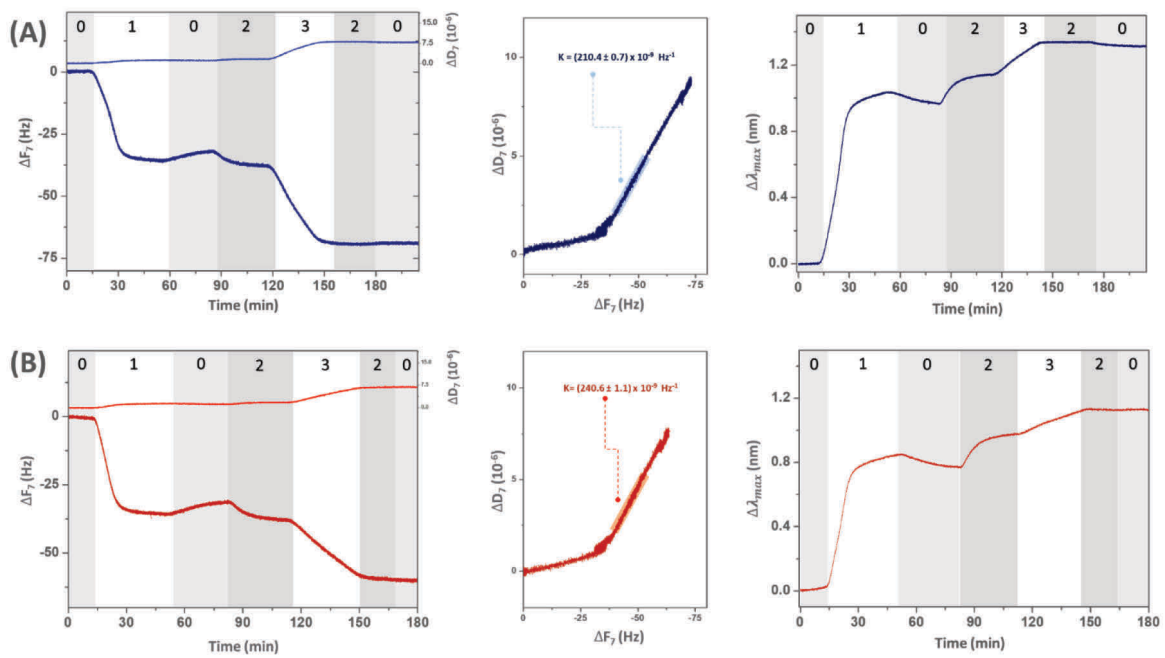
**Table S5. 6.** Piezoelectric immunosensing of 7Q/7Q-EVs ( $1.8 \times 10^{10}$  particles/mL) on anti-CD81 and anti-CD63-coated quartz sensors. Corresponding data are presented in **Figure 5. 3**. K values were determined by linear regression of the D-F plots using Origin software.

	Anti-CD81	Anti-CD63	7Q-EV	
			on anti-CD81	on anti-CD63
$\Delta F$ (Hz)	-15.5	-13.9	- 118.3	- 113.6
$\Delta D$ ( $10^{-6}$ )	0.5	0.5	25.7	25.3
K ( $\times 10^{-9}$ Hz $^{-1}$ )	$31.5 \pm 0.3$	$32.2 \pm 0.4$	$270.7 \pm 0.4$	$270.1 \pm 0.3$
R <sup>2</sup>	0.867	0.773	0.999	0.999

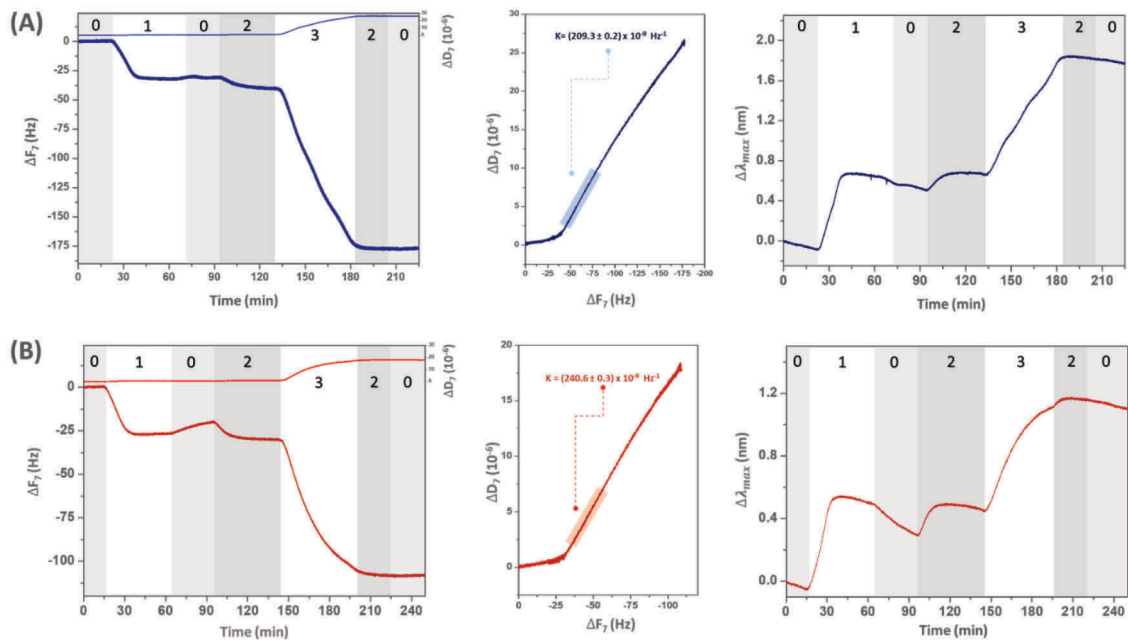
\*: calculated by the Sauerbrey equation (rigid layer)



**Figure S5. 5.** Representative QCM-D sensorgram for the adsorption of 7Q/7Q EVs on planar surface using anti-CD81 as the capture antibody and anti-CD63 as the revelation antibody. Experiment was performed at a flow rate of 10  $\mu$ L/min and  $[EV] = 1.8 \times 10^{10}$  particles/mL. (0): running buffer, (1): anti-CD81, (1'): anti-CD63 antibodies, (2): DPBS-BSA (0.1%) and (3) EV adsorption.



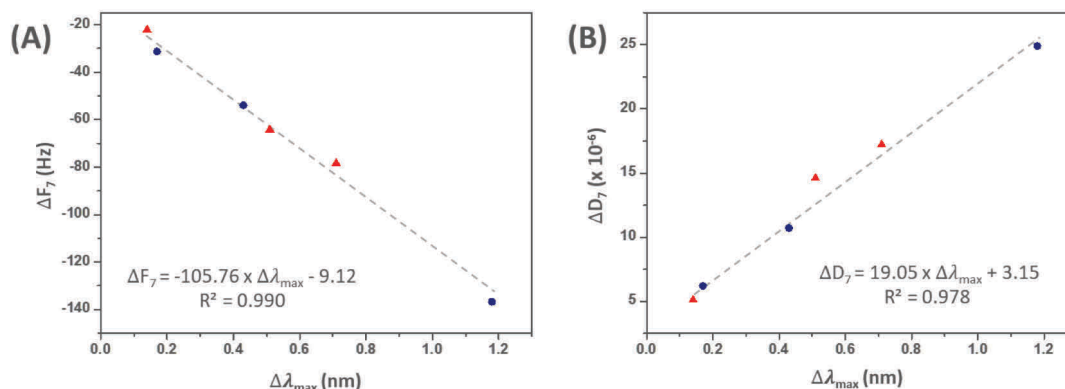
**Figure S5. 6.** Test 2: (A) 7Q/7Q-EV and (B) 109Q/109Q-EV immunosensing on nanostructured sensor with from left to right: QCM-D sensorgram, D-F plot and NPS sensorgram. Experiments were conducted at a flow rate of 10  $\mu\text{L}/\text{min}$ .



**Figure S5. 7.** Test 3: (A) 7Q/7Q-EV and (B) 109Q/109Q-EV immunosensing on nanostructured sensor with from left to right: QCM-D sensorgram, D-F plot and NPS sensorgram. Experiments were conducted at a flow rate of 10  $\mu\text{L}/\text{min}$ .

**Table S5. 7.** Immunosensing of 7Q/7Q-EVs and 109Q/109Q-EVs on anti-CD81-coated nanostructured quartz sensors by QCM-D and NPS. Corresponding sensorgrams are presented in **Figure 5. 4** and **Figure S5. 4-5**.

	Anti-CD81	7Q-EV	109Q-EV
<b>Test 1</b>			
$\Delta F$ (Hz)	$- 29.1 \pm 3.1$	- 54.0	- 64.3
$\Delta D$ ( $10^{-6}$ )	$0.7 \pm 0.1$	10.7	14.6
K ( $\times 10^{-9}$ Hz $^{-1}$ )	$27.0 \pm 10.5$	$201.2 \pm 0.5$	$249.7 \pm 0.9$
R <sup>2</sup>	0.805	0.997	0.996
$\Delta\lambda_{\max}$ (nm)	$0.7 \pm 0.3$	0.43	0.51
<b>Test 2</b>			
$\Delta F$ (Hz)	$- 31.7 \pm 0.4$	- 31.3	- 22.1
$\Delta D$ ( $10^{-6}$ )	1.1	6.2	5.1
K ( $\times 10^{-9}$ Hz $^{-1}$ )	$25.3 \pm 6.6$	$210.4 \pm 0.7$	$240.6 \pm 1.1$
R <sup>2</sup>	0.797	0.991	0.967
$\Delta\lambda_{\max}$ (nm)	$0.9 \pm 0.1$	0.17	0.14
<b>Test 3</b>			
$\Delta F$ (Hz)	$- 25.1 \pm 7.1$	- 136.7	- 78.4
$\Delta D$ ( $10^{-6}$ )	$0.7 \pm 0.2$	24.9	17.2
K ( $\times 10^{-9}$ Hz $^{-1}$ )	$25.1 \pm 2.8$	$209.3 \pm 0.2$	$240.6 \pm 0.3$
R <sup>2</sup>	0.763	0.998	0.997
$\Delta\lambda_{\max}$ (nm)	$0.5 \pm 0.2$	1.18	0.71



**Figure S5. 8.** Linear correlations in (A) frequency change ( $\Delta F_7$ ) to LSPR shift ( $\Delta\lambda_{\max}$ ) and (B) dissipation change ( $\Delta D_7$ ) to LSPR shift ( $\Delta\lambda_{\max}$ ) for the immunosensing of 7Q (▲) and 109Q (●) EVs using anti-CD81 antibody on nanostructured sensor. Linear regression was performed using Origin software.

**Table S5. 8.** K values used for statistical tests presented in **Figure 5. 4D** for the immunosensing of 7Q/7Q-EV and 109Q/109Q-EV on nanostructured quartz sensors. K values were obtained by linear regression of the D-F plots using Origin software and statistical tests were performed using GraphPad Prism 8 software.

	7Q/7Q-EV	109Q/109Q-EV
Test 1		
$K_5$ ( $\times 10^{-9} \text{ Hz}^{-1}$ )	$185.4 \pm 0.2$	$224.9 \pm 0.4$
$R^2$	0.997	0.995
$K_7$ ( $\times 10^{-9} \text{ Hz}^{-1}$ )	$201.2 \pm 0.5$	$249.7 \pm 0.9$
$R^2$	0.997	0.996
$K_9$ ( $\times 10^{-9} \text{ Hz}^{-1}$ )	$222.6 \pm 0.3$	$273.7 \pm 0.5$
$R^2$	0.997	0.995
Test 2		
$K_5$ ( $\times 10^{-9} \text{ Hz}^{-1}$ )	$193.2 \pm 0.4$	$221.0 \pm 0.7$
$R^2$	0.992	0.981
$K_7$ ( $\times 10^{-9} \text{ Hz}^{-1}$ )	$210.4 \pm 0.7$	$240.6 \pm 1.1$
$R^2$	0.991	0.967
$K_9$ ( $\times 10^{-9} \text{ Hz}^{-1}$ )	$220.8 \pm 0.3$	$261.7 \pm 0.5$
$R^2$	0.996	0.992



**Table S5.8.** (continued)

Test 3		
$K_5$ (x $10^{-9}$ Hz $^{-1}$ )	$192.2 \pm 0.3$	$218.6 \pm 0.3$
$R^2$	0.998	0.998
$K_7$ (x $10^{-9}$ Hz $^{-1}$ )	$209.3 \pm 0.2$	$240.6 \pm 0.3$
$R^2$	0.998	0.997
$K_9$ (x $10^{-9}$ Hz $^{-1}$ )	$228.7 \pm 0.2$	$252.8 \pm 0.2$
$R^2$	0.999	0.999
$K_{5-7-9}$ (x $10^{-9}$ Hz $^{-1}$ )	$207.1 \pm 15.1$	$242.6 \pm 18.9$

## References

- (1) Trettel, F.; Rigamonti, D.; Hilditch-Maguire, P.; Wheeler, V. C.; Sharp, A. H.; Persichetti, F.; Cattaneo, E.; MacDonald, M. E. Dominant Phenotypes Produced by the HD Mutation in STHdh(Q111) Striatal Cells. *Hum Mol Genet* **2000**, *9* (19), 2799–2809.
- (2) Huebner, M.; Ben Haddada, M.; Méthivier, C.; Niessner, R.; Knopp, D.; Boujday, S. Layer-by-Layer Generation of PEG-Based Regenerable Immunosensing Surfaces for Small-Sized Analytes. *Biosensors and Bioelectronics* **2015**, *67*, 334–341.
- (3) Zhang, L.; Salmain, M.; Liedberg, B.; Boujday, S. Naked Eye Immunosensing of Food Biotoxins Using Gold Nanoparticle-Antibody Bioconjugates. *ACS Appl. Nano Mater.* **2019**, *2* (7), 4150–4158.
- (4) Salmain, M.; Ghasemi, M.; Boujday, S.; Pradier, C.-M. Elaboration of a Reusable Immunosensor for the Detection of Staphylococcal Enterotoxin A (SEA) in Milk with a Quartz Crystal Microbalance. *Sensors and Actuators B: Chemical* **2012**, *173*, 148–156.
- (5) Ben Haddada, M.; Huebner, M.; Casale, S.; Knopp, D.; Niessner, R.; Salmain, M.; Boujday, S. Gold Nanoparticles Assembly on Silicon and Gold Surfaces: Mechanism, Stability, and Efficiency in Diclofenac Biosensing. *J. Phys. Chem. C* **2016**, *120* (51), 29302–29311.
- (6) Kanazawa, K.; Cho, N.-J. Quartz Crystal Microbalance as a Sensor to Characterize Macromolecular Assembly Dynamics. *Journal of Sensors* **18**.
- (7) Ohlsson, G.; Tigerström, A.; Höök, F.; Kasemo, B. Phase Transitions in Adsorbed Lipid Vesicles Measured Using a Quartz Crystal Microbalance with Dissipation Monitoring. *Soft Matter* **2011**, *7* (22), 10749.
- (8) Ferhan, A. R.; Jackman, J. A.; Cho, N.-J. Integration of Quartz Crystal Microbalance-Dissipation and Reflection-Mode Localized Surface Plasmon Resonance Sensors for Biomacromolecular Interaction Analysis. *Anal. Chem.* **2016**, *88* (24), 12524–12531.
- (9) Jonsson, M. P.; Jönsson, P.; Höök, F. Simultaneous Nanoplasmonic and Quartz Crystal Microbalance Sensing: Analysis of Biomolecular Conformational Changes and Quantification of the Bound Molecular Mass. *Anal. Chem.* **2008**, *80* (21), 7988–7995.
- (10) Theisen, A.; Johann, C.; Deacon, M. . . . P.; Harding, S. . . . E. *Refractive Increment Data-Book for Polymer and Biomolecular Scientists*; Nottingham University Press: Nottingham, 2000.
- (11) Vörös, J. The Density and Refractive Index of Adsorbing Protein Layers. *Biophysical Journal* **2004**, *87* (1), 553–561.



---

---

## **General conclusions and perspectives**

---

---



## General conclusions and perspectives

The objectives of this thesis were multiple, with both fundamental aspects regarding surface functionalization and more applied research projects with the design of label-free immunosensors.

In the first literature review chapter, we highlighted the general features related to IgG type antibody and historical perspective of its applications.

We addressed immunosensors engineering and detection configurations available on planar gold and silica substrates. Indeed, an ideal label-free immunosensor should offer sensitive, specific and reliable detection: IgG surface density and orientation are crucial to achieve the best sensing efficiency. Therefore, the first step towards immunosensor development relies on antibody immobilization which can be achieved *via* antibody modification or surface functionalization.

Hence, the second part of this review chapter comprehensively covered the most investigated methodologies for antibody immobilization on planar gold and silica surfaces *via* physisorption and chemisorption. Chemisorption with affinity-based strategies appear as the best immobilization route as it allows oriented IgG immobilization with high surface density and often display improved sensitivity compared to random physisorption or covalent-based approaches. The last part of this review presented specific features related to immunosensor development such as mixed SAMs and blocking strategies to avoid non-specific interaction and ensure high specificity of the biosensing platform.

These strategies developed on gold and silica surfaces have successfully been implemented within the last decades for label-free immunosensors using various transduction techniques such as Surface Plasmon Resonance (SPR), quartz crystal microbalance (QCM) and electrochemical methods.

In the second and third Chapters, surface functionalization using thiolate Self-Assembled Monolayers (SAMs) on gold surfaces were presented.

In Chapter 2, alkylthiol SAMs bearing alkane ( $\text{CH}_3$ ) and carboxylic acid ( $\text{COOH}$ ) functions with increasing chain length were formed on gold substrate and characterized using Polarization Modulation Infrared Reflection Absorption Spectroscopy (PM-IRRAS), Water Contact Angle (WCA) and X-ray Photoelectron Spectroscopy (XPS). Main results on  $\text{CH}_3$ -SAMs showed that increasing chain length led to the formation of hydrophobic SAMs and to a modification of the coordination mode of sulfur to gold substrate while IR results were quite similar between all investigated samples based on the position of the  $\nu_{\text{CH}_2}^{\text{assym}}$  band.

XPS outcome for short and mid chain length  $\text{CH}_3$ -SAMs ( $n_{\text{CH}_2} = 1,7$ ) revealed the presence of multi-coordinated sulfur at low binding energy ( $\text{S-Au}_{161}$ ) related to molecular adsorption of molecules on the surfaces and to less ordered monolayers, indicating an effect of chain length on the nature of the sulfur-gold interface. SAMs bearing  $\text{COOH}$  terminal groups were able to interact with neighboring molecules through H-bonding and led to hydrophilic monolayers with overall better organization and also to the absence of molecular adsorption for mid length  $\text{COOH}$ -SAMs ( $n_{\text{CH}_2} = 7$ ). In addition, effect of the pH of functionalization, *i.e.* protonation states of the terminal groups, was investigated.

Our study suggested that deprotonation of the terminal groups ( $\text{COO}^-$ ) led to less ordered SAMs with the appearance of multi-coordinated even for longer chain length SAMs ( $n_{\text{CH}_2} = 7, 10$ ) in spite of the low position for the  $\nu_{\text{CH}_2}^{\text{assym}}$  band in IR results. Therefore, we acknowledged that IR analysis was not sufficient to deeply describe SAMs order and XPS appeared to give a more insightful probing of SAMs features such as number of adsorbed species and environment of the chemisorbed thiols molecules with contribution from self-assembly ( $\text{S-Au}_{162}$ ) and molecular adsorption ( $\text{S-Au}_{161}$ ).

Further investigations presented in Chapter 3, were devoted to the evolution of the surface charge of  $\text{COOH}$ -SAMs of increasing chain length. Electrokinetic measurements suggested that chain length influenced the measured zeta potential as well as the IEP values for these SAMs. Furthermore, discrepancies between the surface isoelectric point (IEP) *versus* the  $\text{pK}_a$  of the free molecule in the bulk phase were observed and previously documented in the literature. In future works, we envisioned to investigate the impact of chain length and surface charge on protein uptake with regards to the nature of the protein, *i.e.* size and isoelectric point. In Chapters 4 and 5 were presented two label-free immunosensors respectively for the detection of diclofenac (DCF), *i.e.* a water pollutant, and Extracellular Vesicles (EVs), *i.e.* key mediators in intercellular communication and disease biomarkers.

In Chapter 4, we designed a competitive piezoelectric immunosensor to assay diclofenac in water resources. A sensing layer comprising diclofenac as competitor was built up layer-by-layer on silica-coated quartz sensor chips. Diclofenac immobilization to the amine-terminated PEG layer was investigated using three different activation strategies and the PyBOP chemistry was selected for further experiments. Binding of a highly affine monoclonal antibody to immobilized diclofenac was investigated by combining, in real time, QCM-D and NanoPlasmonic Sensing (NPS).

These measurements allowed to calculate a dissociation constant  $K_D$  of 0.24 nM and an optical mass uptake of 260 ng/cm<sup>2</sup> upon antibody binding, in agreement with the formation of a monolayer of antibodies in a head-on orientation. A hydration percentage of ca. 75% was determined for the antibody layer.

A competitive QCM-D assay was then set up for the detection of diclofenac for which binding of antibody to the DCF-containing sensing layer is inhibited by DCF in solution. After determination of the analytical features of this piezoelectric immunosensor, we conducted the analysis of surface water samples taken at three locations in the rivers Seine and Marne.

The calculated concentrations of DCF in these samples were in good agreement with data published by eaufrance agency. These findings pave the way for a rapid and easy to implement assay of small pollutants in river water.

Future works might use the developed strategy for the detection of other analytes of interest and by using other transduction techniques such as Surface Plasmon Resonance imaging (SPRi) which is a label-free optical method allowing to follow molecular interaction in real time and to work in a multiplex format, *e.g.* different types of ligands and assay parameters.

In Chapter 5, we devised an immunosensor and method based on coupling QCM-D and NPS to precisely characterize EV subtypes across conditions based on their viscoelastic properties, as suggested herein by the comparison of small EVs that are isolated from normal (7Q/7Q) and mutated (109Q/109Q) mouse striatal cells and that are positive for CD81 and CD63.

A sensing layer comprising an antibody directed against the generic exosomal marker CD81 was built up on silica-coated gold nanostructured quartz sensors allowing label-free, simultaneous optical and piezoelectric detection of binding events.

Injection of EV led to a large shift of both the frequency and dissipation, as a result of the specific capture of the EV. The  $\partial D/\partial F$  slope (K value) representing the viscoelastic properties of the layer of EV was found to discriminate small EVs that are secreted by normal or mutated mouse striatal cells.



All in all, 7Q/7Q EVs were found to form a more rigid layer upon physisorption and immunosensing using an anti-CD81 capture antibody in comparison to 109Q/109Q EV.

Our data unveil the potential of label-free immunosensing using QCM-D and NPS to detect changes in viscoelastic properties of EVs subtypes across physiological conditions.

Future investigations regarding the optimization of the sensor with determination of the analytical performances is envisioned, as well as the study of human-derived EVs.

Furthermore, future works related to the investigation of EVs using liquid Atomic Force Microscopy (AFM) is intended to image EV once adsorbed onto the sensor substrate and to determine the mechanical properties of such object.

In conclusion, this thesis manuscript highlighted the experimental strategies employed for the development of immunosensors, ranging from surface functionalization to analyte detection via piezoelectric and optical methods.









---

---

## **Appendixes**

---

---



## Publications and communications

### 1. Publications

**Mazouzi, Y.**; Saliba, V.; Miche, A.; Méthivier, C.; Humblot, V.; Boujday, S. An experimental study of chain length and terminal group effects on the organization of thiolate Self-Assembled Monolayers (SAMs) on gold surfaces. *(to be submitted)*

**Mazouzi, Y.**; Saliba, V.; Humblot, V.; Boujday, S. Effect of surface charge for acid-terminated thiolate Self-Assembled Monolayers (SAMs) on gold. *(in preparation)*

**Mazouzi, Y.**; Sallem, F.; Farina, F.; Loiseau, A.; Rocha Tartaglia, N.; Fontaine, M.; Beito, B.; Salmain, M.; Neri, C.; Boujday, S. A rapid and efficient method for label-free detection of extracellular vesicle subtypes. *(to be submitted)*

**Mazouzi, Y.**; Miche, A.; Loiseau, A.; Beito, B.; Méthivier, C.; Knopp, D.; Salmain, M.; Boujday, S. Design and Analytical Performances of a Diclofenac Biosensor for Water Resources Monitoring. *ACS Sens.* **2021**, 6, 9, 3485–3493.

Pellas, V.; Hu, D.; **Mazouzi, Y.**; Mimoun, Y.; Blanchard, J.; Guibert, C.; Salmain, M.; Boujday, S. Gold Nanorods for LSPR Biosensing: Synthesis, Coating by Silica, and Bioanalytical Applications. *Biosensors* **2020**, 10 (10), 146.

Zhang, L.; **Mazouzi, Y.**; Salmain, M.; Liedberg, B.; Boujday, S. Antibody-Gold Nanoparticle Bioconjugates for Biosensors: Synthesis, Characterization and Selected Applications. *Biosens. Bioelectron.* **2020**, 165, 112370.

Loiseau, A.; Zhang, L.; Hu, D.; Salmain, M.; **Mazouzi, Y.**; Flack, R.; Liedberg, B.; Boujday, S. Core-Shell Gold/Silver Nanoparticles for Localized Surface Plasmon Resonance-Based Naked-Eye Toxin Biosensing. *ACS Appl. Mater. Interfaces* **2019**, 11 (50), 46462–46471.

### 2. Oral and poster communications

#### *Oral presentations*

**Mazouzi, Y.** *et al.* Design and analytical performances of a diclofenac biosensor for water resources monitoring. Journées plénières GdR B2i, Toulouse – **September 2021**.

**Mazouzi, Y.** *et al.* Understanding the organic-inorganic interface of functional molecules on surfaces for biological applications. Doctoral School Days (JED 397), Paris - **November 2020**.

**Mazouzi, Y.** *et al.* Apport de la Spectroscopie de photoelectrons par rayons X pour la fonctionnalisation de surface: adsorption de thiols fonctionnels sur or. Journées de Spectroscopies d'Electrons (JSE), Paris – **January 2020**.

**Mazouzi, Y.** *et al.* Quartz Crystal Microbalance with dissipation (QCM-D) combined with NanoPlasmonic Sensing (NPS) for label-free immunosensing and precision profiling of extracellular vesicles. Biosensor Congress 2020, Korea. **Cancelled participation** (Covid-19).



### *Poster presentations*

**Mazouzi, Y. et al.** Understanding the organic-inorganic interface of functional molecules on surfaces for biological applications. Doctoral School Days (JED397), Paris – **November 2020**.

**Mazouzi, Y. et al.** Investigating effects of chain length and terminal group on the organization of thiolate Self-Assembled Monolayers (SAMs) on gold surfaces. Conférence Internationale CNano – SFNano, Dijon (France) – **December 2019**.

**Mazouzi, Y. et al.** Organization of thiolated SAMs on gold: Effect of chain length and terminal group. Ecole d'été BIOSURF – GdR B2i, Porquerolles – **June 2019**.

## PhD-related activities

### *Teaching. Sorbonne University – Chemistry Department (UFR 926)*

Chemistry tutorials for undergraduate and graduate students (195 hours)

- ✧ Licence 1 – Chimie des Solutions (**1CI002**) – Travaux Dirigés (TD) et Travaux Pratiques (TP)
- ✧ Licence 3 – Matériaux Inorganiques: synthèses, propriétés, cristallographie et diffraction (**3CI013**) – Travaux Pratiques
- ✧ Master 1 – Matériaux, Surfaces et Interface (**4CI703**) – Travaux Pratiques
- ✧ Master 2 – Plasmonics and nano-optics for Chemistry & BioInterfaces (**5P52G**)

### *GdR Or-Nano*

- ▲ Communication Manager: May 2019 – Today
  - ✧ Management of the LinkedIn page
  - ✧ Management of the news section (website)

### *Doctoral School 397 : Materials Physics and Chemistry. Sorbonne University*

- ▲ Elected PhD representative: December 2018 – November 2020
  - ✧ Member of the ED397 council
  - ✧ Jury member for the attribution of doctoral grants
  - ✧ Organization of the Doctoral School Days (2 days conference)

### *Laboratoire de Réactivité de Surface (LRS). Sorbonne University*

- ▲ PhD representative in the ACTS team (Improvement of Working and Safety Conditions): May 2019 – December 2020
- ▲ Communication manager – LinkedIn: December 2019 – Today
- ▲ Science fair stand: October 2018 & 2019
  - ✧ Co-animation of a stand for the science festival: "Escape game: in search of the mystery molecule"

### *International Chemistry Olympiad (ICHO)*

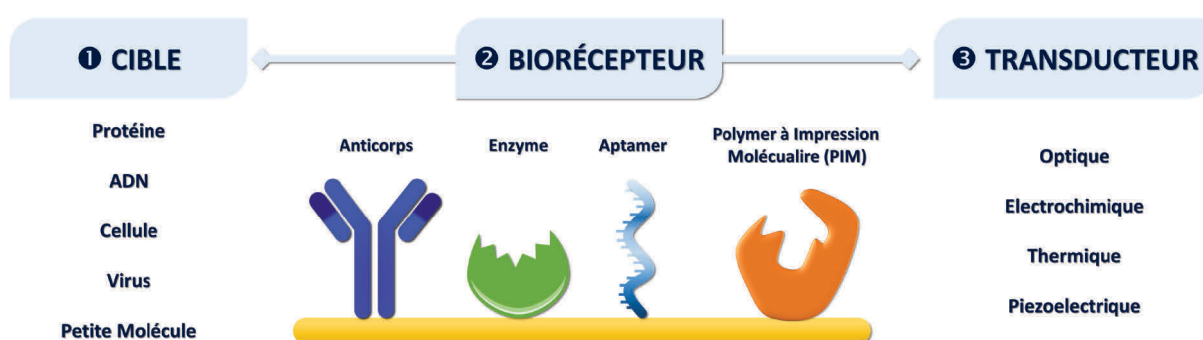
- ▲ Lab Manager: July 2019
  - ✧ Laboratory Inspection & Supervision of the practical exam

## Thesis' synopsis (French)

La détection rapide et sensible d'analytes est cruciale dans la société actuelle, comme l'illustre le développement récent de biocapteurs liés au SARS-Cov2.

Les biocapteurs sont des dispositifs analytiques capables de détecter et de quantifier spécifiquement des cibles d'intérêt dans des milieux complexes.

Quelle que soit l'application envisagée, la composition du biocapteur comprend généralement : un biorécepteur capable de la détecter de manière spécifique et sensible par reconnaissance moléculaire, et un transducteur qui traduira le phénomène de reconnaissance en un signal mesurable par l'expérimentateur.



**Figure 1.** Représentation schématique de la composition d'un biocapteur

Comme il n'existe pas d'approche universelle pour l'ingénierie des biocapteurs, l'élaboration d'une couche de détection est cruciale pour obtenir des plateformes de détection hautement spécifiques et sensibles. Il est donc impératif de maîtriser l'immobilisation du biorécepteur ainsi que sa densité et son accessibilité. Ainsi, il est souvent nécessaire de conférer une fonctionnalité à la surface pour permettre le greffage du biorécepteur tout en évitant les adsorptions non spécifiques sur la surface du capteur qui induiraient de faux positifs.

Les immunocapteurs, *i.e.* les biocapteurs qui utilisent des anticorps comme biorécepteurs, sont l'une des classes de biocapteurs les plus populaires, car les anticorps offrent une grande affinité envers un analyte donné avec de grandes spécificité et sélectivité. Cependant, l'adsorption d'anticorps sur des surfaces implique de nombreux défis à relever, tels que la maîtrise du greffage, la densité et l'orientation des anticorps avec une capacité de reconnaissance conservée. L'immobilisation des anticorps sur des surfaces planes peut être abordée à l'aide de diverses stratégies.

L'adsorption peut simplement reposer sur la physisorption de l'anticorps sur la surface ou adopter des voies plus élaborées *via* la chimisorption de l'anticorps. Cette dernière est souvent préférée, car elle offre un meilleur greffage de l'anticorps et une capacité de bio-reconnaissance accrue. Les stratégies de chimisorption impliquent la modification de groupes fonctionnels de l'anticorps ou la modification de la surface par des approches covalentes ou basées sur l'affinité. Les monocouches auto-assemblées, de l'anglais *self-assembled monolayers* (SAMs), sont l'une des stratégies les plus étudiées pour fonctionnaliser des surfaces, car elles offrent une grande polyvalence liée à la nature des molécules organiques d'ancrage ou des substrats qui composent les SAMs. Allant des alcanethiols sur des surfaces métalliques (*e.g.* or) aux organosilanes sur des surfaces hydroxylées (*e.g.* SiO<sub>2</sub>/Si) et aux acides carboxyliques et phosphates d'alkyle sur des substrats d'oxyde, les SAMs peuvent être employées pour attacher des groupes fonctionnels et fournir des points d'ancrage robustes pour l'immobilisation des anticorps.

Ce manuscrit de thèse est composé de cinq chapitres abordant des objectifs qui vont des aspects fondamentaux aux travaux de recherche plus appliqués. La compréhension fondamentale de l'interface organique-inorganique lors de l'adsorption de molécules fonctionnelles à l'interface solide-liquide est d'abord abordée, puis suivie par des travaux de recherche applicatifs liés au développement d'immunocapteurs utilisant des méthodes de transduction piézoélectrique et optique pour la détection de divers analytes.

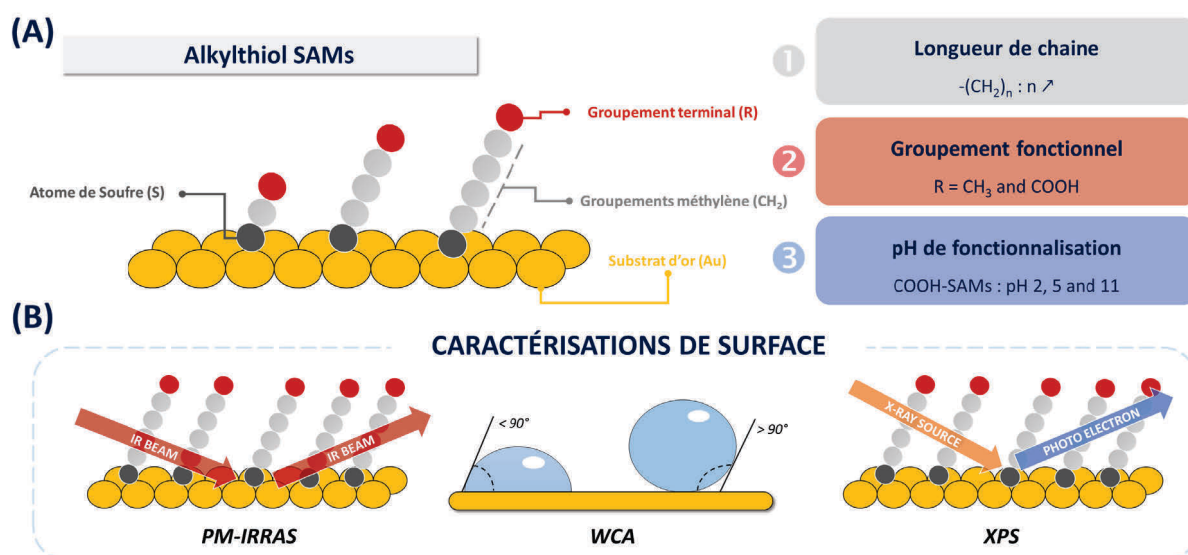
Dans le premier chapitre consacré à la revue de la littérature, nous avons souligné les caractéristiques générales liées aux anticorps de type immunoglobuline G (IgG) et la perspective historique de leurs applications. Nous avons abordé l'ingénierie des immunocapteurs et les configurations de détection disponibles sur des substrats plans en or et en silice. En effet, un immunocapteur idéal sans marqueur, dit *label-free*, doit offrir une détection sensible, spécifique et fiable. La densité et l'orientation à la surface des IgG sont cruciales pour obtenir la meilleure efficacité de détection. Par conséquent, la première étape du développement d'un immunocapteur repose sur l'immobilisation des anticorps, qui peut être réalisée par la modification de l'anticorps ou en employant la fonctionnalisation de surface. La deuxième partie de ce chapitre couvre les méthodologies les plus étudiées pour l'immobilisation d'anticorps sur des surfaces planes d'or et de silice par physisorption et chimisorption.

La chimisorption avec des stratégies basées sur l'affinité apparaît comme la meilleure voie d'immobilisation, car elle permet une immobilisation orientée des IgG avec une densité de

surface élevée et présente souvent une meilleure sensibilité par rapport à la physisorption aléatoire ou aux approches covalentes. La dernière partie de cette revue présente les caractéristiques spécifiques liées au développement d'immunocapteurs telles que les SAMs mixtes et les stratégies de blocage pour éviter les interactions non spécifiques et assurer une haute spécificité de la plateforme de biodétection. Ces stratégies développées sur des surfaces d'or et de silice ont été mises en œuvre avec succès au cours des dernières décennies pour des immunocapteurs sans marqueurs en utilisant diverses techniques de transduction telles que la résonance plasmonique de surface (SPR), la microbalance à cristal de quartz (QCM) et les méthodes électrochimiques.

Dans les deuxième et troisième chapitres, la fonctionnalisation de surface à l'aide de monocouches auto-assemblées (SAMs) de thiols sur des surfaces d'or est présentée.

Dans le chapitre 2, des SAMs d'alkylthiol portant des fonctions alcane ( $\text{CH}_3$ ) et acide carboxylique ( $\text{COOH}$ ) avec une longueur de chaîne croissante ont été formées sur des substrats d'or et caractérisées en utilisant la spectroscopie d'absorption par réflexion infrarouge à modulation de polarisation (PM-IRRAS), la mesure de l'angle de contact (WCA) et la spectroscopie de photoélectrons-X (XPS).



**Figure 2.** (A) Stratégie expérimentale pour la formation de monocouches auto-assemblées de thiol sur or, avec l'étude des effets de : ① la longueur de chaîne, ② les groupements fonctionnels et du ③ pH de fonctionnalisation. (B) Caractérisations de surface des SAMs par PM-IRRAS, WCA et XPS.

Les principaux résultats sur les CH<sub>3</sub>-SAMs ont montré que l'augmentation de la longueur de la chaîne a conduit à la formation de SAMs hydrophobes et à une modification du mode de coordination du soufre au substrat d'or tandis que les résultats infrarouges (IR) étaient assez similaires entre tous les échantillons étudiés basés sur la position de la bande infrarouge liée à la vibration asymétrique des groupements méthylène ( $\nu_{CH_2}^{asym}$ ).

Les résultats XPS pour les CH<sub>3</sub>-SAMs à chaîne courte et moyenne ( $n_{CH_2} = 1,7$ ) ont révélé la présence de soufre multi-coordonné à faible énergie de liaison (S-Au<sub>161</sub>) liée à l'adsorption moléculaire des molécules sur les surfaces et à des monocouches moins ordonnées, indiquant un effet de la longueur de la chaîne sur la nature de l'interface soufre-or.

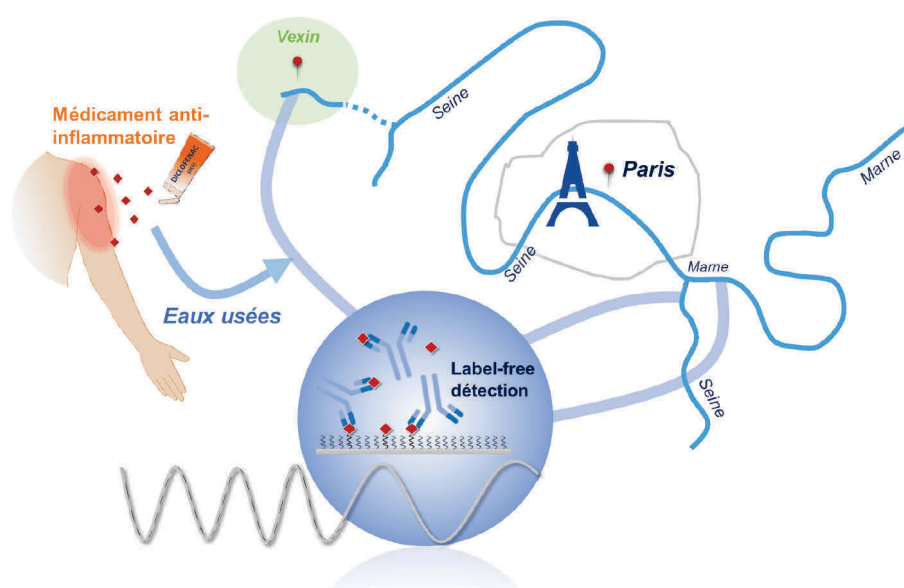
Les SAMs portant des groupes terminaux COOH étaient capables d'interagir avec les molécules voisines par des liaisons H et ont conduit à des monocouches hydrophiles avec une meilleure organisation globale et également à l'absence d'adsorption moléculaire pour les COOH-SAMs de longueur moyenne ( $n_{CH_2} = 7$ ).

De plus, l'effet du pH lors de l'étape de fonctionnalisation, *i.e.* les états de protonation des groupements terminaux, a été étudié. Notre étude a suggéré que la déprotonation des groupes terminaux (COO<sup>-</sup>) conduit à des SAMs moins ordonnées avec l'apparition de soufre multi-coordonné, même pour les SAMs de plus grande longueur de chaîne ( $n_{CH_2} = 7, 10$ ) malgré la position basse de la bande  $\nu_{CH_2}^{asym}$  en IR montrant l'apport des liaisons H en bout de chaîne dans l'organisation des SAMs. Cela montre également que l'analyse IR n'est pas suffisante pour décrire en profondeur l'ordre des SAMs et que la spectroscopie XPS donnerait un aperçu plus représentatif des caractéristiques des SAMs telles que le nombre d'espèces adsorbées et l'environnement des molécules de thiols chimisorbées en discriminant la contribution de l'auto-assemblage (S-Au<sub>162</sub>) de celle de l'adsorption moléculaire (S-Au<sub>161</sub>). Les résultats de ce chapitre sont soumis pour publication au Journal of Physical Chemistry.

D'autres recherches, présentées dans le chapitre 3, ont été consacrées à l'étude de l'évolution de la charge de surface de COOH-SAMs de longueur de chaîne croissante. Les mesures électrocinétiques suggèrent que la longueur de la chaîne influence le potentiel zêta mesuré ainsi que les valeurs du point isoelectrique (IEP) pour ces SAMs. De plus, des divergences entre l'IEP et le pKa de la molécule libre en solution ont été observées. Dans des travaux futurs, nous envisageons d'étudier l'impact de la longueur de la chaîne et de la charge de surface sur l'adsorption des protéines.

Les chapitres 4 et 5 présentent deux immunocapteurs « label-free » pour la détection du diclofénac (DCF), un polluant de l'eau, et des vésicules extracellulaires (EVs), des médiateurs clés de la communication intercellulaire et des biomarqueurs de maladies.

Dans le chapitre 4, nous avons conçu un immunocapteur piézoélectrique compétitif pour quantifier le DCF dans les eaux de rivières. Une couche de détection comprenant du diclofénac comme compétiteur a été construite couche par couche sur des puces de détection en quartz recouvertes de silice.



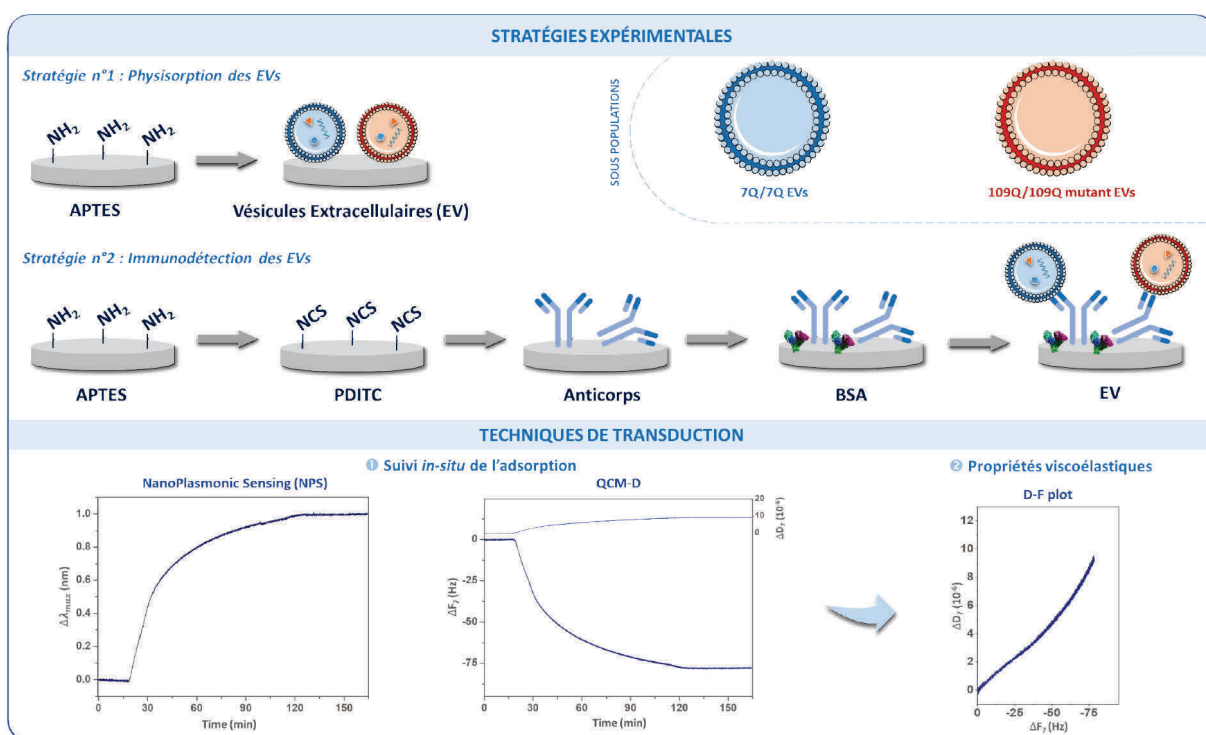
**Figure 3.** Stratégie générale pour la quantification du DCF dans les eaux de rivières.

L'immobilisation du DCF sur la couche de PEG à terminaison amine a été étudiée en utilisant trois stratégies d'activation différentes et la chimie utilisant le benzotriazol-1-yloxytripyrrolidinophosphonium hexafluorophosphate (PyBOP) a été sélectionnée pour les expériences suivantes. En effet pour améliorer le greffage du DCF sur la surface portant des groupements amines, l'activation des groupements acides carboxyliques est généralement étudiée en utilisant des agents « crosslinker ». La liaison d'un anticorps monoclonal au DCF préalablement immobilisé a été étudiée en combinant, en temps réel, la QCM-D et la détection NanoPlasmonic (NPS). Ces mesures ont permis de calculer une constante de dissociation  $K_D$  de 0,24 nM et une masse optique de masse de 260 ng/cm<sup>2</sup> lors de la reconnaissance anticorps-DCF, en accord avec la formation d'une monocouche d'anticorps avec une orientation « head-on ». De plus, un pourcentage d'hydratation d'environ 75 % a été déterminé pour la couche d'anticorps, en accord avec des travaux préalablement menés dans la littérature.

Après avoir déterminé les caractéristiques analytiques de cet immunocapteur piézoélectrique, nous avons procédé à l'analyse d'échantillons d'eau de surface prélevés à trois endroits dans les eaux de rivières, *i.e.* Seine et Marne.

Les concentrations calculées de DCF dans ces échantillons étaient en bon accord avec les données publiées par l'agence eaufrance. Ces résultats ouvrent la voie à un dosage rapide et facile à mettre en œuvre pour la détection de polluants. Les travaux futurs pourraient utiliser la stratégie développée pour la détection d'autres analytes d'intérêt et en utilisant d'autres techniques de transduction telles que l'imagerie par résonance plasmonique de surface (SPRi) qui est une méthode optique sans marqueur permettant de suivre l'interaction moléculaire en temps réel et de travailler dans un format multiplex, *i.e.* différents types de ligands et de paramètres expérimentaux. Ces travaux ont été publiés dans le journal ACS Sensors (ACS Sens. 2021, 6, 9, 3485–3493)

Dans le chapitre 5, nous avons conçu un immunocapteur et une méthode basés sur le couplage de la QCM-D et de la NPS pour caractériser précisément les sous populations d'EVs selon leurs propriétés viscoélastiques, comme le suggère la comparaison de petites EVs isolés de cellules striatales de souris normales (7Q/7Q) et mutées (109Q/109Q) et positifs pour les marqueurs transmembranaires CD81 et CD63.



**Figure 4.** Stratégies expérimentales pour l'étude des EVs par physisorption et immunodétection en utilisant une approche combinée employant QCM-D et NPS.



Une couche de détection comprenant un anticorps dirigé contre le marqueur exosomal générique CD81 a été construite sur des capteurs en quartz nanostructurés en or recouverts de silice permettant une détection optique et piézoélectrique simultanée, sans marqueur, des événements de reconnaissance biomoléculaire.

L'injection d'EVs a conduit à un important décalage à la fois de la fréquence et de la dissipation, en raison de la capture spécifique des EVs. La pente  $\partial D/\partial F$  (valeur K) qui représente les propriétés viscoélastiques de la couche d'EV a permis de discriminer les petites EV qui sont sécrétés par les cellules striatales normales ou mutées de la souris. Dans l'ensemble, on a constaté que les EVs 7Q/7Q formaient une couche plus rigide après physisorption et immunodétection à l'aide d'un anticorps de capture anti-CD81, par rapport aux EVs 109Q/109Q. Nos données dévoilent le potentiel de l'immunodétection « label-free » en utilisant le QCM-D et le NPS pour détecter les changements des propriétés viscoélastiques des sous-types d'EVs dans des conditions physiologiques. Les résultats de ce chapitre sont soumis pour publication dans le journal Chemical Communication.

Des recherches futures concernant l'optimisation du capteur avec la détermination des performances analytiques sont envisagées, ainsi que l'étude des EVs d'origine humaine.

En outre, des travaux futurs concernant l'étude des EVs à l'aide de la microscopie à force atomique (AFM) liquide sont prévus afin d'imager les EVs une fois adsorbés sur le substrat du capteur et de déterminer les propriétés mécaniques de cet objet.

En conclusion, ce manuscrit de thèse met en évidence les stratégies expérimentales employées pour le développement d'immunocapteurs, allant de la fonctionnalisation de surface à la détection d'analyte *via* des méthodes piézoélectrique et optique.

“When in doubt, go to the library.”

---

**Ron Weasley**



## **Développement d'immunocapteurs "label-free" : de la fonctionnalisation à la détection d'analyte**

### Résumé :

La détection rapide d'analytes est cruciale dans la société actuelle, comme l'illustre le développement récent de biocapteurs liés au SARS-Cov2. La conception d'un biocapteur débute par la fonctionnalisation de la surface du transducteur, suivie par la maîtrise de l'immobilisation du biorécepteur et enfin la mesure des performances analytique du dispositif final. Dans ce travail, la compréhension fondamentale de l'interface organique-inorganique lors de la première étape de l'élaboration, *i.e.* : l'adsorption de molécules fonctionnelles à l'interface solide-liquide est d'abord abordée, puis la continuité de l'approche incluant l'immobilisation du biorécepteur et la biodétection est effectuée au travers de travaux de recherche applicatifs liés au développement d'immunocapteurs d'analytes d'intérêt répondant à des enjeux environnementaux et de santé publique. Dans la première partie, nous avons démontré que la longueur de la chaîne et les groupes terminaux (*i.e.* méthyle et carboxylique) de thiols fonctionnels sur surface d'or influençaient l'ordre et la nature de l'interface soufre-or, comme le montrent l'IR de surface, les mesures d'angle de contact (WCA) et la spectroscopie de photoélectrons X (XPS). De plus, des mesures électrocinétiques ont démontrées que la longueur de la chaîne des SAMs carboxyliques influençait le point isoélectrique de surface (IEP). En outre, nous avons développé des immunocapteurs label-free en utilisant des méthodes de transduction piézoélectrique et optique, à savoir la microbalance à cristal de quartz avec dissipation (QCM-D) et la détection nanoplasmonique (NPS). Nous présentons d'abord un immunocapteur piézoélectrique compétitif qui a été utilisé avec succès pour quantifier le diclofénac, un polluant pharmaceutique, dans les eaux de surface de la Seine. Enfin, nous présentons une approche simultanée employant les méthodes QCM-D et NPS pour la détection de vésicules extracellulaires (EV). Nos données dévoilent le potentiel de cette méthode d'immunodétection pour détecter les changements dans les propriétés viscoélastiques des sous-types d'EVs dans des conditions physiologiques.

Mots clés : Fonctionnalisation de surface, biocapteur, immunocapteur, or, monocouches auto-assemblées, diclofénac, vésicules extracellulaires

## **Design of label-free immunosensors: from surface functionalization to analyte detection**

### Abstract:

Rapid detection of analytes is crucial in today's society, as illustrated by the recent development of SARS-Cov2-related biosensors. The design of a biosensor begins with the functionalization of the transducer surface, followed by the controlled immobilization of the bioreceptor and finally the measurement of the analytical performances of the final device.

In this work, the fundamental understanding of the organic-inorganic interface during the first step of the elaboration, *i.e.* the adsorption of functional molecules at the solid-liquid interface is first addressed, then the continuity of the approach, including the immobilization of the bioreceptor and the biosensing, is carried out through applied research works related to the development of immunosensors for analytes of interest addressing environmental and public health issues. Firstly, we demonstrated that the chain length and the terminal groups (*i.e.* methyl and carboxylic) of functional thiols on gold surface influenced the order and nature of the sulfur-gold interface, as shown by surface IR, contact angle measurements (WCA) and X-ray photoelectron spectroscopy (XPS). In addition, electrokinetic measurements demonstrated that the chain length of carboxylic SAMs influenced the surface isoelectric point (IEP). Furthermore, we have developed label-free immunosensors using piezoelectric and optical transduction methods, namely quartz crystal microbalance with dissipation (QCM-D) and nanoplasmonic detection (NPS). We first present a competitive piezoelectric immunosensor that has been successfully used to quantify the pharmaceutical pollutant diclofenac in surface waters of the Seine River. Finally, we present a simultaneous approach employing QCM-D and NPS methods for the detection of extracellular vesicles (EV). Our data unveil the potential of this immunodetection method to detect changes in the viscoelastic properties of EVs subtypes under physiological conditions.

Key words: Surface functionalization, biosensor, immunosensor, gold, self-assembled monolayers, diclofenac, extracellular vesicles

